OPTIMISATION OF GEOTHERMAL RESOURCES IN KENYA BY ENERGY AND EXERGY CONCEPT LINKING SURFACE AND SUB-SURFACE THROUGH RESERVOIR-WELLBORE COUPLING

アルヴィン, キプロノ, ベット

KYUSHU UNIVERSITY

九州大学

A DOCTORAL DISSERTATION

By

Alvin Kiprono BETT

January, 2022

OPTIMISATION OF GEOTHERMAL RESOURCES IN KENYA BY ENERGY AND EXERGY CONCEPT LINKING SURFACE AND SUB-SURFACE THROUGH RESERVOIR-WELLBORE COUPLING

Submitted by

Alvin Kiprono Bett

Dissertation Submitted in Partial Fulfilment of the

Requirements for The Degree of

Doctor of Engineering

(Earth Resources Engineering)

Supervised by

Associate Professor Dr. Saeid Jalilinasrabady

Energy Resources Engineering Laboratory

Department of Earth Resources Engineering,

Graduate School of Engineering, Kyushu University, Japan,

January, 2022

Faith is taking the first step even when you don't see the whole staircase," Dr. Martin Luther King Jnr.

Abstract

Geothermal energy is ubiquitous, and its utilisation has increased rapidly in the last three decades. The main merits of geothermal energy are low carbon emission, renewability, and sustainability. In the Kenyan case, geothermal energy has displaced hydroelectric power as a reliable baseload due to frequent droughts. Kenya is in the Eastern part of Africa and has geothermal potential exceeding 7 GWe along the East African Rift Valley (EARV). In 2021, Kenya had a peak electricity demand of 2.036 GWe, to which geothermal energy supplied 42%. Historically, geothermal energy exploration started around 1950s in Olkaria and Bogoria regions, and two wells were drilled in Olkaria. The first single flash (SF), Olkaria I power plant, was commissioned in 1981. Kenya's mapped and developed geothermal prospects occur mainly along EARV; other prospects on Western highlands of EARV were studied and updated in the geothermal resource map using geochemistry and Quantum Geographic Information System (QGIS). The utilisation of extracted geofluid includes direct and indirect uses. For indirect applications, the hot fluid from the reservoir is separated into steam when pressure is decreased (flashed) at the wellhead. The steam drives the turbine for power generation, and the separated brine is reinjected back to the reservoir. Flash units are the dominant types of geothermal power plants globally as single flash or double flash. In Kenya, most power plants are operated as single flash. For sustainable development of geothermal resources, there is a need to consider an optimisation strategy; previously, energy and exergy analysis has been applied to optimise the single flash units in Olkaria, Olkaria I, II, and IV power plants. Useable energy is the heat available at the wellhead, and in comparison, exergy is the applicable work that can be achieved from a system at a given state in a defined environment. Since different wells have varied wellhead pressures and geochemistry properties, averaging them at the steam separator can lead to energy loss. At the separator, various safety constraints are usually applied to prevent silica scaling and encourage a single steam pipeline strategy of steam gathering. This study utilised exergy analysis as a tool for informing plant performance and capacity to support additional power generation via topping up and binary units. From the results, the available exergy in Olkaria can generate additional power by topping unit using a backpressure turbine between the separator and condensing steam turbine or Organic Rankine cycles utilising the separated hot brine as the heat source. In addition, optimisation of geothermal resources is not limited to the surface only. There is a need to

understand exergetic reservoir conditions to inform how best to set sustainable wellhead exergy parameters. In this research, the wellbore simulator was used to couple the reservoir to the wellbore. In previous studies, simulations have been conducted independently for the reservoir and wellbore. Studies have not linked the surface and sub-surface in Olkaria and other geothermal fields worldwide. The wellbore simulator was used to connect the wellhead and the reservoir simulated pressure and temperature logs for Olkaria Domes in Olkaria, a liquid-dominated geothermal field. The simulation results enabled exergy values at any depth to be calculated using the pressure and temperature values between the reservoir and wellhead. The primary aim of this research was to update the geothermal manifestations map of Kenya and investigate exergy available in the Olkaria field by exergoeconomics analysis. The exergy concept links wellbore and reservoir using the 3-D Kriging method. The outcome of this research will contribute to the overall understanding of optimal utilisation of energy available in surface and sub-surface geofluids in Kenya to improve the sustainable utilisation of geothermal resources.

The contents of the dissertation consist of six chapters below:

Chapter 1: Introduces the background of the study, the introduction of geothermal energy and its uses, the energy situation, and geothermal status in Kenya. This chapter describes the research objectives and methodology.

Chapter 2: Reviews geochemical exploration, energy, exergoeconomics, reservoir simulation, and past reservoir conceptual models in Olkaria geothermal complex and wellbore-reservoir coupling.

Chapter 3: Updates geothermal manifestations in Kenya using geochemistry, isotope analysis and QGIS. Results presented the geochemical analysis of water sampled at six hot spring locations (Kipsegon, Mulot, Eburru, Narosura, Majomoto, and Homa Hills) and literature data from twenty-three geothermal sites (prospects and geothermal wells). The water type was characterised using the ternary plot as carbonate chloride and Mg-bicarbonate, mixed Na-bicarbonate, sodium bicarbonate water and chloride waters with some carbonate and bicarbonate. Temperatures of fluid with depth were estimated using geochemical geothermometers as 219-247°C for Eburru hot spring, while Narosura geothermal reservoir had the lowest reservoir temperatures of 64-95°C with quartz geothermometer. Based on stable isotope, $\delta^{18}O$ and δ^2H, analysis of the six hot springs water, the origin of water for the geothermal prospects is manly meteoric water.

Chapter 4: Focuses on optimising Olkaria I, II, and IV SF power plants, proposing topping unit and three Organic Rankine Cycle (ORC) configurations using different working fluids using energy and exergy concepts. In Olkaria I, combined water-cooled and air-cooled binary power plants were optimised using eight different working fluids by the thermo-economic concept and sustainability index (SI). Net work generated per heat transfer surface area was the optimised objective function, f(obj). Optimisation of exergy at the separated brine of Olkaria II was a combination of exergy and pinch point analysis for ordinary and a regenerative ORC using six different working fluids. The separated brine at a temperature of 156°C at Olkaria I and II with flow rates of 67 kg/s and 206 kg/s, respectively, are the energy sources for ORCs. For Olkaria IV SF, optimisation was considered for a backpressure topping unit and a binary bottoming unit using two working fluids (trans-2-butene and isopentane). Power plant models were modelled and optimised using EES code by energy, exergy, and exergoeconomic analysis. Exergy of 239 MW is being supplied to Olkaria IV SF power plant that generates 140 MWe. Proposed power plants can generate additional 29.29 MWe power by a topping unit. By introducing a backpressure topping unit, exergy efficiencies improved from 56% to 70% and decreased total exergy destruction by 4,056 kW. Bottoming of ORC at Olkaria IV generated 8,788 kWe, and 7,927 kWe net power for trans-2-butene and isopentane, respectively, at optimum turbine inlet pressures between 1,000-3,100 kPa. Trans-2-butene has thermal and second utilisation efficiencies of 13.7% and 49.86%, respectively. On the other hand, isopentane has an optimum turbine inlet pressure of 1,090 kPa, with thermal and second utilisation efficiencies of 12% and 43.96%, respectively. Separated brine at Olkaria I has 7,187 kW exergy into the proposed binary power plant. On the energy and exergy concept, the most suitable plant is a water-cooled type for isobutane and R600a that can generate 2,590 kWe and 2,594 kWe net work, respectively, while R600a is the suitable fluid for air-cooled binary plant generating 2,469 kWe net work with 59.37% utilisation efficiency. Net work of 1,628 kWe to 2,594 kWe was generated in a wet-cooled unit with SI of 1.34 to 1.68 for f(obj) of 1.6 to 1.8. For air-cooled plant, SI ranges were from 1.29 to 1.61 for the net work from 1,446 kWe to 2,469 kWe with utilisation efficiencies of 34.77% to 59.37% and f(obj) values of 0.59 to 0.87. Combining pinch point analysis and exergy optimisation of proposed binary power plants at Olkaria II showed that the optimum pinch point is 8°C for reinjection temperatures above 80°C by varying the turbine inlet pressure and pinch points. For the pinch point of 10°C, the working fluid with a lower net power is trans-2-butene at 5,936 kWe and the highest reinjection

temperatures at 89ºC. The pinch point affects the heat transfer rates and effectiveness in the heat exchangers. The best pinch point is 10ºC since the reinjection temperatures are higher between 83 and 89ºC. The exergy and sustainability index analysis method optimised Olkaria II by varying turbine inlet pressure and reinjection temperatures. Heat exchangers contributed about 60% (2,900 - 4,200 kW) of total exergy destruction. The second utilisation efficiencies were between 26-45%. A Grassman diagram summarised the exergy flow in relation to the input exergy of 19,685 kW into the system.

Chapter 5: Couples reservoir with wellbore simulator. The research investigated liquid-dominated Olkaria Domes wells, OW-901, OW-902, OW-903, OW-904, OW-908, OW-909, OW-910, OW-914, OW-921, and OW-924. Reservoir temperatures from the wellbore simulator are high at 296.8ºC in OW-916. The formation pressures simulated are between 1,077 to 12,487.9 kPa for wellhead pressure of 459 to 1,720 kPa. The thermodynamic parameters (temperature and pressure) from the wellbore simulator were input parameters in the EES code to calculate entropy, enthalpy, and specific exergy. Python console implemented the 3 D Kriging method to couple the wellbore and reservoir. At any required depth, two-dimensional (2-D) contour maps were plotted for Olkaria Domes between the surface and the reservoir for depths between -2,100 to -1,800 m.a.s.l.

Chapter 6: Summarises the overall conclusions and recommends future work optimising geothermal resources in Kenya by energy, exergy, exergoeconomic analysis, and wellbore-reservoir coupling.

Dedication

In loving memory of my parents.

Table of Contents

List of Figures

List of Tables

"Education is the most powerful weapon which you can us to change the world" Nelson
Mandela.

CHAPTER ONE

1.0 INTRODUCTION

Geothermal energy is available everywhere beneath the earth. Geothermal utilisation has been increasing rapidly because of its low carbon emission. Approximately 16 GWe of energy is generated from geothermal resources worldwide as of 2020. Kenya is located in the Eastern part of Africa and has geothermal potential (approximately more than 7 GWe) along the East African Rift Valley (EARV) [1]. Efficient and optimum heat utilisation from the earth is essential for the sustainable development of geothermal power plants and reservoir management. The essential stages in geothermal development include understanding the source of heat, exploration stages, development, operation, and maintenance, returning the brine to the reservoir and closure of projects. There is a need to link geothermal reservoirs' surface utilisation and sub-surface/formation parameters.

1.1 Background of the study

Kenya covers an area of 581,309 km2 and lies on the equator with a tropical climate. Geothermal contributes 47% of the energy in Kenya, with an electricity installed capacity of approximately 3 GWe. The most developed geothermal field for power generation in Kenya is Olkaria, with an installed capacity above 800 MWe. The other field with a power plant is the Eburru geothermal field, a wellhead unit of 2.5 MWe installed capacity[2], [3].

With the current development scenario in Kenya and Olkaria geothermal field, the optimum utilisation of the resource has been mainly on exploration, energy, well test analysis, or reservoir simulation and management. The exploration, surface, and sub-surface have been studied independently. The available energy termed as exergy has been applied to classify and optimise power plants [4]–[6]. Exergy is a powerful optimisation tool for surface facilities, mainly power plants.

This study will optimise the geothermal resources in Kenya. Geochemistry and Quantum Geographic Information System (QGIS) methods will be used to map new hot springs outside the EARV. Geothermal power plants, existing and proposed, will be optimised by exergy analysis in Olkaria geothermal field. A conceptual exergy model is proposed to connect sub-surface and surface using a wellbore simulator. The wellbore simulator is applied to connect

surface and liquid dominated geothermal reservoirs. The 3-D Kriging method implemented in the Python programming language is used to couple wellbore and reservoir.

1.2   Geothermal energy

Geothermal energy is a renewable form of energy converted from heat within the earth. Geothermal energy is ubiquitous and associated with active volcanic areas close to plate tectonic boundaries [7], [8]. The geothermal energy is mainly distributed along the "ring of fire" [9]. Geothermal has been identified in over 90 countries and utilised in at least 70 nations [8]. Geothermal capacity in the world has been growing since its first industrial application in 1912 in Italy [10]. The total installed capacity from worldwide geothermal power plants is currently around 16 GWe. Exponential forecasting of geothermal power generation and was expected to increase to 21 GWe in 2020 [11].

There is a need to switch the energy sources to renewable and sustainable resources globally. As the world heads towards zero carbon emissions, geothermal will play a more significant role in the future energy mix, even though geothermal power cannot be a quick fix for power supply. Geothermal energy is considered stable renewable energy unlike wind and solar identified as variable renewable energy (VRE) and can contribute to sustainable development and a transition towards a low-carbon economy [12]–[15]. Generally, scientific scholars attribute global warming to fossil fuel emissions [16]. Every renewable source requires an input energy source from fossil [14].

A geothermal system has three elements: a heat source, caprock, and brine for transporting the heat from the reservoir to the surface [17]–[19]. For the sustainable development of any geothermal system, there should be a reliable recharge mechanism [20]. To access geothermal, the geological and hydrological framework should be studied and understood [7], [21]. Surface manifestations such as hot springs, fumaroles, geysers or warm pools, and volcanoes indicate geothermal energy availability [20]. Most of the geothermal prospects in the world are associated with subduction volcanoes [21]. Between the earth's surface and the crust, the average temperature gradient and heat fluxes are $3.1^{\circ}C/100$ m and 1.2×10^{-6} cal/cm$^{2 \cdot}$s, respectively [7]. The rocks in the crust are responsible for natural heat to the surface. Granite, basalt, and peridotite rock types contain radioactive isotopes of uranium, thorium, and potassium release heat by nuclear reactions [7]. Hydrothermal systems have fluid circulating in permeable zones where heat flow is available. Geothermal energy outranks other renewable energy sources environmentally and economically [22].

Geothermal energy will have to be used for the best scenario depending on the nature and characteristics of the brine and reservoirs. For the optimum application of geothermal energy, investment is required from conception to project retirement. The main exploration techniques include geochemistry, geophysics, and environmental and/social-economic studies.

1.3 Classifications of geothermal energy

Geothermal systems generally have similar characteristics. Geothermal systems have been classified mainly based on the reservoir temperatures as low, medium and/or high temperature. The types of geothermal systems according to [23], [24] have been classified as;

  i.   Hot water systems containing brine and boiling does not occur before or during production.

  ii. Two-phase liquid systems where boiling occurs during utilisation due to pressure decline. This category is further sub-divided into low enthalpy, medium enthalpy, and high enthalpy.

  iii. Two-phase vapour-dominated systems produce steam and immobile water and are mainly associated with low permeability reservoirs.

Table 1.1: Classification of geothermal systems according to [23], [24].

Classification	Enthalpy	Temperature (^{o}C)	Enthalpy (kJ/kg)
Hot water		T<220	h<943
Two-phase liquid dominated	Low	220<T<250	943<h<1100
	Medium	250<T<300	1100<h<1500
	High	250<T<350	1500<h<2600
Two-phase vapour dominated		250<T<350	2600<h<2800

Lee (2001) classified geothermal resources according to their ability to do thermodynamic work as low, medium or high-quality for specific exergy indices (SExI) less than 0.05, 0.05< SExI<0.5 and SExI> 0.5, respectively [25]. SExI was applied to classify geothermal resources in Japan [15]. Operating power plants in Indonesia have high exergy resources with SExI exceeding 0.5, according to Bina (2018), while the power plants with SExI between 0.05 and 0.5 are medium geothermal resources [26]. Fričovský (2018) and Kuzgunkaya (2018) classified geothermal systems according to SExI as low and moderate thermodynamic quality [27], [28]. The geothermal systems in Madagascar have been categorized by geological and tectonic context combined with temperature and potential reservoir as liquid dominated moderate-

temperature, fossil magmatic liquid dominated and sedimentary liquid dominated low temperature [29].

1.4 Uses of geothermal energy

The main uses of geothermal energy are direct, ground source heat pumps (GHPs), and indirect use/power generation [30], [31]. Application of thermal energy for heating or cooling is referred to as direct utilisation of geothermal energy.

Direct uses include bathing, district heating, industrial usage (food/crop drying, milk pasteurization, honey processing, among others), use energy harnessed from the hot springs or reservoirs [32]–[34]. High-temperature geothermal sources tapped from the reservoir by drilling wells are mainly for power generation in flash or binary power plants [35]–[39]. The high-grade form of geothermal energy is utilised for power generation with the classification of geothermal power plants as dry steam, single flash, binary, hybrid and back pressure [5], [39]. The global share of geothermal energy was about 0.3 % in 2020 [30]. Other uses of geothermal energy are ground source heat pumps, district heating with examples in Iceland, Italy, US, and greenhouse heating (Kenya and Japan) [40]–[43].

The utilisation of geothermal energy is usually site-specific concentrated along the ring of fire in the world. The amount of useful energy will depend on the available exergy with reference to the surrounding. The heat can be extracted from (steam or fluid) at the surface as hot springs or steam from fumaroles and at depths of up to 4 km below the surface [19].

In most of the cases, geothermal resources with temperatures less than 150°C are utilised for binary power plants [44]–[47]. Figure 1.1 shows direct and indirect uses of geothermal energy based on the temperature of the brine according to [48]. Shallow geothermal systems (<200 m) have been designed for ground source heat pumps to allow repeated operational and avoid soil thermal depletion [43].
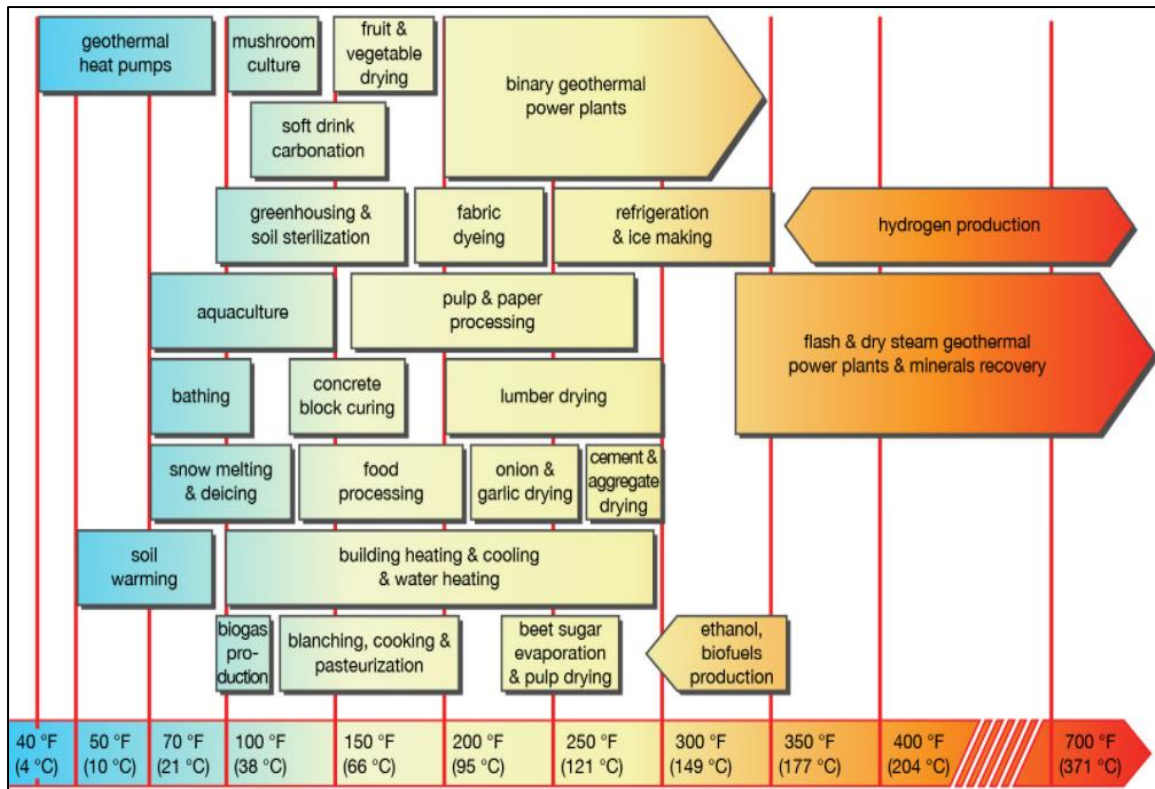
Figure 1.1 Uses of geothermal energy depends on temperatures. The direct use of heat is enormous and requires more development [48].

1.5 World geothermal status

Electricity generation from geothermal is in 26 countries, with United States and Indonesia leading at 3,700 MWe and 2,289 MWe, respectively, in 2020 [11]. The nations that are not using geothermal are at advanced exploration and/or plant construction [11]. In the geothermal status forecast, the development faces a stiff challenge from other renewables [11]. Figure 1.2 shows the world geothermal by region between 1990 and forecasted 2025, while Figure 1.3 shows the installed capacity for each country between 1995 and 2025. The data shows that there is a strong possibility of increasing installed capacity worldwide.
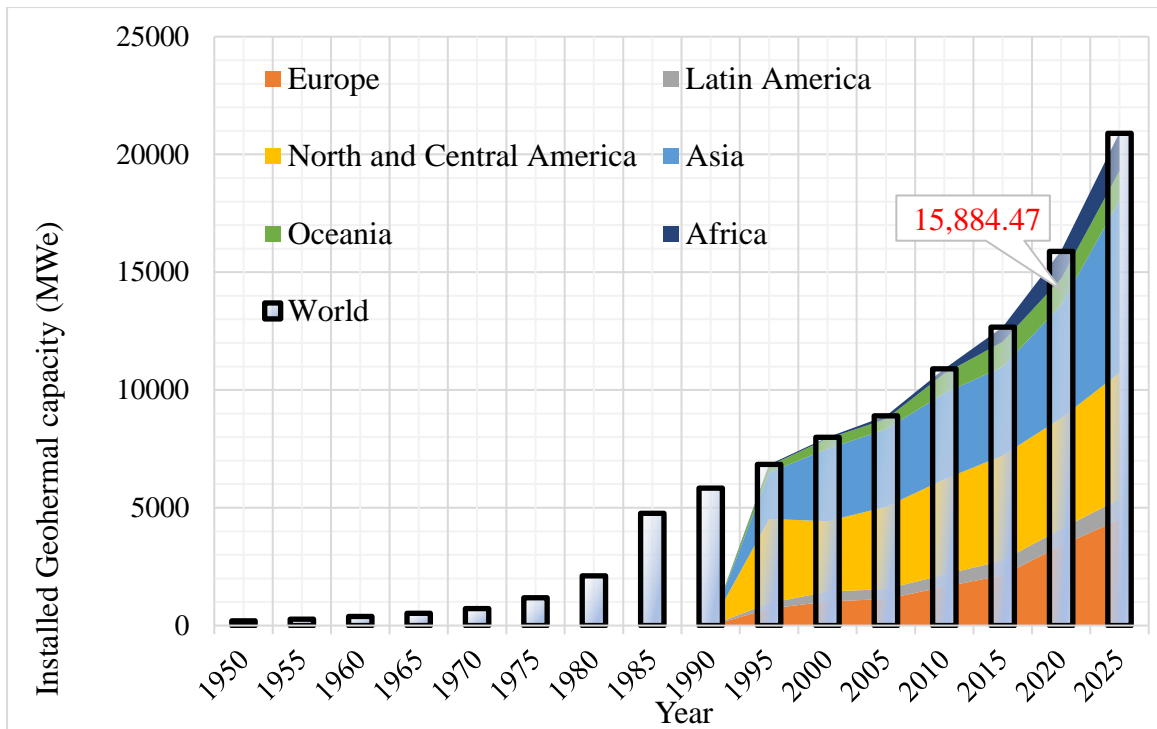
Figure 1.2: World geothermal status (1950-2025) by region (1990-2025).
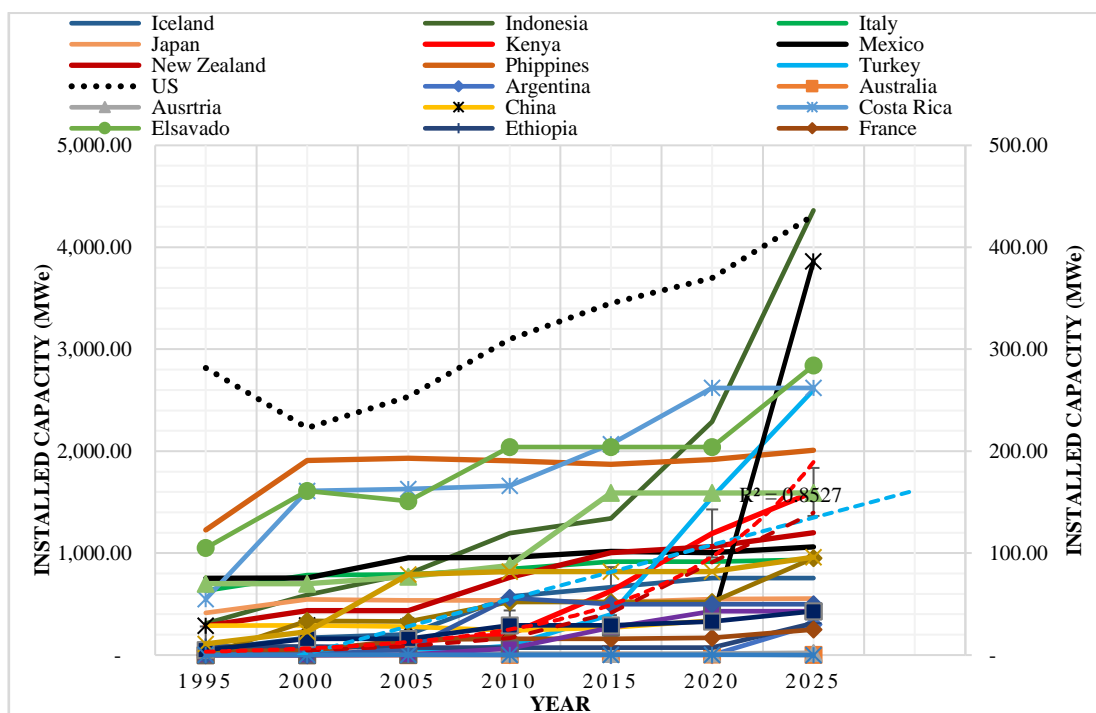
Figure 1.3: Geothermal status for each country. The lines marked corresponds to the secondary axis.

The top ten countries are US-3,700 MWe, Indonesia 2,289 MWe, Philippines – 1,918 MWe,

Turkey -1549 MWe, Kenya – 1,193 MWe, New Zealand - 1,064 MWe, Mexico – 1,005 MWe,

Italy – 916 MWe, Iceland – 755 MWe and Japan - 550 MWe [11], [49]–[53].

1.6 Energy situation in Kenya

Kenya's main primary energy sources are electricity, petroleum, and biomass accounting 6%, 19%, and 75%, respectively. Biomass is the main source of fuel in remote areas [54]. Kenya's installed capacity consists of about 70% renewables. The target is to have at least 65% of electricity penetration by 2022 [55]. The government is focused on encouraging more renewable power plants [56]. The electricity sources are mainly hydropower and geothermal power plants at 25% and 35% of installed generation capacity, respectively. Of the total installed capacity of 3 GWe, geothermal is ranked first with an installed capacity of 1,193 MWe [57]. Wind energy is ranked first in Africa, with an installed capacity of 336 MWe [55], [58].

Table 1.2: Electricity installed capacity in Kenya 2014-2020 [50], [54], [59]–[61].

Sources	2014	2015	2016	2017	2018	2019	2020
	Installed capacity (MWe)						Forecasted Capacity (MWe)
Hydro	822	828	829	834	837	837	921
Geothermal	366	619	663	673	847.4	1,193	1,984
Wind	6	26.1	26.1	26.1	336.1	336.1	786
Solar	17	31	32	38	93	95	430
Thermal	-	833.6	801.6	806.9	807.7	749.3	751
Cogeneration	-	26	28	28	28	28	28
Bioenergy/Bagasse	67	38	88	88	88	88	108
Gas turbine	60	60	60	60	60	60	60
Total renewable	1,211	1,504.1	1,550.1	1,571.1	2,113.5	2,461.1	4,121
Total non-renewable	60	919.6	889.6	894.9	895.7	837.3	839
Total capacity	1,271	2,423.7	2,439.7	2,466	3,009.2	3,298.4	4,960

Table 1.2 and Figure 1.4 show the energy sources in Kenya between 2014 and 2020. As the installed capacity increases, renewables have increased rapidly compared to non-renewable energy sources. Geothermal is the main contributor to renewable energy development.
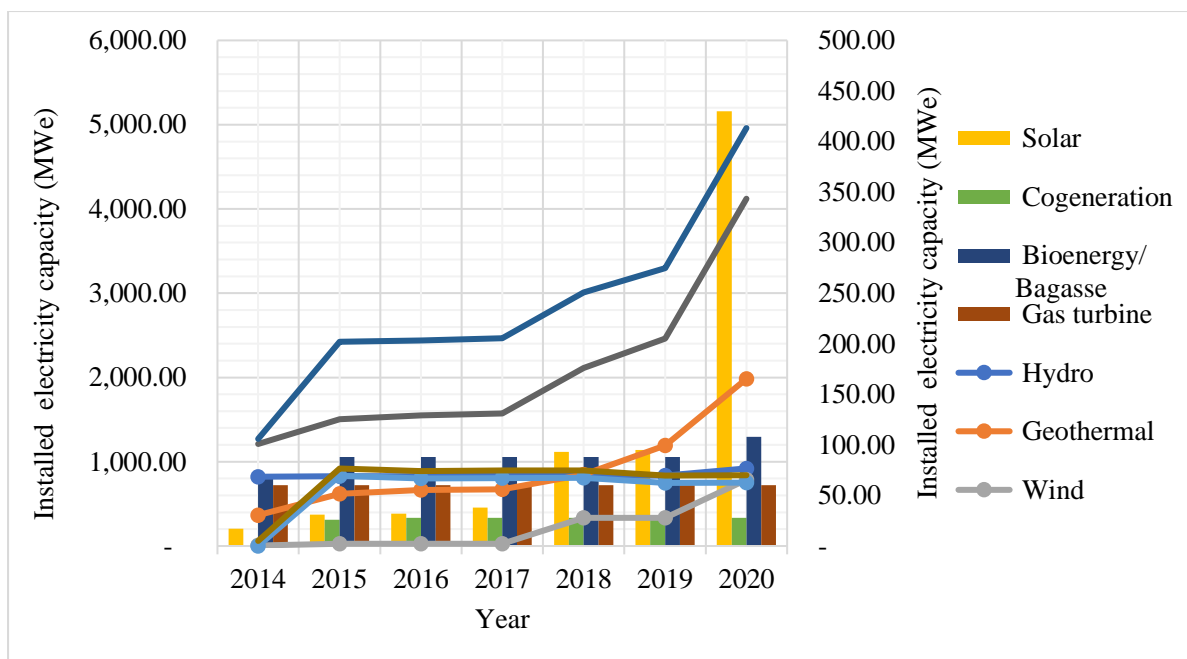
Figure 1.4: Energy sources in Kenya between 2014 and 2020. The line graph corresponds to the left vertical axis, and bar graphs are to the right hand side axis.

The installed capacity of other sources in 2019 are; thermal 749 MWe, hydro at 837 MWe. and wind energy at 336 MWe. Figure 1.4 shows the major energy sources of electricity in Kenya. For the last seven years, geothermal is the only source that proliferated from 366 MWe to 1.2 GWe in 2019. Figure 1.5 shows geothermal is the leading energy source at 35%, with the least being co-generation at 1%.
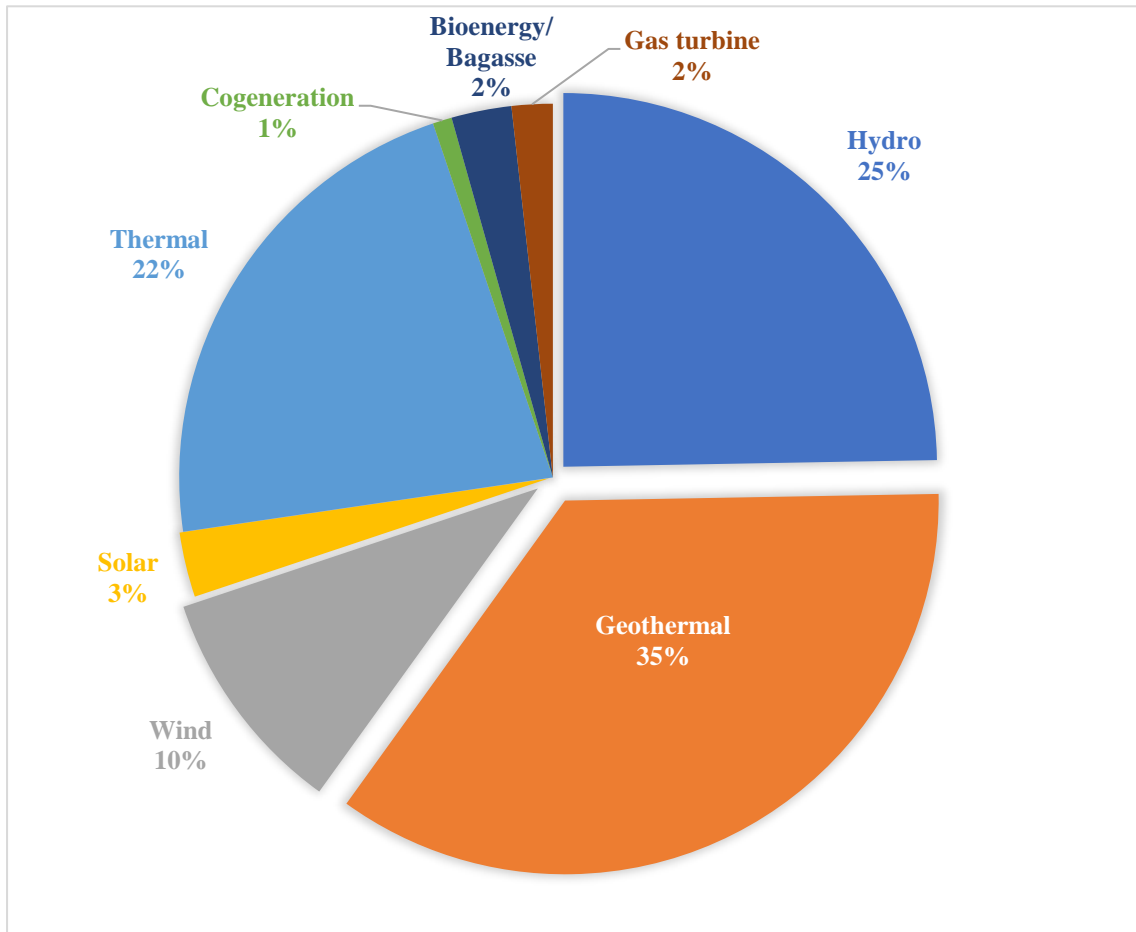
Figure 1.5: Kenya energy mix as of 2019.

The installed electricity capacity was forecasted to reach approximately 4.2 GWe in 2020. The energy mix is shown in Figure 1.6. Wind energy is one of the renewable sources that is likely to replace fossil energy sources. The benefits of renewable energy sources include reducing greenhouse gas emissions, decreasing imports of fossil fuels, and lower cost of energy. Among the renewable sources, geothermal has the desired baseload qualities.

1.6.1 Geothermal status in Kenya

Kenya has geothermal energy manifestations and prospects, mainly along the Great East African Rift. Geothermal exploration and forecasting in Kenya started around the 1950s in Olkaria and Bogoria regions, and six exploration wells were drilled in Olkaria in 1976 [50]. The first drilling of geothermal wells started in Olkaria geothermal field in 1956-1959 [62]. The first power plant, Olkaria I, was commissioned in 1981 [63].
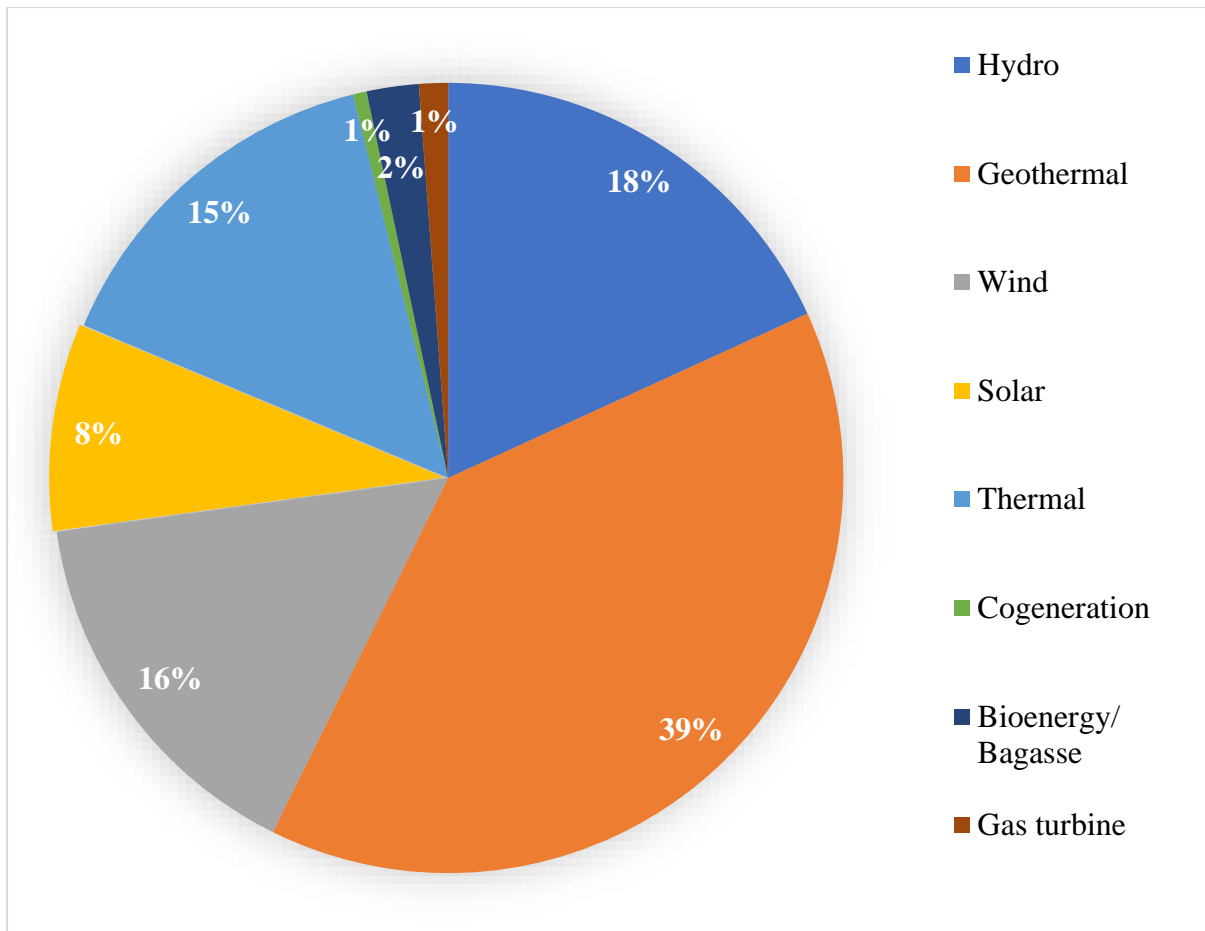
Figure 1.6: Energy mix that was forecasted for 2020.

The areas developed are Olkaria and Eburru geothermal fields with Menengai caldera at advanced development stages [64], [65]. Figure 1.7 shows the distribution of the geothermal manifestations mainly associated with quaternary volcanic complexes in the GEAR [65]. The rock types in Olkaria are pyroclastic occurring between depths of $0 - 100$ m, and consists of tuffs, pumice, volcanic glass, obsidian, and rhyolitic fragment [66]. The reservoir is estimated to be in the trachyte formation with intrusion indicating the heat source in Olkaria at depths of 900-3,000 m [67]. The alteration and oxidation signify a permeable geothermal system.

Geothermal energy contributes 35% of the total installed capacity of approximately 3 GWe in Kenya. During 2015-2020, geothermal power generation in Kenya added 546 MWe to a total installed capacity of 1,193 MWe [50]. Olkaria geothermal field is the largest and most developed site with a current installed capacity of 1.2 GWe, while Eburru field has an installed capacity of 2.52 MWe [2], [50]. Most of the geothermal power plants are single flash (SF), namely, Olkaria I, Olkaria II, Olkaria III, Olkaria IV, and Olkaria V. There is also a new upcoming Olkaria AU I, and other numerous well-head technologies under way[68]–[70].
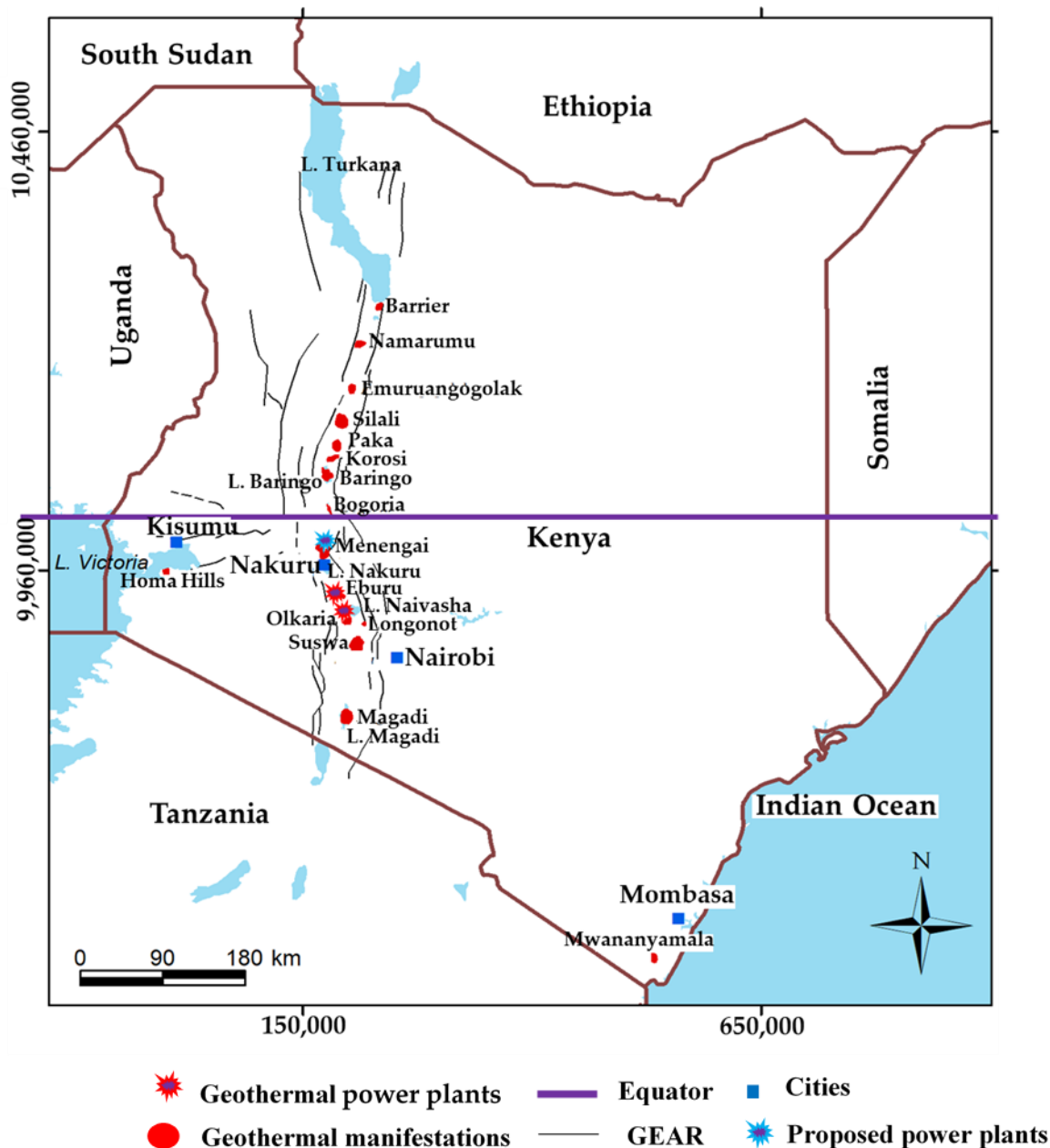
Figure 1.7: Map of Kenya showing geothermal manifestations, developed fields, and major economic hub cities [65], [71].

There is expected expansion and development of geothermal power plants in Kenya to have an installed capacity of about 5 GWe by 2030. The leading key developers of geothermal energy in Kenya are Kenya Electricity Generating Company (KENGEN) and Orpower [50].

The areas that have reported geothermal resources are at advanced exploration. The prospects out of GEAR have not attracted much attention.

1.7   Research objectives

This research aims to optimise geothermal energy in Kenya by exergy concept. Darcy flow of single-phase flow in the wellbore will be evaluated to link surface and sub-surface

exergy. Parameters that include pressure, temperature, enthalpy, and steam quality at the wellhead are simulated using a wellbore simulator.

1.7.1 Main objective

The main objective of the study is feasibility study on optimal utilisation of geothermal energy in Kenya.

1.7.1.1 Specific objectives

In general, the loop that links and show optimum utilisation of the geothermal energy is investigated to meet the following research objectives:

1. To update geothermal manifestations in Kenya using QGIS and geochemical analysis.
2. To optimise geothermal energy at Olkaria Domes geothermal field by energy and exergoeconomic analysis concepts.
3. To couple geothermal surface and sub-surface (reservoir) conditions using a wellbore simulator.

1.8 Problem statement

Geothermal manifestations' studies in Kenya have been along with the East African Rift System. There is a need to map other signs of geothermal resources using QGIS and geochemistry methods to locate potential sites for further studies.

Energy and exergy concepts have been used at surface reference points to optimise power plants. The cooling tower has not been included in the recent studies on exergy analysis. To understand the exergoeconomic of the power plant, a complete exergoeconomic that include cooling towers is carried out for single flash and organic Rankine cycle power plants.

Numerical simulations of wellbore and reservoirs are usually carried out separately in most geothermal fields. The wellbore and reservoir knowledge are essential to link surface and sub-surface for optimal use of the available energy. The fluid phase will dictate several parameters; pressure, temperature, enthalpy, and entropy that need to be well defined.

This study aims to update geothermal manifestations in Kenya, conduct a complete exergoeconomic analysis of current and proposed geothermal power plants at Olkaria in Kenya, and propose an exergy loop to link surface and sub-surface exergy using a wellbore simulator for liquid-dominated geothermal reservoir.

1.9 Justification

Kenya's geothermal prospects and manifestations have been mapped mainly along the East African Rift Valley. Other naturally occurring hot springs in Kenya needed to update the current prospects/manifestation map to optimise the natural heat from the earth for other viable projects or studies. Updating the geothermal resource map will increase the use of thermal energy in Kenya.

Single flash units in Olkaria have been optimised by energy and exergy analysis. The available exergy at the wellheads can generate additional power by topping or using organic Rankine cycles and conducting a complete exergoeconomic analysis. For decision making, exergoeconomic of all the components from the wellhead to the cooling tower is required.

The heat energy in the geothermal field is stored in the reservoirs and delivered by the wellbore. Reservoir and wellbore simulations have been modelled independently in Olkaria and other geothermal fields globally. A wellbore simulator is proposed to connect the surface/wellhead and the sub-surface/reservoir. The main thermodynamic parameters recorded or simulated in the geothermal reservoir of the wellbore are temperature, pressure, and specific enthalpy. Exergy has two components specific and actual exergy. Since each geothermal well records flow rate, actual exergy in the reservoir can be calculated. Actual exergy is applied to locate heat source/reservoir and flow directions of brine. The resultant model will be an exergy conceptual model termed an exergy wellbore coupled geothermal reservoir. Ambience varies with region and seasons. Standard ambient conditions are usually 25°C at 101 kPa (atmospheric).

1.10 Methodology

Various tools and methods were applied to optimise geothermal energy in Kenya to answer the stated objectives. Figure 1.8 shows the research flow chart and the tools focused on achieving the research objectives. The research output is the desired answers to optimising available exergy in geothermal fields in Kenya. An exergy conceptual model for Olkaria Domes for reservoir management and decision making is proposed.
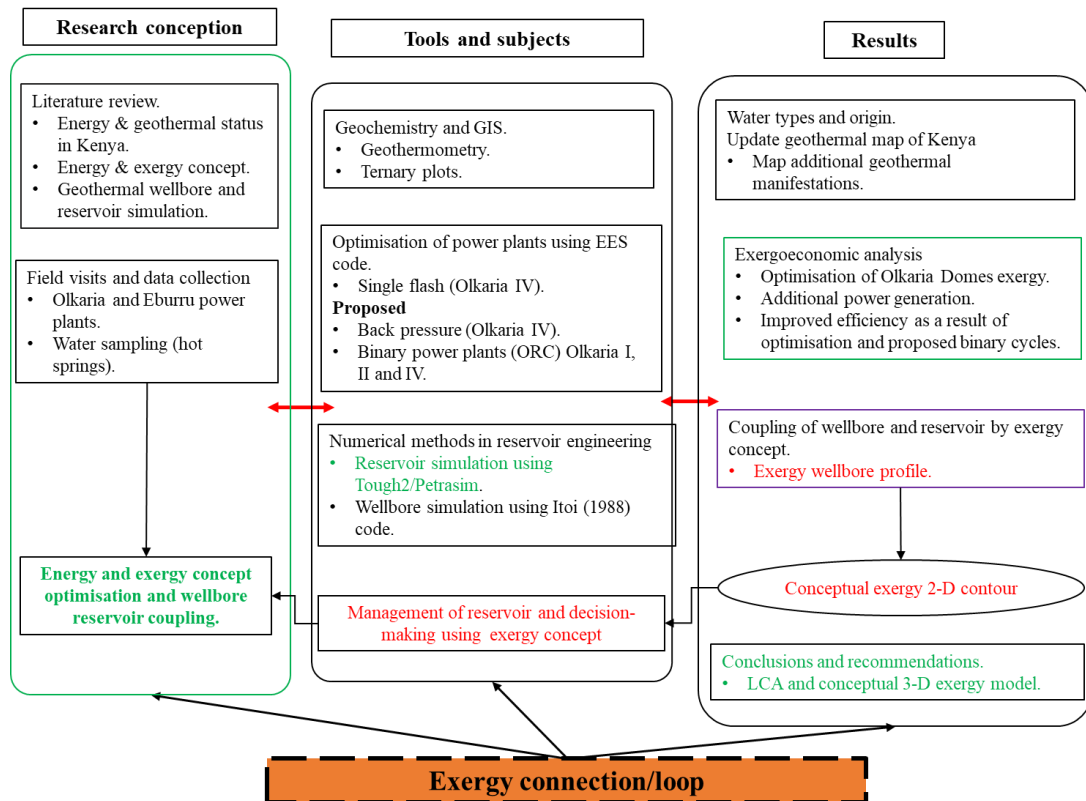
Figure 1.8: The research flow chart shows the study conception, tools and results. The red colour is the motivating concept for the dissertation, while the green coloured part is the recommendation for future/detailed studies.

Figure 1.8 shows the stages and studies in geothermal research, while Figure 1.9 shows the desired results graphical model.

Figure 1.9 shows the details of a geothermal system linking surface and sub-surface by exergy concept. Meteoric water recharges the reservoir, heated, and delivered to the surface for power plants (SF and ORC) at wellhead properties, P, T, x, h, e and m, which are pressure, temperature, steam quality, enthalpy, specific entropy and mass flow rate, respectively. Available exergy is calculated at wellhead reference conditions using output P and T wellbore results as input in the exergy equation in the EES code.
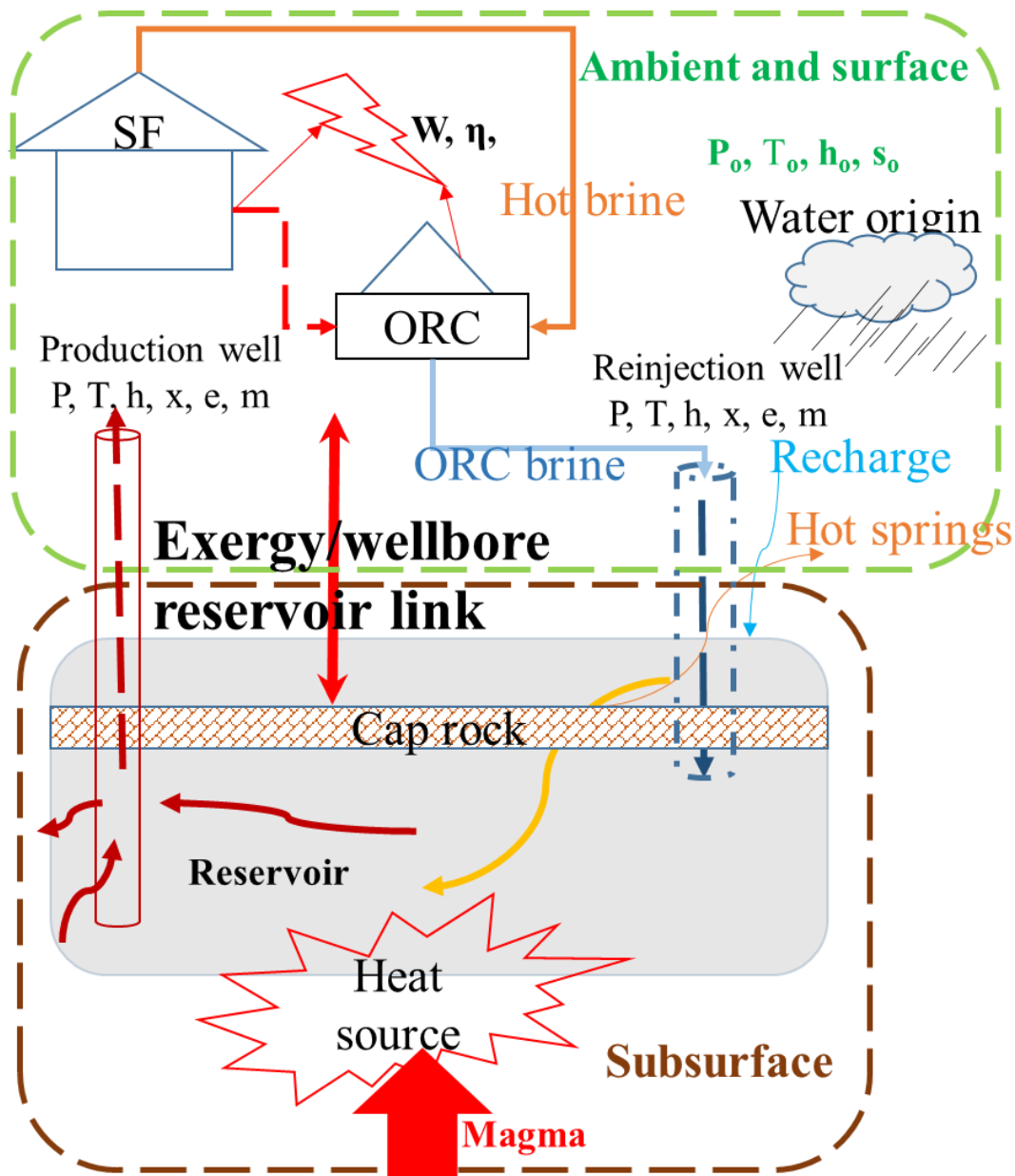
Figure 1.9: A schematic diagram showing a geothermal system linking surface and sub-surface by exergy concept.

1.10.1 Geochemistry and QGIS update of geothermal field and prospects in Kenya

Water samples were collected in polythene bottles and sealed with tape tightly on site. Figure 1.10 shows the six locations of the hot springs. Five hot springs are located outside the Rift system, while Homa Hills, S6, is on the Nyanza rift, which relates to the East Africa Rift System. The samples were treated or untreated on-site, depending on the analysis to be conducted in the lab. The treated samples had 2 ml of 0.1M HCl added to preserve cations. Untreated samples were used for anions determination, laboratory pH and conductivity. On the

site, pH, temperature, and conductivity were recorded. Atomic Absorption Spectrometry analysed cations after filtering through 0.45 μm Millipore membrane. Chloride analysis was performed using Mohr's (argentometric titration) method. Quartz and total silica analysis were done using silicomolybdate, a photometric method. The back titration method was used for the analysis of carbonate alkalinity.

Geochemistry is essential in geothermal exploration. The most contributing factor is geothermometry to infer the reservoir estimated temperatures from the chemical compositions of the geothermal fluids. Temperature equilibria control the concentration of the dissolved constituents [72]. Geochemical exploration also gives information on the origin, flow directions and helps to identify the sub-surface reservoirs. Chemical compositions, isotope analysis, and geothermometry were applied to estimate the reservoir temperature of the thermal springs in Kenya. QGIS tool shows the location of developed geothermal fields and prospects in Kenya. The thermal manifestations sampled are shown in Figure 1.10. The sampling methods and analysis are outlined by Arnorsson (2000) and Ellis and Mohan (1977), where they gave detailed geochemical procedures specifically for geothermal waters. The ternary diagrams were plotted using the liquid analysis spreadsheet developed by Powell and Cunning (2010).
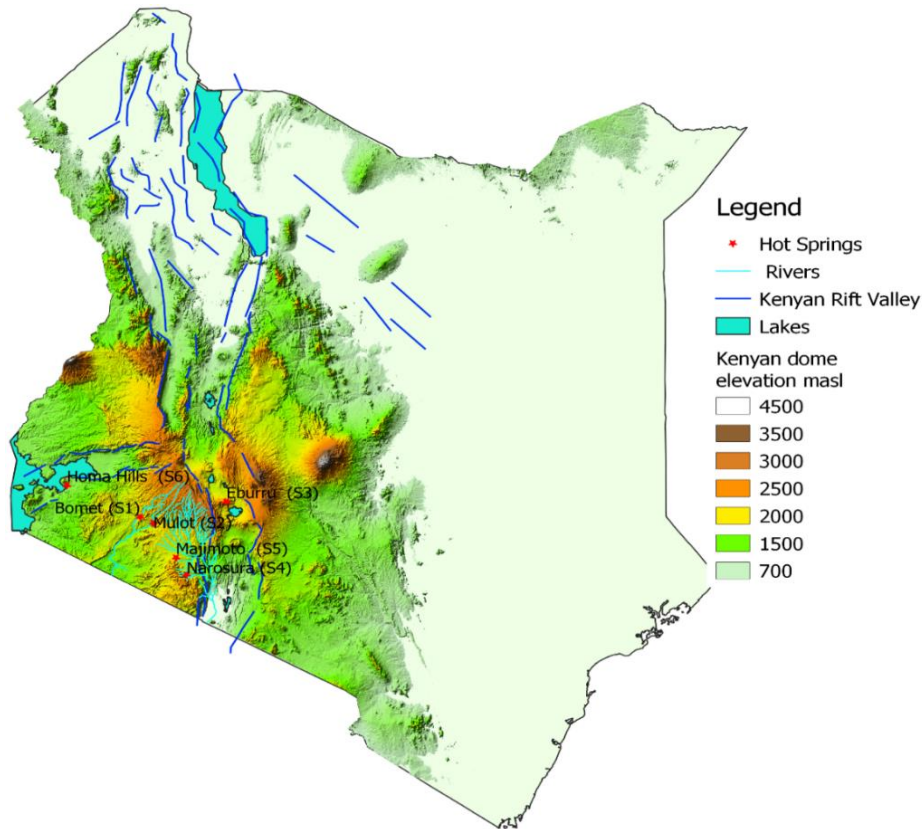
Figure 1.10: Map of Kenya showing the hot springs that were sampled for analysis in 2019. Physical features: Kenya Rift Valley, elevation, lakes and rivers are included.

1.10.2 Energy and exergy concept

A thermodynamic system involves energy and energy transformations. Energy is an essential aspect of life and exists in thermal, kinetic, mechanical, potential, or chemical forms. The first law of thermodynamics (energy can be transformed from one form to another) is based on energy conservation and its quantity. Available energy to be used is termed exergy based on the second law of thermodynamics (dealing with quality of energy, reversible work, entropy generation and exergy destruction) explained by Çengel and Boles (2006) in detail. Exergy is zero when the system and the surroundings reach equilibrium. For the given location, the thermodynamic reference parameters (23°C at 86 kPa) are used to calculate the exergy efficiencies of the system. Details of the equations used for the analysis are defined in Chapter 4 of the thesis. Jalilinasrabady (2011) optimised geothermal power plants in Japan by exergy concept. This concept with modification of objective function was applied to optimise geothermal power plants; the existing single flash (SF), Olkaria IV and proposed binary geothermal power plants in Olkaria. Available exergies of Olkaria I and II brine were considered for different binary configurations. Olkaria IV in Domes field, exergy was

calculated at the wellhead and considered for optimum utilisation for the single flash unit, topping backpressure, and bottoming ORC binary units. Power plants were modelled and optimised using Engineers Equation Solver (EES) code. The main optimisation variables investigated by Syed (2015), Sun (2019), Astolfi (2014) and others include; exergy efficiency, maximum power generated, plant efficiency and user-defined objective functions [73]–[80]. Most parameters like turbine pressure and temperatures are obtained from simulation results of the EES code. Energy and mass balance equations and pinch points are used to calculate the unknown parameters [76]. Each modelled power plant was optimised for the best/highest exergy or objective function defined. ORCs were optimised based on the user-defined objective function [81]. The temperature of the geothermal fluid reinjected is usually advisable to be above 100°C to avoid scaling challenges [73], [81]. Binary cycles transfer heat from hot geothermal brine to secondary working fluid in heat exchangers (pre-heater, evaporator, and regenerator). The engineering term used to define and design heat transfer and temperature difference between the hot and cold side of the heat exchanger is pinch point. The pinch point affects the temperature distribution in heat exchangers. Exergy and pinch point analysis are combined for optimisation of ORC units.

1.10.3 Olkaria reservoir simulation

Geothermal resources can be estimated based on stored heat in the reservoir. Numerical simulation methods are used to approximate the size and amount of energy that can be extracted from the reservoir. The extensive Olkaria reservoir has been modelled using TOUGH2 Petrasim software. Most of the developed numerical models for Olkaria have been the entire field by Rop (2018), Kandie (2016) and others [82]–[86]. Of the six geothermal fields in Olkaria, the Domes area is a high enthalpy, high-temperature liquid-dominated geothermal resource. The Domes area is at the border of Olkaria geothermal field and borders another prospect, Longonot geothermal area. Another study of the Domes area has been on well production tests by Rop (2012) and concluded that each well has an average power equivalent of 7.1 MWe. Understanding the reservoir at the boundary will be important in developing the Longonot prospect. The heat source and upflow will project the connection between Olkaria Domes, other fields and the undeveloped Longonot geothermal field. The Domes conceptual model will be checked with the wellbore simulation results.

1.10.4 Wellbore simulation

The estimated amount of energy stored in the reservoir is delivered for optimisation at the surface via a geothermal well. The quality (exergy) of delivered brine was calculated based

on wellhead reference conditions. EES code calculates thermophysical parameters, P, T, h, and entropy. A wellbore simulator simulates the pressure-temperature profiles of geothermal wells in Olkaria Domes field data. A wellbore model developed by Itoi (1988) used the following assumptions [87], [88]:

i. Steady and isenthalpic flow.
ii. Average specific volume for two-phase flow.
iii. Mass flow rate as a boundary condition.
iv. There is no effect of dissolved chemicals and non-condensable gases (NCG) in geothermal brine.

Brine and steam flow rates measured at the wellhead in Olkaria fields were input parameters in the wellbore simulator. The input data measurements are wellhead pressure (bar), flow rates, well diameter, true vertical length (TVD) (shallow/first depth and deep/second depth), and the pipe surface roughness. Directional wells assume a kick-off point (KOP) angle of 20°C to the vertical at depths of 400 m below the wellhead. The second (2nd) depth is between the shallow and the deep reservoir/the total drilled depth. The wellbore simulator gave temperature and pressure profiles and the formation pressure with the available flow rates, wellhead pressure, and wellbore specifications. The obtained parameters and the well log recorded data plotted the reservoir exergy profiles for the wells in Olkaria Domes in the EES code. Table 1.3 shows some of the wells in Domes supplying steam to the Olkaria IV power plant. The other inputs for wellbore simulation, such as flow rates, not in Table 1.3 are in Chapter five of the dissertation.

Table 1.3: Some of the wells locations and characteristics of the liquid dominated geothermal wells in Olkaria Domes.

Well	KOP (m)	Drilled depth (m)	2nd depth (m)	TVD (m)	Production casing depth (m)
OW-901	-	2199.15	1440.68	2199.15	758.47
OW-902	-	2,201	1552.72	2,201	648.28
OW-903	-	2,202	1504.86	2,202	697.14
OW-903A	400	2,810	2,353	2,782.78	1,197
OW-904	-	2,799	1,549	2,799	1,250
OW-904B	400	2,820	1,597.74	2,792.67	1,204
OW-908	-	2,988	2,143.08	2,988	1,201
OW-910	-	3,000	2,050	3,000	950
OW-914	-	3,000	2,048	3,000	952
OW -924	-	3,000	2,050	3,000	950

Figure 5.2 in Chapter 5 shows a basic wellbore for steady-state flow expressed by conservation of energy and mass balance equations [87]. An exergy profile is proposed to identify feed zones and reservoir layers to couple wellbore and reservoir.

1.10.5 Exergy and reservoir wellbore coupling

Other researchers have simulated wellbore and reservoirs independently. This dissertation proposes to loop the preceding methods and optimise geothermal resources by coupling reservoir and wellbore by exergy concept.

The wellbore data, pressure and temperature obtained from the wellbore simulator are the main parameters used to calculate the exergy, enthalpy and entropy using EES code. Exergy profiles show exergy gains and losses at various depths—the thermophysical parameter for each well tabled for wellbore reservoir coupling. A geostatistical method was applied to couple the wellbore and reservoir using the Eastings(x), Nothings(y), and depth(z) coordinates for each well. The contours are pressure, temperature, exergy and entropy, and flow rates values. 3 D kriging code implemented using Python counsel was used to map pressure, enthalpy, entropy, exergy, and flow rate contours. The coupling idea resulted in the Olkaria Domes exergy conceptual 2-D model.

1.11 Thesis Outline

The contents of the dissertation consist of six chapters below:

Chapter 1 introduces the background of the study, the introduction of geothermal energy and its uses, the energy situation and geothermal status in Kenya. This chapter describes the research objectives and methodology.

Chapter 2 reviews geochemical exploration, energy, exergoeconomics, reservoir simulation, and past reservoir conceptual models in Olkaria geothermal complex. Also, chapter two assesses wellbore simulation and wellbore reservoir coupling.

Chapter 3 updates geothermal manifestations in Kenya using geochemistry and QGIS. Results presented the geochemical analysis of water sampled at six hot spring locations (Kipsegon, Mulot, Eburru, Narosura, Majomoto and Homa Hills) and literature data from twenty-three geothermal sites (prospects and geothermal wells). The results showed that types of water from hot springs and geothermal fields in Kenya are carbonate chloride and Mg-bicarbonate type, mixed Na bicarbonate, sodium bicarbonate water and chloride waters with some carbonate and bicarbonate species along with the CO_3 and HCO_3 on the Piper diamond

plots. The reservoir estimated temperatures in the hot springs using geothermometers were 234-247°C for Eburru, while Narosura geothermal reservoir has the lowest reservoir temperatures of 64-95°C. The origin of the water for the geothermal prospects is mainly meteoric from the isotopic analysis.

Chapter 4 focuses on exergy and optimisation of the Olkaria I, II, and IV SF power plants by proposing topping unit and three organic Rankine cycle (ORC) configurations using different types of working fluids. In Olkaria I, combined wet-cooled and dry-cooled binary power plants were optimised using eight different working fluids by the thermo-economic concept and sustainability index (SI). Net work generated per heat transfer surface area was the optimised objective function, f(obj). Optimisation of exergy at Olkaria II separated brine was a combination of exergy and pinch point analysis for basic ORC and a regenerative ORC using six different working fluids. The separated brine at a temperature of 156°C at Olkaria I and II with flow rates of 67 kg/s and 206 kg/s, respectively, are the energy sources for ORCs. For Olkaria IV SF, optimisation considered a backpressure topping unit and a binary bottoming unit using two working fluids. Power plant models for energy, exergy and exergoeconomic analysis were modelled and optimised using EES code.

Exergy of 239 MW is being supplied to Olkaria IV single flash power plant to generate 140 MWe. Proposed power plants can generate additional 29.29 MWe power by a topping unit. By introducing a backpressure topping unit, exergy efficiencies improved from 56% to 70% and decreased total exergy destruction by 4,056 kW. Bottoming of ORC at Olkaria IV generated 8,788 kWe, and 7,927 kWe net power for trans-2-butene and isopentane, respectively, at optimum turbine inlet pressures. Trans-2-butene has thermal and second utilisation efficiencies of 13.7% and 49.86%, respectively. On the other hand, isopentane has an optimum turbine inlet pressure of 1,090 kPa, and thermal second utilisation efficiencies of 12% and 43.96%, respectively.

Separated brine at Olkaria I has 7,187 kW exergy into the proposed binary power plant. On the energy and exergy concept, the most suitable plant is a water-cooled type for isobutane and R600a that can generate 2,590 kW and 2,594 kW net work, respectively, while R600a is the suitable fluid for air-cooled binary plant generating 2,469 kW net work with 59.37% utilisation efficiency. Net work of 1,628 kWe to 2,594 kWe was generated in a wet-cooled unit with SI of 1.654 to 2.701 for f(obj) of 1.5 to 1.8. For air-cooled plant, SI ranges were from 1.286 to 1.612 for the net work from 1,446 kWe to 2,469 kWe with utilisation efficiencies of 34.77% to 59.37% and f(obj) values of 0.56to 0.89.

Combining pinch point analysis and exergy optimisation of proposed binary power plants at Olkaria II showed that the optimum pinch point is 8°C for reinjection temperatures above 80°C by varying the turbine inlet pressure and pinch points. For the pinch point of 10°C, the working fluid with a lower net power is trans-2-butene at 5,936 and the highest reinjection at 89.05^{o}C. The pinch point affects the heat transfer rates and effectiveness in the heat exchangers. The best pinch point is 10°C since the reinjection temperatures are higher between 83 and 89°C. The exergy and sustainability index analysis method optimised Olkaria II by varying turbine inlet pressure and reinjection temperatures. Heat exchangers contributed about 60% (2,900 - 4,200 kW) of total exergy destruction. The second utilisation efficiencies were between 26-45%. A Grassman diagram summarised the exergy flow in relation to the input exergy of 19,685 kW into the system. The exergy reinjected were 18% and 34% for R236ea and trans-2-butene, respectively.

Chapter 5 couples reservoir with wellbore simulator using 3 D Kriging method. The research investigated liquid-dominated Olkaria Domes wells, OW-901, OW-902, OW-903, OW-904, OW-908, OW-909, OW-910, OW-914, OW-921, and OW-924. Reservoir temperatures from the wellbore simulator are high at 296.8^{o}C in OW 916. The formation pressures simulated are between 1,077 to 12,487.9 kPa for wellhead pressure of 459 to 1,720 kPa. The thermodynamic parameters (temperature and pressure) from the wellbore simulator were input parameters in the EES code for calculating entropy, enthalpy, and specific exergy. Python console implemented the 3 D Kriging method to couple the wellbore and reservoir. At any required depth, two-dimensional (2-D) contour maps were plotted for Olkaria Domes between the surface and the reservoir for depths between 2,100 to -2001 m.a.s.l.

Chapter 6 summarises the overall conclusions and recommends future work optimising geothermal resources in Kenya by energy, exergy, exergoeconomic analysis and wellbore-reservoir coupling.

CHAPTER TWO

2.0 LITERATURE REVIEW

2.1 Overview

This chapter describes the research on geothermal optimisation in Kenya, including geochemical results from geothermal hot springs and highlights energy and exergy analysis. The optimisation of geothermal energy in Kenya is a broad topic. Methods for optimum utilisation of the energy from the earth in Kenya are; exergy analysis of power plants, update of conceptual reservoir models, and well test and production analysis. Energy optimisation of geothermal energy in Kenya has been on single flash units and proposed binary units. Kwambai (2005) and (2010) analysed Olkaria I power plant by exergy analysis. However, Kenya is the leading geothermal developer in Africa, with optimisation on power plants and reservoirs that limit the overall idea of linking the surface and sub-surface. Also, the mapped geothermal prospects are mainly in the Rift system. Nonetheless, there is a need to report and update geothermal manifestations in Kenya and apply the exergy concept to connect surface and sub-surface thermophysical parameters.

2.2 Introduction

In light of the increasing demand for a carbon-free planet, researchers have shown keen interest in optimal use of the available geothermal energy. For the best use scenario of the geothermal resource, the main stages are exploration, development and application. The methods for exploration include geophysics and geochemistry. In this study, geochemistry estimates the reservoir temperatures and maps new manifestations. The exergy concept is the best optimisation tool and proposed to link surface and sub-surface on the developed field. Available energy is exergy and is the maximum available work generated by the system [89]. A thermodynamic system in equilibrium with the environment is in a dead state. Numerical methods in reservoir simulation involve several parameters that include permeability, porosity and physical fractures. The main output parameters to measure the reservoir characteristics are temperature and pressure from the numerical methods. The simulated thermophysical brine parameters help calculate other values of exergy, entropy, and enthalpy.

2.3 Geochemistry and QGIS update of geothermal prospects in Kenya

The geothermal manifestations in Kenya are prominently warm springs located in the Great Eastern African Rift (GEAR), Kenya. The manifestations are a small area as either a single source of warm springs or a few spots. Most thermal waters reported in Kenya by Tole (1992) have a constant flow rate for an extended period, also Minissale et al., (1997) reported

43

constant flows of thermal springs in central Italy [90], [91]. Hydrochemistry of the Cl/Br ratio of geothermal fluids in Alps ranges showed the presence of trapped seawater in formations from infiltration during different marine intrusion periods. The Cl/Br method showed the presence of brines in crystalline aquifers and waters discharge along faults diluted by meteoric waters [92].

Warm waters at 25 -75°C and total dissolved solids (TDS) values between 0.7 and 5.8 g/l and silica geothermometers have delineated the potential of geothermal fields reservoir temperature ranging between 92 and 104°C [93].

Tole (1992), (2002) and Kamondo (1988) sampled and analysed water springs within and outside the Rift zone [91], [94], [95]. In the previous studies included, ionic balance is beyond the tolerance of +-5%, thus the need to re-evaluate the analysis. Majimoto, mapped by Tole (1992), is in geologically quaternary volcanic and tertiary volcanoes with low temperatures of 46°C [96]. The hot springs discharge approximately six kg/s at the contact between tertiary volcanic tufts and underlying gneisses and schists of the Precambrian Mozambique belt system [94]. Low enthalpy geothermal waters have attracted less scientific and economic inquisitiveness [94].

Isotope analysis by Mutonga et al., (2010) and Kanda (2019) shows that most geothermal prospects water origin is meteoric. A stable isotope comparison of Menengai and Olkaria geothermal fields showed the origin of geothermal waters [97]. Olkaria field is enriched in $\partial^{18}O$ and ∂^2H indicating high reservoir temperatures, while depleted Menengai field points that meteoric waters recharge Menengai with little residence time. The reservoir temperatures for the Olkaria field and Domes area are estimated to be above 230°C. Major gases reported are CO_2, H_2S, H_2, N_2, NH_3, CO, and O_2, CO_2 accounting for above 80% of the total non-condensable gases [98].

2.4   Energy and exergy concept and exergoeconomics of geothermal power plants

Application of energy, exergy, and entropy in geothermal energy analysis has been on power plant and surface conditions. In connection to economics, Yari et al., (2015) applied exergoeconomic as a tool to connect thermal, exergy, and investment [99]. Coskun et al., (2011) used exergy to illustrate the application of exergy and cost analysis of for the Tuzla geothermal power plant system (Tuzla GPPS), (7.5 MWe installed capacity) in Turkey [100]. Exergy parameters most studies (like Rodríguez (2013); Dippipo (2008); Caliskan (2012)) presented are at wellhead conditions for optimisation of surface facilities [68], [101], [102].

Exergy analysis of various geothermal power plants configurations presented maximum first-law efficiency of 11.8 % for a flash binary using R123 working fluid [103]. Golberg (2015) applied eco-exergy to derive the measurement of eco-system ability to do work [104].

To calculate the cost of products from the power plant, the input parameter from the reservoir is geothermal fluid. The economic term used for exergoeconomic analysis is fuel cost. Average fuel cost for brine of 1.3 $/GJ applied in exergoeconomic analysis of geothermal power plants [81], [105], [106]. Energy and exergoeconomic analysis of ORC optimisation with the objective function of heat exchanger area with optimum reinjection temperatures between 79 – 116°C had efficiencies of 16.37% and 48.8% for energy and exergy, respectively [81]. Overall power plant exergoeconomic links invested and operational exergy expenditures for optimum resource utilisation [104].

Thermo-economic optimisation of various ORCs and Single Flash (SF) power plant by the variable metric searching method has shown the maximum energy and exergy efficiency of 20.57% and 63.72%, respectively, and the lowest energy production cost and the lowest total energy costs being 25.1 $/GJ and 2.47 M$ per year, respectively [107]. Bina et al., (2017) reported maximum thermal efficiency and minimum production cost rate of between 25.1-28.4 $/GJ for ORC power plant generating 3,860 kWe by direct method optimisation. Energy, economic and environmental (3E) aspects of internal heat exchanger thermo-economic evaluation used to determine optimum cycle for Sabalan power plant exhaust [108]. Thermo-economic comparison of pure and mixed working fluids by Pareto-optimal solutions of four models using 0.7R245fa/0.3R227ea showed mixtures are better based on exergy but not economically y (Levelized energy cost) [109].

The energy and exergy concept has been applied to identify exergy losses in geothermal power plants and suggestions for improvement considering the investment cost and equipment maintenance [110]. In a study of geothermal power plants, average exergy of 45.2% was related to capital cost and exergy destruction for the Tuzla GPPS [111]. Exergy losses in power plants and systems are accounted as irreversibilities due to entropy generation.

In exergy and energy investigation of systems that include heat exchangers, the highest exergy destruction is associated with the heat exchangers [76], [112]. The heat exchangers are evaporators, condensers, preheaters, and cooling towers used in power plants and absorption chillers.

Considering Southern Negros Geothermal field [113], proposed linking reservoir and surface exergy. A *wellbore simulator* is a primary tool that links the surface and sub-surface. The obtained P and T in the well will be used in EES code to calculate exergy profile and formation/reservoir specific and total exergies. The resultant idea will be the exergy conceptual model of Olkaria Domes.

2.5 Pinch point analysis

Exergetic optimisation has many constraints coupled with energy and mass balance equations and heat exchangers. The secondary working fluid receives heat for the binary units that vaporise the fluid for power generation in the turbine. In heat exchangers, the pinch point is the minimum temperature difference between the heat source and sink. The pinch point calculates heat exchangers' area using logarithmic mean temperature difference (LMTD). Value of pinch point also contributes to exergy and energy/thermal efficiencies.

Pan and Shi (2016) investigated pinch point position in heat exchangers. Heat source temperature (in this case, geothermal brine) influence pinch point location. These vital heat exchangers' parameter is in bubble point and dew point in the evaporator and condenser, respectively [114]. Application of minimum pinch point in different working fluids ranking performance indicated a net power improvement of 13.6% using zeotropic mixtures compared to pure fluids [115]. Optimisation based on exergy recovery and exergy destruction perspectives found that the ranges of pinch points in the evaporator are between 8-12°C and were closely related to the investment cost of the evaporator [116]. An optimal pinch point in the heat exchangers lowers the cost per unit exergy in isobutane ORC using a heat source at 150°C [117]. The thermo-economic analysis of ORC by Heberle and Brüggemann (2016) shows that in a zeotropic mixture with a 90% mole fraction of isobutane, the specific cost per unit exergy was lower than R245fa, pure isobutane and isopentane. In evaluating power generation from hot springs of 60 – 140°C, different working fluids applied a pinch point of 5°C to obtain 19 kWe power output, and the evaporator accounted for 44% of exergy destruction [118]. The selection of optimal pinch points in the evaporator depends on the manufacturers' experience, while studies have applied between 3 and 11°C [76], [108], [117], [119]. Andreasen et al., (2019), applied a constant pinch point of 10°C comparing pure and zeotropic working fluids. The use of zeotropic mixtures working fluid increased net power output by 2.56% based on the performance ranking of 30 different working fluids [115].

Past researchers have considered different working fluids and pinch point optimisation in binary power plants in various geothermal fields. The studies have considered pinch point

optimisation. The pinch point values were in ranges or fixed same values for different working fluids. Exergy optimisation and pinch point analysis is needed to calculate reinjection temperature for the proposed binary power plants in Kenya geothermal fields. Higher reinjection temperatures avoid silica scaling issues, but the reinjected exergy increase with temperature.

2.6   Cooling towers

There are two basic cooling types of thermal power plants: evaporative/wet-cooling and non-evaporative/dry-cooling, applied in heat rejection of power plants [105]. The mechanical draft cooling tower has a lower investment than air-cooled condensers in ORCs optimisation [120]. Dry-cooled units reduce water consumption by 90% but have high operation costs in dry areas [121], [122]. In the ORC units, wet-cooling tower exergoeconomic contributes to the overall power plants' capital costs [111]. Combined cooling using lithium bromide absorption chiller, heat source from geothermal brine increased energy efficiency from 9.3% to 47.3% but exergy efficiency reduced from 15.6% to 4.6% [123]. It indicates high exergy destruction using an absorption chiller for cooling in ORC. The option would be to consider combined air cooling and wet cooling option.

Most studies have considered cooling tower designs and analyses as separate units in power plants [120], [124]. The cooling tower performance has increased exergy destruction with increased wet bulb temperature and the water-air ratio [125]. Experimental and numerical analysis of hybrid cooling towers on different working conditions showed an inverse proportion between exergy efficiency and exergy destruction [126]. Various cooling tower configurations are essential for exergoeconomic optimisation. To develop an exergy-economic equation, a complete analysis of SF or ORC power plants from the wellhead to the cooling tower. The central contribution of cooling towers is exergoeconomic analysis that requires more detailed studies.

2.7   Reservoir simulation

Geothermal, hydrothermal systems could be liquid or vapour-dominated [127]. Balanced mass, momentum, and energy equations describe mathematical flow fluid models in porous systems [127], [128].

Surface conditions and reservoir status are linked using a wellbore simulator to predict the future performance of geothermal reservoirs. A numerical simulation of geothermal reservoirs using three-dimensional flow composed of partial differential equations posed in fluid pressure

and enthalpy has been developed [129]. For gravity segregation in fluid flow, the reservoir is assumed to have good vertical communication and averaged terms of pressure and enthalpy [127], [130]. The pressure enthalpy diagram for pure water shows three states of liquid and vapour-dominated regions in the reservoir..

2.8 Olkaria geothermal fields

The geological and reservoir conceptual models of the Olkaria field have been undergoing updates based on data availability. The geological model that cuts across the West-East direction is shown in Figure 2.1 [1]. The reservoir development uses geological models and other developed models for stratification and boundary conditions.

2.8.1 Rock types and layers in Olkaria field

In Olkaria geothermal field, pyroclastic occurs between depths of 0 – 100 m and is a mixed fragment of tuffs, pumice, volcanic glass, obsidian, and rhyolitic fragment [66]. The fluid movement has altered tuff and basalt occurring at depths of 400-850 m. Tuff and basalts are the caprock in Olkaria. Trachytes, volcanic rock with an aphanitic or porphyritic texture of sanidine phenocryst, exist from the depths of 900-3,000 m depending on wells, as shown in Figure 2.2. The reservoir is estimated to be in the trachyte formation with intrusion indicating the heat source in Olkaria [67].

The presence of alteration minerals such as pyrite, calcite, and oxidation signifies that the Olkaria geothermal systems wells are permeable. The alteration mineral distribution of wells shows a trend where low alteration temperature minerals like zeolite and chalcedony occur at the upper part of the well replaced by moderate temperature alteration minerals like quartz, wairakite, and sphene. Higher temperature minerals like prehnite, epidote, and actinolite exist in deeper depths [67].
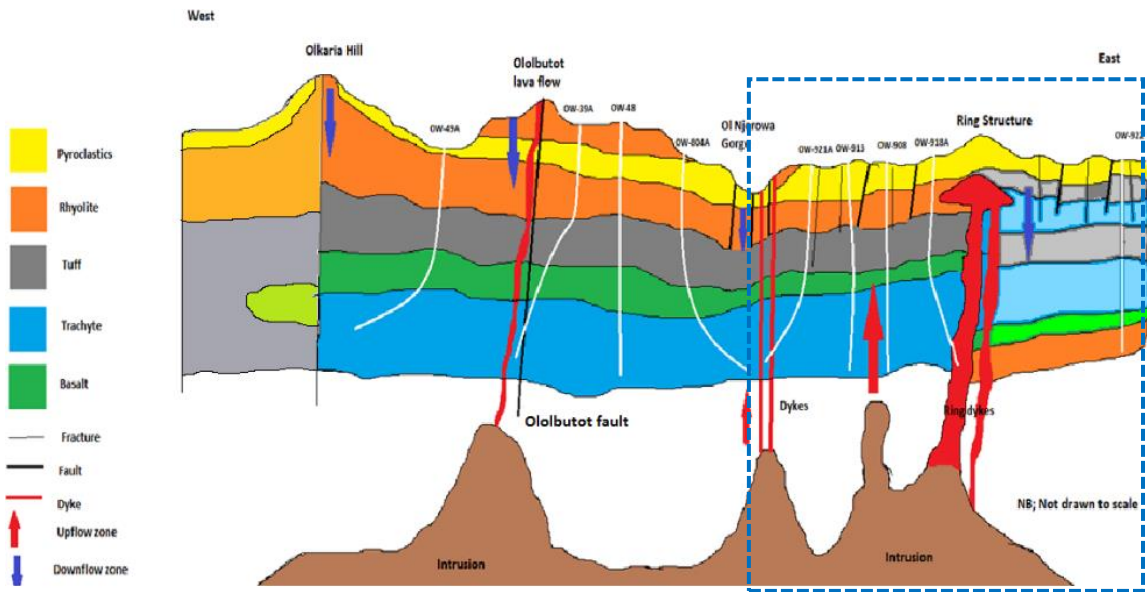
Figure 2.1: Schematic geological conceptual model of Olkaria showing relative locations of mapped faults East of Domes field modified from [1]. The dotted blue rectangle shows the Olkaria Domes field.
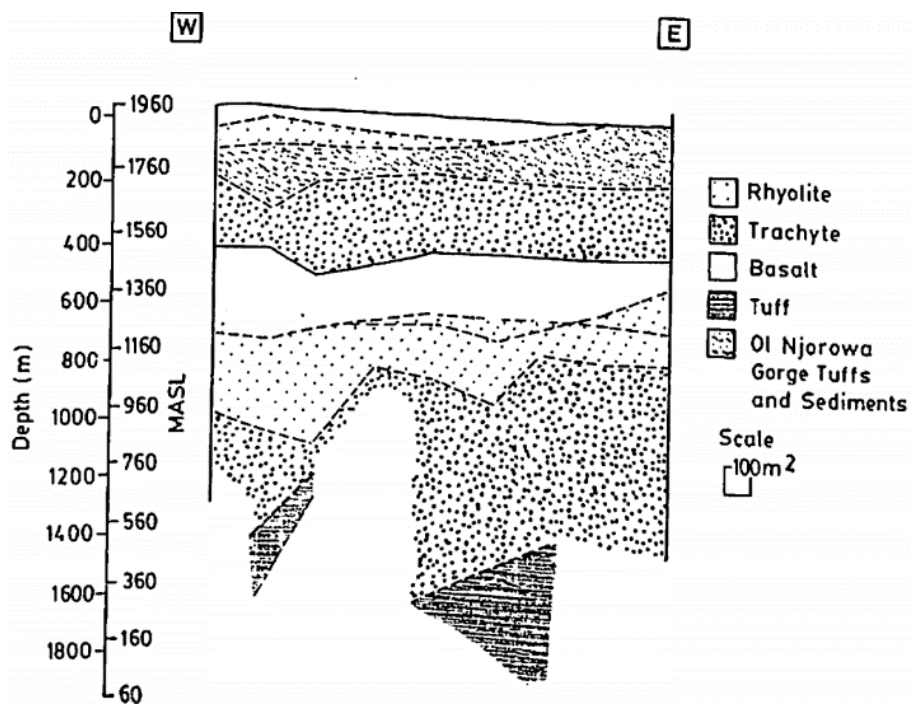
Figure 2.2: West-East stratigraphy section of Olkaria field [131].

49

The initial reservoir model of the Olkaria geothermal field was developed in 1976 and was simple [82]. From Figure 2.3, it was hypothesized that a boiling water reservoir with a tuffaceous caprock with meteoric recharge and temperature range of 260ºC – 320ºC.
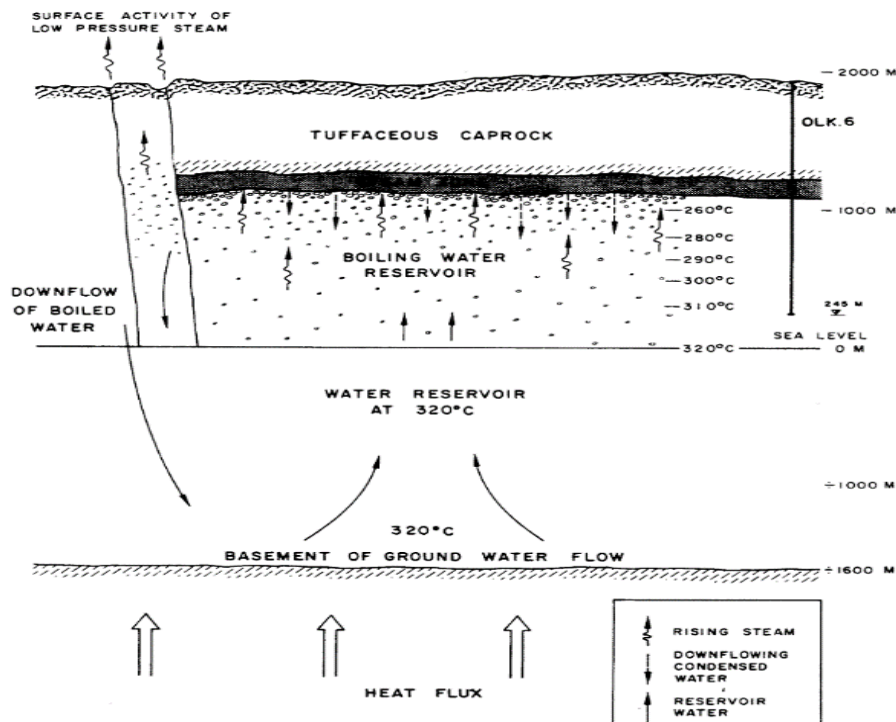
Figure 2.3: SWECO and Virkir (1976) first conceptual model of Olkaria geothermal field [82].

2.8.2 The conceptual Model by Axelsson et al., (2013) [132].

Two parts characterize the Olkaria geothermal resources as heavily explored and less explored. The conceptual model for the developed region is more detailed because of data availability, whereas; the other section is less detailed and more speculative. The heat source of the geothermal system is assumed to be deep-seated magma chambers at depths of 6 – 8 km (possibly partially molten) beneath Olkaria Hill (Olkaria West), Gorge Farm volcanic centre, and the Domes area.

The temperature and pressure model identified the up-flow zones related to four heat sources;

1. up-flow zone feeding the West field associated with the Olkaria Hill heat source,
2. up-flow zones, feeding the Northeast field and feeding the East field and the Northwest corner of the Domes,
3. associated with the heat source body beneath the Gorge Farm volcanic centre and

50

4. up-flow zone associated with the ring structures in the southeast corner of the Domes field.

Cl- concentration and Na/K temperature estimates and resistivity data have supported the locations of up-flow zones.

The updated conceptual models in Olkaria have been for the entire field by Rop et al., (2018), Okoo et al., (2017,) and Koech (2017). The latest available field data and Axelsson et al., (2013) model update applied to the Olkaria conceptual model reservoir. The 2018 model shown in Figure 2.4 shows one of the two central intrusions in the Olkaria in the Domes. The fault lines, Ololbutot and George farm faults, are the primary recharge locations.

NW-SE and NE-SW trending faults and ring structures control the permeability. Coldwater flows through the N-S fault system along the Ololbutot fault and possibly into the Domes area from the NE. The Ololbutot fault presents a flow barrier between the eastern and western halves of Olkaria. Olkaria fluids appear to be 50% or more deep Rift Valley water, variability between sectors. The Olkaria geothermal reservoir extends to the Southeast in Olkaria Domes and could be beyond Suswa prospects.
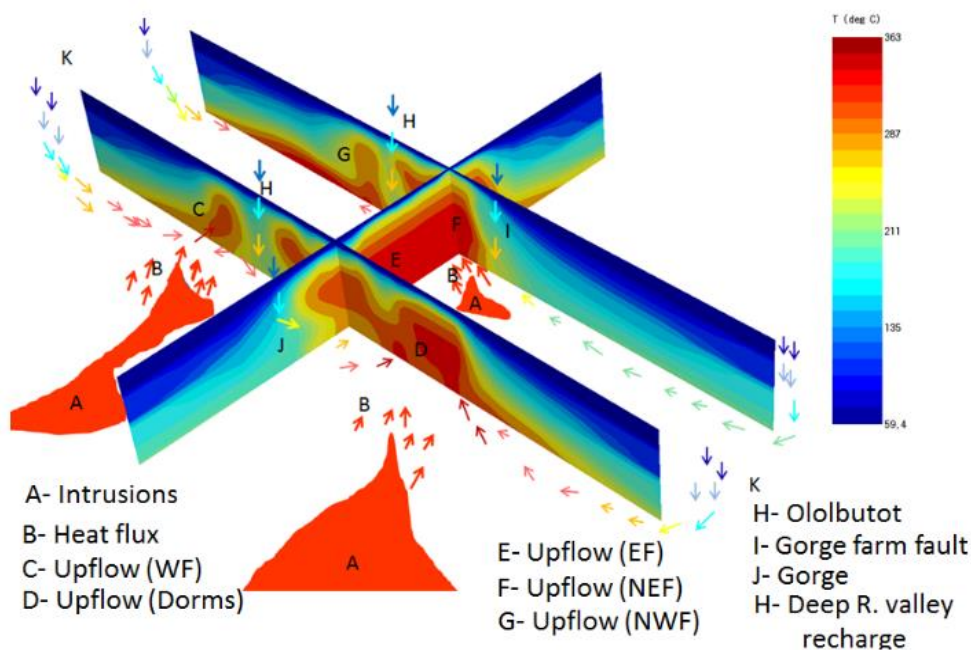
Figure 2.4: 3- D updated conceptual model of Olkaria field, in 2018 [83].

2.9   Wellbore simulation

The link between the reservoir and the surface is wellbore, delivering the resource for utilisation. In geothermal power plants, exergy analysis has been performed based on wellhead conditions. Faust and Mercer (1979) developed a numerical simulation of geothermal reservoirs using three-dimensional flow composed of partial differential equations posed in fluid pressure and enthalpy.

Liquid-dominated geothermal systems have fluid flowing in the wellbore from the reservoir as compressed water [87]. The application of geothermal energy mainly depends on the thermodynamic specification, geographical situation, resources' thermal energy, or electricity [26]. The evaluation point is at wellhead conditions for energy, exergy, environmental or exergoeconomic analysis. Evaluation at the wellhead would not relate clearly to the source of the geothermal reservoir. Prediction of the life-cycle of the reservoir-power plant is by a conceptual model developed to connect reservoir and power plant using production and reinjection wells [133].

Available reservoir simulators simplify the wellbore analysis for coupling the reservoir and the surface facilities [134]. In the study to couple of reservoir simulators for steady and Darcy flow, temperature, pressure, and flow rates were considered enthalpy in respect with time [134]. The results of the production test analysis of 29 wells in Olkaria Domes show wells are high temperatures with an average power equivalent of 7.1 MWe per well [135]. The coupling of heat transfer and fluid flow equations gives pressure drop and temperature change profiles [136]. 3D visualisation of Olkaria Domes shows that one of the up-flow zones is below 914 [84]. Wellbore simulator was used to calibrate the suitability of downhole measurements for matching analysis application, and it included impurity content estimation of CO_2 and NaCl [137]. Flow data is necessary to analyse and design power plants. Computer modelling has been a standard practice applied in the planning, developing, and managing geothermal fields [138]. Wellbore simulation of the Hatchobaru power plant showed that the simulated pressures agreed with actual pressure decline in the fluid gathering system[139].

Wellbore radius is usually infinitely small compared to the extent of the geothermal reservoir. In calculating the pressure drop, the line source solution approximation can be applied and using the superstition concept to determine the effects of boundary conditions by studying pressure distribution in several wells [140].

2.10 Exergy and wellbore reservoir coupling

Geothermal systems involve mass, energy, and transport through a porous medium. The models used in linking wellbore and reservoir have been developed from the oil industry [141], [142]. Vertical wellbore assuming isenthalpic flow coupled with the radial horizontal flow with a uniform reservoir thickness shows initial water saturation does not significantly affect steam flow for low wellhead pressure [143]. A multi-feed zone wellbore simulator with arbitrary feed zones was used to estimate flow rates and enthalpies of each feed zones during discharge and injection [144]. In developing a stand-alone feed zone wellbore simulator, the main output parameters were mass flow rate, pressure, temperature, and velocity profiles [145]. FloWell wellbore simulator can be used with TOUGH2 to couple wellbore and reservoir [142]. The wellbore simulators developed are either one-dimensional or stand-alone. Validation of simulators is well-flowing data. The obtained temperature and pressure profiles with flow rates can couple of wellbore and reservoir to generate 2-D profiles for reservoir analysis and management.

With the highlights of previous studies, the subsequent chapters present results and discussions on the exploration method (geochemistry and QGIS update). New hot springs mapped in Kenya and reservoir temperature estimated using geothermometers.

CHAPTER THREE

3.0 GEOCHEMISTRY AND QUANTUM GEOGRAPHIC INFORMATION SYSTEM (QGIS) UPDATE OF GEOTHERMAL PROSPECTS IN KENYA

3.1 Introduction

This chapter describes water chemistry to determine sub-surface temperatures and the mixing/boiling relations in geothermal manifestations in Kenya. The steps involved, geothermal map of Kenya update, sampling, field & laboratory analysis, and data interpretation. The predictions of estimated sub-surface temperatures of the geothermal manifestations, especially new prospects, is expected from the data..

3.2 Hydro Geochemistry

Thermal, geothermal resources are optimised using chemical geothermometry and QGIS tools. The existing qualitative and quantitative geothermometers (silica and cation) (Fournier, (1977), Truesdell, (1979) and others predict reservoir characteristics before drilling and preliminary mapping at exploration stages [17]. The heat of high latent and specific vaporisation heat makes water a highly efficient medium to transfer heat due to the extensive hydrogen bonding in liquid [146], [147].

Water chemistry is crucial for understanding the quality of water. The presence of lithium, rubidium, caesium, boron, arsenic, carbon dioxide and hydrogen sulphide is evidence of magmatic high-temperature waters [98], [146]. Mwangi (2013) estimated that the Olkaria temperature is above $230^{o}C$ using geothermometers. The geothermometers equations will estimate the reservoir temperatures, especially for the new fields. The data from the literature will be synchronised to check variations of sub-surface temperatures with time. Thermal reservoir temperatures are crucial in geothermal field evaluation potential. Isotopic analysis is the best tool for hydrological investigations to understand the fluid sources, recharge, infiltration rates, location, depths, temperature, and aquifers location [17]. The aqueous concentrations of water (chemical and isotopic components) discharges at the surface are controlled by equilibrium with minerals in aquifer rocks [148].

Concentration plots and ternary diagrams are generated from the measured and analysed chemical species. The input values are ppm and stable isotope data per mil [149]. Charts produced for data analysis and discussion include the famous Giggenbach Na-K-Mg geothermometer ternary, temperature geoindicators, stable isotope, Cl-enthalpy, and trace element ternary plots [149].

Geochemical surveys predict the sub-surface temperature and help predict the origin and the flow direction conditions at the depth [148]. Conservative constituents are applied in geochemistry to trace the origin of geothermal fluid, whereas reactive are helpful for physical reservoir states like temperature [98], [148].

Underground temperatures of 260-289°C have been indicated by applying geothermometers and mixing models in Iceland's Geyser, Hveravellir and Landmannalaugar fields [150]. The primary evidence of mixing models is boron and chloride, showing a linear relationship. A mixing model that can be applied for distinguishing boiled and non-boiled waters is the carbonate-silica model by interpreting the data from warm springs [150]. Geochemistry also quantifies the tendencies of corrosion and scaling challenges in surface development of geothermal projects [151].

Basic ingrained assumptions in sub-surface temperature estimations include [147], [152]:

i.   Temperature-dependent reactions occur at depth involving rock and water to fix the amount of dissolved constituents in the water.

ii. The constituents involved in a temperature-dependent reaction are abundant (supply is not a limiting factor).

iii. Water-rock equilibration occurs at the reservoir temperature.

iv. Little or no re-equilibration or change in composition occurs at lower temperatures as the water leaves the reservoir to the surface.

The hot water from deep in the system does not mix with cooler shallow groundwater. The two main temperature-dependent reactions are solubility and exchange reactions [146].

The first three assumptions are probably suitable for a few reactions that occur in many places, while the last two are not valid for many hot-spring systems; therefore, information obtained is for the shallower parts of those systems [152].

3.3   QGIS update of Geothermal prospects in Kenya

The research on geothermal energy in Kenya has been along the Rift valley. Mapping or focusing on the main structured control manifestations have led to little activities in remote areas with low-temperature hot springs. Tole (1992) reported low-temperature hot springs outside the Rift valley. The geothermal map of Kenya is updated using QGIS to include low enthalpy resources. The study aims to map more prospects and those outside the rift valley.

3.4 Water Chemistry

Natural hydrothermal water systems can be defined as juvenile, magmatic, meteoric, connate, or metamorphic water [146]. High heat flow regions (averagely above 1.4×10^{-6} cal $cm^{-2} sec^{-1}$) are usually associated with mountain building at crustal edges and volcanism [146]. Estimating the outflow in geothermal fields will be important in estimating tons of dissolved salts in correlation with the laboratory chemical analysis. Geothermal water ascension and surface emergence may cool in the process by boiling, conducting, or mixing with shallow water. At pH 8.3, all carbonate occurs as HCO_3^- and on titration to 3.8 with 0.1 M HCl, all carbonate occurs as CO_2 [150].

To assure all the significant ions are analysed in samples and to check on the data quality, ionic balance formula (equation(3.1))is applied [153]:

$$\sum_{cations} \frac{c_i}{M_i \times z_i} = \sum_{anions} \frac{c_i}{M_i \times z_i}$$

(3.1)

where c is the concentration (mg/L), M is the molar mass (g/mol), and z is the valance (-).

$$\%dev = \frac{\sum_{cations} - \sum_{anions}}{\sum_{cations} + \sum_{anions}} \cdot 100$$

(3.2)

Equation (3.2) shows the electroneutrality condition for checking the data quality before processing, where $\sum_{cations}$ and $\sum_{anions}$ represent the concentrations of cations and anions, respectively.

Classification of the geothermal systems should relate to the field situation. Geochemistry's two main classifications of geothermal systems are cyclic and storage systems [146]. Chemical geothermometers are used before drilling and reconnaissance exploration [17]. The fluid sources are determined by hydrologic investigations by isotopic analysis technique and the quantitative estimate of infiltration obtained by hydrologic balance by the relation I=P-E-R, where I, P, E and R are infiltration, precipitation, evapotranspiration and runoff, respectively [17].

3.4.1 Cyclic Systems

Meteoric water percolates to great depths, gets heated, rises through convection, and may not be continuous due to interaction with permeable zones[146]. Such systems require rock formations that allow deep circulation, source of heat, water, sufficient time and surface area, and the return path [146]. The cyclic systems are mainly sub-divided into three categories

of high-temperature systems associated with recent volcanism, high-temperature in non-volcanic zones, and warm waters in near-normal heat flow zones [146].

3.4.2 Storage Systems

Water is stored and heated in rocks for geologically long periods as either fluid within formation or water of hydration (water stoichiometrically bound into a crystal) in minerals. Triangular plots for the anions and cations are used to peruse the thermal waters from Kenya. The main geothermometers that have been consistently applied in the geochemical analysis of geothermal sub-surface and reservoir estimations include Fournier and Truesdell (1973); Fournier and Potter (1979); Arnnorsson et al.,(2000) [153]. Surface temperatures recorded in the field varied from 30-74°C. The geochemical characteristics of the thermal waters will be used to estimate the reservoir temperatures and possible development scenarios. Analysis carried out by spectrometry, ion chromatography, and ion coupled plasma showed the type of water in this research.

3.4.3 Silica geothermometer

In any geothermal field, silica is the most worrying element. In hydrothermal areas, silica occurs in various forms as chalcedony, cristobalite and amorphous silica (gelatinous silica, sinter and opal) [146]. Quartz is the stable form of silica with the lowest solubility, unlike other forms that should not have equilibrium solubility, and the silica content can be correlated with the last temperature of equilibration with quartz using Figure 3.1 [146], [147].
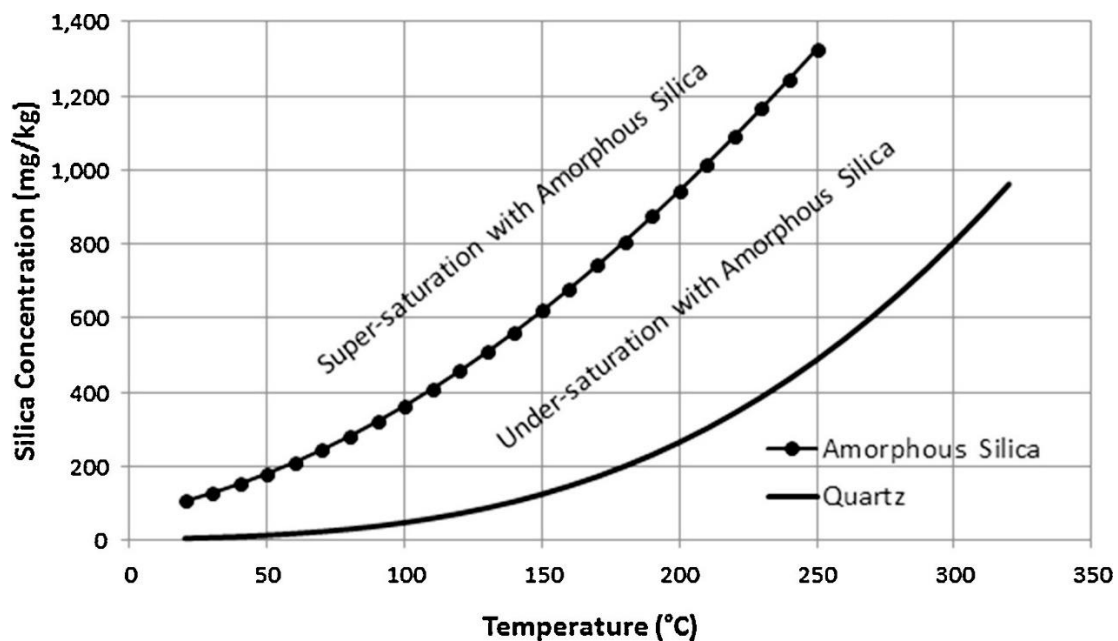
Figure 3.1. Solubility of quartz and amorphous silica as a function of temperature [154].

57

Quartz geothermometers estimate reservoir temperatures and are good indicators of the possibility of scaling in the surface facilities and reinjection wells. Sub-surface temperatures increase assuming mixing cold and hot groundwater, but without mixing, they decrease [17]. Geothermometry estimation might predict the central up-flow zones depth corresponding to the highest temperatures [155].

Geothermal systems associated with sizeable silicic magma bodies located in subduction zones are the hottest and most easily identified bodies and take a long time to cool (for example, 5 km chamber takes 2 million years to cool from $\approx 850^{\circ}C$ to ambient temperature) [17]. The latest volcanic eruptions are believed to still be at their eruption temperatures. Water quartz equilibrium is rapidly attained and are reasonable estimates of changing reservoir but is receptive to cooling and mixing; thus, it is suitable for hot springs estimates [17].

3.4.4   Cation geothermometer

The cation geothermometric approach is susceptible to differences in fluid and reservoir compositions [17]. Equilibrium constants for exchange and alteration reactions are temperature dependent, and the ratios of dissolved constituents change with changing temperature of equilibration [147]. Low values of Na-K-Ca geothermometer estimates indicate re-equilibration below $100^{\circ}C$ evaporative sequence perturbation [17], [147]. Due to the retrograde solubility of calcium carbonate, springs supplied directly from hot aquifers have the highest Na/Ca ratios [147].

3.4.5   Mixing Models

Thermal water usually consists of deep hot water mixed with shallow cold aquifer water. After mixing, partial or complete chemical equilibration may or may not occur [147]. The temperature of the hot-water estimation based on an exchange reaction using a ratio of dissolved constituents is affected by mixing in two ways;

  i.   The deep hot water is relatively concentrated in the indicator elements than the shallow water.
  ii. Little or no chemical reaction occurs after mixing to change the relative concentrations of the indicator elements.

Low Mg on concentration reveals the possibility of extensive mixing with cold water during water movement to the surface[156].

3.4.6   Isotopic Analysis

Fluid isotopic compositions reflect temperature conditions in a geothermal system [148]. Analysis of oxygen 18- and deuterium isotopes trace the source of groundwater. Stable analysis shows that most geothermal waters in Kenya originated from meteoric water [97], [157], [158]. Isotope and geochemical data combination give a more reliable and accurate estimation of the available/estimated geothermal resource.

3.5   Results and discussion
3.5.1   Water chemistry

Table 3.1. summarises the laboratory geochemical and isotopic analyses results. The chemical composition of the sampled water and the analysis carried out in other fields are relatively investigated in the relative composition of major anions and cations and total silica using triangular and isotopic diagrams. The charge balance errors calculated using equation (3.2) in the research were less than 5% for most of the samples. From Table 3.1, the samples from Kipsegon, Mulot, Mwanamanyalla, Majimoto, Narosura, Meru, Homa Hills, and Silali have near-neutral pH values between 6.16 and 7,84. The Eburru, Magadi and Bogoria samples have pH between 8.18 and 9.8. In the geothermal wells of Olkaria, pH values vary, ranging between 7.43 and 10.28, with most of the wells having pH above 9.

3.5.2   Geochemical geothermometers

The water chemistry results were used to estimate the sub-surface temperatures. For the temperature calculation in Tables 3.1 and 3.2, the geothermometers used are Quartz and cations (Na_K, Na-K-Ca and Na-K-Ca-Mg).

Silica geothermometers are of different forms and are valid up to temperatures of less than 250°C [7], [152], [159], [160]. Due to the water and rock interaction complexity, several geothermometers shown in the Appendix section have been developed [161].

.

Table 3.1: Total concentration of constituents for the geothermal brine and thermal springs in some of the manifestations in Kenya.

Sample Location	Lab Number	Temp (°C)	pH	Li	Na	K	Ca	Mg	SiO₂	B	Cl	F	SO₄	HCO₃	CO₃	NH₄	Cond. umhos/cm	del ¹⁸O	del D	Charge Balance
⁺Kipsegon	S1	33.5	6.58		17	7	8.7	1.71	57	-	2	1	9	73	-		1.64E+02	-3.63	-15.8	0%
⁺Mulot	S2	46.2	6.16		37	15	25.4	20.50	96	-	5	1	4	293	-		4.76E+02	-4.35	-19.7	-1%
⁺Eburru	S3	49.3	8.18	0.01	41	26	0.7	0.06	452	-	50	1	10	61	-		254	-4.61	-26.0	-4%
⁺Narosura	S4	30	6.37		15	6	10.4	4.43	43	-	9	1	21	61	-		1.90E+02	-5.09	-28.5	-1%
⁺Majimoto	S5	56.3	6.66		31	12	18.2	7.50	88	-	50	1	23	61	-		344	-5.33	-29.0	4%
⁺Homa Hills	S6	74.9	7.84	0.4	6,980	13	1.2	0.22	143	-	1,900	90	2,100	12,000	-		2.03E+04	-3.48	-12.8	1%
⁼Homa Hills	S7	87.5	8.76		7,330	174	0.6	0.40	188	-	5,800	7	502	10,252	-					-3%
⁼Meru	S8	21	7.39		1,688	126	200.0	101.00	54	-	344	0		5,197	-					0%
⁼Mwanamanyala	S9	66.6	6.32		1,550	48	9.7	5.04	129	-	1,942	1	1	967	-	92.0				3%
⁼Mwanamanyala	S10	79	6.89		1,576	37	8.9	4.64	132	-	1,896	1	0	1,051	-	90.0				3%
⁼Homa Hills	S11	82	8.24		6,710	97	1.5	0.85	135	-	1,397	8	1477	15,502	-	2.0				-5%
⁼Magadi	S12	84.6	8.85	1.17	10,900	186	1.0	0.40	80	8	5,250		163	18,910	-					2%
⁼Magadi	S13	81.3	9.47	1.13	11,400	195	1.0	0.40	86	9	5,950		159	21,900	-					-3%
⁼Magadi	S14	82	9.18	1.18	10,300	158	1.0	0.40	88	8	5,300		153	19,900	-					-3%
⁼Bogoria	S15	94	8.1	0.56	1,265	26	1.3	0.37	108	0	220	59	62	2,868	-	0.3				-2%
⁼Bogoria	S16	95	9.5	0.38	7,360	162	0.8	0.02	216	3	1,737	285	86	15,864	-	3.7				0%
⁼Bogoria	S17	96	9.8	0.36	5,980	113	0.3	0.02	180	2	1,347	209	67	12,810	-	5.1				1%
⁼Silali	S18	77	7.8	0.98	2,180	57	3.0	0.20	-	-	290	-	199	4,830	-					3%
⁼Silali	S19	75	7.7	0.94	2,100	55	2.6	0.20	-	-	295	-	196	4,840	-					1%
⁼Silali	S20	81	7.7	0.06	2,150	57	3.0	0.20	-	-	295	-	197	4,710	-					3%
⁼Magadi	S21	66.6	8.96	0.78	11,100	157	1.0	0.40	83	8	5,850	1	134	20,900	-					-2%
*OW-914	S22	-	10.06	2.75	1,569	461		0.01	650	3	514	270	88	-	1,400					2%
*OW914A	S23	-	7.43	1.26	891	217	0.91	0.04	685	2.89	381		51.6	-	877					4%
*OW-914B	S24	-	10.1	0.87	776	158	1.86	0.05	293	3.01	324	275	79.8	-	356					1%
*OW-914C	S25	-	9.51	1.57	896	278	-	-	997	0.96	386	234	47.1	-	706					-1%

*OW-915C	S26	-	10.16	1.63	1,338	264	-	-	1,832	1.19	619	235	110.6	-	847					4%
*OW-915D	S27	-	10.28	1.61	918	337	-	-	1535	1.2	698	264	137	-	342					1%
*OW-916B	S28	-	9.69	1.89	711	171	-	-	1161	0.98	352	230	83.1	-	434					-4%
*OW-921	S29	-	9.76	1.77	563	153	0.4	0.08	1117	2	339	71	80	-	273.0					**9%**

Key for Tables 3.1 and 3.2.

+ denotes the samples collected during the field visit and data collection (new geothermal manifestations).

= represents data sampled from literature; these samples do not include isotope analysis. It was one of the motivations to consider the isotopic analysis of new hot springs (already mapped in other studies, e.g., Tole (1992) and (2001).

*samples are from a developed geothermal field in Olkaria. The analysed results from the literature are for actual producing wells; some of the wells are considered in Chapter five of the thesis.

Cond. is conductivity.

- not detected in Table 3.1, or not calculated in Table 3.2.

Table 3.2: Calculated geothermometers temperatures (°C) for the geothermal waters from the fields investigated [149].

Sample Name	Amorphous Silica	Alpha Cristobalite	Beta Cristobalite	Chalcedony conductive	Quartz conductive	Quartz adiabatic	Na-K-Ca	delta T R>5	Na-K-Ca Mg corr	Na/K Fournier 1979	Na/K Truesdell 1976	Na/K Giggenbach 1988	Na/K Tonani 1980	Na/K Nieva & Nieva 1987	Na/K Arnorsson 1983	K/Mg Giggenbach 1986
+Kipsegon	-9	58	10	79	108	108	86	-6.3	86	380	419	380	489	364	407	80
+Mulot	15	84	36	108	135	131	96	69.0	27	374	409	375	478	358	398	68
+Eburru	119	197	148	234	247	219	317	0.0	317	451	538	440	630	433	510	172
+Narosura	-20	45	-2	64	95	97	77	17.2	59	380	418	379	488	364	406	66
+Majimoto	11	80	31	103	130	127	94	38.7	55	364	394	366	459	348	384	74
+Homa Hills	36	108	59	134	158	150	82	-26.7	82	15	-36	36	-23	6	-23	124
=Homa Hills	52	126	76	154	176	165	203	0.0	203	118	72	139	94	108	83	213
=Meru	-11	55	8	76	106	106	185	150.6	35	193	158	210	190	180	167	102
=Mwanamanyala	30	101	52	127	152	145	164	76.5	88	134	88	153	113	122	100	117
=Mwanamanyala	32	103	54	128	154	146	152	72.7	79	118	71	138	93	107	83	111
=Homa Hills	33	104	55	130	155	147	166	2.4	166	93	44	114	64	83	56	172
=Magadi	6	74	26	97	125	122	187	0.0	187	101	53	122	73	91	65	216
=Magadi	10	78	30	101	129	126	188	0.0	188	101	53	122	74	91	65	218
=Magadi	11	80	31	103	130	127	180	0.0	180	96	47	117	67	86	59	209
=Bogoria	21	91	42	115	142	136	157	3.3	155	111	63	131	85	100	75	139
=Bogoria	61	136	86	165	186	172	196	0.0	196	114	67	135	89	104	79	290
=Bogoria	50	123	73	151	173	162	192	0.0	192	106	58	127	80	96	70	268
=Silali	-	-	-	-	-	-	171	0.0	171	124	78	144	101	113	89	180
=Silali	-	-	-	-	-	-	172	0.0	172	124	78	144	101	113	89	178
=Magadi	-	-	-	-	-	-	172	0.0	172	125	78	145	102	114	90	180
*OW-914	8	77	29	100	127	124	177	0.0	177	92	43	113	63	82	55	208
*OW914A	155	235	187	277	294	245	-	0.0	-	331	343	336	400	315	339	393
*OW-914B	161	241	193	283	303	249	319	0.0	319	307	309	315	361	292	308	287
*OW-914C	83	159	109	191	209	190	289	0.0	289	287	279	296	327	272	281	261
*OW-915C	207	288	244	337	425	280	-		-	338	353	342	412	322	348	-
*OW-915D	308	386	353	450	1453	339	-		-	283	275	293	322	268	276	-
*OW-916B	275	354	317	413	927	320	-		-	361	389	363	453	345	380	-
*OW-921	229	310	267	362	530	294	-		-	306	306	314	358	291	306	-

.

3.5.3 Ternary and enthalpy plots

For simple understanding and explanation of results, samples were subdivided into two sets of S_1-S_{14} and S_{15}-S_{29}, as shown in Figure 3.2 - Figure 3.13. Figure 3.2 shows the graphical representation of the chemistry for samples S_1-S_{14} studied. The apexes of the plot Ca, Mg and Na+K for cations, while for the cations, the apexes are sulphate, Cl and carbonate. The anion and cation plats are projected on the diamond by matrix transformation to graph total anions (Cl+SO$_4$) and cations (Na+K). The dominant hydro-chemical facies for S_1-S_{14} are sodium carbonate and Na+K facies.

S_2 and S_4 are non-dominant water types falling near the cation triangle's central section and Mg-bicarbonate type. S_1 is a mixed Na bicarbonate water type. S_8 is a sodium bicarbonate water type. The other samples (S_3, S_5, S_6, S_7, S_9, S_{10}, S_{11}, S_{12}, S_{13}, and S_{14}) are chloride types with some carbonate and bicarbonate species along the HCO$_3$ edge of the Piper diamond plot. TCSH plot in Figure 3.3 shows most of the samples S_1-S_{14} are of carbonate-chloride type [162], [163].
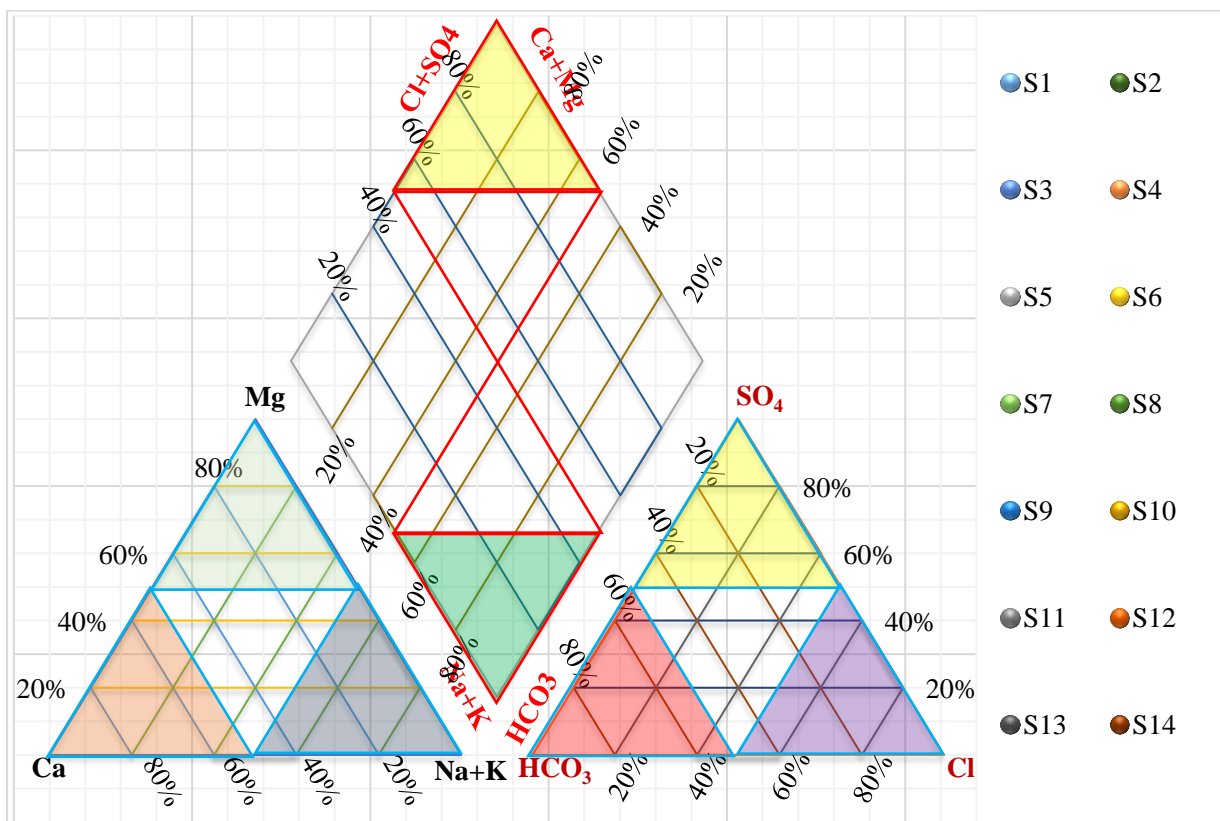
Figure 3.2: Piper plot for samples S_1-S_{14}. The detailed classification facies of the Piper plot is shown in the Appendix section.

Samples S_9 and S_{10} are the only mature species of the samples plotted. The other samples S_1-S_8, and S_{11}-S_{14}, fall in the peripheral water type region. The samples have high and moderate chloride and carbonate contents with low sulphate content.

From the Piper plot, Figure 3.4, most samples are Na-Cl type because of high chloride content. Figure 3.5 shows S_{15}-S_{21} samples are mapped on peripheral water region while S_{22}-S_{29} are in the mature waters section and closer to the Cl apex. For samples S_{15}-S_{29}, no dominant and mixed type of geothermal/spring for the water identified in the central regions of the Piper plots [164], [165]. The high chloride indicates continual groundwater flow in the source rocks.

Giggenbbach (1988) plot uses Na-K-Mg geoindicators to classify geothermal waters as immature, partially equilibrated and fully equilibrated water [163]. The plots for the samples studied in Kenya are shown in Figure 3.6 and Figure 3.7 for S_1-S_{14} and S_{15}-S_{29}, respectively.
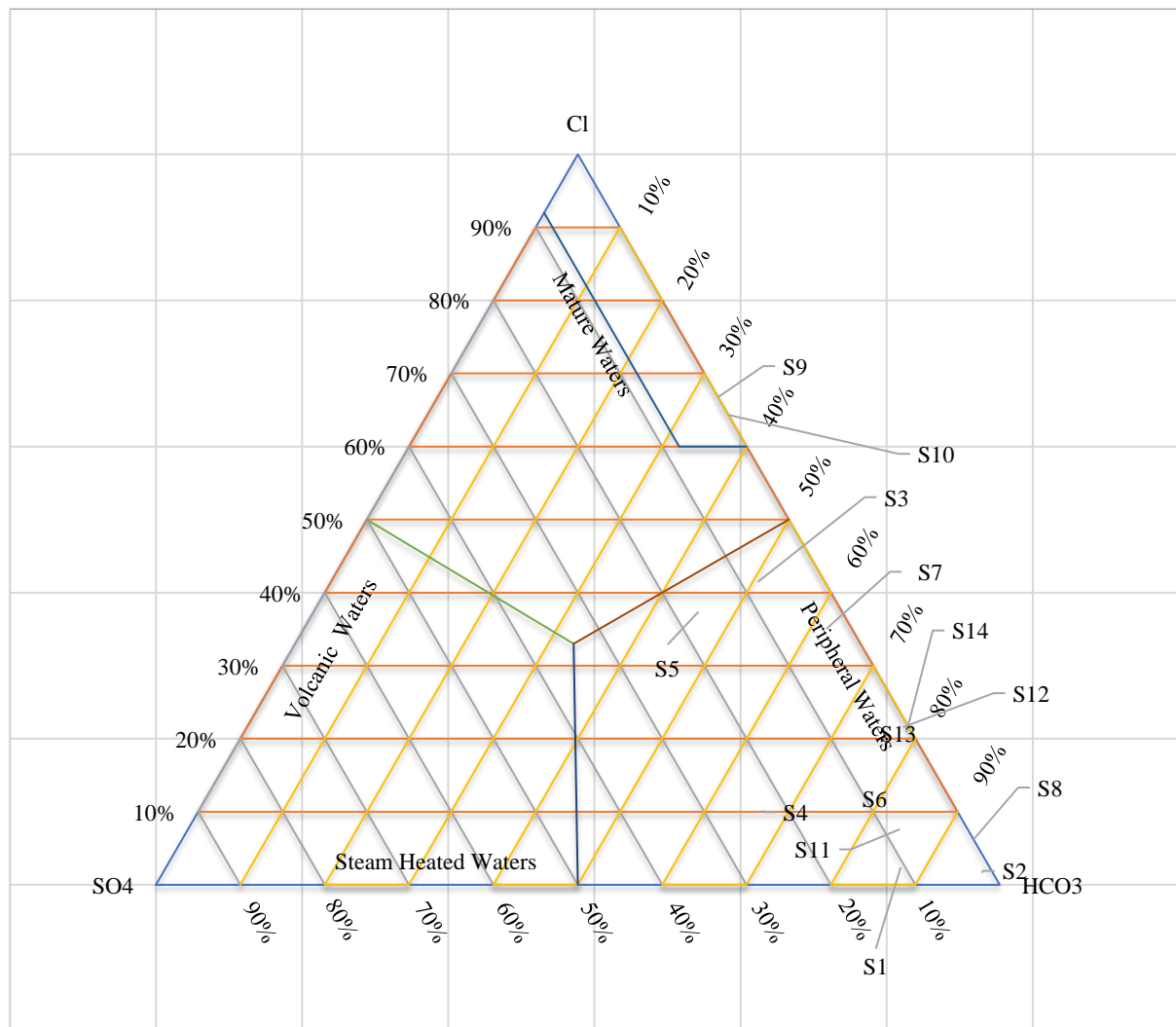
Figure 3.3: Cl-SO$_4$–HCO$_3$ ternary anion plot showing the significant anions proportions of Kenya's geothermal/spring waters for samples S_1-S_{14}.
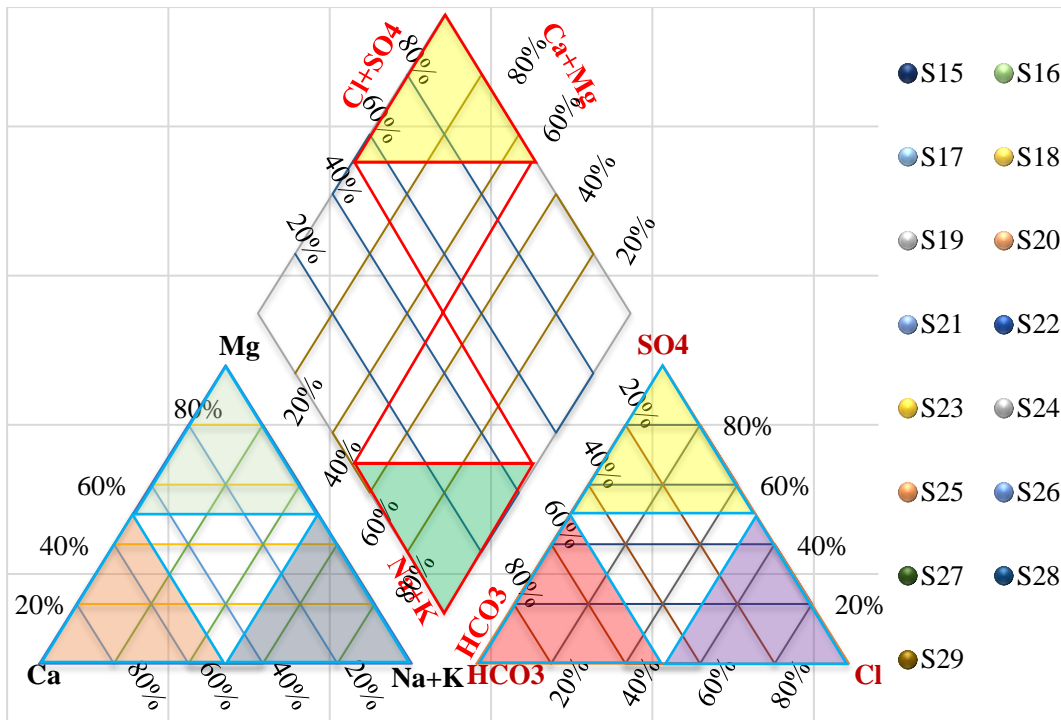
Figure 3.4: Piper ternary plot for samples S_{15}-S_{29}.
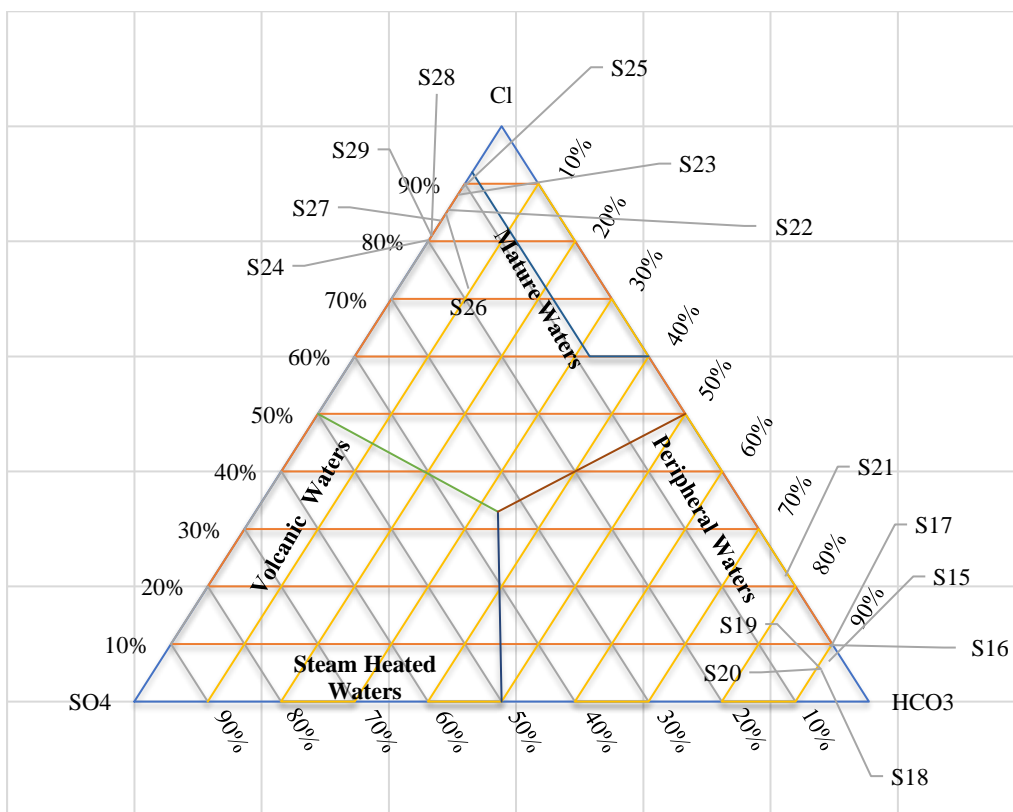
Figure 3.5: Cl-SO$_4$–HCO$_3$ ternary anion plot showing the major anions proportions of Kenya's geothermal/spring waters for samples S_{15}-S_{29}.
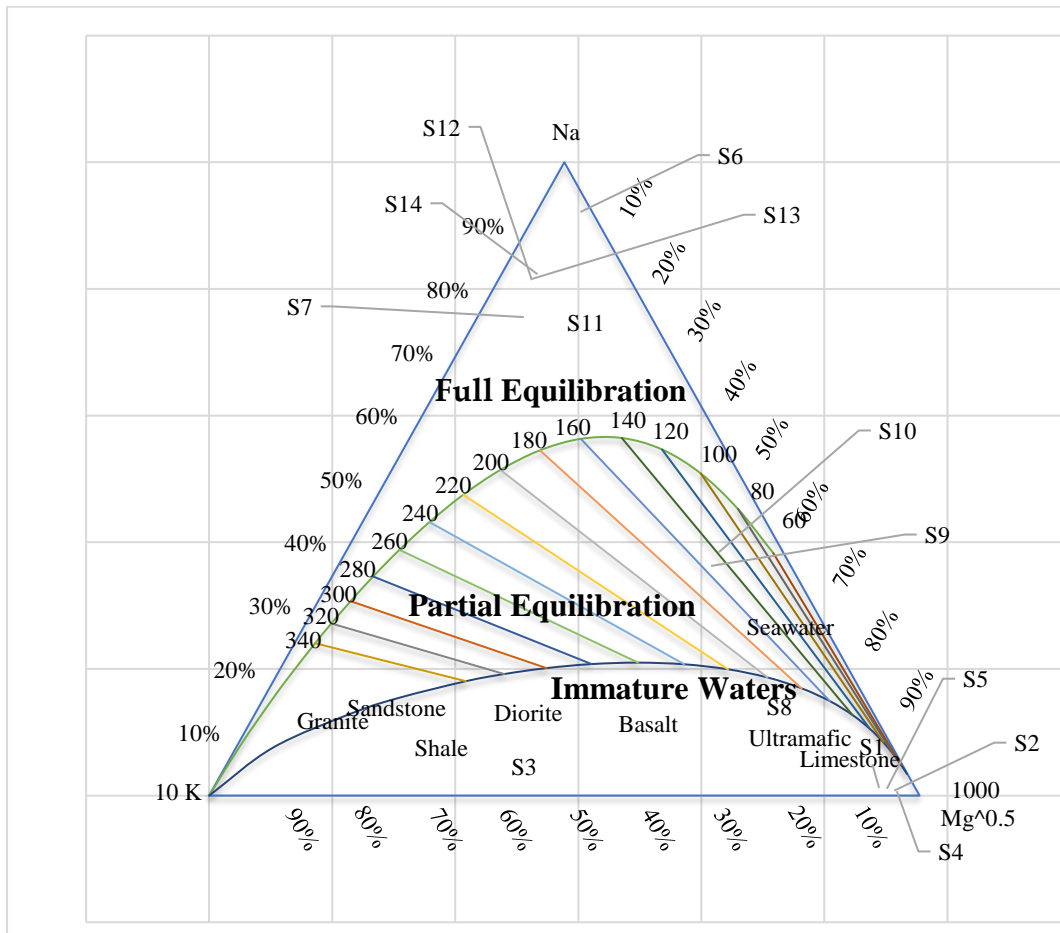
Figure 3.6: Giggenbach ternary graphical plot for S_1-S_{14} for evaluating the water-rock equilibration.

For the first split/section of samples studied, S_1-S_5 and S_8 are immature water; thus, the cations geothermometry should be examined [166]. S_9 and S_{10} are partially equilibrated. The new fields (S_1-S_5) mainly have immature waters. The samples in the partial equilibration and mature water region can have a certain degree of certainty in evaluating temperatures [167]. Figure 3.6 shows samples S_6, S_7, S_{11}, S_{12}, S_{13}, and S_{14} in the region of fully equilibrated waters that may have circulated deeply at high temperatures in the sub-surface.

Figure 3.7 presents the Na-K-Mg ternary plot for S_{15}-S_{29} water samples and geothermal brine from Olkaria geothermal field. The water is partially or fully equilibrated, as seen in Figure 3.7.
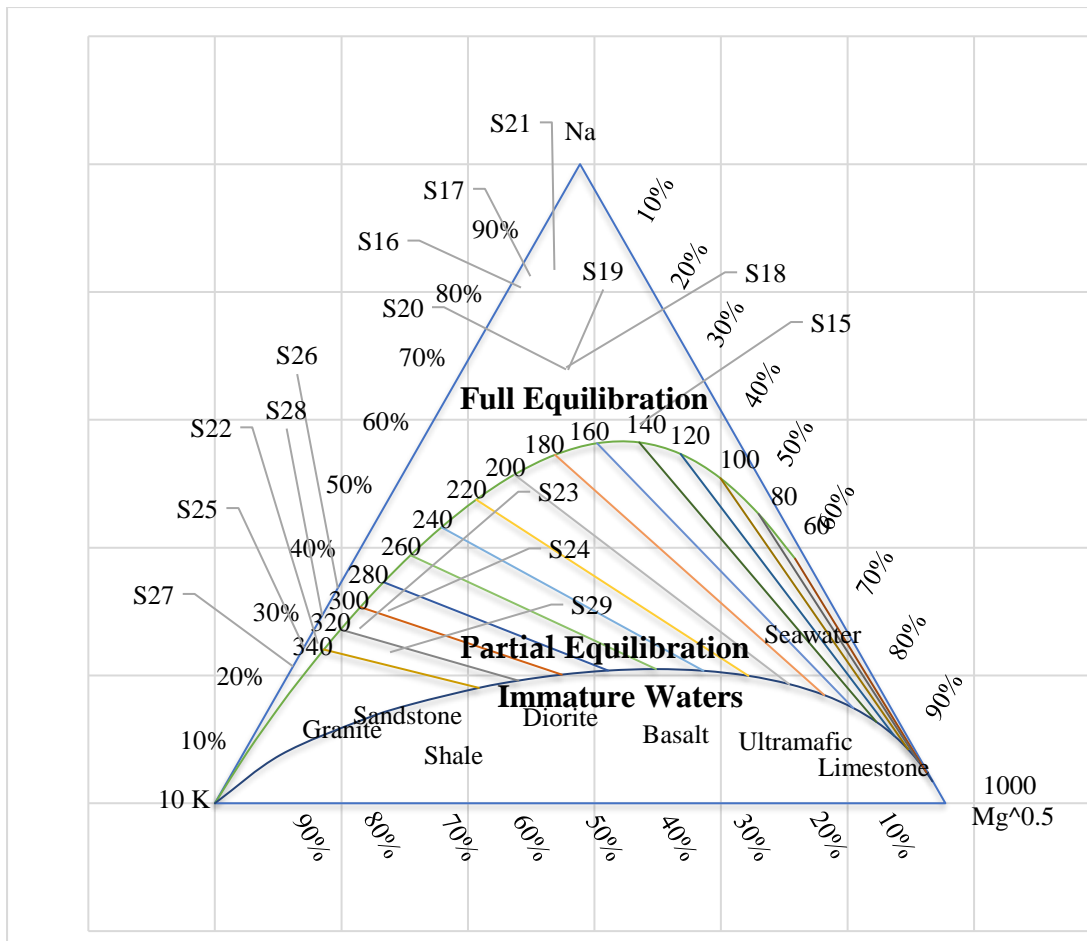
Figure 3.7: Giggenbach ternary graphical plot for S_{15}-S_{29} for evaluating the water-rock equilibration.

The samples are aligned along the ternary side of Na-K because of the high Na contents. Most of the S_{15}-S_{29} have lower ranges of Mg. None of them is closer to the Mg apex in the ternary plot, showing less hot and cold-water mixing.

The Giggenbach and Goguel plot [163] in Figure 3.8 and Figure 3.8 show the range of temperature predictions of the samples. Figure 3.8 is for samples S_1 –S_{14}. S_1 and S_4 on the boundary line of Chalcedony and Alpha Cristobalite temperatures are between 60-80°C. Only S_8 is in the Chalcedony with an estimated temperature close to 100°C. In the Beta, Cristobalite region are S_2 and S_5, with a temperature range between 60-80°C and S_3 at approximately 170°C. The other samples have high temperatures, with the quartz geoindicator appropriate for estimating the sub-surface temperatures for S_7, S_{11}-S_{14}.
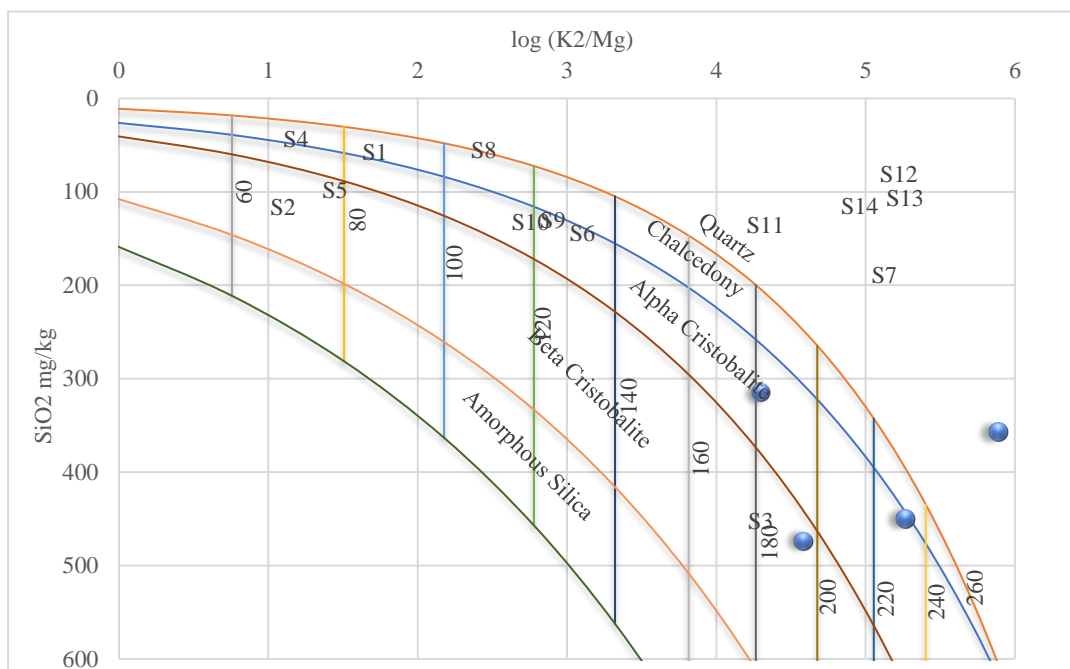
Figure 3.8: Plot of K^2/Mg (Xkms) versus silica geothermometer for the water samples S_1-S_{14}.

The Xkms plots (Figure 3.8 and Figure 3.9) show that the samples close to seawater have high-temperature prediction and quartz section. Figure 3.9 shows the temperature estimates for samples S_{15}-S_{29}. Most species are in the quartz section with temperatures above 160°C except for S_{15} in the Chalcedony region and temperatures close to 140°C.
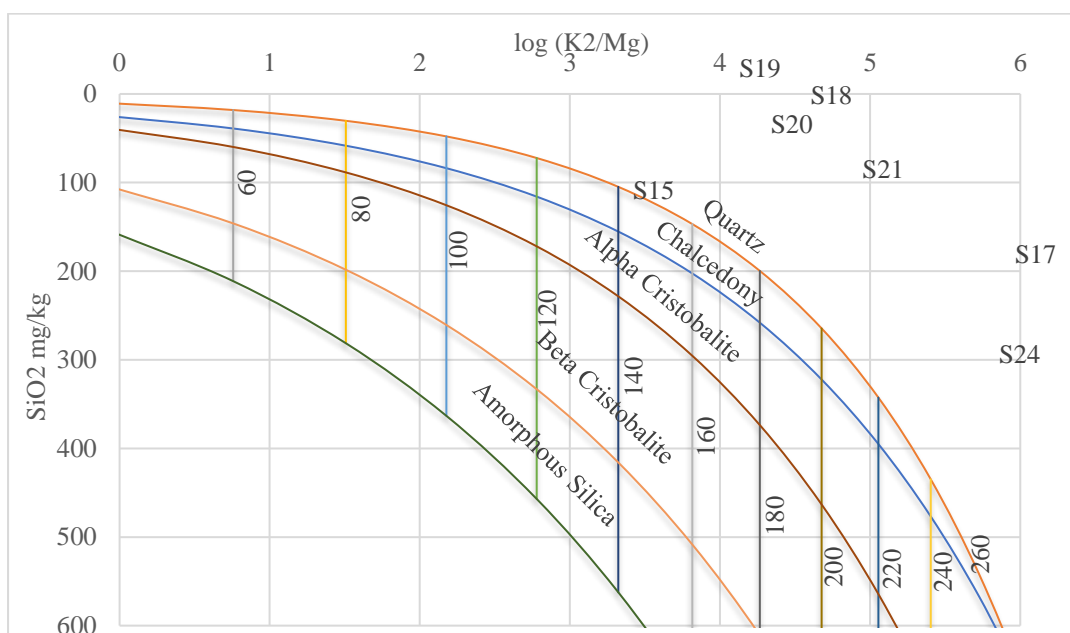
Figure 3.9: Xkms versus silica geothermometer plot for the water samples S_{15}-S_{29}.
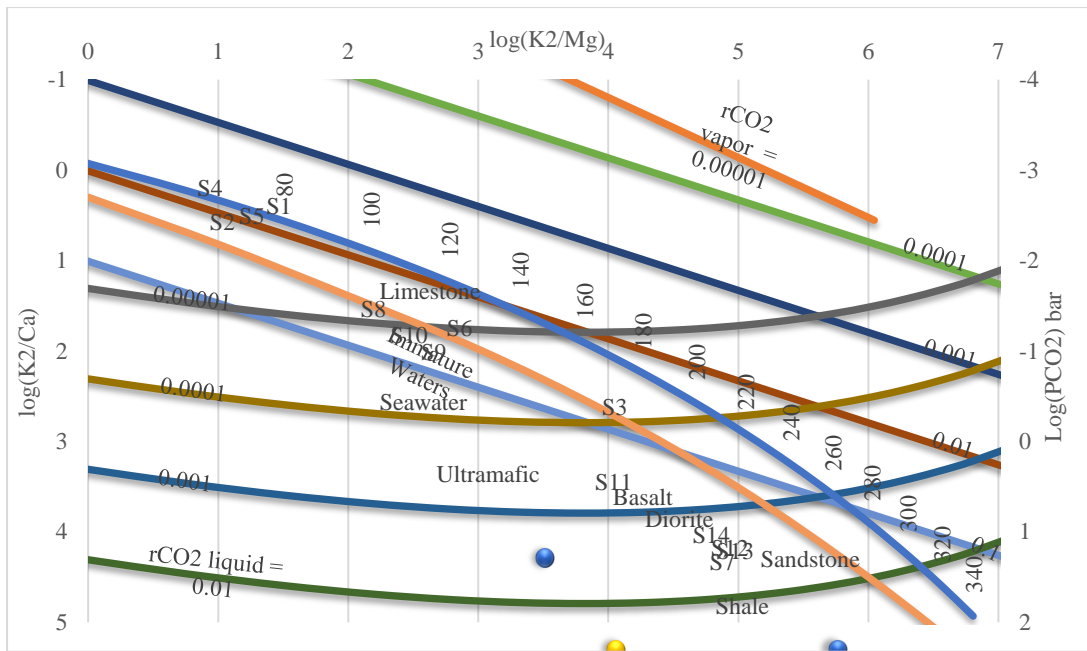
Figure 3.10: Plot of Log K^2/Ca, Log K^2/Mg (Xkmc) for samples S_1-S_{14}.
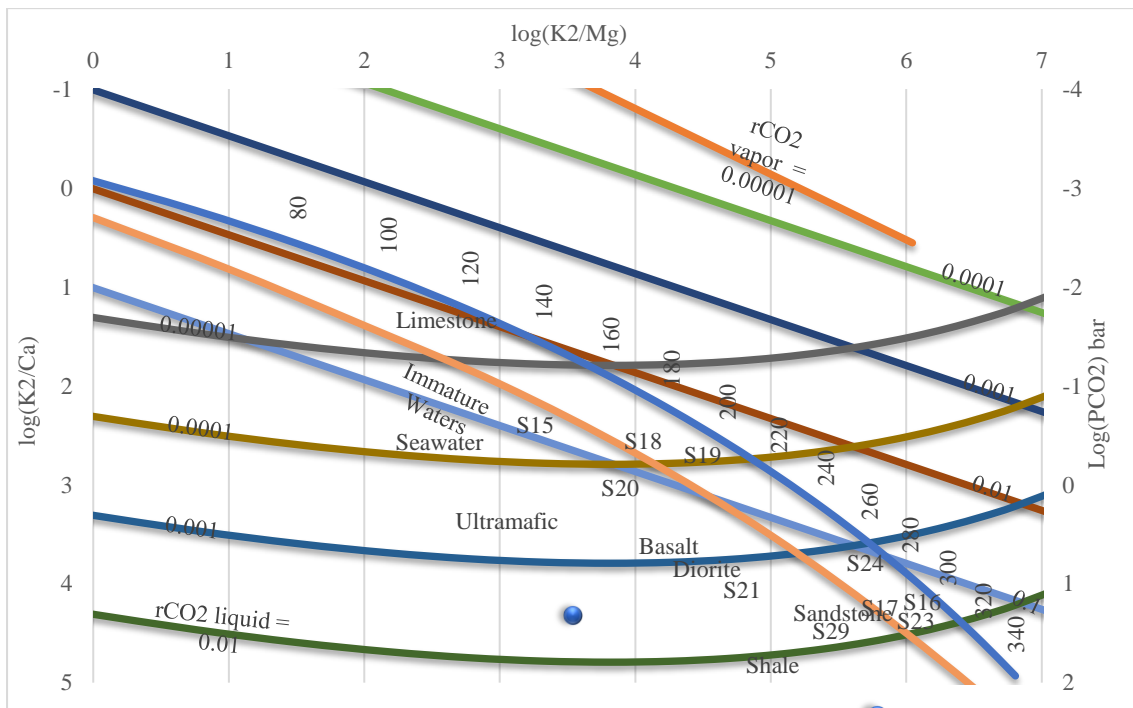
Figure 3.11 Xkmc plot for S_{15}-S_{29} water samples.
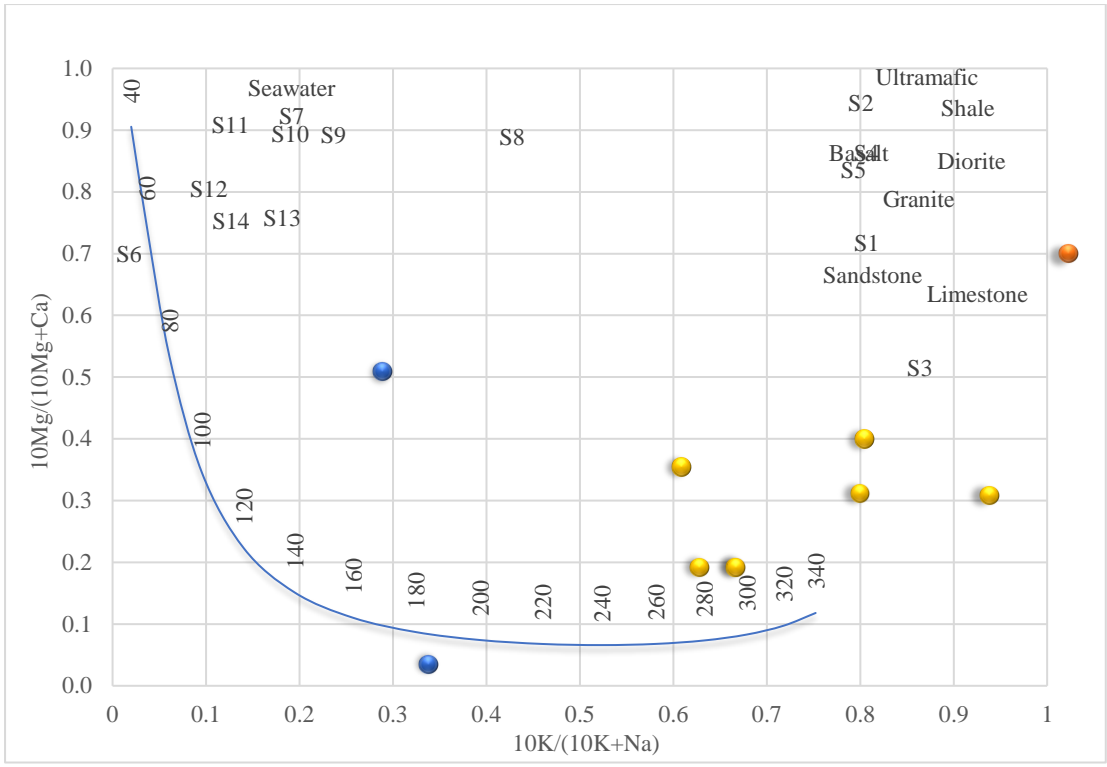
Figure 3.12: Giggenbach and Goguel plot for S_1-S_{15}.
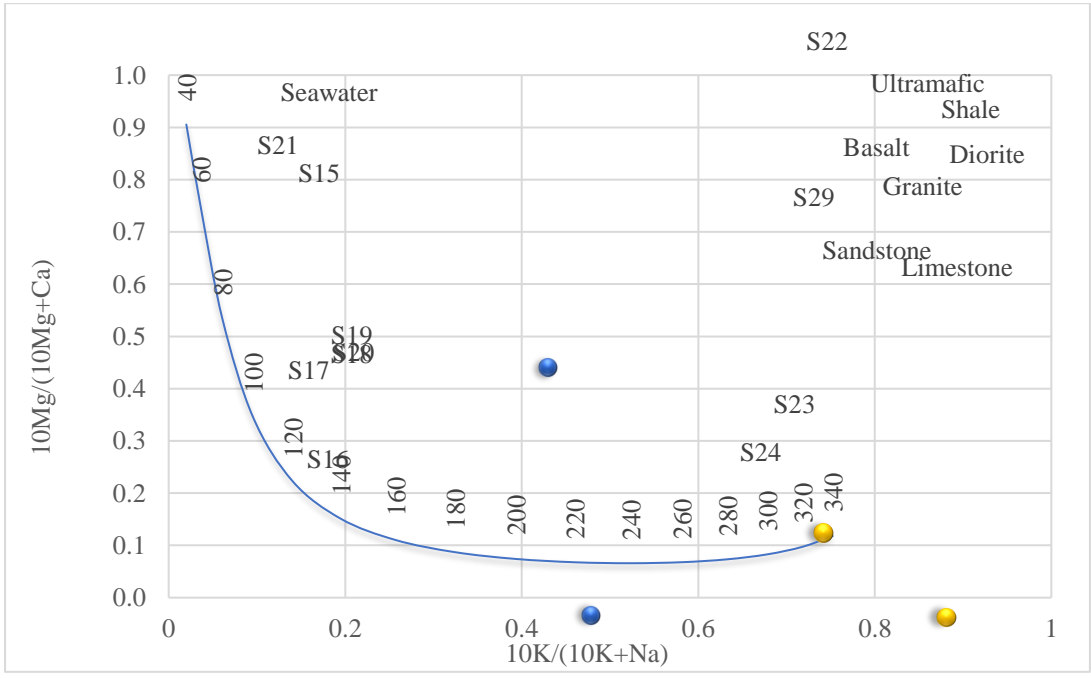
Figure 3.13: Giggenbach and Goguel plot for S_{15}-S_{29}.

Figures 3.12 and 3.13 show the cation geoindicator (Xmckn) plots for the geothermal and hot springs waters studied. Xmckn plot is a good predictor for water-dominated fields by rock chemistry [149], [168]. Figure 3.12 represents S_1-S_{14}. Figure 3.13 shows the samples S_{15}-S_{29} geoindicator representation. From the plots (Figure 3.12 and Figure 3.13), the water samples close to seawater are S_6-S_{14} and S_{15} and $S_{21.}$ Water relative to seawater indicates the dissolution of wall rocks due to mixing with the seawater.

The new fields' isotopic analysis of six samples (S_1, S_2, S_3, S_4, S_5 and S_6) corresponds to the meteoric trend line. Figure 3.14 supports that the origin of the water is meteoric. The isotopic study of the unmapped manifestations shows that the fields could be fed by waters that do not have long residence time. The six manifestations studied are likely to be recharged by water from the highlands region. The primary water source is rainfalls in the water catchment areas to the West of Rift Valley. The origin of the water samples hypothesized in this study supports other isotope studies that inferred that most water recharge is rainfall [97], [158], [169].
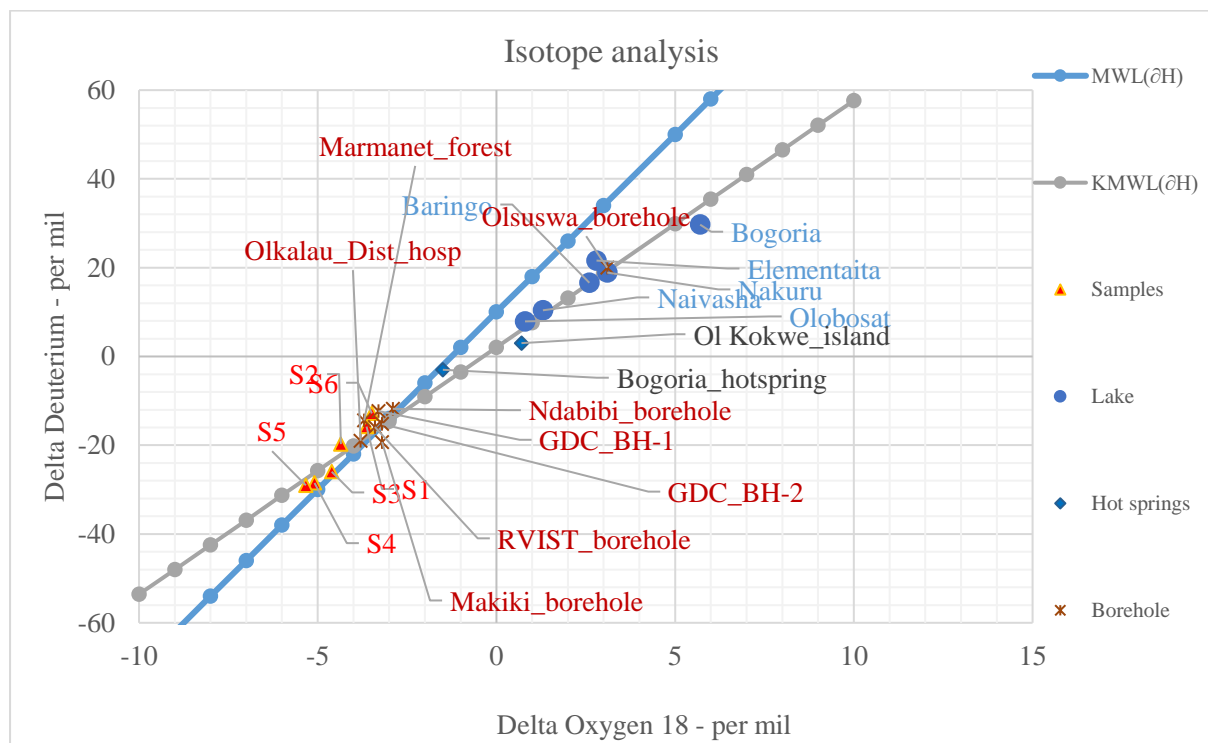
Figure 3.14: δ^{18}O - δ^2H plot shows the isotopic composition of samples S_1-$S_{6.}$ The six samples were collected during the field study in 2019. MWL: Meteoric Water Line. KMWL: Kenya Rift Valley Meteoric Water Line. The lake, borehole (BH) and hot springs data are from [169].

3.6   QGIS update of geothermal prospects in Kenya

Figure 3.15 shows the updated locations of low enthalpy fluid flow in Kenya. Barrier and Kapedo hot springs discharge waters at 48-79.9°C and 39-51.9°C, respectively, in Suguta valley. The Arus Bogoria is an extensive area spanning West from Lake Bogoria with numerous hot altered grounds, rich fumarolic activity, and hot springs near river valleys. This area has a general high geothermal gradient since some boreholes produce warm waters at shallow depths of 100-200 m. The regions to the immediate West and Northwest of Menengai caldera show high geothermal gradient at shallow depths as boreholes drilled to a maximum depth of 250-280 m in this region produce warm water at temperature ranges of 33-54°C. The Fumarolic activities around Eburru and Badlands Elementaita produce large amounts of steam/vapours at 97-100°C condensed by nearby communities for water. The area also has a few warm water boreholes with several hot springs discharging inside the tip of Lake Elementaita. Lake Magadi lacks perennial surface inflow, but it is recharged by 25 hot springs that have saline waters at a range of 34-86°C to form warm spring ponds within the trona tables. Kuro hot springs within Isiolo county are located 65 km southwest of Merti town. The Biliqo community uses the Kuro springs to water their animals, deworm animals, and cure skin ailments [170]. Mwana Nyamala hot springs in Kwale County near the extreme southern tip of Kenya. The four hot springs discharge from jointed and faulted deltaic and fluvial-lacustrine sandstones of Duruma sandstone. The heat source at Mwana Nyamala is assumed to be one or several satellite intrusions and lamprophyre dykes [171].
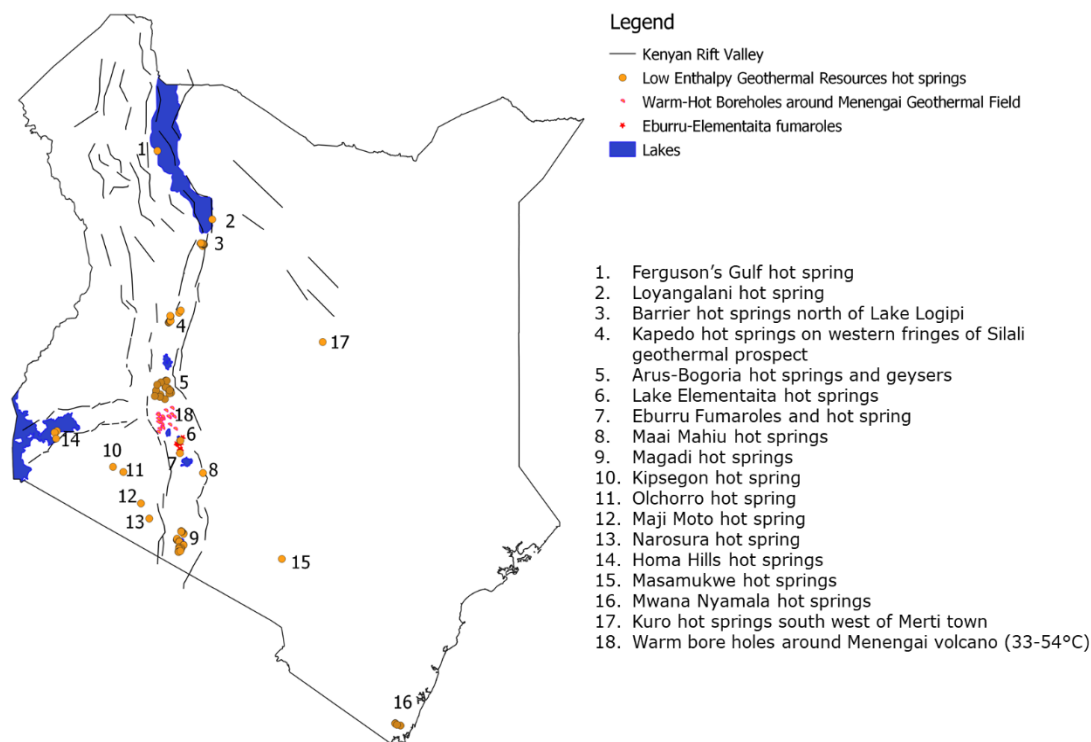
Figure 3.15: Updated locations of low enthalpy geothermal resources in Kenya (Modified from [171].

3.7 The utilisation of low enthalpy geothermal resources in Kenya

Low geothermal resources come with utilisation challenges, especially in remote areas far from cities and developed electric grids. Hence many policymakers prioritise high enthalpy geothermal resources for exploration, development, and exploitation. In Kenya, high enthalpy reservoirs of Olkaria and Menengai have been developed for electricity generation, but the low enthalpy geothermal resources have been left unexplored. However, as Kenya develops and the population grows, the remote geothermal resources are surrounded by farming activities and are gaining accessibility via roads. Resources such as Magadi, Narosura, Maji Moto, Homa Hills, Loyangalani, and many others are gaining popularity in domestic tourism, hiking, and hot spring swimming/bathing. As stated before, Kuro, Maji Moto, Narosura, Homa Hills hot springs provide water for domestic use, irrigation of vegetable farms, watering livestock, aquaculture, among other uses. Ol Njorowa hot springs are drinking points for wild animals within Hell's Gate National Park. The fumaroles from Eburru to Badlands Elementaita are all condensed for hot water for domestic washing. The slightly saline waters of Homa Hills hot spring are used as saltlicks and for deworming domestic animals. The concentrations of boron

73

and fluoride in most of these hot spring waters are undetectable, and they are considered safe for domestic and livestock use.
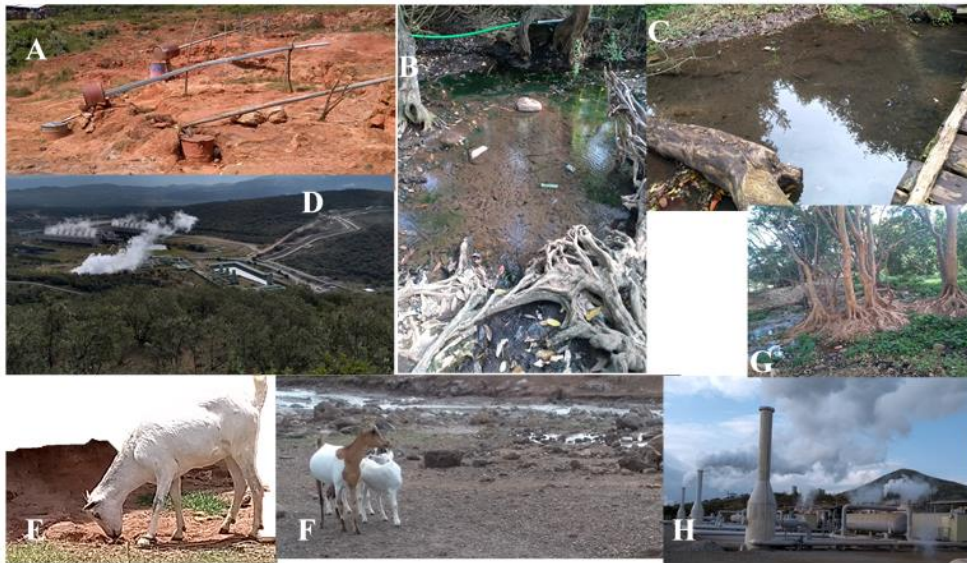
Figure 3.16: Image of geothermal fields in Kenya showing fields visited in 2019. A) Shows Eburru residents condensate harvesting for general and domestic uses. B) is the Majimoto Hotsprings in Narok county. C) shows the sampling point and Kipsegon Hotsprings (new field not in the previous maps. D) Olkaria IV SF power plant. E) A goat lick altered ground in the Eburru area while in F) Goats in the vicinity of hot springs in Homa Hills. G) Narosura warm water point and H) is the well-head 914 units in the Olkaria Domes field.

However, these resources are utilised naturally without optimal infrastructures like wells, brine piping, animal drinking troughs, swimming ponds and water pumps. The inadequate infrastructure limits their potential/optimum utilisation. In addition to the geothermal potential, demand for the proposed resource utilisation is significant. The utilisation of these resources depends on their reservoir temperatures and their location (which will dictate or justify the utilisation method). Reservoir temperatures of <120°C might be used for direct uses such as drying, spa, greenhouse warming, while >120<200°C could be used for direct uses and electricity generation via binary systems. Reservoirs with >200°C, such as Eburru, can also be used for direct and electricity generation through steam turbines. Steam turbines are preferred because they produce electricity at a lower cost per kWh since parasitic pumping load is smaller than ORC systems.

Identifying water origin and estimating temperatures in the reservoir for hot springs are essential for future development. As the new fields undergo more studies and exploration, the

developed ones need to be managed and utilised optimally to set the base for the upcoming developments. The following section considers developed geothermal field by exergy optimisation of power plants (Olkaria I, II and IV) and proposed ORC cycles using available exergy.

3.8   Conclusion
3.8.1   Water chemistry

The geothermal waters have different chemical compositions and vary from one field to another. Geothermal manifestations in Kenya have been mapped mainly along the EARS with high potentials. The map is updated using QGIS to optimise the potential of thermal units/available in Kenya, with the newest fields being Olchoro, Kipsegon, and others being Narosura and Majimoto. These geothermal manifestations are in remote areas and have not been researched exhaustively like Olkaria, Eburru or Menengai and other EARS prospects.

The water investigated from geothermal prospects and geothermal fields are of three types; immature, partially equilibrated and fully equilibrated, as depicted in the Na-K-Mg ternary plot. The immature is closer to the Mg pole, while the partial equilibrated types are in the central centroid of the plot. The fully equilibrated types are found towards the Na apex. Isotope analysis of six new sites shows that the origin of the water/recharge is from rainfall. In terms of geothermometers, Eburru has the highest estimated reservoir temperatures of 234-247°C, while Narosura geothermal reservoir has the lowest reservoir temperatures of 64-95°C.

According to stable isotopic analysis, the recharge for most of the reservoirs in Kenya is meteoric water and fed mainly from high altitudes. The study of geothermal sites in Kenya indicates that water chemical composition determines the sub-surface temperatures using geothermometry.

3.8.2   Update of geothermal manifestations in Kenya

The low geothermal resources occur mainly within the Kenyan dome and the satellite intrusions on the Eastern side of the Kenyan Rift. The Rift Valley floor contains both high and low enthalpy geothermal resources, sometimes close to each other. This research added to the map the Kipsegon hot spring in Bomet County, Eburru hot spring at Nakuru County, and Olchorro hot spring in Narok County. Homa Hills, Narosura, and Maji Moto hot springs' geochemistry was re-confirmed, and their locations were updated on the map. The five low enthalpies geothermal resource visited exhibit neutral to slightly alkaline bicarbonate waters while waters from Homa Hills are slightly saline, slightly alkaline bicarbonate-chloride waters.

While underground meteoritic waters may have significantly diluted most hot springs water, waters from Homa Hills hot springs have a significant value of total dissolved substances and plots in mature waters in the Giggenbach diagram.

CHAPTER FOUR

4.0 OPTIMISATION OF POWER PLANTS IN OLKARIA BY ENERGY, EXERGY AND EXERGOECONOMIC CONCEPTS

4.1 Introduction

This chapter will investigate the performance of geothermal power plants in Kenya, obtaining data from KENGEN for the Olkaria IV power plant (in the Domes area). Olkaria field is the most developed geothermal field. The existing power plants are single flash (SF) operated by KENGEN. Among the SF units are Olkaria I, Olkaria II and Olkaria IV. The study will propose, model and design binary units (three configurations/cycles), back-pressure, and optimise by energy, exergy, and exergoeconomic concepts. In the development of power plants, the critical decisions are estimating power generating costs for selling geothermal energy to the consumer for every exergy input [17]. Thermodynamics is an intersection of energy, exergy, and entropy [172], where entropy considers the effects of irreversibility in a system resulting from exergy destruction/entropy generation. Exergy aims to maximise/optimise available energy for better utilisation from an optimum usage view perspective [76].

4.2 Energy and exergy analysis

The analysis is based on the fundamentals of thermodynamics' first and second laws and the principles of mass and energy conservation. The three efficiencies that will be discussed and calculated are thermal, exergy and second utilisation efficiencies. Thermal efficiency is the ratio of net work to heat energy into the power plant. Exergy efficiency is the ratio of et work to exergy in, while second utilisation efficiency is the ratio of net work to the available exergy. In calculating the available exergy, reinjection temperatures are considered to less the exergy of brine returned to the formation. The details of each component's equations are in the Appendix section's EES code

Equation (4.1) shows the gross work, $\dot{W}_{\text{gross}}$, turbine generates.

$$\dot{W}_{\text{gross}} = \dot{m}_{steam}\Delta h \qquad (4.1)$$

The net power generated, $\dot{W}_{\text{net}}$, (kW) by the power plant is determined by equation (4.2);

$$\dot{W}_{\text{net}} = \dot{W}_{\text{gross}} - \dot{W}_{parasitic} \qquad (4.2)$$

For the overall system, the parasitic load ($\dot{W}_{parasitic}$) includes the work done by cooling tower fans, equivalent power for non-condensable gases (NCG) removal, and the power consumed by the pump.

Equations (4.3) and (4.4) show the general steady-state mass and energy equations, respectively, where $\dot{m}_{in}$ is the mass flow rate of fluid into the system in kg/s; and $\dot{m}_{out}$ is the mass flow rate of fluid leaving the system in kg/s [81], [116]. The generated power is because of isentropic steam expansion in the turbines, which results in an enthalpy drop, Δh (kJ/kg).

$$\sum \dot{m}_{in} = \sum \dot{m}_{out} \tag{4.3}$$

$$\dot{Q}_{in} - \dot{W}_{gross} + \sum \dot{m}_{in} h_{in} - \sum \dot{m}_{out} h_{out} = 0 \tag{4.4}$$

The energy/thermal efficiency (η_{th}) of the system is calculated using equation (4.5) for the net work generated for the heat rate in at the wellhead, $\dot{Q}_{in}$ (kW):

$$\eta_{th} = \frac{\dot{W}_{net}}{\dot{Q}_{in}} \tag{4.5}$$

Equation (4.6) shows the general expression for specific exergy, e (kJ/kg), involving environmental thermal interaction and entropy generation [7], [76], [105].

$$e = h - h_0 - T_0(s - s_0) \tag{4.6}$$

Equations (4.7) and (4.8) show ideal air exergy and exergy destruction, respectively for air-cooled condenser [103], [110].

$$e_{air} = c_{p,air}\left(T - T_0 - T_0 \ln\left(\frac{T}{T_0}\right)\right) + R_{air} T_0 \ln\left(\frac{P}{P_0}\right) \tag{4.7}$$

$$Ex_{DC} = T_0[\dot{m}_{wf} \times (s_{in} - s_{out})_{wf} + \dot{m}_{air} \times (s_{in} - s_{out})_{air}] \tag{4.8}$$

Exergy input, output, and exergy destruction equations are given by equations (4.9), (4.10), and (4.11), respectively, for each component [7];

$$\dot{Ex}_{in} = \dot{E}_Q + \sum_{i=1}^{k} \dot{m}_i e_i \tag{4.9}$$

$$\dot{Ex}_{out} = \dot{E}_W + \sum_{j=1}^{k} \dot{m}_j e_j \tag{4.10}$$

$$\Delta \dot{Ex} = \dot{Ex}_{in} - \dot{Ex}_{out} = \dot{E}_Q + \sum_{i=1}^{k} \dot{m}_i e_i - \dot{E}_W - \sum_{j=1}^{k} \dot{m}_j e_j \tag{4.11}$$

where i, is for all incoming streams and j for all outgoing streams for a kth component [7]. Exergy losses are subdivided into each component in the thermodynamic process. For a control volume, the general exergy balance is that the total exergy output is always less than the total exergy input [37], [173]. Each component has an exergy destruction rate expressed as exergy destruction ratio to the total exergy destruction as shown in equation (4.12):

$$\dot{Ex}_{ratio} = \frac{\Delta \dot{Ex}}{\sum \Delta \dot{Ex}}$$
(4.12)

4.3 Main components in geothermal power plants

Geothermal power plants consist of many components from the reservoir to the re-injection point. In the exergy and exergoeconomic analysis of geothermal power plants, the significant features include separator, turbine, condenser, pumps, cooling tower, non-condensable gas ejectors, fans, and pumps. Other studies have presented most of the components of geothermal power plants (flashing units and different binary layouts) by exergy and energy analysis (e.g. Shokati et al., 2015; Bina et al., 2017, 2018) [174], [175]. A cooling tower is one of the central and critical components used in power plants. One of the research objectives is to include the exergoeconomic part of the cooling unit. The following sub-section of the chapter presents the cooling tower basic energy equations.

4.3.1 Cooling tower basic equations

A cooling tower is a heat exchanger designed to reduce condensate temperature in thermal power plants. The heat and mass transfer in the counter flow-induced draft cooling tower is mainly analysed using the Merkel equation [126], [176]. Enthalpy difference in the air at the surface of the water and the mainstream air transfer heat and water vapour into the atmosphere. Range, Ra, (^{o}C) of the wet cooling tower is given by equation (4.13):

$$Ra = T_{in} - T_{out}$$
(4.13)

Water air flow ratio (L/G) (-) from energy and mass balance equations is shown in equation (4.14) as:

$$L/G = \frac{(h_{airout} - h_{airin})}{c_{p,air}(T_{in} - T_{out})}$$
(4.14)

In this research, the focus is on the mass flow rate of the cooling water to propose an exergoeconomic equation for the cooling tower as a function of water flow rate. The equations will connect the cooling tower and other units in exergoeconomic analysis of power plants. The exergoeconomic part of the wet-cooling tower needs more studies [177], [178].

Utilisation/exergy (η_u) and second utilisation (η_{u2}) efficiencies are calculated using equations (4.15) and (4.16), respectively [7], [101]. Utilisation efficiency is the ratio of the actual work to the exergetic power, while second utilisation efficiency is the ratio of the actual work to the exergy available between the wellhead and reinjection point.

$$\eta_u = \frac{\dot{W}_{net}}{\dot{Ex}_{in}} \tag{4.15}$$

$$\eta_{u2} = \frac{\dot{W}_{net}}{\dot{Ex}_{available}} \tag{4.16}$$

The sustainable development of geothermal energy requires the efficient use of available resources. The sustainability index, SI (-), is defined as equation (4.17) as a function of exergy efficiency [81], [179].

$$\text{SI} = \frac{1}{1 - \eta_u} \tag{4.17}$$

The above equation will be modelled for the binary power plants and process flow in the analysis to propose sustainability cost as a measure for sustainable development. Irreversibility of the system accounted for using equation (4.18) to balance the exergy out, ($\dot{Ex}_{out}$), and the summation of exergy destruction, $\dot{Sum}_{exd}$ (kW), for each component and the whole system.

$$\dot{Ex}_{irr} = \dot{Sum}_{(EX|D)} - \dot{Ex}_{out} \tag{4.18}$$

In the exergy and economic analysis of power plants, exergoeconomic equations are balanced for each sub-unit from the exergy inlet point (wellhead) to the exit point (reinjection). Each component cost product is calculated in the EES code for the 1.3 \$/GJ unit exergy cost.

4.4 Exergoeconomic equations for optimisation of geothermal power plants in Kenya

Recent and related research on the exergoeconomic analysis of power plants has provided a complete understanding of the thermal flow processes. One of the main components in industrial and power plant designs is the cooling tower, but most related works do not include the wet-cooling tower. The cooling tower exergoeconomic introduced for optimal utilisation of geothermal energy.

The exergy and economic aims are to evaluate the cost per unit exergy of the product stream. Heat exchangers' area (A_{total}) and the overall plant cost influences the cost of power to consumers in binary power plants.

In the exergy and economic analysis of power plants, the connecting term is exergoeconomic. The main components' cost equations developed are product functions from the component or main design parameter. The cost equation for the turbine is the gross work generated; heat

exchangers are the area, while pumps and fans are the work required to run them. The missing link in the exergoeconomic of geothermal power plants is the cooling tower, thus the motivation to carry out complete exergoeconomic of the power plants in Olkaria, Kenya. Table 4.1 shows the economic and thermal parameters applied with the exergoeconomic equations to calculate the cost rates for each power plant. Table 4.2 shows the cost relations for the components.

Table 4.1: Economic and thermal assumption parameters.

Parameter(s)	Value	Reference
Number of years, n	30	Primary
Interest rate, I (%)	10	Primary
Annual plant operation hours, τ (hours)	8,322	Primary
Maintenance factor, γ (-)	1.06	[81]
Nominal escalation rate r_n (%)	5	[81], [175]
The unit cost of exergy, c_f ($/GJ)	1.3	[81], [106], [175]
Condenser and pre-heater overall heat transfer coefficient U, (Wm^{-2} K^{-1})	500	[180]
Evaporator overall heat transfer coefficient U, (Wm^{-2} K^{-1})	600	[180]

The cost of each component is calculated from the equations in Table 4.2. Equation (4.19) is used to calculate the cost rate, $\dot{Z}_k$, using the capital recovery factor (CRF) in equation (4.20) [175].

$$\dot{Z}_k = \frac{(Z_k \times CRF \times \gamma)}{\tau} \tag{4.19}$$

$$CRF = \frac{i(1+i)^n}{(1+i)^n - 1} \tag{4.20}$$

Exergoeconomics applies the flow cost rate parameter, $(\frac{\dot{C}\$}{hour})$ in a system defined for each component in equation (4.21) [172]:

$$\dot{C}_{q,k} + \sum_i \dot{C}_{i,k} + \dot{Z}_k = \sum_j \dot{C}_{j,k} + \dot{C}_{w,k} \tag{4.21}$$

where $\dot{C}_{q,k}$ and $\dot{C}_{w,k}$ are the cost rates associated with the input heat energy and output work equivalent of each component, respectively. Using equation (4.21), the average cost per unit exergy is expanded to obtain equation (4.22) [172].

$$\sum \left(c_j \dot{E}x_j\right)_k + c_{w,k}\dot{W}_k = c_{q,k}\dot{E}x_{q,k} + \sum \left(c_i \dot{E}x_i\right)_k + \dot{Z}_k \tag{4.22}$$

for

$$\dot{C}_n = c_n \dot{Ex}_n \tag{4.23}$$

Fuel exergy, $\dot{Ex}_{F,k}$, product exergy, $\dot{Ex}_{p,k}$, and exergy destruction, $\dot{Ex}_{D,k}$, relationships are balanced using equation (4.24) [175], [181]:

$$\dot{Ex}_{F,k} = \dot{Ex}_{p,k} + \dot{Ex}_{D,k} \tag{4.24}$$

Equation (4.25) expresses the total cost rate associated with products, $\dot{C}_{P,total}$, for the system as a function of the fuel cost rate, $\dot{C}_{fuel}$ and the annual investment cost rate of the power plant, $\dot{Z}_{k,plant}$ [172], [182].

$$\dot{C}_{P,total} = \dot{C}_{fuel} + \dot{Z}_{k,plant} \tag{4.25}$$

The annual investment is calculated from direct equipment cost based on the optimised component parameters presented in Table 4.2. The $\dot{Z}_k$ term in equation (4.26) is the sum of the cost rates for capital investment ($\dot{Z}_k^{CI}$) calculated using equation (4.27) and operating maintenance (OM) related cost rates [181]–[183]:

$$\dot{Z}_{plant} = \dot{Z}_k^{CI} + \dot{Z}_k^{OM} \tag{4.26}$$

$$\dot{Z}_k^{CI} + \dot{Z}_k^{OM} = \frac{(Z_k \times CRF \times \gamma)}{\tau} \tag{4.27}$$

Cooling tower exergoeconomic analysis was investigated in this research. The cooling system is an integral part of every thermal unit and contributes to economic and thermodynamic aspects. The capital cost (Z_{CT}) and operating & maintenance ($Z_{CTO\&M}$), associated costs in \$ for the cooling tower were obtained as a function of the water flow rate, $\dot{m}_{gal}$, in gallons per minute using equations (4.28) and (4.29), respectively [184].

$$Z_{CT} = -10^{-10}\dot{m}_{gal}^{3} - 10^{-5}\dot{m}_{gal}^{2} + 70.552\dot{m}_{gal} + 61609 \tag{4.28}$$

$$Z_{CT,O\&M} = -8 \times 10^{-6}\dot{m}_{gal}^{2} + 13.291\dot{m}_{gal} + 13850 \tag{4.29}$$

An exponential equation is proposed for the cooling tower exergoeconomic, with Z_{CT} as a function of cooling water mass flow rate by curve fit estimation. The correlations used in this analysis were stated in the form of turbine work output, pumps power, heat exchangers surface area, the mass flow rate for cooling tower, and the airflow rates for the fan work in cooling.

Exergy rate matrix obtained from exergy analysis and purchase cost vector from the economic analysis are solved using equation (4.30) as:

$$[\dot{Ex}_{Dplant}] \times [c_{plant}] = [\dot{Z}_{plant}] \qquad (4.30)$$

to evaluate exergy factor, (c_{plant}). The cost of exergy waste $(\dot{C}_D)$ in each system is evaluated based on the total exergy destroyed [185].

Table 4.2: Cost equations for each component in the power plant.

Component	Capital cost (Z_k) ($)	Reference
Turbine	$Z_T = 4405 * \left(W_T\right)^{0.89}$	[107]
Condenser	$Z_{CD} = 1397 * (A_{CN})^{0.89}$	[107]
Pumps and fans	$Z_{\frac{p}{fan}} = 1120 \times \left(W_{\frac{p}{fan}}\right)^{0.8}$	[186]
Evaporator and Pre-heater	$Z_{\frac{EV}{PH}} = 130 * \left(\dfrac{A_{\frac{EV}{PH}}}{0.093}\right)^{0.78}$	[184]

$$[\dot{Ex}_{Dplant}] \times [c_f] = [\dot{C}_D] \qquad (4.31)$$

Exergoeconomic factor (f) is applied to relate specific costs between exergy inlet and outlet streams. The factor in equation (4.32) compares the investment cost rate and the cost associated with exergy destruction [187].

$$f = \frac{\dot{Z}_{plant}}{\dot{C}_D + \dot{Z}_{plant}} \qquad (4.32)$$

Factor f can be expressed in terms of cost rates from equations (4.30), (4.31) and (4.33) as shown in equation (4.33) [81];

$$f = \frac{c_{plant}}{c_f + c_{plant}} \qquad (4.33)$$

4.5 Geothermal power plants in Kenya

Chapter one of the dissertation discussed exploration activities in Olkaria prospects. Olkaria I, unit 1, was the first power plant developed in Africa and commissioned in 1981 and has a rated capacity of 15 MWe and units two and three followed, in 1982 and 1985, respectively. Kenya's total geothermal installed capacity is above 1 GWe. In 2010 a wellhead unit was commissioned at Eburru field. The geothermal power plants have been developed

mainly in Olkaria geothermal prospect. The other field with an operational power plant is Eburru, with a wellhead unit generating 2.52 MWe [3]. Power plants operating in the Olkaria field are Olkaria I, Olkaria II, Olkaria III (OrPower 4), Olkaria IV, Olkaria V, and a few wellhead units. Table 4.3 shows the geothermal power plants operating and proposed in Kenya.

In Table 4.3, Orpower and Oserian are private independent geothermal power generating companies in Kenya. Ormat International owns Orpower [70].

4.6 Optimisation of Olkaria IV single flash geothermal power plant

Olkaria IV power plant is the first unit developed in the Olkaria Domes field. Olkaria IV has an installed capacity of 140 MWe with two condensing steam turbine units (Table 4.3). It started operating in 2014 when the two 70 MWe turbines were commissioned [69]. The Olkaria Domes field's thermodynamic parameters have shown that enthalpy has remained constant between 1,300 and 2,700 kJ/kg. Figure 4.1 shows a simplified schematic diagram of the SF Olkaria IV geothermal power plant. A typical SF power plant consists of a reservoir, production well, separator, turbine, condenser, NCG removal system, cooling tower, and reinjection well. The steam gathering system, production and injection wells, and station separators for the two units of Olkaria IV are shown in the Appendix section.

Table 4.3: Geothermal power plants in Kenya installed and planned capacity as of 2019 [50].

Location	Power plant	Year of commission	Type	Installed capacity (MWe)	Planned (MWe)	Energy efficiency (%)	Exergy efficiency (%)	Available exergy (MW)
Olkaria	Olkaria I unit 1	1981	SF	15		14.5 [70]	34.6 [70]	159
	Olkaria I unit 2	1982	SF	15				
	Olkaria I unit 3	1985	SF	15				
	Olkaria II units 1 & 2	2003	SF	70				
	Olkaria II units 3	2010	SF	70				
	Wellhead 16 units	2013,2014	SF	81.1				
	Olkaria IV units 1 & 2	2014	SF	150		15.9 [68]	54.9 [68]	
	Olkaria I unit 4	2014	SF	75				
	Olkaria I unit 5	2019	SF	75				
	Olkaria V	2019	SF	173.2				
	Olkaria I unit 6	2020	SF		83.3			
	Oserian	2014 & 2016	Binary, SF	3.6				
	OrPower 4 - Unit I	2000	Binary	52.8				
	OrPower 4 -Unit II	2008		39.6				
	Orpower 4 - Unit III	2014		17.6				
	Orpower 4	2015-2018	Binary	45				
	Olkaria PPP	2022	SF		140			
Eburru	Eburru wellhead	2010	SF	2.52				
Menengai	Menengai	2021	SF		105			
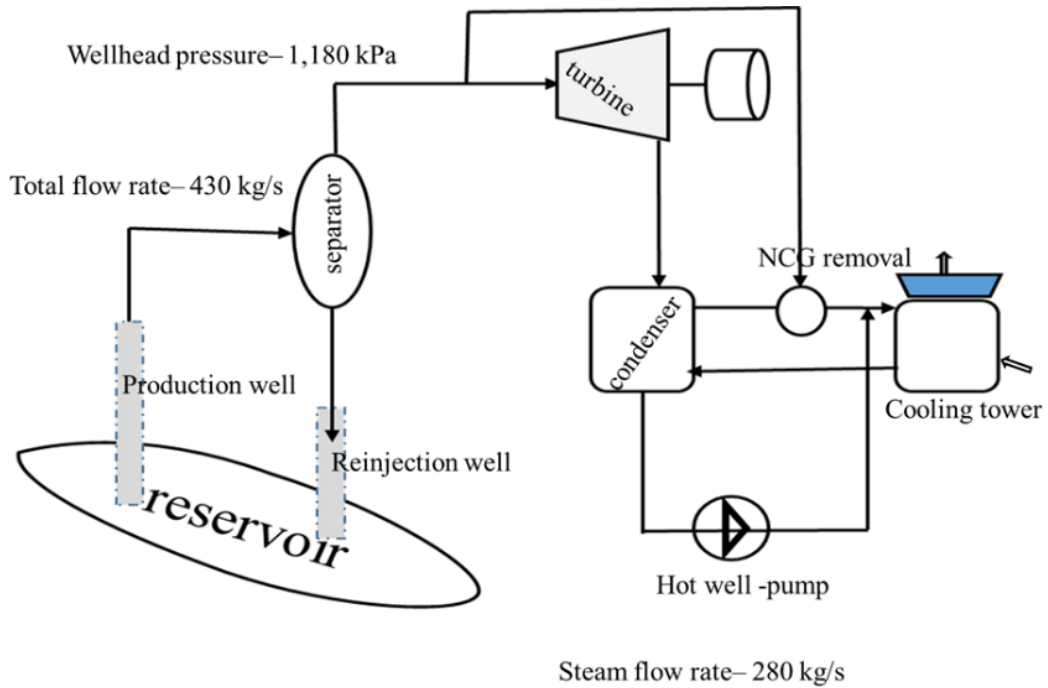
Figure 4.1: Schematic diagram of current Olkaria IV power plant. Two-phase brine separated at 520 kPa and hot brine reinjected at 187°C. Geothermal water at the reinjection temperature has exergy that can be utilised for power generation and direct use. Topping and bottoming units are possible.

4.6.1 Exergoeconomic analysis of Olkaria IV back pressure topping unit

The exergoeconomic analysis was then carried out for the current power plant and the proposed topping unit. The objective was to compare the cost of products and the overall power plant cost rates for the two plants.

Table 4.4: The systems common operating conditions at Olkaria geothermal complex.

Parameter	Value
Wellhead pressure	11,800 kPa
Generator efficiency	98 %
Turbine isentropic efficiency (η_T)	85-90%
Pumps isentropic efficiency (η_p)	75%
Ambient pressure (P_0)	86 kPa
Ambient temperature (T_0)	23°C

In the current scenario, the available exergy of 239 MW is utilised for 140 MWe, and the brine at 187°C is reinjected. Each turbine has a steam inlet pressure of 520 kPa and a pressure drop from wellhead pressure of 1,180 kPa.

4.6.2   System description

The modelled unit is a modification of the Olkaria IV (Figure 4.1), which is shown in Figure 4.2, identical to the energy analysis unit in [69]. The power plant is analysed exergoeconomically, including the cooling tower section, for optimum utilisation of the available exergy at Olkaria Domes. After flashing, the two-phase brine in the separated, the flashing pressure at Sate 4 is optimised for a back-pressure turbine before the steam is directed to the condensing steam turbine. The steam quality across the back-pressure turbine equals to 1.
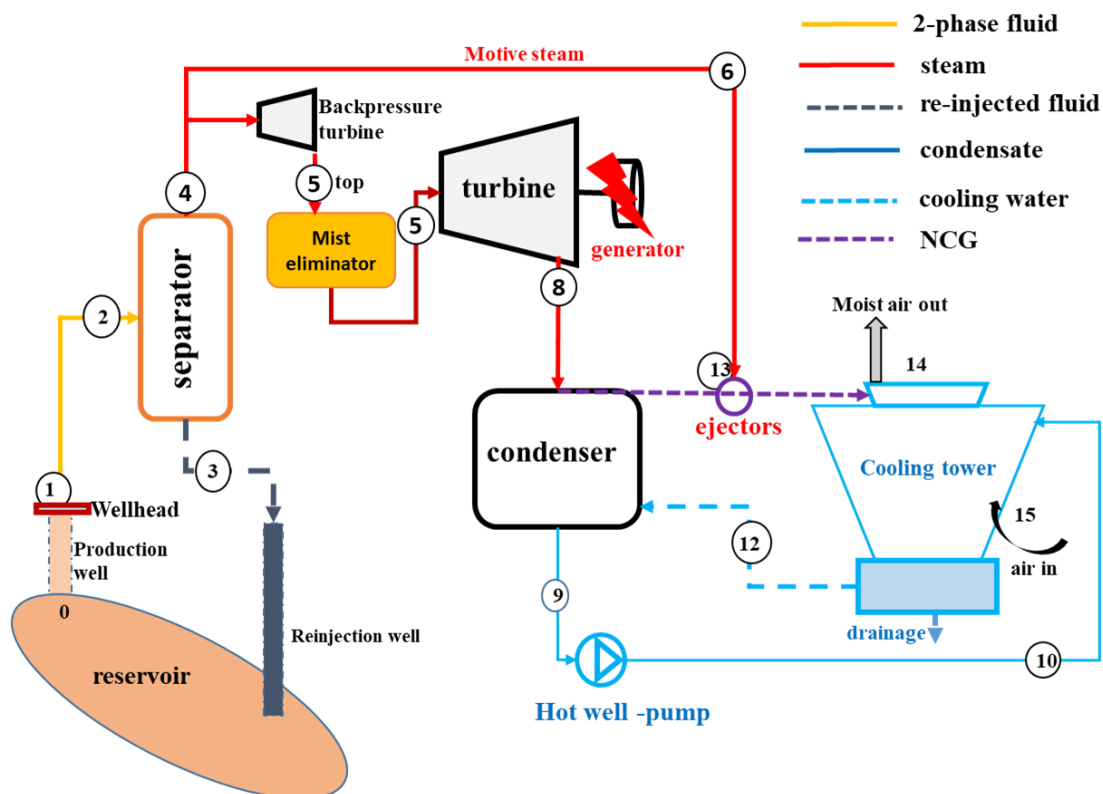
Figure 4.2: Schematic diagram of proposed modification at Olkaria IV SF power plant The enthalpy drop between States 4 and 5 is considered to check the optimum work equivalent generated. The steam quality is assumed to be 1.

4.6.3 Results and discussion
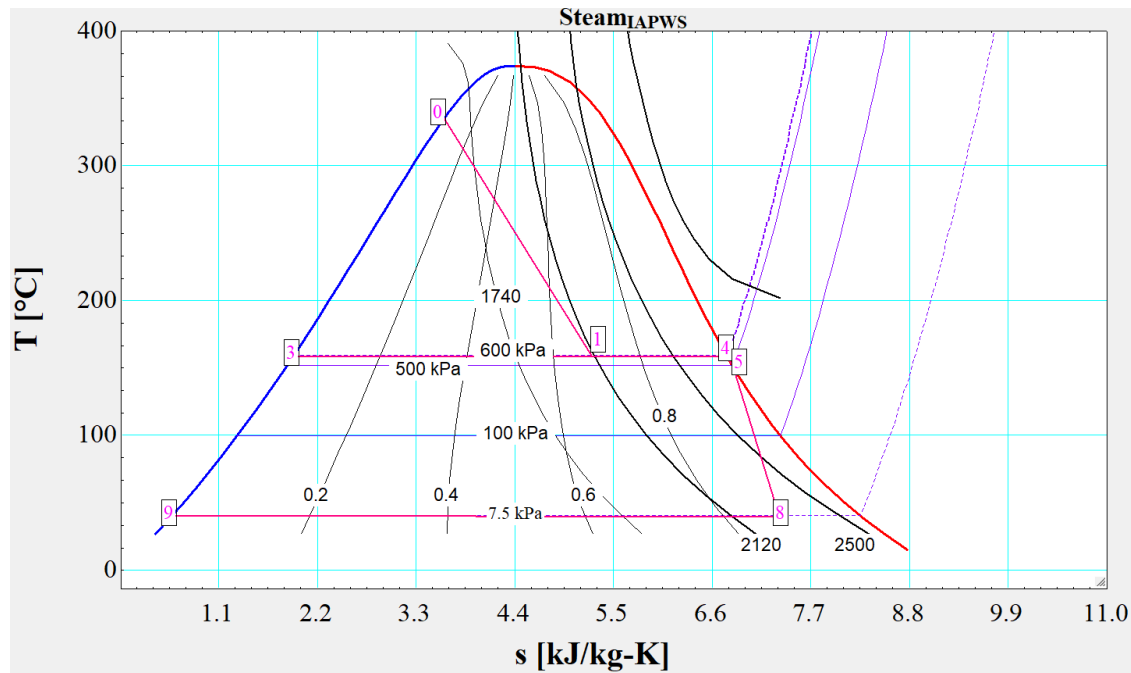
Figure 4.3: T-s diagram of the Olkaria IV power plant, numbers 0-9 correspond to the states in Figure 4.2.

The property/T-s diagram of the steam utilised for power generation in the geothermal power plants is presented in Figure 4.3. The T-s diagram shows the temperature and specific entropy changes of water in the thermodynamic process. Representation of energy transfer system by T-s diagram help to understand and visualise the work done by or on the system, and heat added or rejected from the cycle. Figure 4.3. shows the Ts diagram of the Olkaria IV power plant from the reservoir state to the cooling tower. States 4 and 5 show high-quality steam considered for a topping backpressure turbine with a pressure drop from 640 to 500 kPa. At 500 kPa in state five, maximum efficiencies are attained, as shown in Figure 4.4. Optimal utilisation of geothermal decision parameters should be exergy or second utilisation efficiencies, as shown in Figure 4.4. Thermal and second utilisation efficiencies are calculated using equations (4.5) and (4.16), respectively. Thermal/energy efficiency is 18%, whereas utilisation/second efficiency is 70%.

Thermodynamic and economic parameters are simulated using the EES code. Based on thermal analysis, work generated, efficiencies and total exergy destruction are tabulated in Table 4.5 and the economic parameters. With a topping unit of backpressure, the net power generated increased by 29,294 kW, increasing efficiencies by 3% and 14% for energy and exergy

efficiencies, respectively. Adding a topping unit at Olkaria IV improves the power plant performance, decreasing total exergy destruction by 4,056 kW. Topping unit turbine pressure varied between Olkaria IV turbine pressure of 500 kPa and wellhead pressure, 1,100 kPa shows optimum values at 630-640 kPa for work generated in Figure 4.5. The cost of products shows a sharp decline from 500 kPa to 550 kpa and increases gradually as pressures increases because the net work decreases with pressure increment. An increase in the turbine inlet pressure causes a decrease in the steam flow, thus shooting up the product cost. The turbine pressure increase also raises the specific enthalpy of the saturated vapour. The steam forms more liquid at higher inlet turbine pressures, and steam forms more gas at the lower exit pressures [188].
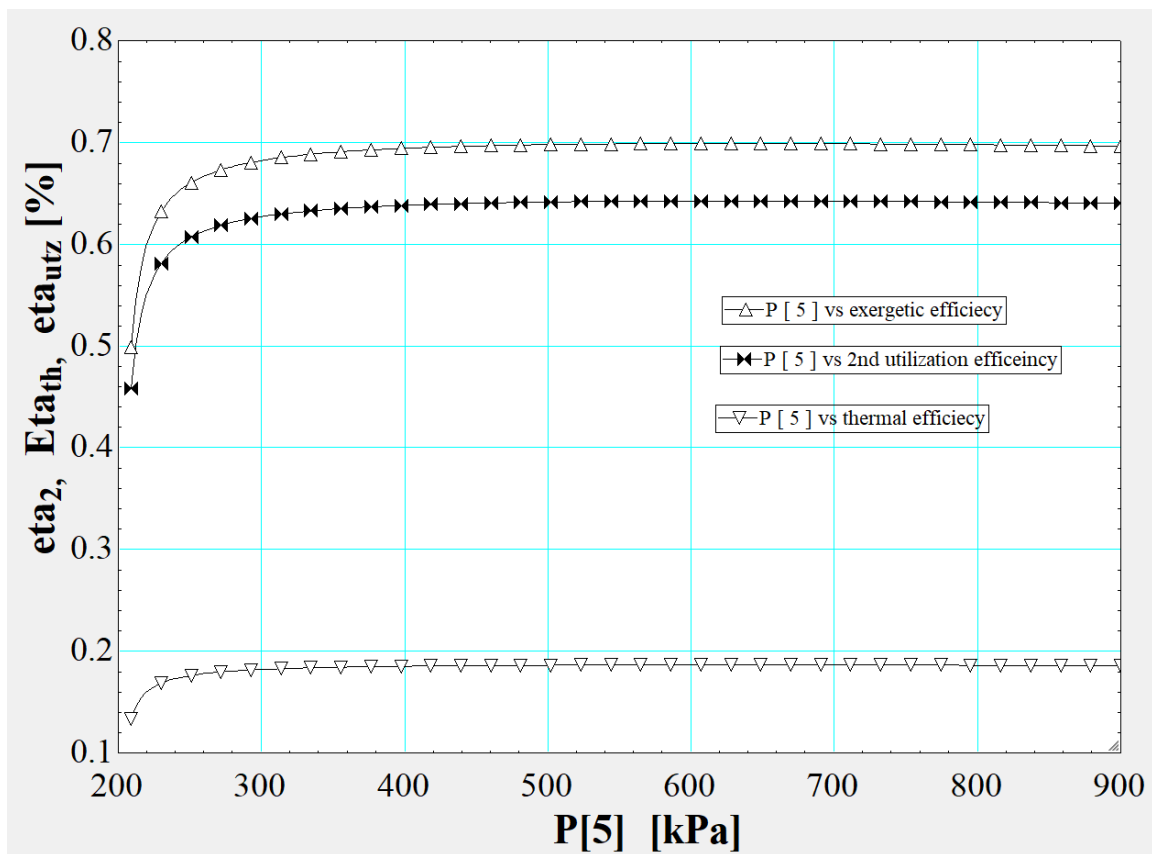
Figure 4.4: Effect of optimising the turbine inlet pressure on the three primary thermodynamic efficiencies.
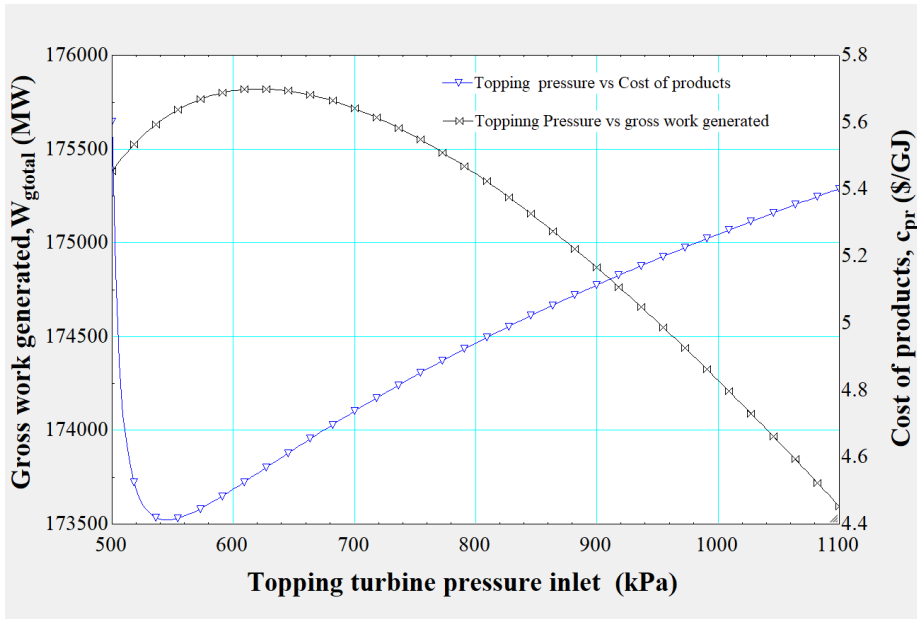
Figure 4.5: Effect of optimising the topping turbine inlet pressure and the cost of products from the modified power plant.
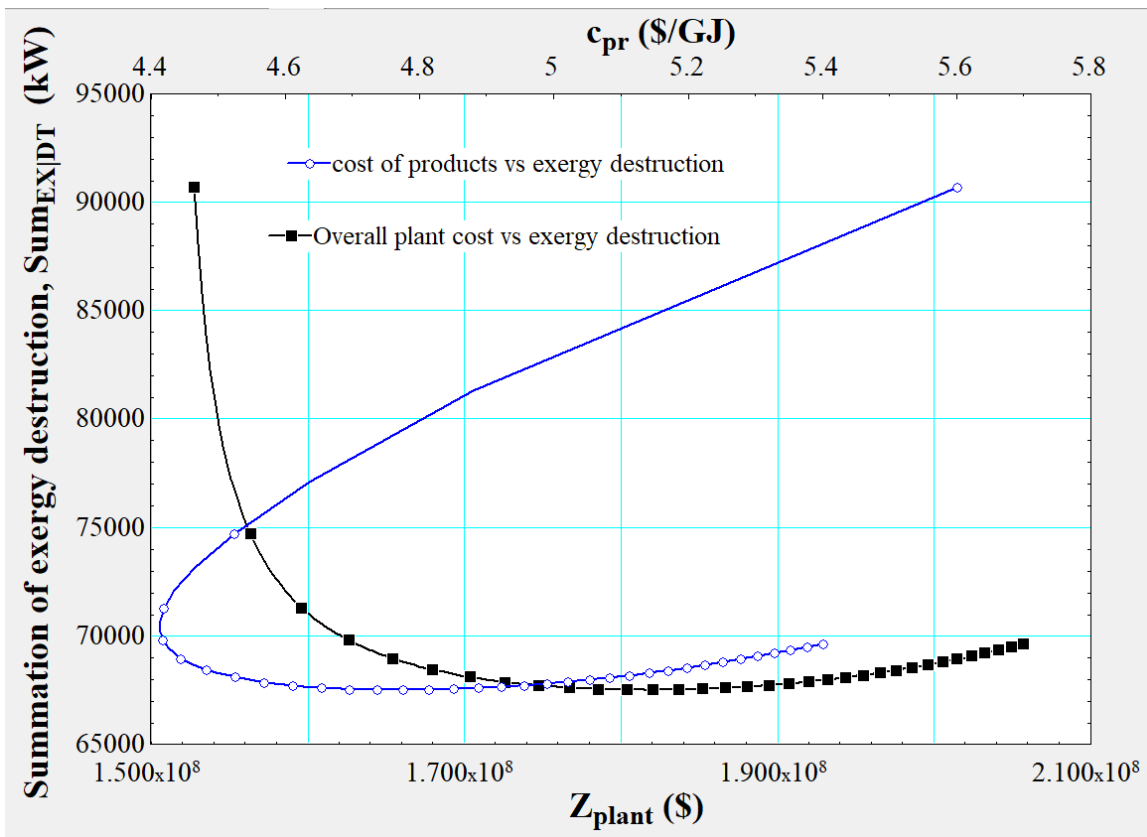
Figure 4.6: The relation of exergy destruction and the overall cost of the power plant.

With the addition of power generation, the overall cost of products is reduced from 5.947 to 5.679 $/GJ. With exergy efficiency improvement, the cost of exergy destruction reduces 323 to 304 $/hr, as presented in Table 4.5.

90

Table 4.5: Exergy and exergoeconomic calculated parameters at Olkaria IV power plant.

Parameter	Olkaria IV	Modified with top
Net power generated (kW)	136,150	165,444
Energy efficiency (%)	15.17	18.43
Exergy efficiency (%)	56.87	70.81
Sum exergy destruction (kW)	69,141	65,085
Cost of products ($/hr)	5.949	5.679
$\dot{Z}_k$ ($/hr)	2,500	,2971
$\dot{C}_{K,total}$ ($/hr)	2,915	3,400
Z_{plant} ($)	1.850E8	2.199E8

Figure 4.6 shows how the power plant investment cost varies with the total exergy destroyed. More capital is required for the plant to have better exergy performance, as shown in the capital vs exergy destruction curve, Figure 4.6. With higher exergy destruction, the cost of products increases. The figure shows that the more exergy destruction in the system, the higher the plant's costs. From the cost of products point of view, it is advisable to optimise power plant by exergy concept. If the exergy destruction is minimised, the plant will operate with an expectation of a reasonable investment return.

4.7 Exergoeconomic analysis of bottoming binary units in Olkaria IV, I and II power plants

For optimum utilisation of the available exergy supplied to Olkaria field (Olkaria I, Olkaria II and Olkaria IV power plants), three binary configurations (Figure 4.7 and Figure 4.25) are proposed, and exergoeconomically optimised. The brine was reinjected after the separator at State 3 in Figure 4.2. The proposed models are basic binary power plants with evaporator and pre-heater, and a regenerative cycle with an evaporator (Figure 4.7) [1,50] and air-cooled cooling systems as shown in Figure 4.25 [7]. For the three types of binary plants, the working fluids selected for investigation, their thermodynamic properties were from the EES code. The geothermal brine heat energy is transferred to a secondary working fluid in a binary power plant unit, usually organic fluid types with lower boiling points. The brine with lower temperature is then transferred to reinjection pads or direct use depending on the field characterisation. One of the main advantages of this type of power plant is the reduced atmospheric emissions because of the closed-loop of organic fluid. The plume is not noticed in water-cooled towers, but it can be eliminated using an air-cooled condenser. Another merit of

the binary is that the aggressive geothermal brine does not contact most power plant units like turbines and cooling towers.

4.7.1 Binary power plants system description

Upon flashing the brine from the steam field, the brine destined for reinjection is utilised for the proposed basic binary using different working fluids. For the simple ORC, Figure 4.7 (a), the brine (State A) from the separator enters the ORC evaporator at (156°C for the case of Olkaria I and Olkaria II, and 187°C for the case of Olkaria IV) [63], [69], [71], [189]. Working fluid enters the pre-heater and evaporator at States 4 and 5, respectively, and is changed to saturated or super-heated vapour (State 1). For an optimisation pressure, P_1, the vapour expands isentropically in the turbine coupled to a generator. The condenser temperature, T_2, is set at 46.5^{o}C [78]. At State 3, the sub-cooled fluid is pumped to the pre-heater and evaporator to complete the closed ORC. The turbines and pumps isentropic efficiencies are 85% and 75%, respectively. In the other unit of Figure 4.7 (b), the geothermal brine passes only through the evaporator (States A and B). The working fluid entered the evaporator at State 6 and vaporised at State 1. The main difference in the system's configurations is the regenerator in States 2-3 and 5-6 replacing the pre-heater as in the simple ORC case. After the condenser, the working fluid is pumped at State 4, passes through the regenerator, and completes the cycle in the evaporator at State 6.

Cooling water circulates in a closed loop in the condenser and cooling tower for wet-cooling, whereas in dry-cooling, air passes through the radiators to take away heat from the working fluids. In the cooling tower, the hot water loses heat to ambient air between Sates 10-11, and the process involves heat and mass exchange between water and air [7].
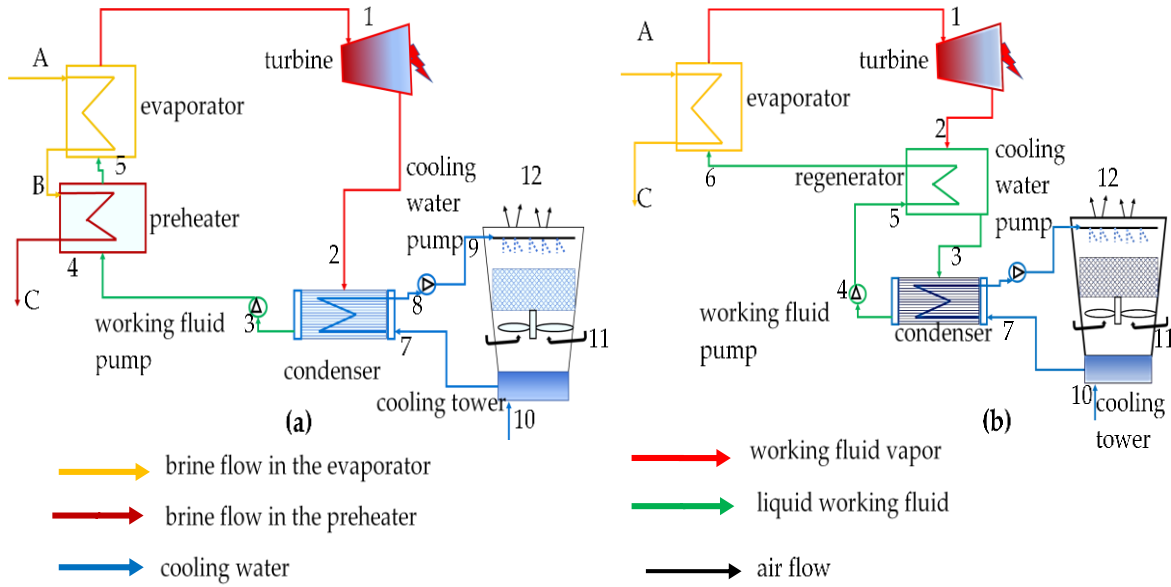
Figure 4.7: Schematic diagrams for the proposed water-cooled plant basic binary units designed and analysed using EES code, (a) simple ORC cycle; (b) regenerative ORC cycle without pre-heater.

Shell and plate heat exchanger types have a high heat transfer coefficient with a compact and robust size, maximising the available space. Pinch point temperature difference (PPTD) affects heat exchangers' thermodynamic and economic performance [81], [190]. The assumption is that heat exchangers are well insulated to transfer most heat between the brine and working fluid. Figure 4.8 shows the thermodynamic (temperature - heat transfer or T-Q) diagram examined in designs of heat exchangers.

Using equations (4.34) and (4.35) and pinch points, pre-heater exit temperature/reinjection, Tc, is calculated in EES code [7].

$$\dot{m}_{brine} c_{brine} (T_A - T_B) = \dot{m}_{wf} \left(h_1 - h_{\frac{6}{5}} \right) \tag{4.34}$$

$$\frac{T_a - T_c}{T_a - T_b} = \frac{h_1 - h_4}{h_1 - h_5} \tag{4.35}$$
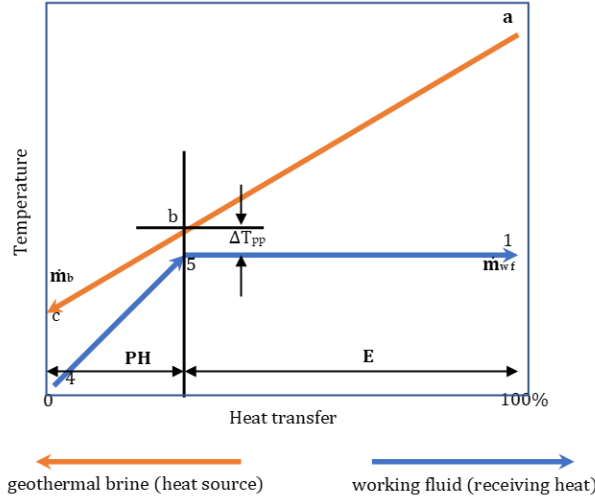
Figure 4.8. Temperature-heat transfer diagram for pre-heater and evaporator; geothermal brine enters evaporator at a and exits at b entering pre-heater and leaves at c to reinjection, the working fluid enters the pre-heater at 4 and exits as a saturated liquid at 5, enters the evaporator and exits to the turbine at 1 [1].

The heat exchanger(s) heat transfer area is calculated using equation (4.36):

$$\dot{Q}_{\substack{EV \\ \overline{PH}}} = \overline{U} \, A \, \Delta TLMTD \tag{4.36}$$

$$\Delta TLMTD_{EV} = \frac{(T_a - T_1) - (T_b - T_5)}{\ln\left(\frac{T_a - T_1}{T_b - T_5}\right)} \tag{4.37}$$

$$\Delta TLMTD_{PH} = \frac{(T_b - T_5) - (T_c - T_4)}{\ln\left(\frac{T_b - T_5}{T_c - T_4}\right)} \tag{4.38}$$

where A is the heat exchanger surface area, $\dot{Q}_{\substack{EV \\ \overline{PH}}}$ is the heat transfer rate in the heat exchanger (evaporator/pre-heater), ΔTLMTD given by equations (4.37) and (4.38) for evaporator and pre-heater, respectively, as in Figure 4.8; and $\overline{U}$ is the overall heat transfer (W/m^2.K).

Table 4.6: Constraints for optimisation parameters for ORC power plants.

Variable	Upper bound	Lower bound
Turbine pressure (kPa)	Less than P_{cr}	1,000
Condenser pressure (kPa)	451	700
f(obj) (W_{net}/Area$_{Total}$) *(kW/m^2)*	Optimisation	Optimisation
Reinjection temperature (^{o}C)	70	100

The objective functions are maximising net work, SI, and f(obj) while minimising total heat exchangers area, total cost, and summation of total exergy destroyed. The decision variables

are the turbine and condenser pressures and reinjection temperature. The equation defines the optimisation methods as (maximising the objective function, and the constrained terms are turbine inlet, P_1, out pressures, P_2, and reinjection temperatures, T_C). Table 4.6 shows the upper and lower limits.

Max f(obj) (P_1, P_2 and T_C).

Table 4.6 shows the parameters varied to find the optimal values of f(obj). Turbine inlet pressure and exit pressures vary from 1,000 kPa to a value less than critical pressure, P_{cr} and between 451-700 kPa, respectively. The reinjection temperature was between 70 to 100°C to avoid silica scaling problems. The three parameters are as per ORCs analysis based on energy, exergy, and exergoeconomics [80], [191]. SI is a function of exergy and, f(obj) is a function of the heat exchangers' net work and total area. Minimising the total area lowers parasitic loads in the cooling tower and condenser. The smaller the condenser size, the lower the power for operating fans and the lower the heat load in the cooling tower. To achieve optimal values, the *f (obj)* is optimised. The variable metric method (Davidon-Fletcher-Powell (DFP) Quasi-Newton Method) adjusts the hessian matrix to ensure the negative or positive definiteness [192], [193]. Exergoeconomic is a commodity of value in a system. It assigns costs to exergy variables and determines the appropriate allocation of economic resources to optimise the power plants' design and operation. The economic feasibility of any system is predicted by obtaining the actual costs of products [194]. The cost rate assigned to SI and cooling tower exergoeconomic equation are proposed in this research.

Different working fluids were selected for the modelled units, and the system optimised. The following assumptions were applied [109]:

    i.   The systems operate under steady conditions.

    ii.   Heat exchangers are counter-flow and well-insulated except for the cooling tower.

    iii.   Geothermal brine is considered to have thermophysical properties of IAPWS [107], [195].

    iv.   The turbine and all pumps are adiabatic with constant isentropic efficiencies.

    v.   Working fluid exits the evaporator as saturated vapor and saturated liquid in the condenser.

The research investigates the entire power plant from the wellhead to the cooling tower exergoeconomically for combined wet and dry cooling binary power units. Cooling systems are either dry or wet. Cooling tower designed to accommodate the heat load from the condenser.

The wet cooling tower is an induced draught and discharges heat to the surrounding air. This type of cooling is compact with an assured air supply [196]. Cooling tower performance mainly depends on the ambient temperature. The wet cooling tower analysis determines heat load based on heat lost by cooling fluid in the condenser. The water to air ratio (L/G) was calculated at a wet-bulb temperature. In this complete study, the design characteristics of the cooling tower are based on the power plant requirements but not on assumptions of L/G.

4.7.2 Working fluid selection

Working fluid selection is an essential matter in binary power plant design. Working fluids, in most cases, are organic compounds or mixtures; this affects the performances of binary plants [7]. The choice of working fluid is constrained by; thermodynamic properties, critical temperature, T_{cr}, and critical pressure, P_{cr}, health, safety, and environmental impacts [197]. The temperature of the brine/heat source is also a factor considered in fluid selection. Figure 4.9 shows classifications of the working fluids as dry, isentropic or wet type [198]. Better working fluid should have a positive slope in the temperature-entropy diagram (dT/ds) [107], [199].
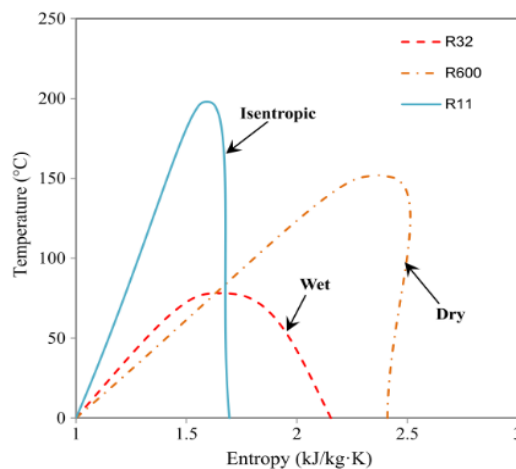
Figure 4.9: Types of working fluids [198].

Chlorofluorocarbons (CFCs) have good thermal properties but release chlorine which catalyses the destruction of the ozone layer [200]. The suitable alternatives for CFCs are hydrofluorocarbons (HFC's) handled with proper precautions to avoid environmental and human health impacts [201]. The different working fluids investigated agreed/are constrained with the energy and mass balance equations [7], [202]. Most of the world's installed ORC cycles operate as sub-critical cycles [203] using hydrocarbons (Figure 4.10). The application of hydrocarbons has an installed capacity of about 83%, while the least is chloro-fluoro carbons at just 1% [197]. Suitable working fluids should have stable thermodynamic and chemical

properties like low ODP and low GWP [204]. Chloro-fluoro carbons are among the most atmospheric devastating pollutants if released into the environment. Chloro-fluoro carbons are hazardous to respiratory and cardiac functions [205]. There is a need to curb the CFCs working fluids on environmental and health concerns. The working fluid identified as the most suitable characteristic is the hydrocarbons. Among them is R-600, which has been investigated as one of the most suitable working fluids [188]. The butane group of hydrocarbons has been identified for most applications and is dry-type [206], [207]. Table 4.7 shows some of the working fluid properties considered during fluid selection [7]. Working fluid selection according to temperature should be well informed since fluids become chemically unstable at temperatures above 327°C [208]. Suitable working fluids should have stable thermodynamic and chemical properties, low ODP, and low GWP [204].

A generalized figure of merit, ξ, is directly proportional to turbine size was developed by Milora and Tester [17]. The ξ in Table 4.7 is expressed as:

$$\xi \propto T.E.A = \frac{\sqrt{m}\left(v_g^{sat}\right)_r}{P_{cr}\left(h_{fg}\right)_r} T_{CD} \left(\frac{g}{gmole}\right)^{\frac{1}{2}} bar^{-1} \tag{4.39}$$

where m is the fluid's molecular weight, P_{cr} is the critical pressure, h_{fg} is reduced latent heat and v_g^{sat} is the reduced gas specific volume evaluated at condensing temperature, T_{CD} and T.E.A is turbine exhaust area [17]. From equation (4.39), it is correlated that the lower the condenser temperature, the smaller the turbine translating to lower plant cost. Working fluid se

Table 4.7. Properties of some candidate working fluids for binary [105], [209].

Fluid	Formula	T_{cr}	P_{cr}	Relative T.E.A	ODP	GWP	Flammability	Toxicity
Ammonia	NH_3	133.7	11.7	1.0	0	0	Lower	Toxic
Propane	C_3H_8	97	4.2	2.3	0	3	Very high	Low
i-Butane	i- C_4H_{10}	136.0	3.7	4.1	0	3	Very high	Low
n-Butane	C_4H_{10}	150.8	3.7	5.5	0	3	Very high	Low
i-Pentane	i-C_5H_{12}	187.8	3.4	12.2	0	3	Very high	Low
Carbon dioxide	CO_2	-	-	-	0	1020	Non	Non
R-134a	$C_2H_2F_4$	-	-		0	1300	Non	Very low
R-12	CCl_2F_2	112	4.1	-	1.0	4500	Non	Non
Water	H_2O	374.1	22.1	-	0	-	Non	Non

	Hydro-carbons	Unknown working fluids	Fluoro-carbons	Ammonia water-mixture	Chloro-fluoro carbons
■ Installed Capacity (MW)	1282.05	122.733	102.63	29.6	14.35
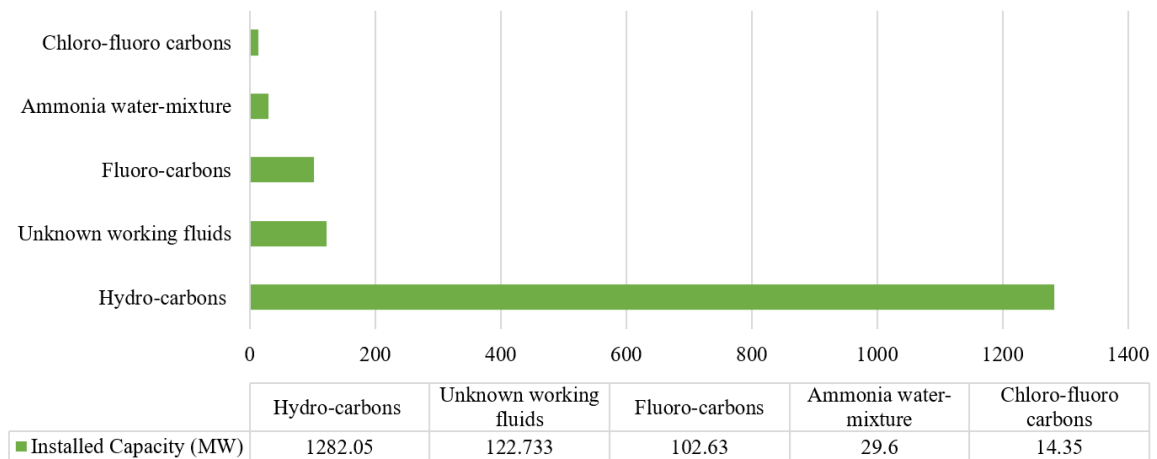
Figure 4.10. Installed capacity of binary plants and their working fluids. Most plants are utilising hydrocarbons because of the low levels of global warming potential, low toxicity, and no effect on the ozone layer.

4.8   Proposed Olkaria IV binary power plant

The two working fluids investigated for optimisation of Olkaria IV available exergy are isopentane and trans-2-butene. The steam gathering system in Olkaria domes geothermal field is shown in the Appendix. For the two types of binary plants, two working fluids (isopentane and trans-2-butene) are optimised for the reinjected brine at 187ºC. EES code used to analyse the performance of Olkaria IV power plant is in the Appendix section.

4.8.1   Results and discussion

The proposed Olkaria IV bottoming binary power plant was optimised using EES code. The power plant objective function was maximum power generated. Turbine inlet pressure was varied to find the optimum point for maximum net work generated and minimum heat exchangers area. The presented tables and figures show the constraints' relationship and the objective functions. Figure 4.11 shows the effect of turbine inlet pressure on the work net generated and the total exergy destruction for trans-2-butene. Optimum turbine inlet pressure is noted to be between 2,000 and 3,500 kPa.
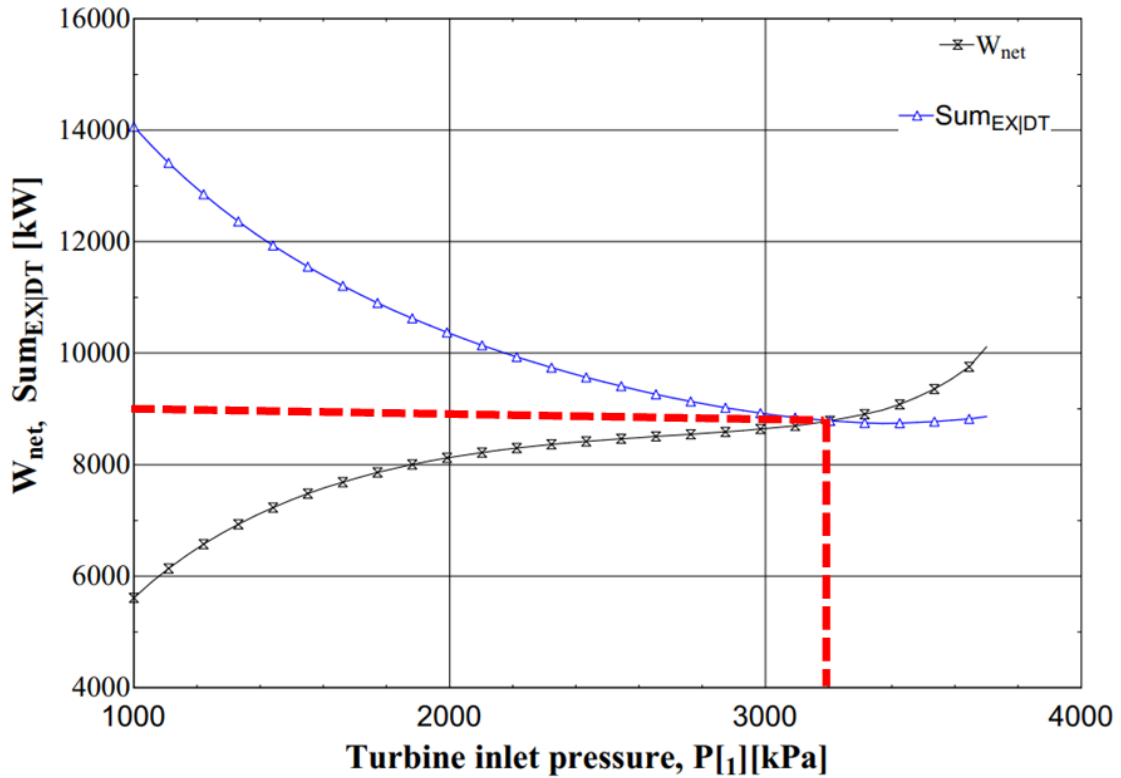
Figure 4.11: Effect of turbine inlet pressure on the net work generated and the summation of exergy destruction for trans-2-butene.

Exergy destruction decreases with an increase in turbine pressure. Exergy is an entropy function, and in the turbine exit pressure, isentropic expansion is assumed. The increase in pressure decreases the exergy destruction. The apex pressure for trans-2-butene is 3,100 kPa, shown in Figure 4.11, where the exergy destruction and net work generated are the same, 9,000 kWe.
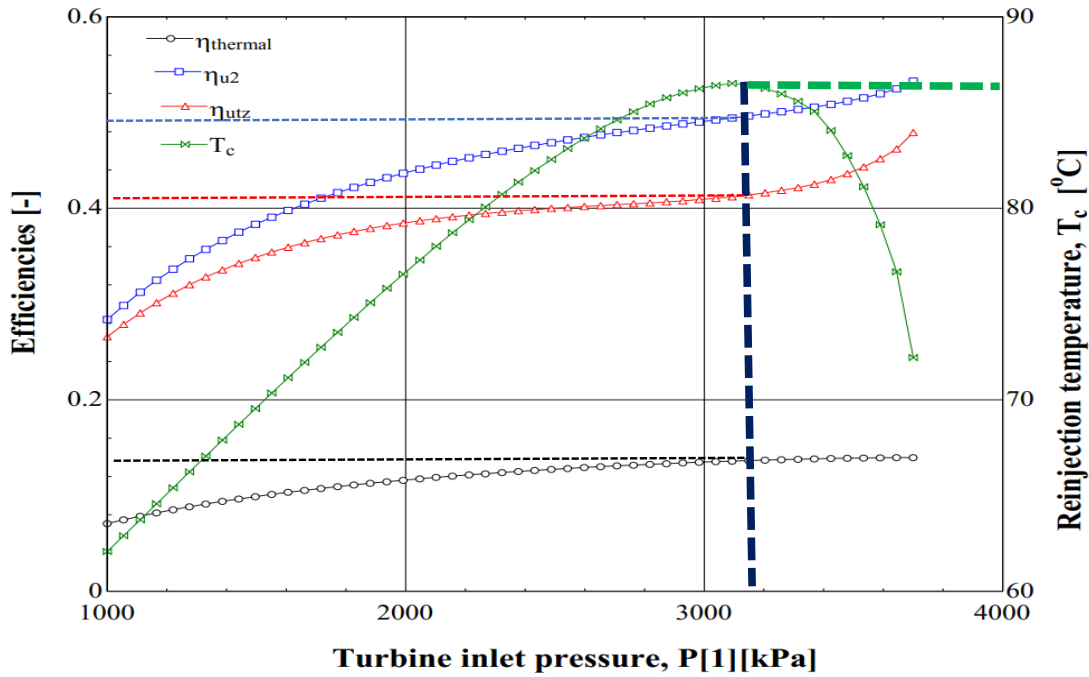
Figure 4.12: Effect of turbine pressure on efficiencies and the reinjection temperature of brine for trans-2-butene working fluid.

Figure 4.12 shows the optimisation of Olkaria IV brine by efficiencies and reinjection temperature using trans-2-butene. The maximum reinjection temperature is above 85°C at optimum turbine pressure of 3,204 kPa, as in the exergy destruction "apex" point. At the optimum turbine inlet pressure, the thermal and second utilisation efficiencies are 13.7% and 49.86%, respectively.

Figure 4.13 shows the effect of turbine inlet pressure on total heat exchangers area and user-defined objective function, f(obj). The optimum value of the objective function for trans-2-butene is *1.73 kWkm^{-2}* at a turbine inlet pressure of 2,800 kPa. From Figure 4.13 the total area is 5,258 m^2. The orange triangle in Figure 4.13 shows the optimum region for designing a proposed water-cooled ORC using trans-2-butene working fluid for Olkaria IV power plant.
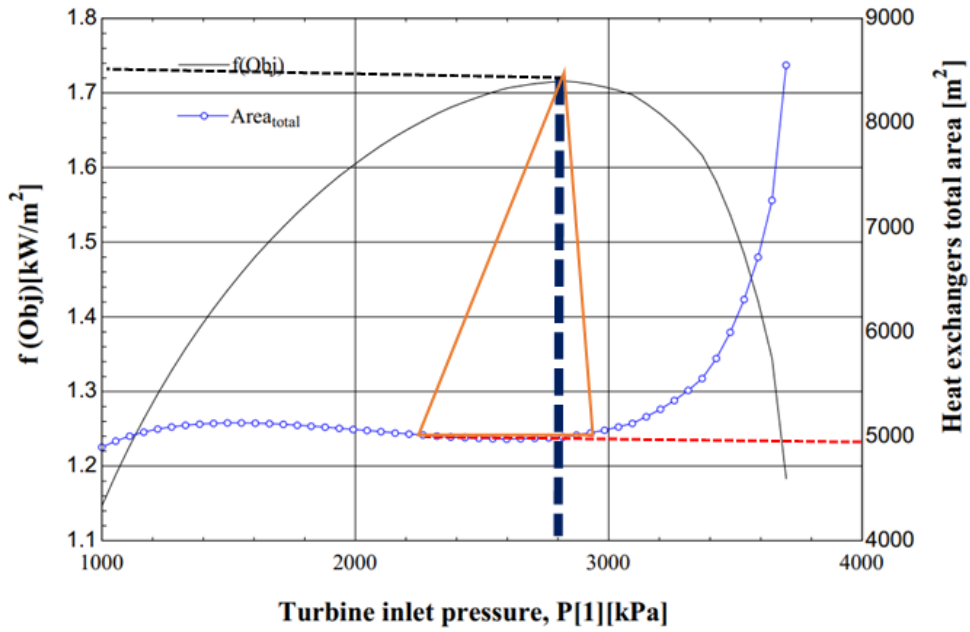
Figure 4.13: Effect of optimisation of the turbine inlet pressure on an objective function defined and the total area of the heat exchangers for trans-2-butene working fluid.

Isopentane working fluid has a higher critical temperature compared to trans-2-butene.
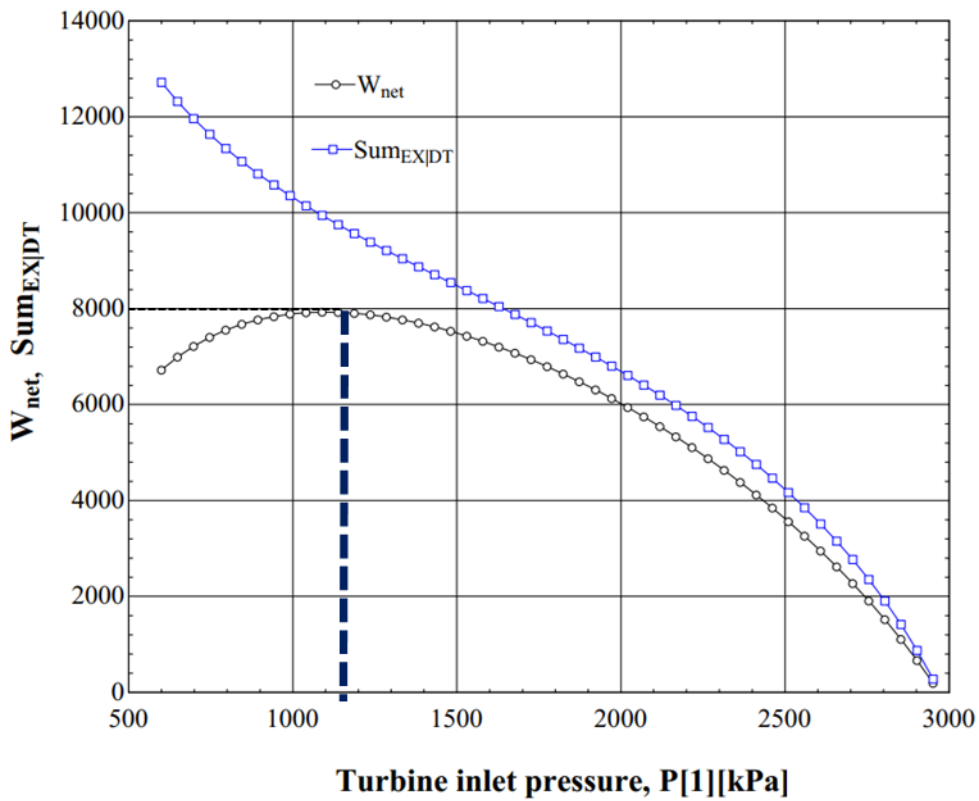
Figure 4.14: Relationship of turbine inlet pressure on the net work generated and the summation of exergy destruction for isopentane working fluid.

Figure 4.14 shows the optimum turbine inlet pressure for isopentane working fluid and exergy destruction. At a turbine inlet pressure of 1,090 kPa, isopentane working fluid generates 7, 927 kWe net power. The convergence apex for isopentane does not coincide with the optimum pressure. Exergy destruction is above the energy generated from the ORC cycle using isopentane at 9,942 kW.
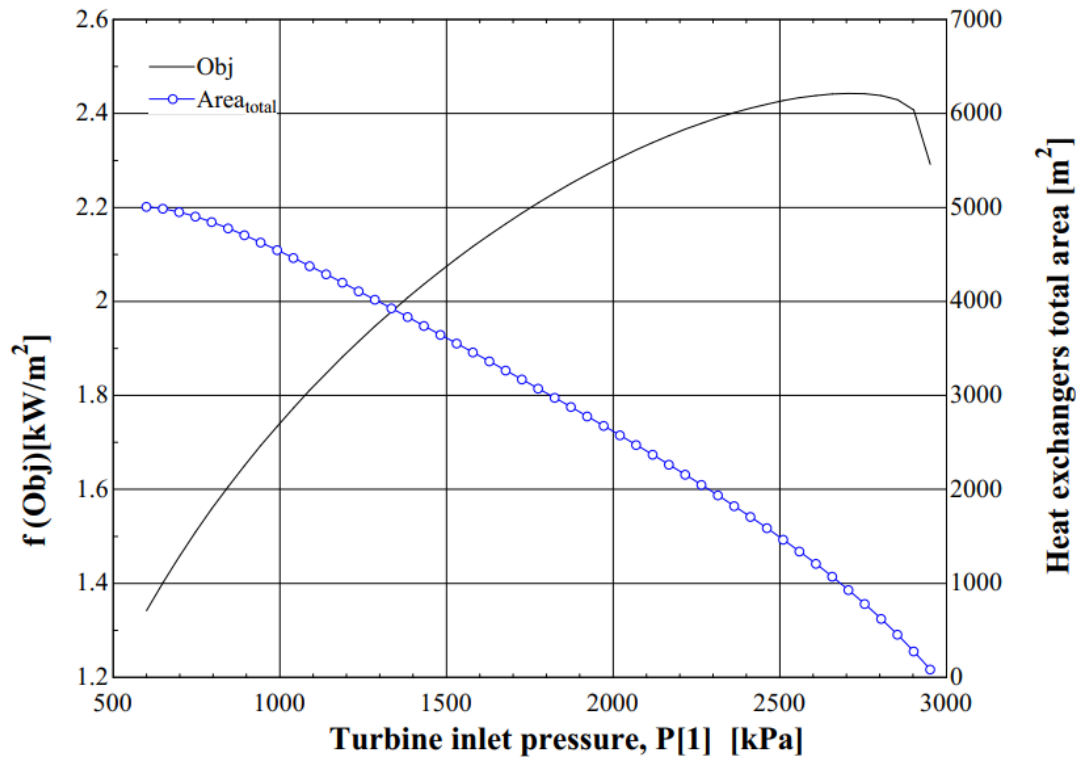
Figure 4.15: Effect of optimisation of the turbine inlet pressure on an objective function defined and the total area of the heat exchangers for isopentane working fluid.

Figure 4.15 shows the effect of turbine inlet pressure on the objective function and the area of heat exchangers. At the optimum pressure of 1,090 kPa, the total area of heat exchangers is 4,377 m^2. Second utilisation efficiency is 43.96%, while thermal is 12% at the optimum turbine inlet pressure.. Figure 4.16 presents the effect of turbine inlet pressure on the efficiencies and reinjection temperature for ORC using isopentane. The calculated reinjection temperature from the EES code was 82.37°C.
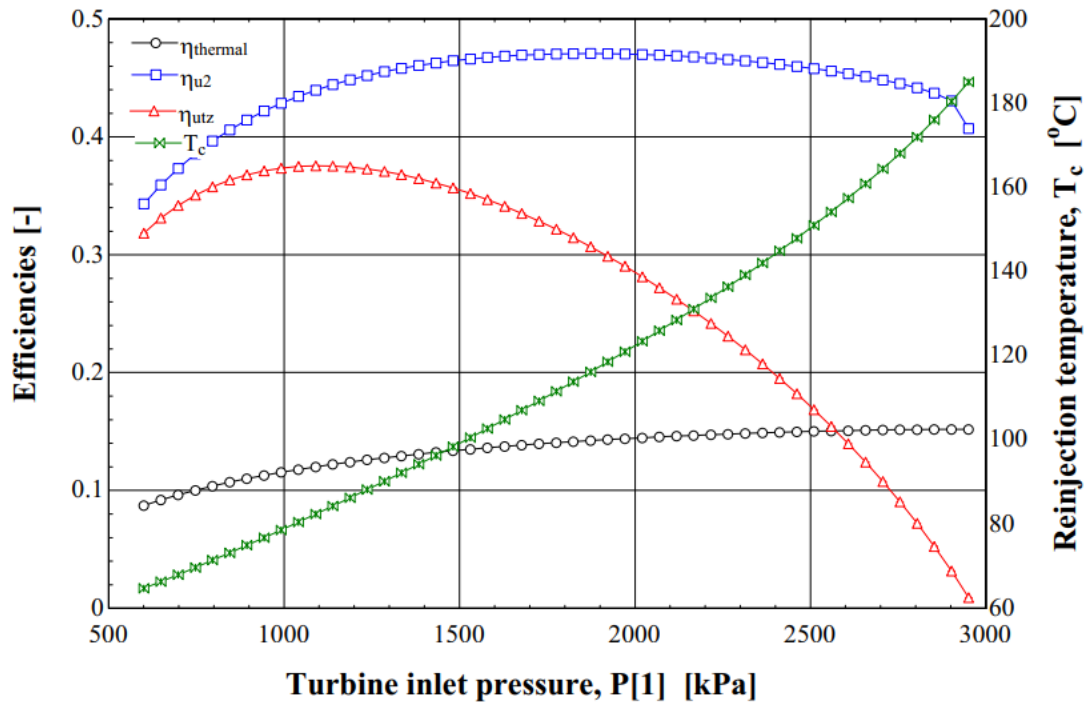
Figure 4.16: Effect of turbine pressure on efficiencies and the reinjection temperature of brine for isopentane working fluid.

4.9 Optimisation of a proposed Olkaria I binary with combined wet and dry cooling

Olkaria geothermal field has supported SF Olkaria I for more than 30 years. The brine reinjected has the exergy to add more power using a binary power plant. Two ORC unit configurations are studied to optimise the exergy wasted. In the cooling towers, the cooling could be wet or dry depending on the location and availability of water. Comparing the two systems is worth future investment in regions where geothermal resources are available, but water may be scarce.

A complete exergoeconomic comparison of wet and dry-cooled binary power plants was carried out. Simple organic Rankine cycles (ORC) for Olkaria geothermal field in Kenya using eight isobutane types of working fluids were proposed for analysis by the thermo-economic concept and sustainability index (SI). Net work generated per heat transfer surface area was the optimised objective function, f(obj). Variable metric optimisation method implemented in Engineers Equation Solver (EES) was applied to optimise plants. In the EES code, different optimisation methods are available. The methods include; Golden section search, quadratic approximations, conjugate directions method, variable metric method, Nelder-Mead Simplex method, Direct algorithm and Genetic method. From the figures on the effect of turbine inlet pressure on efficiencies or objective function, the method selected was the Variable Metric

optimisation method. The method solves nonlinearly constrained problems. The plots from varying turbine inlet pressure are nonlinear and show maxima and minima points. The variable metric method (Davidon-Fletcher-Powell (DFP) Quasi-Newton Method) adjusts the hessian matrix to ensure the negative or positive definiteness [192], [193].

4.9.1 System description

The proposed models are binary power plants with water and air-cooled cooling systems as in Figure 4.7 and Figure 4.25 [7]. Eight working fluids (butene, cis-2-butene, isobutane, nbutane, R600, R600a and trans-2-butene) were selected for investigation for the two types of binary plants whose thermodynamic properties were from the EES code. The main parameters known are brine flow rate ($\dot{m}$) and the brine temperature, T_a. After optimisation by the variable metric optimisation method, other thermodynamic properties and parameters are obtained from the EES code.

4.9.2 Results and discussion

Exergoeconomic analysis of two ORC units with different cooling configurations was conducted. EES code was used to model and optimise the proposed binary power plant for Olkaria. The ratio of the net work generated to the surface areas (objective function) of heat exchangers is optimised. The size of heat exchangers influences the cost in exergoeconomic analysis and the overall investment in plant operation and maintenance.

Mass, energy, and exergy balance equations were applied for steady-state conditions for the power plants. The exergy into the system calculated for the brine entering the evaporator and exergy from the systems is the summation of reinjected exergy after pre-heater and the net work generated. Exergoeconomic and thermal values calculated for each fluid at optimum operating turbine and condenser pressures and reinjection temperature calculated based on variable method metric by maximising the f(obj), objective function.

Some of the thermal and economic parameters in power plant designs include turbine inlet pressure, size of heat exchangers, efficiencies, and reinjection temperature, among other variables. For optimisation applied in this research, a ratio of net work generated to total areas of heat exchangers is identified as the objective function. Optimisation results of the ORC units for eight different working fluids were presented and discussed.

Figures 4.17 and 4.21 show the effect of turbine inlet pressure on the f (obj) and SI in power plant optimisation. The optimum values of f(obj) for most working fluids achieved at turbine inlet pressures are 2,000-3,000 kPa. Sustainability indices are at maximum values at 1,750 kPa.

The multi-criteria optimisation method can achieve the best performance in the turbine. Increasing the turbine inlet pressure push SI and objective function and, optimal operating pressures are between 2,000-3,000 kPa for most of the working fluids.

Figure 4.18 shows an increase in f(obj) with a decrease in the cost of products. At optimum f(obj), there is a relative reduction in the cost of products. As the objective function increases, the cost of products decreases, as shown in Figure 4.18. Effects of the net work on the cost of products translate to a reduction in exergy destruction. The price of products is high at lower values of the objective function, and the aim of improving binary plants is to reduce the exergy destruction and lower the cost of products.
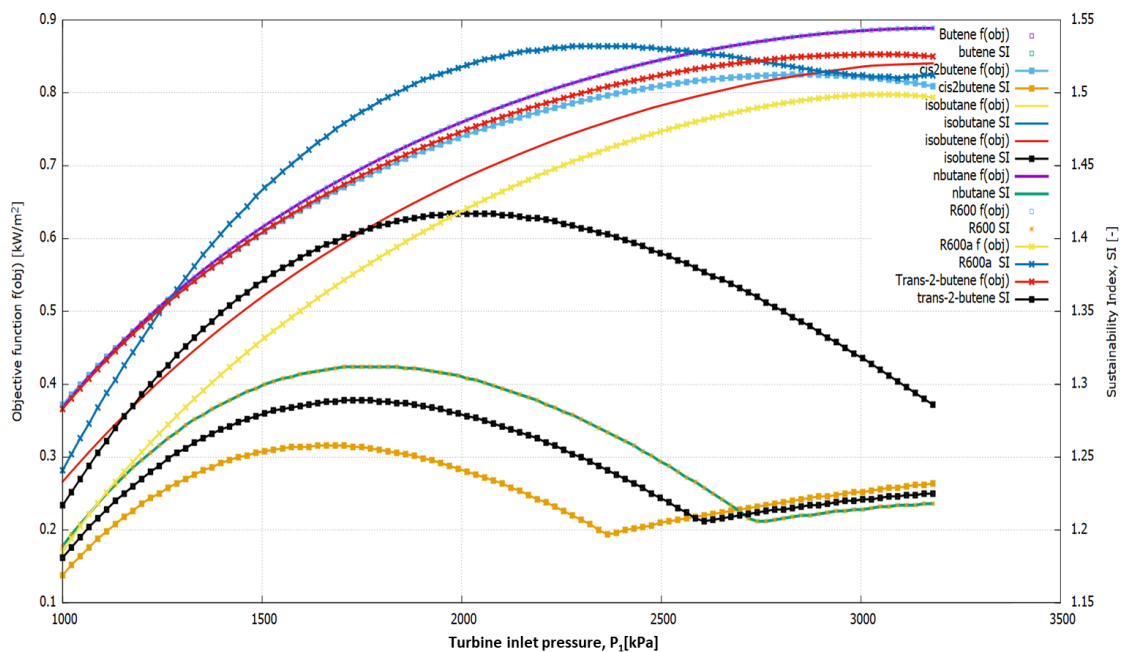
Figure 4.17: Plot of objective function f(obj) and sustainability Index vs turbine inlet pressure for the air-cooled binary plant.
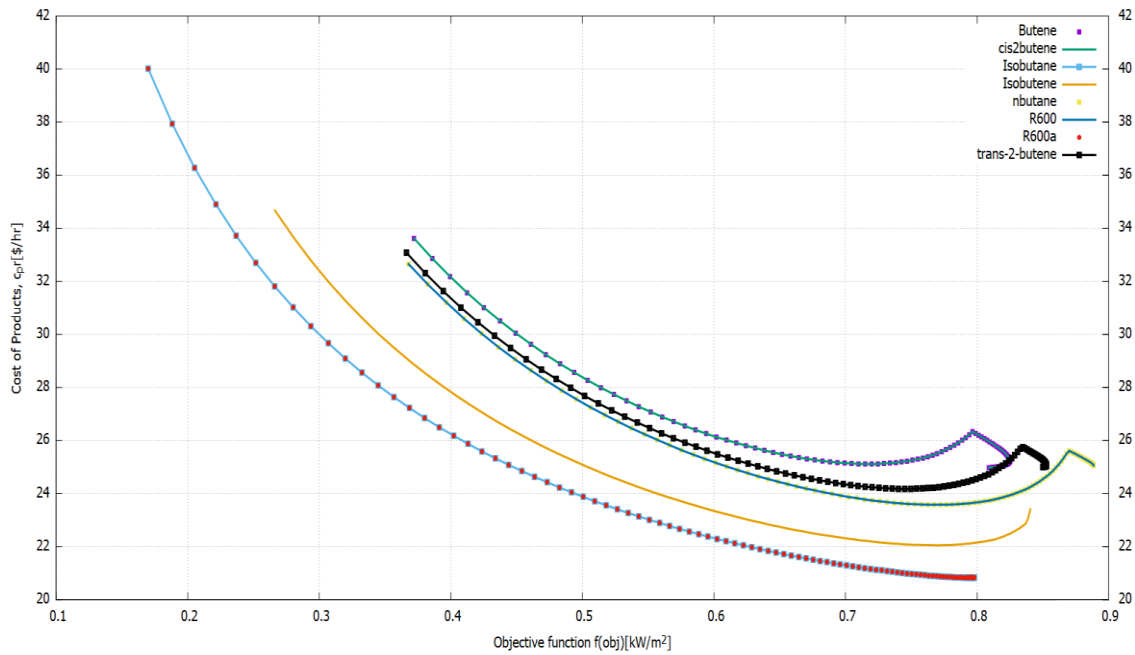
Figure 4.18: Cost of products vs. objective function for air cooled power plant.

The cost of products decreases as the objective function increases in all the investigated fluids, as shown in Figure 4.18. As the ratio of power generated to heat exchangers' area, the efficiency of the power plant improves and reduces exergy destruction.

Exergoeconomic concept in power plants is summarised mainly based on the cost of products ($\dot{C}_{K,total}$), power plant cost rate ($\dot{Z}_{K,plant}$), exergoeconomic factor, f, thermo-economic coefficient, $\dot{C}_D$ and the proposed sustainability index cost, SI_{cost}. Figure 4.19 and Figure 4.23 show exergy analysis of binary plants. The total exergy destruction decreases with increased turbine inlet pressure. Optimum operating pressures calculated in the EES code are in the range corresponding to the lower exergy destruction. Unaccounted exergy ($\dot{Ex}_{irr}$) accounts for the systems' irreversibility. Tables 4.8 and 4.9 show $\dot{Ex}_{irr}$ is higher for the dry cooling systems with values of between 66.65 kW for butene and 396.8 kW for cis-2-butene whereas, in wet cooling, the range is between 8.978 kW for n-butane and 20.84 kW cis-2-butane. In both plants, cis-2-butene has the highest entropy generated. The least entropy generated in wet-cooling is with n-butane and butene. Energy and exergy concepts show the net work generated is between 1,628 kWe and 2,594 kWe, with the utilisation efficiency between 39.53% - 62.97%. In a wet cooling system, the lowest SI is 1.654, and the highest is 2.701, while for the dry-cooling power plant, it is between 1.286 - 1.612. For both units, cis-2-butene working fluid has the lowest SI.

The plant net work generated in the air-cooled binary is between 1,446 kWe and 2,469 kWe, with utilisation efficiency between 34.77% and 59.37%.
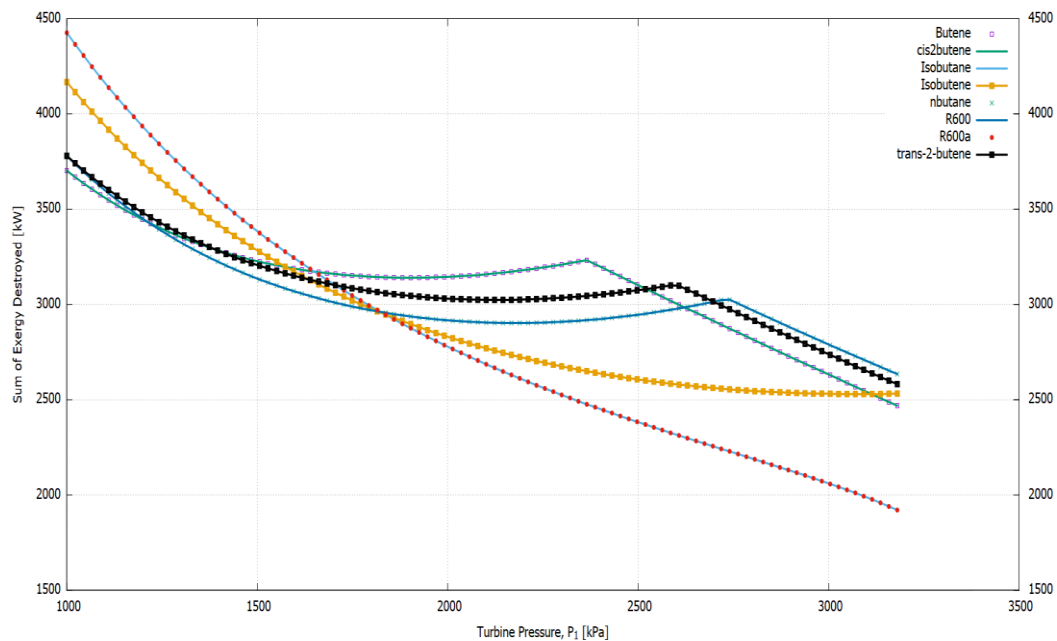
Figure 4.19: Effect of turbine inlet pressure on of total exergy destruction in water-cooled binary power plant.

Figure 4.20 and Table 4.11 show that the cost of products for the water-cooled system is lower than that of air-cooled plants. R600 and isobutane have the lowest cost of products at 18.3 $/GJ for wet-system and isobutane is the least for dry-cooling at 20.87 $/GJ. The plant cost rate of 140.9 $/hr for R600a is the highest value for the wet-cooled unit, and the estimated overall cost of the plant is 7.8 million $. Exergoeconomic factor *(f)* is lower for the wet systems varying between 39% and 47%, while in the dry condenser power plant, they are between 89% and 91%. The lower values of f in wet cooling are because of the higher overall plant cost rate. The proposed sustainability index cost rate is between 49.12 $/hr and 73.66 $/hr in the first model and ranges from 17.04 $/hr to 102.3 $/hr for an air-cooled power plant. Energy and exergy concepts show the suitable plant is the water-cooled unit for isobutane or R600a that can generate 2,590 kWe. The corresponding thermal and utilisation efficiencies are 16.01% and 62.97%, respectively. On the same technique, R600a is the most suitable fluid for air-cooled binary plants generating a 2,469 kWe net work with 14.07% thermal efficiency, 59.37 % utilisation efficiency, and 1.612 SI.
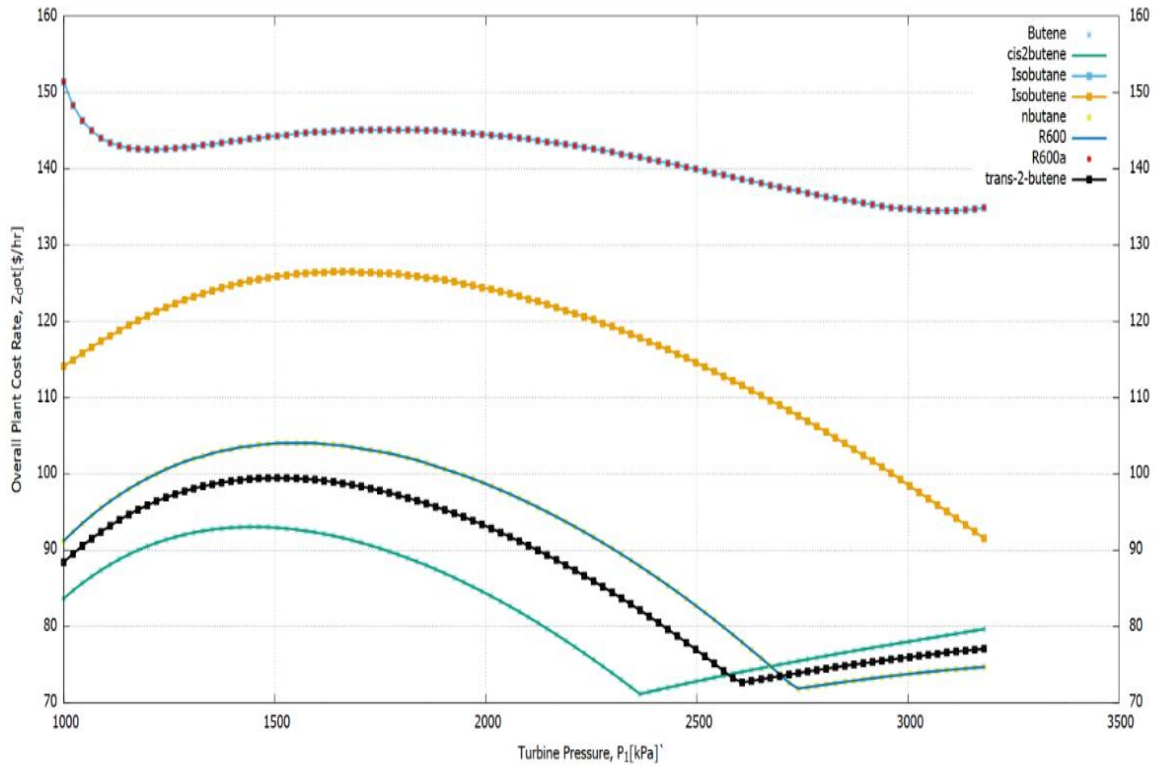
Figure 4.20: Effect of turbine inlet pressure on the overall plant cost rate for water-cooled plants.

Figure 4.21 shows the effect of turbine inlet pressure on objective function and SI. Isobutane has the highest SI and objective function, while trans-2-butene has the lowest. The curves show the optimum values of the objective function, and SI is at maxima. The variable metric optimisation method will locate optimal turbine inlet pressure for each working fluid. The cost rate directly relates to the turbine inlet pressure, as shown in Figure 4.21.
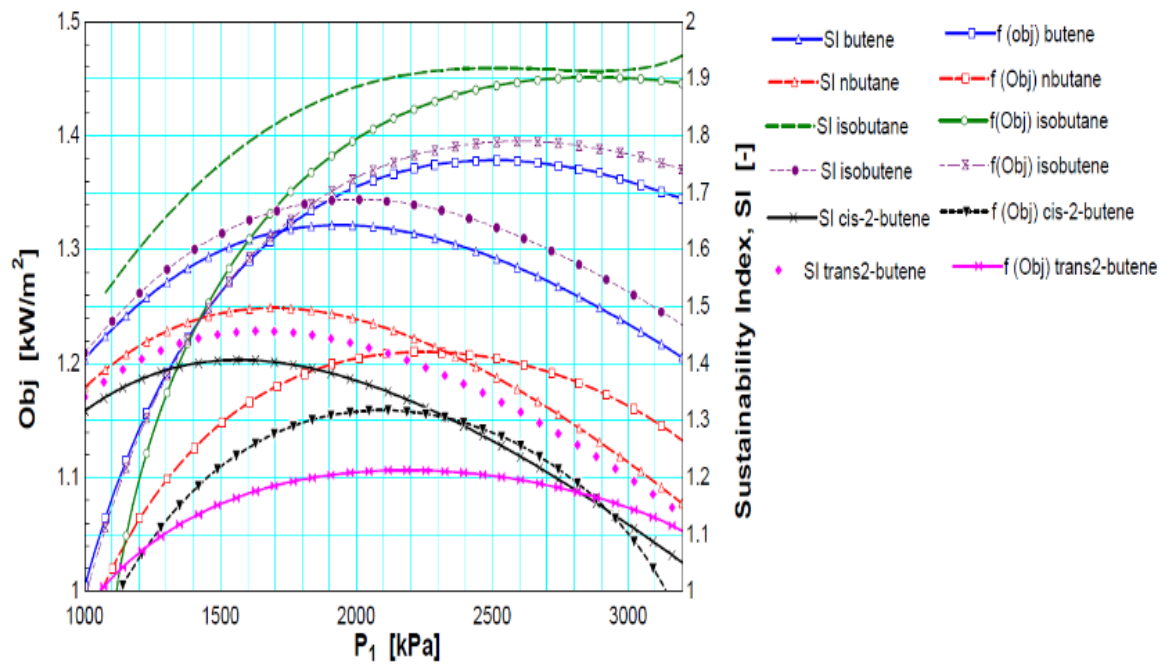
Figure 4.21: Plot of the objective function f(obj) and sustainability Index vs. turbine inlet pressure for the wet cooling unit.
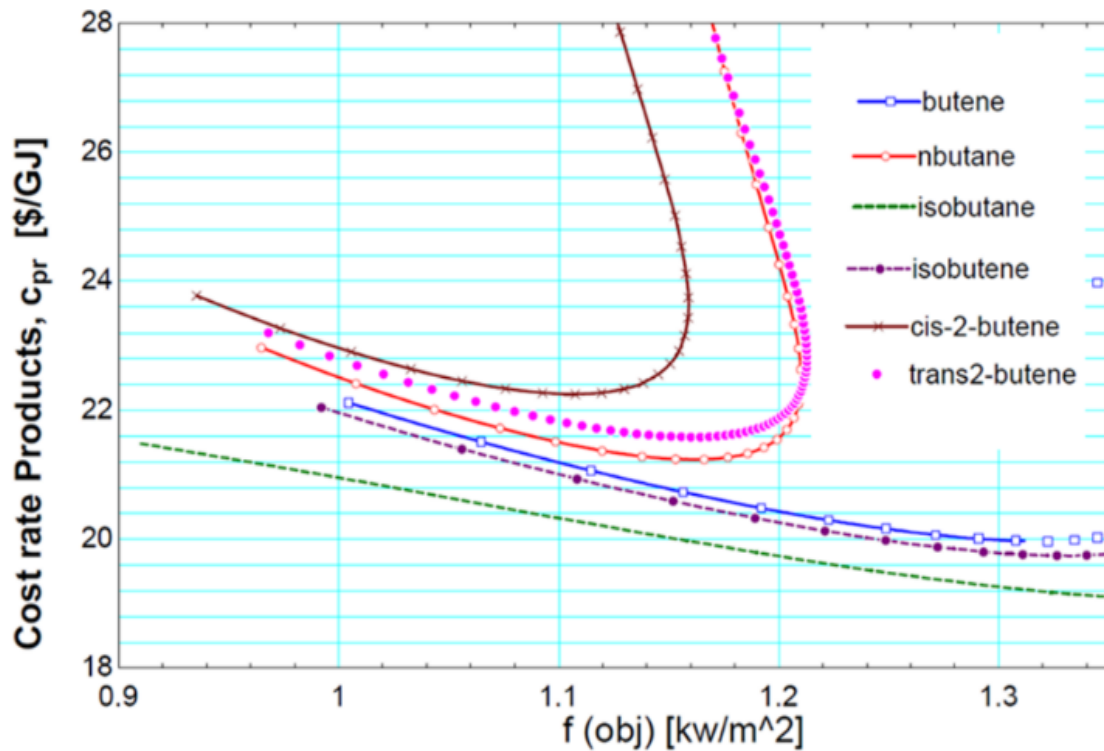
Figure 4.22: Cost of products vs. objective function for wet cooling.

Isobutane working fluid performs better for the wet cooling unit with higher SI and objective function values. It shows that the net work generated per area of heat exchangers is maximum.

Figure 4.22 shows how the cost of products changes with the objective function. Isobutane is better working fluid that could be selected from Figure 4.22 and Table 4.10, while cis-2-butene performed the least, with lower objective function and higher cost of products.
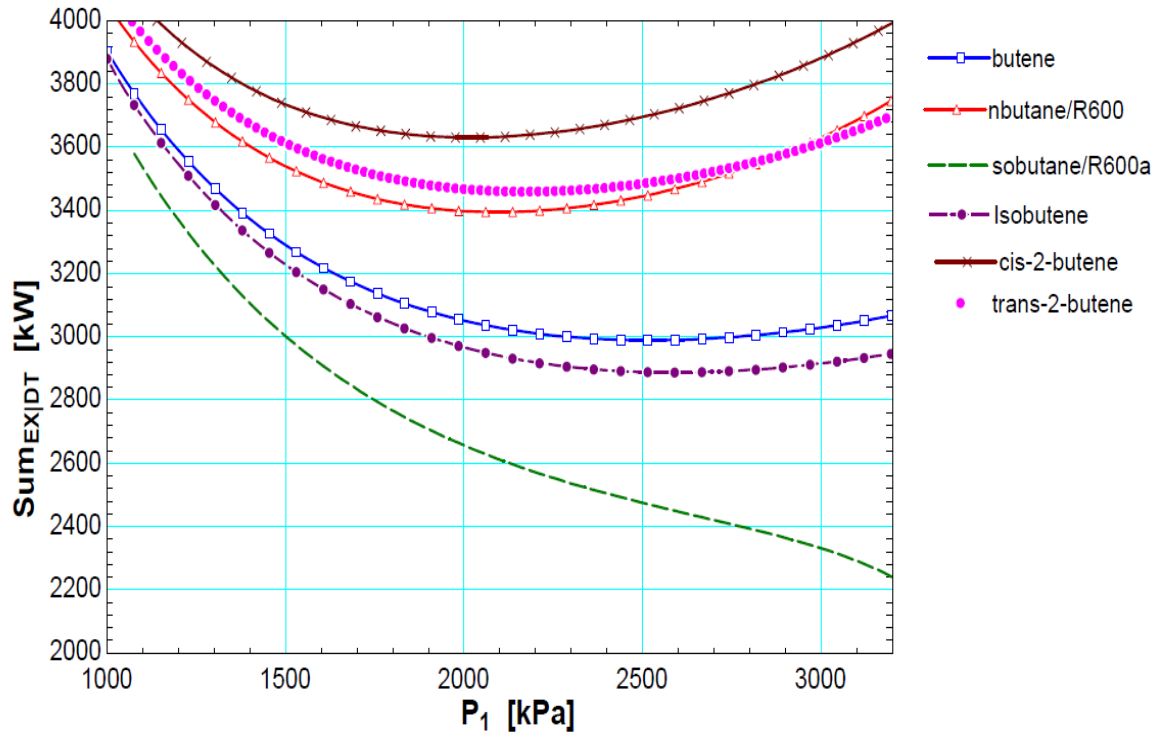
Figure 4.23: Effect of turbine inlet pressure on the summation of total exergy destruction for water-cooled power plant.

Power plant exergy performance shows how close it is to the maximum possible theoretical operation. Increasing turbine inlet pressure lowers the total exergy destroyed. Optimum pressures are between 1,500 - 2,500 kPa for water-cooled as shown in Figure 4.23. On the exergy destruction criteria, isobutane/R600a is a better-working fluid. Figure 4.24 presents turbine inlet pressure vs overall power plant cost. The plant costs are related to the turbine size and net work generated.
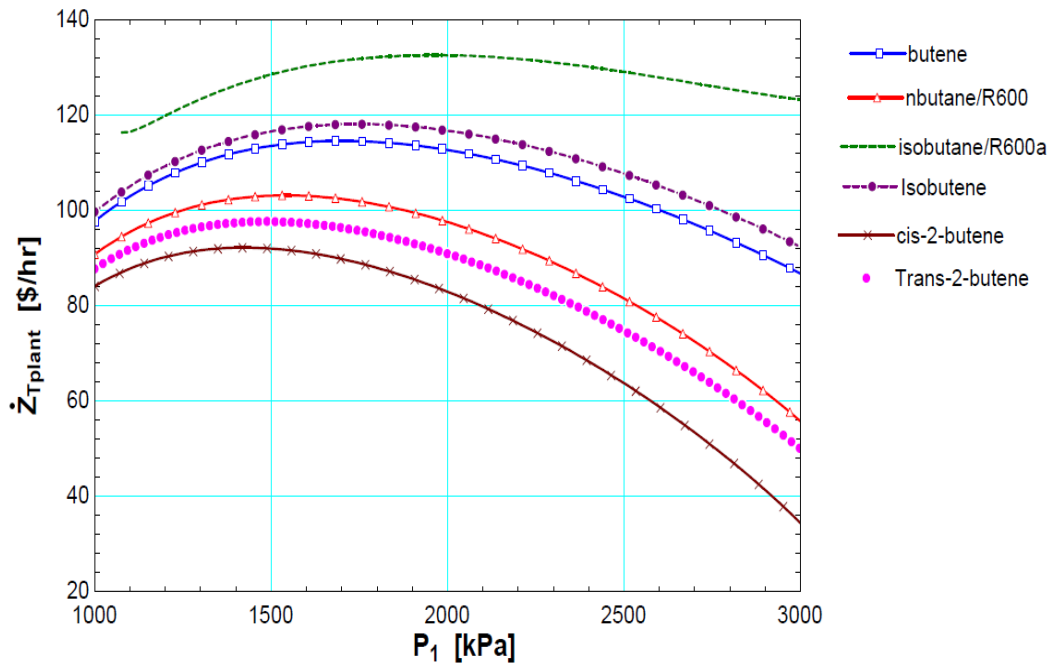
Figure 4.24: Effect of turbine inlet pressure on the overall plant cost rate for the air-cooled plant.

Figure 4.23 and Figure 4.24 show the relationships between turbine pressure inlet pressure, the objective function, exergy destruction, cost of products and power plant cost rate. The plots show curves are polynomials whose maxima and minima are obtained by the variable metric optimisation method. The method optimised the objective function by ensuring the negative or positive definiteness of the hessian matrix. Matrix generated in EES by varying the decision variables between the lower and upper values to get optimum. The optimised power plants by exergoeconomic analysis tabulated to present the results. From figures plotted and literature, the curves of turbine inlet pressure versus net-work are non-linear line graphs.

Tables 4.8 and 4.9 show f(obj) for optimised power plant units vary between 1.566 to 1.758 for wet cooling and 0.5949 to 0.8656 for air-cooled condenser type. The lower values for dry-cooling are a result of a larger heat exchangers area. The main component contributing to the area in dry-cooling is the condenser. The total area of the heat exchangers for wet cooling is almost half the areas of dry cooling.

Table 4.8: Optimised model for different working fluids for proposed Olkaria I wet-cooling power plant.

Fluid	P_1 (kPa)	P_2 (kPa)	P_{cr} (kPa)	T_C (^{o}C)	f(obj)	$\dot{W}_{net}$ (kWe)	$\dot{Ex}_{irr}$ (kW)	$\dot{Sum}_{EXd}$ (kW)	η_{th} (-)	η_u (-)	η_{u2} (-)	SI	$\dot{m}_{wf}$ (kg/s)
Isobutane	2,302	500	3,640	100	1.619	2,590	18.48	1,513	15.98	40.45	62.88	1.679	58.83
Isobutene	2,300	530	4,010	100	1.613	2,260	18.75	1,838	13.99	35.3	54.87	1.546	46.57
Trans-2-butene	2,298	550	4,027	100	1.652	1,972	13.15	2,224	11.63	29.23	45.44	1.413	31.32
Butene	2,205	550	4,005	100	1.566	2,405	17.98	2,556	12.66	31.96	49.65	1.470	46.03
R600a	2,302	531.6	3,640	100	1.619	2,594	15.68	1,509	16.01	40.51	62.97	1.681	58.83
n-butane	2,298	340	3,796	100	1.758	2,177	8.978	1,916	13.52	34.00	52.85	1.515	34.82
R600	2,298	340	3,796	100	1.758	2,177	8.9798	1,916	13.52	34.00	52.85	1.515	34.82
cis-2-butene	2,297	376.4	4,226	100	1.614	1,628	20.84	2,470	10.12	25.43	39.53	1.341	26.50

Table 4.9: Optimised model for different working fluids for proposed air-cooled unit at Olkaria I.

Fluid	P_1 (kPa)	P_2 (kPa)	P_{cr} (kPa)	T_C (^{o}C)	f(obj)	$\dot{W}_{net}$ (kWe)	$\dot{Ex}_{irr}$ (kW)	$\dot{Sum}_{exd}$ (kW)	η_{th} (-)	η_u (-)	η_{u2} (-)	SI	$\dot{m}_{wf}$ (kg/s)
Isobutane	2,929	699.9	3,640	99.98	0.8154	2,156	98.61	1,904	11.73	33.15	51.55	1.496	51.55
Isobutene	2,929	699.9	4,010	99.98	0.8472	1,587	246.7	2,334	8.732	24.25	37.95	1.320	35.48
Trans-2-butene	2,011	570.0	4,027	100	0.8299	1,572	388.6	2,199	9.067	24.16	37.79	1.319	37.3
Butene	2,011	570.7	4,005	100	0.6764	2,038	66.65	2,054	11.73	31.32	49.00	1.459	49.63
R600a	2,011	570.7	3,640	100	0.5949	2,469	287.2	1,977	14.07	37.95	59.37	1.612	63.29
n-butane	2,019	534.4	3,796	100	0.8656	1,778	278.2	2,102	10.23	27.34	42.76	1.376	40.94
R600	2,019	534.4	3,796	100	0.8656	1,778	278.2	2,102	10.23	27.34	42.76	1.376	40.94
cis-2-butene	2,010	548.3	4,226	100	0.8337	1,446	396.8	2,316	8.383	22.22	34.77	1.286	32.81

Table 4.10: Exergy and exergoeconomic results of the optimised water-cooled power plant.

Fluid	c_{pr} ($/GJ)	$\dot{C}_{D,plant}$ ($/hr)	$\dot{Z}_{plant}$ ($/hr)	Z_{plant} ($)	f (%)	c_{plant} ($/GJ)	SI_{cost} ($/hr)	$Area_{total}$ (m^2)
Isobutane	18.3	12.29	140.7	7.750E6	46.29	15.84	73.86	1,600
Isobutene	18.89	11.7	123.8	6.819E6	41.15	13.47	64.96	1,401
Trans-2-butene	19.84	9.548	103.7	5.713E6	34.7	11.63	49.86	1,133
Butene	19.54	11.85	113.9	6.277E6	39.03	12.58	63.67	1,306
R600a	18.29	12.63	140.9	7.760E6	44.31	14.83	73.66	1,602
n-butane	18.8	8.979	117.3	6.464E6	47.47	16.99	55.36	1,238
R600	18.79	8.979	117.3	6.646E6	47.47	16.99	55.36	1,239
cis-2-butene	20.76	8.798	90.9	5.008E6	39.28	13.43	49.12	968.9

Table 4.11: Exergy and exergoeconomic parameters of the optimised air-cooled power plant.

Fluid	c_{pr} ($/GJ)	$\dot{C}_{D,plant}$ ($/hr)	$\dot{Z}_{plant}$ ($/hr)	Z_{plant} ($)	f (%)	c_{plant} ($/GJ)	SI_{cost} ($/hr)	$Area_{total}$ (m^2)
Isobutane	20.87	11.39	110.8	6.104E6	92.11	15.17	88.88	2,644
Isobutene	22.74	10.92	83.11	4.579E6	90.04	11.75	74.76	1,862
Trans-2-butene	22.83	10.29	83.15	4.581E6	90.57	12.48	74.93	1,894
Butene	22	12.85	110.2	6.074E6	91.14	13.37	90.77	3,017
R600a	21.53	15.61	135.5	7.466E6	91.35	13.73	102.3	4,150
n-butane	21.78	10.65	91.8	5.058E6	91.12	13.34	79.42	2,054
R600	21.78	10.65	91.8	5.058E6	91.12	13.34	79.42	2,054
cis-2-butene	23.4	10.34	76.92	4.238E6	89.39	10.95	71.04	1,724
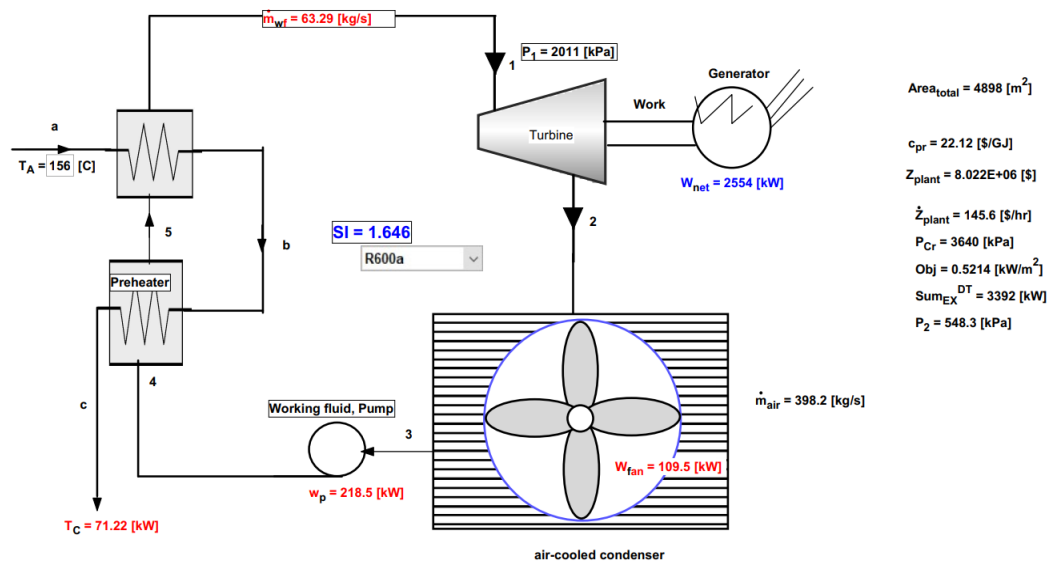
Figure 4.25: Optimised air-cooled binary power plant utilizing R600a working fluid modelled and analysed using EES code.

Selection of the suitable plant on exergoeconomic is air-cooled systems with lower plant costs rates of between 76.92 $/hr and 135.8 $/hr translating to power investment cost of worth between 4.2 million $ and 7.6 million $, respectively. In this research, the exergoeconomic rate of the cooling tower is proposed from the analysis of the water-cooled power plant. The estimated cooling tower cost rate results were approximated using exponential curve fit. The idea is to bring a complete exergoeconomic analysis of power plants. The cooling tower is a crucial and paramount part of the power plants.

The cooling system is mainly a factor or influenced by the ambient temperatures. Figure 4.26 (T-Q diagram) shows the effect of ambient temperature on the heat rejection capacity. Heat capacity (Q) decreases with increasing temperature for the same temperature range. Air-cooled capacity is higher than water-cooled units. The difference contributes to the condensers' size and the cooling medium's heat capacity. The cooling capacity range will have a direct influence on the objective function. Water has specific heat capacity of 4.2 kJkg-1K-1 while air specific heat capacity is 0.993 kJkg-1K-1, thus the disparities in the heat rejection capacity.

Density also is a factor that contributes to smaller condensers in the water-cooled unit. Water is 784 times denser than air. The heat capacities are 2,489-2,466 kW for isobutene, 2,975 – 2,947 kW for isobutane, 1,501-1,486 kW for cis-2-butene and, 1,887- 1,870 kW for n-butane for ambient temperatures between 0°C and 40°C. Wet cooling is mainly the exchange of latent

heat of vaporization with the ambient air passing through the cooling tower. From Figure 4.26, wet coolers would work better in hot climates or summer.

Heat rejection for the air-cooled unit is much higher than for the water-cooled. Figure 4.26 shows the values of air-cooled plotted versus the ambient temperature on the second y-axes. Large areas are required over the same weather conditions. The heat capacities are 20,806-20,610 kW for isobutene, 24,153-23,928 kW for isobutane, 13,727-13,595 kW for cis-2-butene and, 16,772-16,611 kW for n-butane for ambient temperatures between 0°C and 40°C. Application of air-cooled units would be advisable where water is scarce and in colder regions because of the huge heat capacity requirements and the area of heat exchangers. Dry cooling can eliminate heat without damaging the outside environment (no direct contact with ambient) since makeup water is not required (State 12 in Figure 4.7). Environmental contaminants that could be related to wet-cooling are eliminated by using dry-coolers. The dry-cooling can also be an option in regions where plume (State 11 in Figure 4.7) is not allowed in restricted and protected areas.
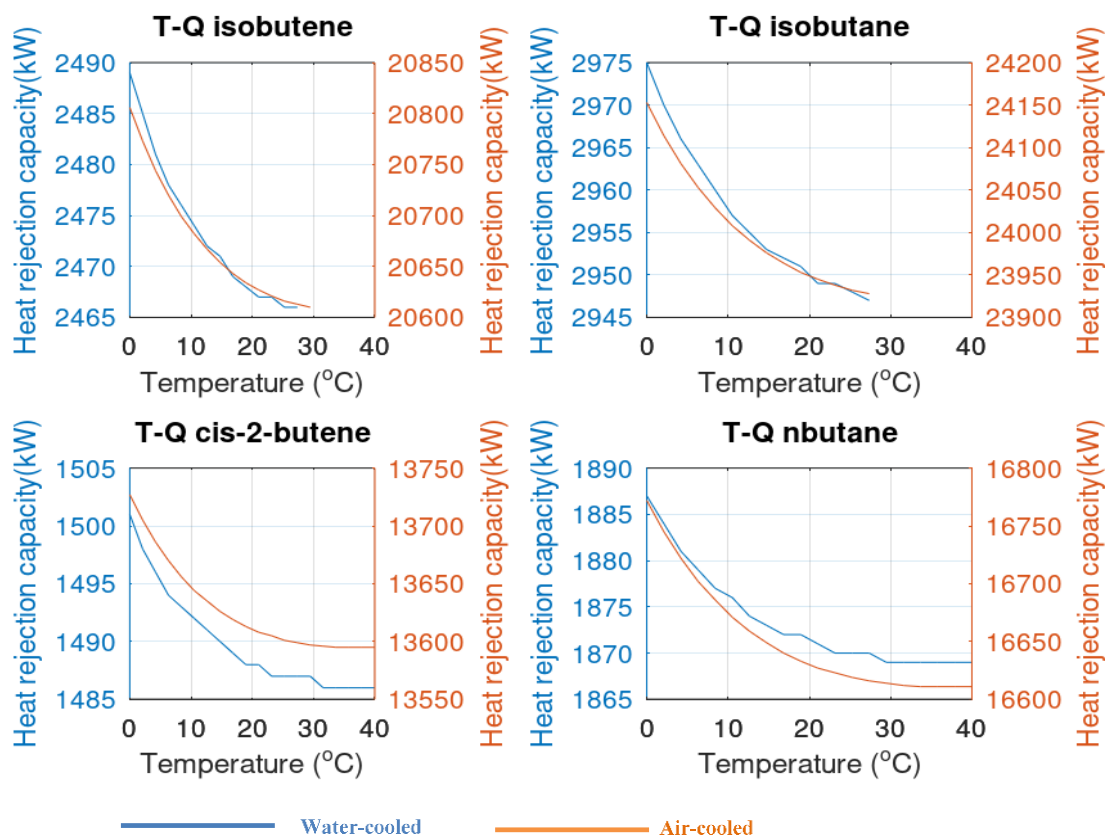
Figure 4.26: The effect of ambient temperature on heat rejection capacity in the condensers of air-cooled and water-cooled power plants.

To add the exergoeconomic equation, exponential and power forms curve fit equations are used to check the best curve fitting. Butene exponential curve in which the investment cost of the cooling tower is a function of the cooling water flow rate is the best fitting curve. From Figure 4.27, the best and approximate curve fit the calculated cost of the water-cooled cooling tower proposed as:

$$63,596e^{0.0138772\dot{m}_{cw}} \tag{4.40}$$

In equation (4.40), $\dot{m}_{cw}$ is the cooling water flow rate in kg/s. Butene has the best exponential fit curve proposed and used for the other working fluids and compared with the calculated cost rates using equation (4.28).

R600/n-butane   Butene   Cis-2-butene

isobutene   Isobutane/R600a
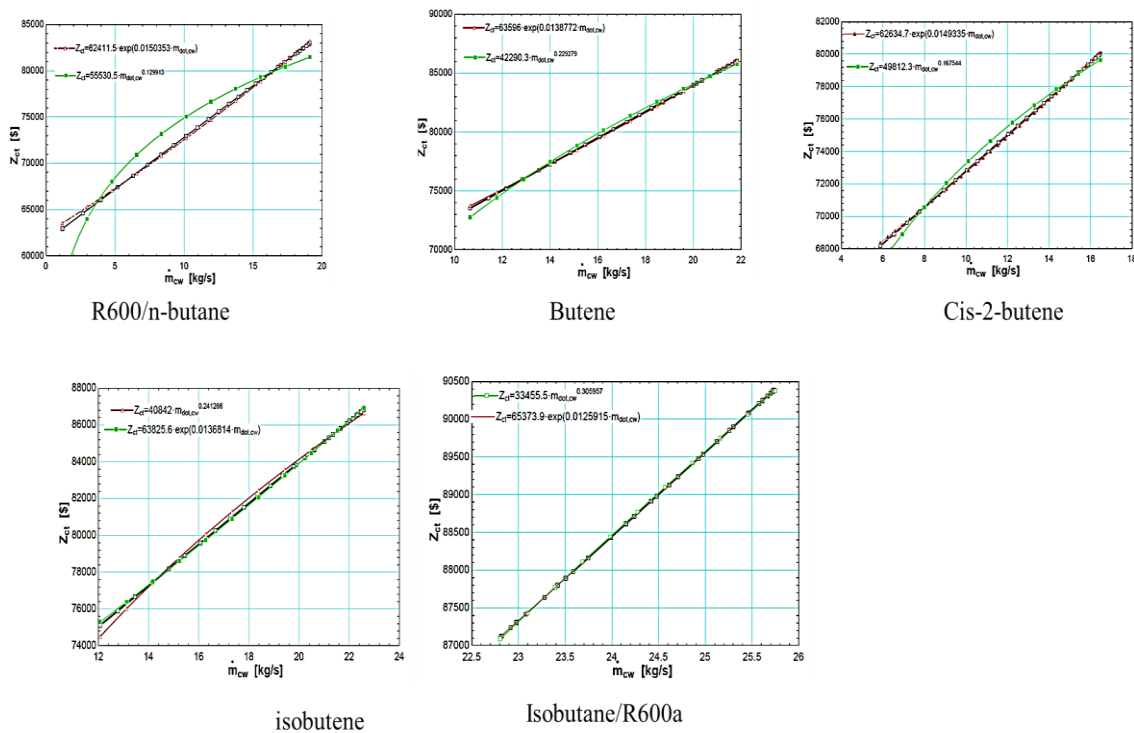
Figure 4.27: Power and exponential power equations for approximating the cooling tower investment cost, Z_{ct} as a function of cooling water flow rate. From the polynomial fitting, butene shows the best curve fit proposed for cooling tower exergoeconomic and shows an accuracy of about 99% compared to the equation applied.

4.9.3   Validation of exergoeconomic optimisation of Olkaria I binary power plant

Results of this paper are validated using the available literature sources of related studies on exergy and economic optimisation. The research related to this work has some differences. The systems are of similar operations but have different layouts and working fluids. The difference is also in the power plant layout, where a regenerative pre-heater was included by El-Emam and Dincer (2013).

Table 4.12 shows the optimal values of the two models investigated compared to related studies on the exergoeconomic analysis of power plants. The most suitable working fluid is isobutane. Table 4.12 shows that isobutane or R600/1 working fluids are the most applied. Kazemi Ehyaei (2018) calculated SI for the study, but the working fluid was R245fa. The main parameters in the exergoeconomic investigation of power plants by Bett (2020), Coskun (2011), Catrini (2020), Calise (2015) and others are energy and exergy efficiencies, optimum turbine inlet pressure, total exergy destruction, heat exchangers total area, and an objective function [40], [108], [210]. For the validation of the objective function (net power generated per meter square of heat exchanger), similar calculated parameters tabulated for this optimisation research and similar studies; include energy and exergy efficiencies, cost of products, and total areas of heat exchangers. The cost of products calculated is similar to exergoeconomic literature results. The variation is because of different plant layouts, different mass flow rates of working fluids, different reinjection temperatures, and turbine inlet pressures. In this research, the f(obj) defined the two types of plants by introducing an exergoeconomic cooling tower. There is a scarcity of data linking geothermal power plants' exergy and exergoeconomic with the cooling tower. Table 4.13 shows the absolute error calculated is less than 1%, the proposed equation for the cooling tower exergoeconomic is 99% accurate compared to [184] equation. The proposed equation could be applicable in cooling towers exergoeconomic studies in exergy and economic optimisation of power plants.

If developed, the brine in Olkaria one will add more renewable power to Kenya's energy mix. In line with the country's vision 2030, there is a potential in the brine reinjected in Olkaria.

Olkaria II SF brine has the exergy possible for bottoming binary units. The binary power plant proposed for bottoming at Olkaria II was modelled and optimised using EES code. Two optimisation scenarios are applied: exergy and pinch point analysis and exergy and sustainability index optimisation.

Table 4.12: Model validation with similar studies.

Reference	Fluid	Turbine pressure (kPa)	Sum of exergy destroyed (kW)	Exergy efficiency (-)	Energy Efficiency (-)	SI (-)	Area total (m^2)	Cost of products ($/GJ)	Mass flow rate of working fluid (kg/s)
[185]	R245fa	4,278	-	21.3	18.2	-	1,863	-	12
[81]	Isobutane	-	-	28.27 to 48.8	16.37 to 17.48	1.394 to 1.953	1,270 to 1,305	-	70.56 to 78.06
[182]	R601	1,491	-	-	-	-	2,835	25.72-27.35	44.03
[211]	isobutane	3,280	-	49.17	34.98	-	-	22.4	12.44
[212]	n-butane	-	-	21.01	10.2		-	16.49	100
Air-cooled	Isobutane	2,929	1,904	33.15	11.73	1.496	2,644	20.87	51.55
	R600a	2,011	1,977	37.95	14.07	1.612	4,150	21.53	63.29
Water-cooled	R600	2,298	1,513	52.85	13.52	2.121	1,239	18.3	34.82
	Isobutane	2,302	1,916	62.88	15.98	2.694	1,600	18.79	58.83

Table 4.13. Comparison and percentage error calculated for the proposed cooling tower equation equation(4.40) and Nourani et al., (2019), equation (4.28).

Working fluid	Exponential fitting curve	Proposed equation	Calculated [184]	Proposed equation	% error
Isobutane	$63{,}373.9e^{0.0125915\dot{m}_{cw}}$		93,151	94,066	0.9822
Isobutene	$63{,}825.6e^{0.0136814\dot{m}_{cw}}$		80,464	80,362	0.1268
Butene	$63{,}596e^{0.0138772\dot{m}_{cw}}$	$63{,}596e^{0.0138772\dot{m}_{cw}}$	78,538	78,464	0.0944
R600a	$65{,}373.9e^{0.0135915\dot{m}_{cw}}$		91,516	92,520	0.767
n-butane /R600	$62{,}411.5e^{0.0150353\dot{m}_{cw}}$		86,488	86,600	0.1297
cis-2-butene	$62{,}634.7e^{0.010149335\dot{m}_{cw}}$		80,053	79,953	0.1248

4.10 Optimisation of Olkaria II exergy for a binary unit by combining exergy and pinch point analysis

Olkaria II single flash units generate 105 MW from three condensing turbo-generating units of each 35 MWe [189]. Two-phase fluid is separated in the separator at 462.25 kPa, 156.4°C into brine and steam. The steam quality is 0.52, and the flow rate of 227.4 kg/s, while the brine flow rate is 206.9 kg/s. The brine re-injected at this state has energy and exergy that can generate power using a binary unit. The brine exergy at the separator exit is 21.5 MW of 196.6 MW exergy. Other parameters are; condenser (temperature, 44.97°C, turbine inlet pressure, 699.7 kPa, condensate flow rate, 2,372 kg/s, cooling water flow rate, 2,194 kg/s) [189]. By constraining parameters; this research optimised two ORC cycle configurations for six different working fluids.

4.10.1 System description

The proposed units are shown in Figure 4.7. The addition of the binary power plant will increase the power output and efficiencies of the available exergy in Olkaria II. The main parameters known are flow rate ($\dot{m}$) and temperature of the brine. For both models, a water-cooled surface condenser condenses the working fluid. The thermodynamic analysis focused on the ORC cycle. A cooling tower was considered in the case of Olkaria I (air-cooled and water-cooled). In this section, the cooling towers are assumed to be similar, and their impact is on the economic part of the power plant. For the exergy analysis, the local temperature at Olkaria is 20°C and ambient pressure of 86 kPa [105].

Six different working fluids (isobutane, isobutene, butene, trans-2-butene, R236ea and R142b) were selected for the modelled binary power plants. The fluids investigated have critical temperatures below the heat source temperature of 156°C.

The parameters optimised were turbine inlet pressure, pinch point in the heat exchangers and reinjection temperatures. For turbine inlet pressure, the values were between 1,000 kPa and lower than critical pressures for each fluid. Exergy efficiencies and work net generated plots were used to identify the optimum operating pressures by varying the turbine inlet pressure. The pinch point temperatures varied from 5 to 15°C. The pinch points affected net power, working fluid flow rates and efficiencies, and reinjection temperatures. Pinch points of 5, 8, and 10°C were used to show the effect of pinch point selection on the reinjection temperature, net power generated, and exergy efficiency.

The optimum pinch point dictates the reinjection temperature at the outlet of the heat source in the pre-heater. This research aims to present the optimisation of binary power plants by employing the energy & exergy, pinch point, and sustainability index for six different working fluids. Two cycles configurations were studied. One cycle consists of pre-heater and evaporator heat exchangers, while the other has only an evaporator and a regenerator positioned between the turbine and condenser. The analysis of the cycles combines exergy and pinch-point optimisation by varying turbine inlet pressure and pinch point values. Graphical plots are used to select optimum pinch points to analyse exchangers. This research includes the most effective pinch point in pre-heater and evaporator and the relation of the exergy's concept with sustainability index as a function of utilisation efficiency in the Olkaria geothermal field. The energy and mass balance equations calculate the brine exit temperature from the pre-heater.

4.10.2 Results and discussion

For optimising available exergy for Olkaria II, combined exergy and pinch point analyses to optimise two binary cycles of the geothermal power plant. At the steady-state conditions, energy, mass, and exergy balance equations apply at each state. In the study, eight working fluids were selected based on the validity of the energy and mass balance equations in the heat exchangers (evaporator and pre-heater) with the same three pinch points ($5^{o}C$, $8^{o}C$, and $10^{o}C$).

The input temperature required varies for each working fluid. The brine reinjection temperature depends on the pinch point selection. The pinch point factor affects the effectiveness of the heat exchangers and the calculation of reinjection temperatures. The pinch point also affects the mass flow rate of the working fluid, the net power output generated from the plant, and the reinjection temperature. Results show that low pinch point values correspond to have lower reinjection temperatures. The optimum pressures were identified using exergy efficiency, net power generated, reinjection temperature, and pinch point temperature plots. Figures 4.28, 4.29 and 4.30 show the effects of varying turbine inlet pressure on net power generated, efficiencies, and reinjection temperatures, respectively. As the pressure increases, the efficiencies and net power generated work increased to optimal values as presented in Figure 4.28 (a) and Table 4.14 at 1,955 kPa for isobutene, 2,378 kPa for isobutane, 1,888 kPa for butene, 1,563 kPa for trans-2-butene, 1,845 kPa for R236ea and 2,302 kPa for R142b for the simple ORC cycle. The condenser temperature and pinch point were fixed in the analysis while varying turbine inlet pressure.

120
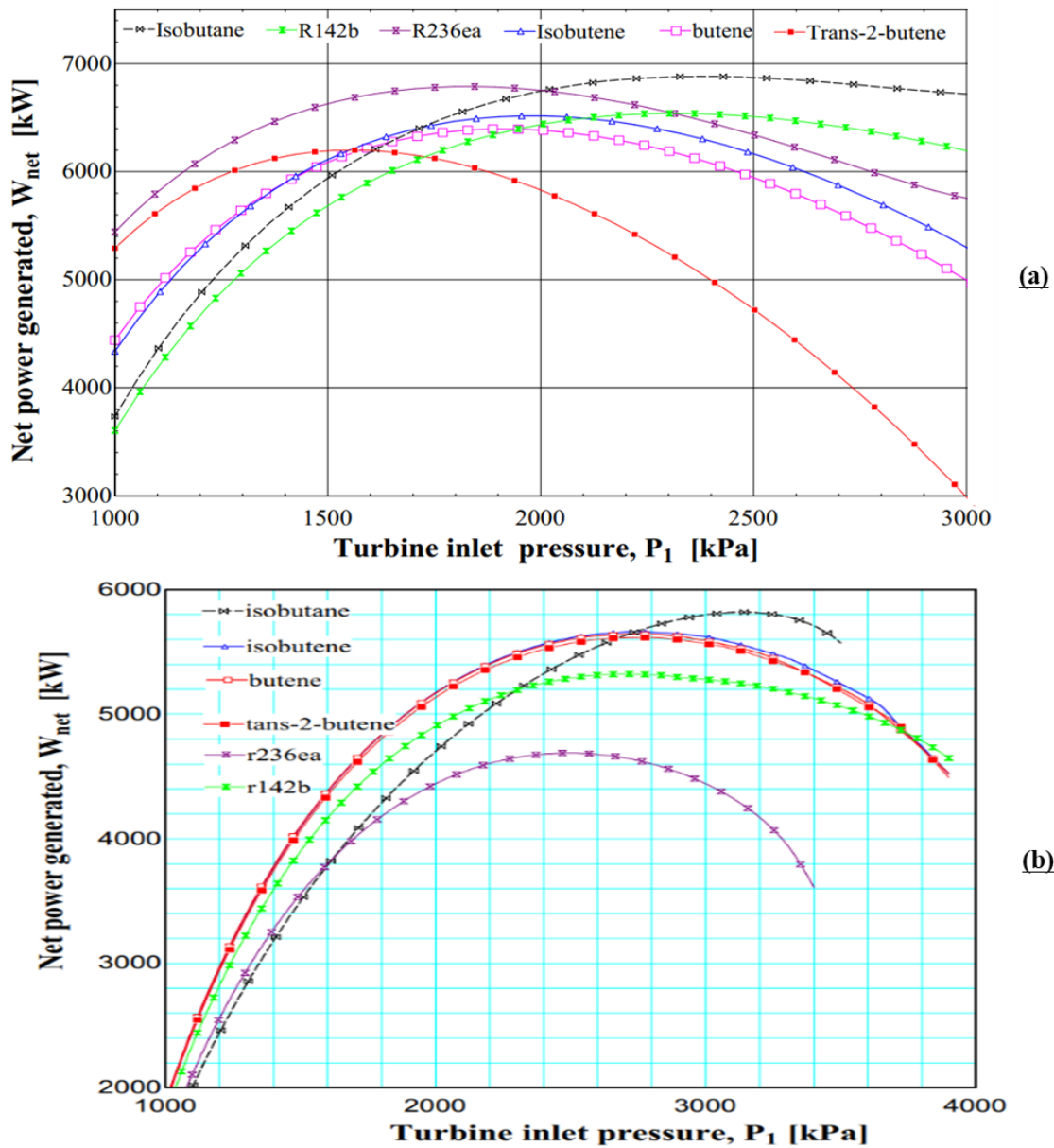
Figure 4.28: Turbine inlet pressure vs the net power generated (a) simple ORC, optimum pressures below 2,000 kPa, and (b) is a regenerative cycle with optimum turbine inlet pressures above 2,000 kPa for the different fluids investigated.

Figure 4.28 (a) shows the optimum turbine inlet pressures for the simple ORC and are less than in the regenerative cycle. Figure 4.28 (b) shows the effect of turbine inlet pressure on net power for different working fluids for the regenerative cycle. At the condenser temperature of 46.7°C., the turbine outlet pressures were:

- 557.5 kPa for isobutene,
- 627.4 kPa for isobutane,
- 543.7 kPa for butene,
- 438.9 kPa for trans-2-butene,

- 412.3 kPa for R236ea and 622.9 kPa for R142b

listed in Table 4.14. The inlet turbine pressure is the main parameter for identifying the optimal operating pressures in binary power plants [107], [210]. Figure 4.29 illustrates the effect of turbine inlet pressure on exergy efficiencies while other parameters (pinch point and condenser temperature) are assumed to be constant. Increasing turbine inlet pressure will decrease the exergy difference between inlet and outlet brine, thus reducing the mass flow rate of the working fluid; consequently, exergy efficiency decreases.

Figure 4.30 shows that turbine pressure varies with the working fluid and cycle configuration. The trends illustrated are due to different values of critical temperature and pressure. Figure 4.29 (a) shows that optimum turbine inlet pressure for simple ORC is lower than for the regenerative ORC cycle (Figure 4.29 (b)). Simple ORC has higher efficiencies between 20 to 35% due to more heat recovered in the pre-heater than regenerative ORC. In the regenerative cycle, reinjection temperature was fixed, unlike in simple ORC, where it was simulated using EES code. Exergy efficiencies for the regenerative cycle were between 15% to 27%.

An increase in the turbine inlet pressure led to changes in the enthalpy drop between the turbine inlet and outlet pressures. With constant condenser temperature, optimum pressures yield the maximum power generated and exergy efficiencies. Figure 4.30 shows the effect of varying turbine inlet pressure on the reinjection temperature of the brine. For temperatures above 89°C, most of the working fluids are suitable. The limiting factor will be the geothermal water geochemistry. Once optimum reinjection temperature had been selected, the pinch point was checked.

Pinch point of 8°C has reinjection temperatures above 80°C for a simple ORC (Figure 4.31 (a)). An increase in pinch point decreases the heat transfer in the heat exchangers, thus reducing the flow rate of the working fluid. The net power output is directly proportional to the mass flow rate of the working fluid. Figure 4.31 (b) shows the effect of varying reinjection temperature for the case of a regenerative cycle between 70 and 100°C.
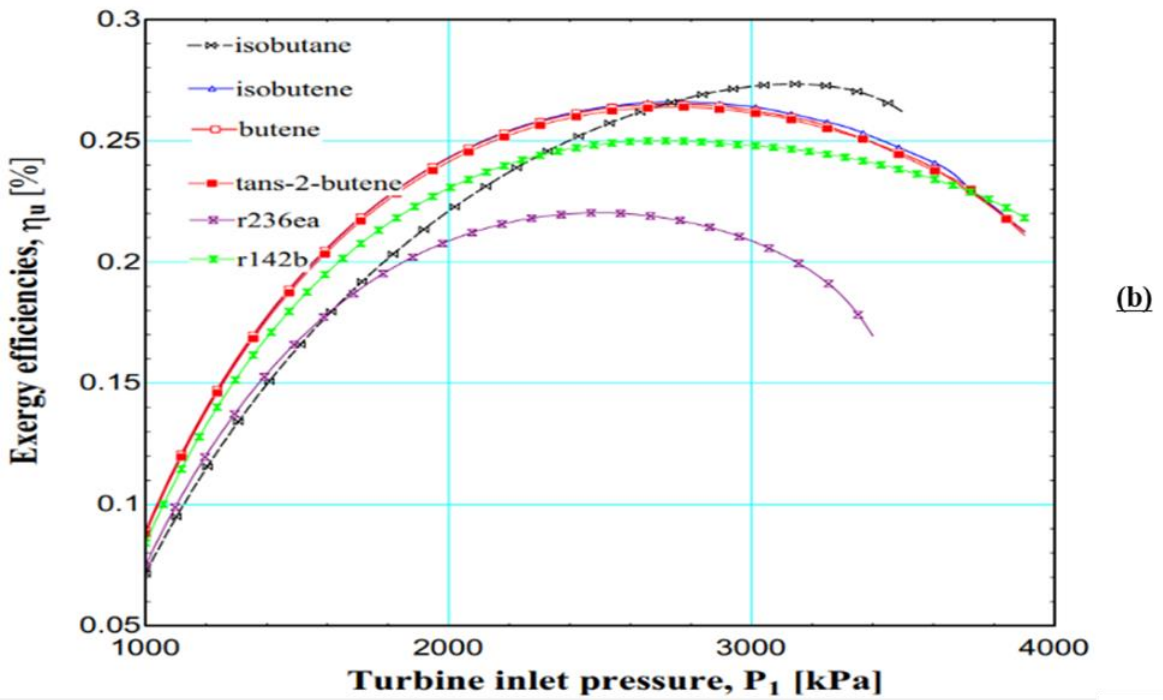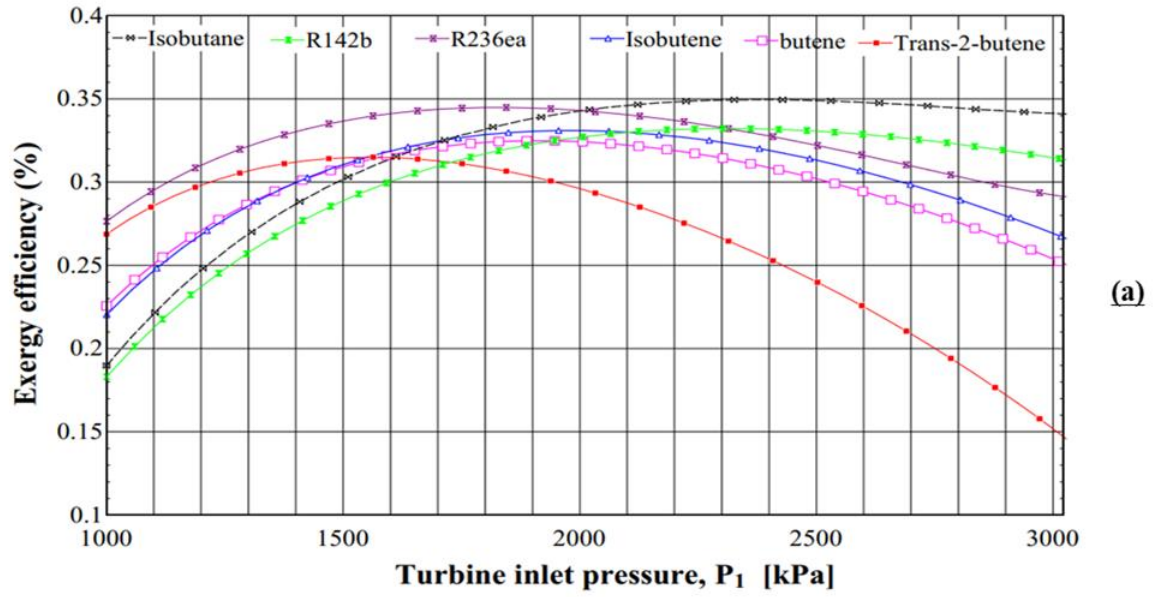
Figure 4.29: Effect of turbine inlet pressure on the exergy efficiencies of the binary cycles (a) for simple ORC showing optimum pressures are 1,500 and 2,000 kPa and (b) for regenerative ORC cycle illustrating the trend of optimum pressures between 2,000 and 3,000 kPa.
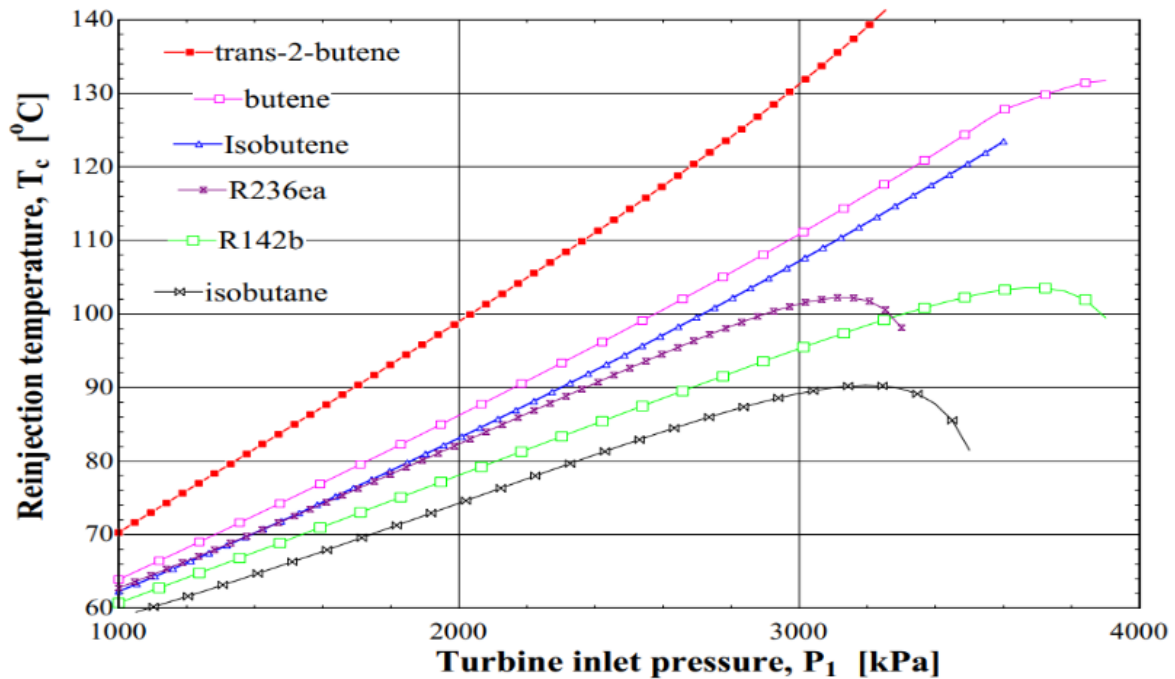
Figure 4.30. Variation of turbine inlet pressure with reinjection temperatures of brine for the simple ORC. The highest reinjection temperature is 89°C for trans-2-butene.

By increasing pressure, the amount of vapour decreases with increasing temperature and specific enthalpy [213]. The effect of turbine inlet pressure is related to the parasitic load. As the turbine inlet pressure increases, heat transfer between brine and working fluid decreases, and the pump power consumption increases, decreasing the total power output [214], [215]. Figure 4.31 shows the effects of varying pinch points between 5 -15°C on net power output and reinjection temperature. The net power generated decreases as the pinch point temperature increases, but reinjection temperature, T_C, increases.

From Figure 4.31, pinch point selection is a crucial parameter that weighs between net power generated and brine reinjection temperature. Lower values of power and higher reinjection temperatures are obtained at higher pinch point differences because of the reduced mass flow rate of the working fluid. The reduction in the flow rates of the working fluid will reduce the heat exchangers' duty and gives higher reinjection temperatures. The reinjection temperatures are above 80°C for pinch points above 8°C. Higher pinch points above 8°C should be considered in the design of heat exchangers because of higher reinjection temperatures than 5°C.

124
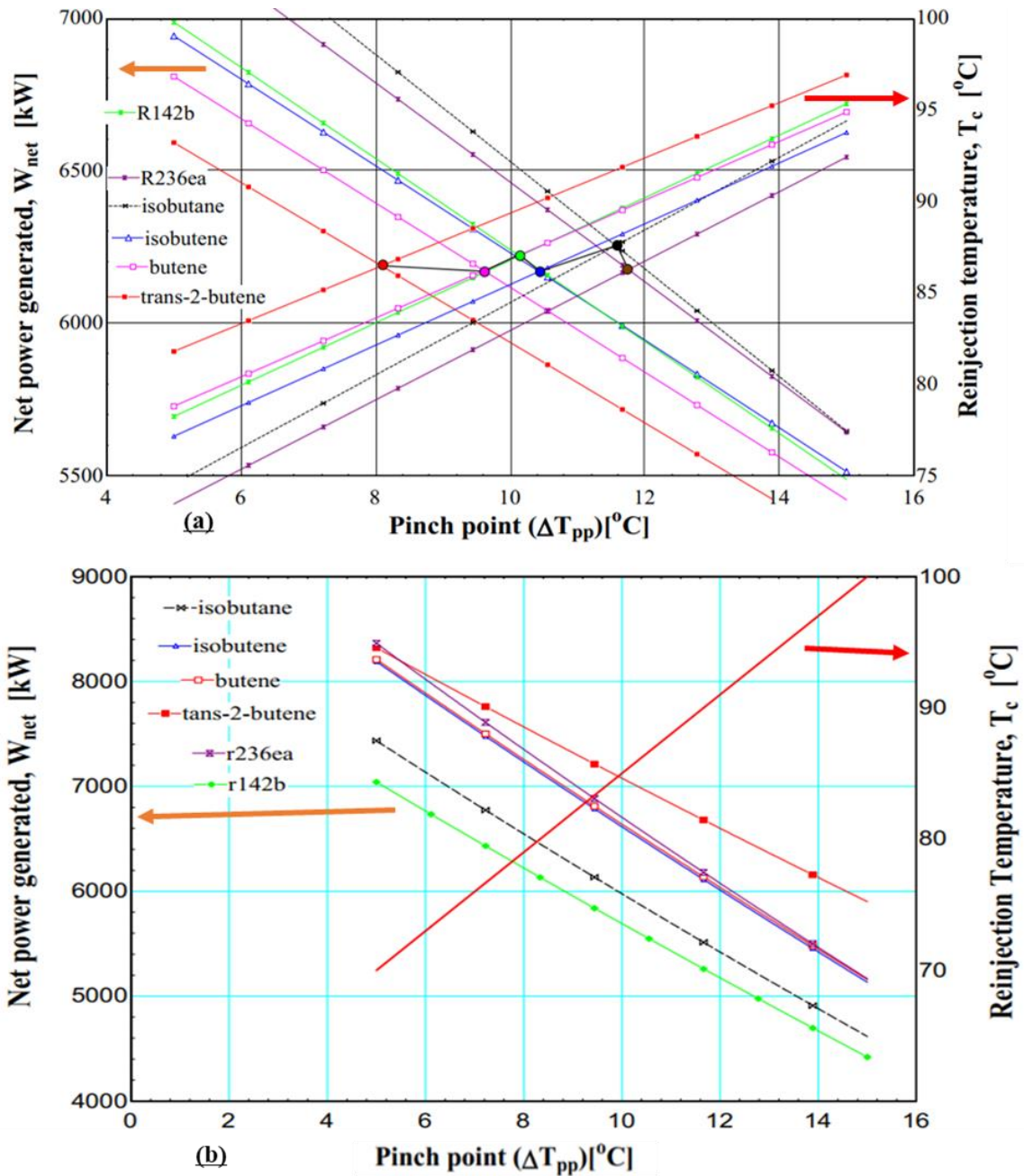
Figure 4.31. Effects of pinch point on the net power output and reinjection temperature for the working fluids investigated.

The combination of exergy and pinch point optimisation shows the analysis and optimisation call for critical analysis to include other thermodynamic parameters. Table 4.14 shows R236ea has the lowest reinjection temperature, 73.47°C, as in the constrained energy and mass balance equations. At the optimum turbine pressure, the highest second utilisation efficiency of 44.93% with isobutane, and the lowest value is with trans-2-butene at 42.33%. The main factor in

efficiency calculation is the reinjection temperature. At high reinjection temperatures, the exergy available is reduced.

Table 4.15 shows the effects of the 8°C pinch point chosen for the analysis. The reinjection temperatures are between 79 and 86°C. The net power generated for the 8°C pinch point is lower than for the 5°C pinch point. The lower pinch point has lower mass flow rates, thus generating less power. The sustainability index is between 1.71 and 1.78. R236ae having at 398.2 kg/s, on the other hand, has a higher power output of 7,273 kWe and the lowest reinjection temperature of 73.47°C for a 5°C pinch point. Tables 4.14- 4.19 show the results of the cycles operating at optimum turbine inlet pressures for pinch points of 5, 8, and 10°C and as in the case of simple ORC, increasing the pinch point lowers the net power output because of reduced mass flow rates of the working fluids. From Tables 4.14-4.19, the exergy efficiencies are between 8.75-11.46%. Mass flow rates contribute to the net power generated. The mass flow rates of working fluids are 151.7 kg/s, 167.8 kg/s, 150.9 kg/s, 140.6 kg/s, 355.3 kg/s and 273 kg/s for isobutene, isobutane, butene trans-2-butene, R236ea and R142b, respectively. The highest net power generated is 7,057 kWe using trans-2-butene, while the east is 5,388 kWe using R142b.

Table 4.14. Optimised model for different working fluids for 5°C pinch point for the simple ORC at Olkaria II.

Fluid	P_1 (kPa)	P_4 (kPa)	P_{cr} (kPa)	T_C (°C)	W_{net} (kWe)	$Sum_{EX|D}$ (kW)	η_{th} (%)	η_u (%)	η_{u2} (%)	SI (-)	$\dot{m}$ (kg/s)
Isobutene	1,955	557.5	4,010	77.15	6,942	9,100	10.12	35.26	42.98	1.545	173.4
Isobutane	2,378	627.4	3,640	74.55	7403	9,051	10.41	37.61	44.93	1.603	191.6
Butene	1,888	543.7	4,005	78.8	6,808	9,050	10.13	34.58	42.73	1.529	170.3
Trans-2-butene	1,553	438.9	4,027	81.52	6,589	8,873	10.19	33.47	42.33	1.503	154.4
R236ea	1,845	412.3	3,429	73.47	7,273	9,251	10.16	36.95	43.79	1.586	398.2
R142b	2302	622.9	4,055	78.23	6,987	8,970	10.3	35.49	43.64	1.550	317

Table 4.15. Optimised model for different working fluids for 8°C pinch point for the simple ORC model.

Fluid	T_C (°C)	T_{cr} (°C)	W_{net} (kWe)	$Sum_{EX|D}$ (kW)	η_{th} (%)	η_u (%)	η_{u2} (%)	SI (-)	$\dot{m}$ (kg/s)
Isobutene	82.13	144.9	6,516	8,897	10.11	33.1	42.09	1.495	162.4
Isobutane	80.5	134.7	6,881	8,803	10.40	34.95	43.81	1.537	177.6
Butene	83.62	146.1	6,394	8,803	10.12	32.48	41.87	1.481	159.7
Trans-2-butene	86.04	155.5	6,200	8,623	10.19	31.49	41.55	1.460	145.0
R236ea	79.15	139.3	6,788	9,020	10.15	34.48	42.72	1.526	370.8
R142b	83.35	137.1	6,540	8,720	10.29	33.22	42.72	1.497	296.1

Table 4.16. Optimised model for different working fluids for 10°C pinch point for the simple ORC model.

Fluid	T_C (°C)	W_{net} (kWe)	$Sum_{EX\|D}$ (kW)	η_{th} (%)	η_u (%)	η_{u2} (%)	SI (-)	$\dot{m}$ (kg/s)
Isobutene	85.73	6,229	8,672	10.14	31.64	41.62	1.463	154.4
Isobutane	84.15	6,534	8,640	10.35	33.19	43.00	1.497	169.1
Butene	84.69	6,114	8,931	9.82	31.06	40.45	1.451	158
Trans-2-butene	89.05	5,936	8,434	10.18	30.17	41.05	1.432	138.8
R236ea	82.94	6,462	8,829	10.15	32.83	42.05	1.489	352.5
R142b	86.77	6,241	8,524	10.28	31.7	42.13	1.464	282.2

Table 4.17. Optimised model for different working fluids for 5°C pinch point for the proposed regenerative ORC at Olkaria II power plant.

Fluid	P_1 (kPa)	P_4 (kPa)	W_{net} (kWe)	$Sum_{EX\|D}$ (kW)	η_{th} (%)	η_u (%)	η_{u2} (%)	SI (-)	$\dot{m}$ (kg/s)
Isobutene	2,776	557.5	6,459	5,988	10.49	31.45	42.14	1.46	156.5
Isobutane	2,582	627.4	5,864	6,554	9.56	28.55	38.26	1.40	174
Butene	2,716	543.7	6,476	5,975	10.52	31.53	42.25	1.46	155.5
Trans-2-butene	2,894	438.9	7,259	5,235	11.79	35.34	47.36	1.55	144.6
R236ea	2,469	412.3	6,596	5,807	10.71	32.11	43.03	1.47	369.3
R142b	2,657	622.9	5,553	6,880	9.02	27.03	36.23	1.37	281.4

Table 4.18. Optimised model for different working fluids for 8ºC pinch point for the regenerative ORC model.

Fluid	W_{net} (kWe)	$Sum_{EX|D}$ (kW)	η_{th} (%)	η_u (%)	η_{u2} (%)	SI (-)	$\dot{m}$ (kg/s)
Isobutene	6,339	6,162	10.30	30.86	41.35	1.45	153.5
Isobutane	5,738	6,744	9.32	27.93	37.43	1.39	170.2
Butene	6,360	6,143	10.33	30.96	41.49	1.45	152.7
Trans-2-butene	7,137	5,406	11.59	34.74	46.55	1.53	142.2
R236ea	6,444	6,027	10.47	31.37	42.04	1.46	360.7
R142b	5,453	7,034	8.86	26.54	35.57	1.36	276.3

Table 4.19. Optimised model for different working fluids for 10ºC pinch point for the regenerative ORC model.

Fluid	W_{net} (kWe)	$Sum_{EX|D}$ (kW)	η_{th} (%)	η_u (%)	η_{u2} (%)	SI (-)	$\dot{m}$ (kg/s)
Isobutene	6,262	6,274	10.17	30.48	40.85	1.44	151.7
Isobutane	5,657	6,865	9.19	27.54	36.9	1.38	167.8
Butene	6,285	6,251	10.21	30.6	41	1.44	150.9
Trans-2-butene	7,057	5,516	11.46	34.36	46.04	1.52	140.6
R236ea	6,347	6,167	10.31	30.9	41.4	1.45	355.3
R142b	5,388	7,132	8.75	26.23	35.15	1.36	273.0

The combination of exergy and pinch point optimisation shows the analysis and optimisation call for critical analysis to include other thermodynamic parameters. The main factor in efficiency calculation is the reinjection temperature.

Tables 4.14 - 4.19 show that the pinch point affects the net output power. The Tables indicate that increase in pinch point decreases the net output power. Increasing the pinch point decreases the working fluid mass flow rate because of the lower heat absorption in the heat exchangers.

The sustainability indices are between 1.36 and 1.55. Exergy destruction for the regenerative cycle is less than in the simple ORC. The regenerative cycle exergy destruction in the pre-heater is excluded, unlike in the case of simple ORC. The heat exchangers contribute most of the exergy destruction in the ORC power plants. The following parameters should be considered in design and optimisation, available geothermal temperature ranges, the limit of reinjection temperature, turbine inlet pressure, and pinch point specifications.

4.11 Optimisation of Olkaria II binary unit by exergy analysis and sustainability index

Reinjected brine at 156°C with exergy of 20 MW is considered. For the proposed power plant, exergy, energy, and sustainability index were carried out. The power plant layout used is shown in Figure 4.7 (a).

4.11.1 Results and discussion

ORC cycle utilising geothermal brine from Olkaria II power plant in Kenya analysed by energy, exergy, sustainability index, and parametric analysis. The cycle included an investigation on the effects of eight different working fluids in a binary geothermal power plant simulated using EES code. Tables 4.20, 4.21 and 4.22 show the results of the analysis. Grassman diagram (Figure 4.36) summarises the exergy flow.

Tables 4.20 and 4.21 show that the lowest pre-heater brine exit temperature is 78.51°C for R236ea with the highest TC, 99.14°C for trans-2-butene. The eight working fluids studied, R600a, generated the highest net work of 6,792 kWe. Parameters vary with the type of fluid, turbine inlet pressure, and reinjection temperatures. Work generated is a function of flow rate that varies with ammonia having the lowest value of 58 kg/s, whereas other working fluids have flow rates of between 150 and 378 kg/s. The energy and mass balance equations calculate the working fluid flow rates.

Table 4.20: Results of the optimised model for different working fluids.

Fluid	P_1 (kPa)	P_{cr} (kPa)	T_C (°C)	W_{net}	$Sum_{EX|D}$	η_{th} (-)	η_u (-)	η_{u2} (-)	SI	$\dot{m}$ (kg/s)
Ammonia	6,119	11,333	88.04	5,984	7,601	9.902	29.94	40.31	1.43	58.3
Isobutane	2,394	3,640	81.02	6,791	7,562	10.35	34.5	43.44	1.52	176.9
Isobutene	2,000	4,010	83.37	6,461	7,654	10.16	32.82	42.21	1.49	159.9
Trans-2-butene	2,000	4,027	99.14	5,790	5,972	11.67	29.41	45.18	1.42	115.4
Butene	1,909	4,005	84.33	6,343	7,656	10.11	32.22	41.81	1.48	158.4
R600a	2,356	3,640	80.41	6,792	7,646	10.27	34.51	43.22	1.53	178.5
R152a	3,667	4,520	90.00	3,794	9,748	6.561	19.27	26.50	1.24	324.2
R236ea	1,800	3,429	78.51	6,750	8,014	10.02	34.29	42.44	1.52	376.1

Table 4.21: Each component exergy analysis for the analysed power plant. State(s) represent the working fluid and geothermal fluid phases across the components as in Figure 4.7.

	Fluid	Ammonia		Isobutane		Isobutene		Trans-2-butene		Butene		R600a		R152a		R236ea	
State(s)	Component	$\dot{Ex}_d$ (kW)	ε (%)	$\dot{Ex}_d$ (kW)	ε (%)	$\dot{Ex}_d$ (kW)	ε (%)	$\dot{Ex}_d$ (kW)	ε (%)	$\dot{Ex}_d$ (kW)	ε (%)	$\dot{Ex}_d$ (kW)	ε (%)	$\dot{Ex}_d$ (kW)	ε (%)	$\dot{Ex}_d$ (kW)	ε (%)
1-2	Turbine	1,065	85.88	1,210	86.26	1,127	86.15	996.1	86.19	1,107	86.11	1,208	86.26	1,431	73.58	1,141	86.43
2-4 & 8-9	Condenser	3,563	1.471	3.980	1.542	3,833	1.48	2,948	1.701	3,774	1.471	4,017	1.527	2,498	1.45	4,223	1.393
4-5	Pump$_{wf}$	134	76.84	184.2	76.82	126.6	76.78	96.72	76.85	118.8	76.78	181.9	76.81	156.8	76.87	118.7	76.78
5-6 & B-C	Pre-heater	893.4	72.12	1,478	77.23	1,274	74.6	1,367	70.55	1,230	73.28	1,452	77.28	495.7	86.05	1,406	76.54
6-1 & A-B	Evaporator	3,011	73.63	1,920	79	2,420	76.48	1,559	80.92	2,533	75.91	1,996	78.6	6,597	38.75	2,266	77.29

Table 4.22: Corresponding number exergy destruction percentage (%) for each component shown in exergy flow Grassman diagram Figure 4.36.

Working Fluid	1	2	3	4	5	6	7	8
Ammonia	25.22	15.30	4.54	5.41	30.40	18.10	0.68	0.35
Isobutane	20.17	9.75	7.51	6.15	34.50	20.22	0.94	0.77
Isobutene	22.24	12.29	6.47	5.73	32.82	19.47	0.64	0.34
Trans-2-butene	34.90	7.92	6.94	5.06	29.41	14.98	0.49	0.30
Butene	22.94	12.87	6.25	5.62	32.22	19.17	0.60	0.33
R600a	20.16	10.14	7.38	6.14	34.50	20.41	0.92	0.36
R152a	19.95	33.51	4.71	7.27	19.27	12.69	0.79	1.80
R236ea	18.86	11.51	7.14	5.80	34.29	21.45	0.60	0.34

Figure 4.32 and Table 4.22 show R152ea has high exergy destruction (9,748 kW) and a high flow rate, while trans-2-butene has low exergy destruction (5,972 kW). In Figure 4.32, ΔEt is the exergy destroyed in the turbine, ΔEcn is exergy destroyed in the condenser, $\Delta Epwf$ is exergy destroyed in the working fluid pump, ΔEph is exergy destroyed in the pre-heater, and ΔEv is the exergy destroyed in the evaporator. Most of the exergy losses are in the heat exchangers sections/states.
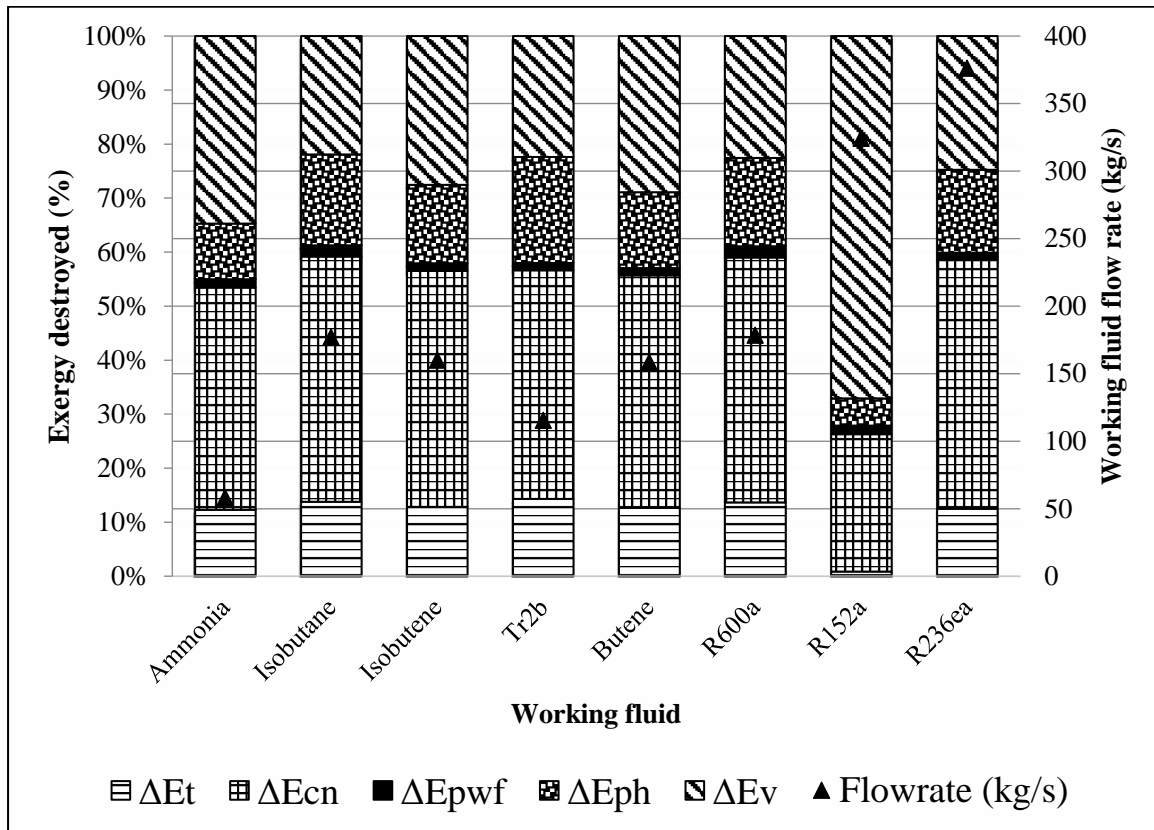
Figure 4.32: Relationship between exergy destroyed and different working fluids flow rates.

Each component's exergy efficiency/effectiveness for the different working fluids is presented in Table 4.21, with the turbine having the highest efficiency at an average of 86%. Exergy efficiencies for the different working fluids show relative to turbine isentropic efficiency assumed in the analysis, 85%. Isentropic efficiencies of turbines and pumps can also be defined as exergy efficiencies in design and manufacturing. Exergy analysis shows the highest rate of exergy destruction is in the heat exchangers (condensers, evaporators, and pre-heaters), accounting for about 60% due to low heat transfer rate at lower temperatures as shown in Figures 4.33 and 4.35 for most of the working fluids. For the different working fluids, exergy

analysis for each component shows the highest rate of exergy destruction is in the heat exchangers (condensers, evaporators, and pre-heaters). The condenser has the most exergy destruction because of two fluid masses (working fluid and cooling water). The compressed fluid is heated to supercritical vapour to reduce exergy losses in the heat exchangers, especially evaporators. Figure 4.34 shows that sustainability indices (SI) for the different working fluids are between 1.24 for R152a and 1.53 for R600a. From Figure 4.34, it is seen that SI variations are not much as compared to efficiencies; thus, SI is a parameter that can be used to classify power plants.
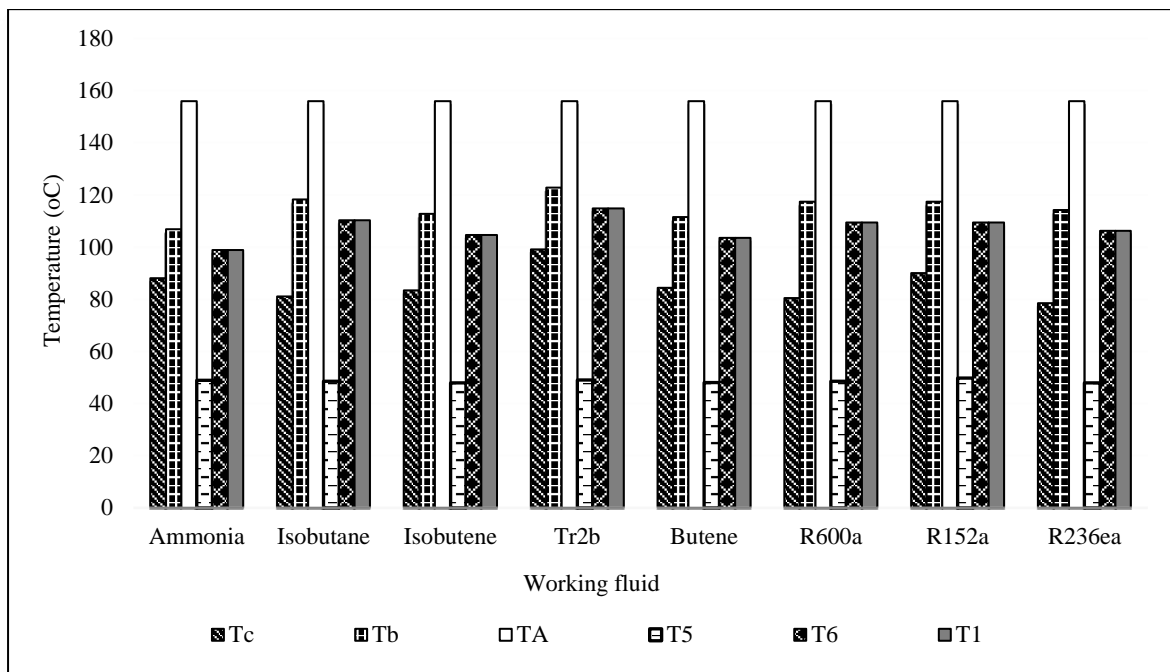
Figure 4.33: Temperature for the main states in the ORC cycle. T1, T6, and T5 are working fluid temperatures obtained from the EES code, while TA (separator temperature), TB, and TC (reinjection temperature) are the brine temperatures.

Figure 4.35 shows that the total exergy destroyed is greater than the net work generated for the different working fluids. The highest exergy destruction for different working fluids is in the condenser, with R236ea destroying 4,223 kW. The least is trans-2-butene destroying 2,948 kW, while the least is in the working fluid pump of small enthalpy change between States 4 and 5, as shown in Table 4.21. Figure 4.35 shows that the turbine inlet pressures for the butane group of working fluids have similar values, unlike ammonia, R152a, and R236ea. The higher the pressure does not translate to more work but decreases the working fluid entropy. Turbine pressure is a crucial parameter in power plant optimisation.

Exergy in relation to the input exergy of 19,685 kW into the system is summarised for the eight working fluids in a Grassman diagram shown in Figure 4.36. The proportion of exergy destruction contributed by each component is presented in Figure 4.34.
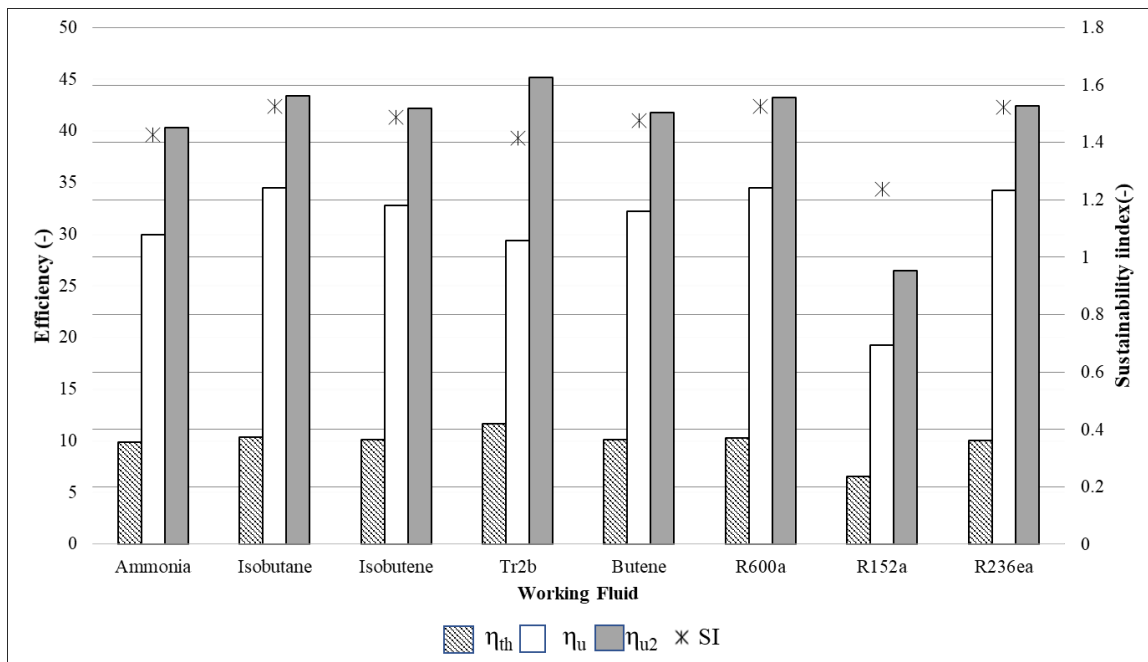
Figure 4.34: Efficiencies and sustainability indices for the eight different fluids investigated.
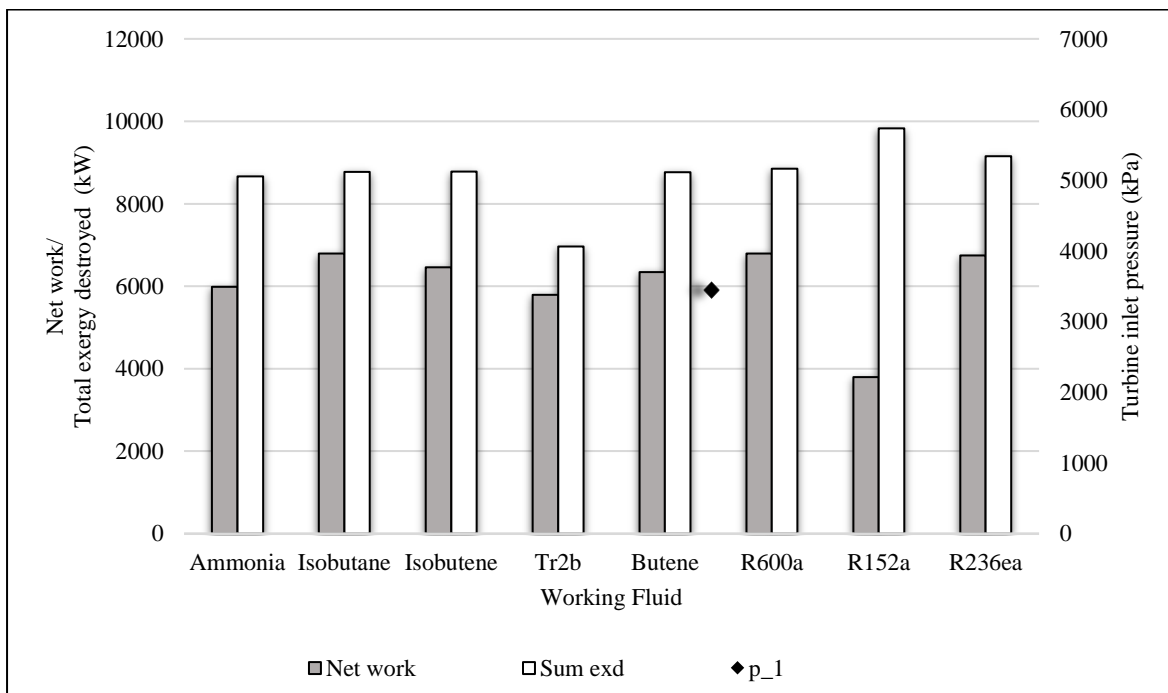
Figure 4.35: Relationship of net work generated, summation of exergy destroyed (Sum EX|D), and turbine inlet pressure (P_1) for the different working fluids.
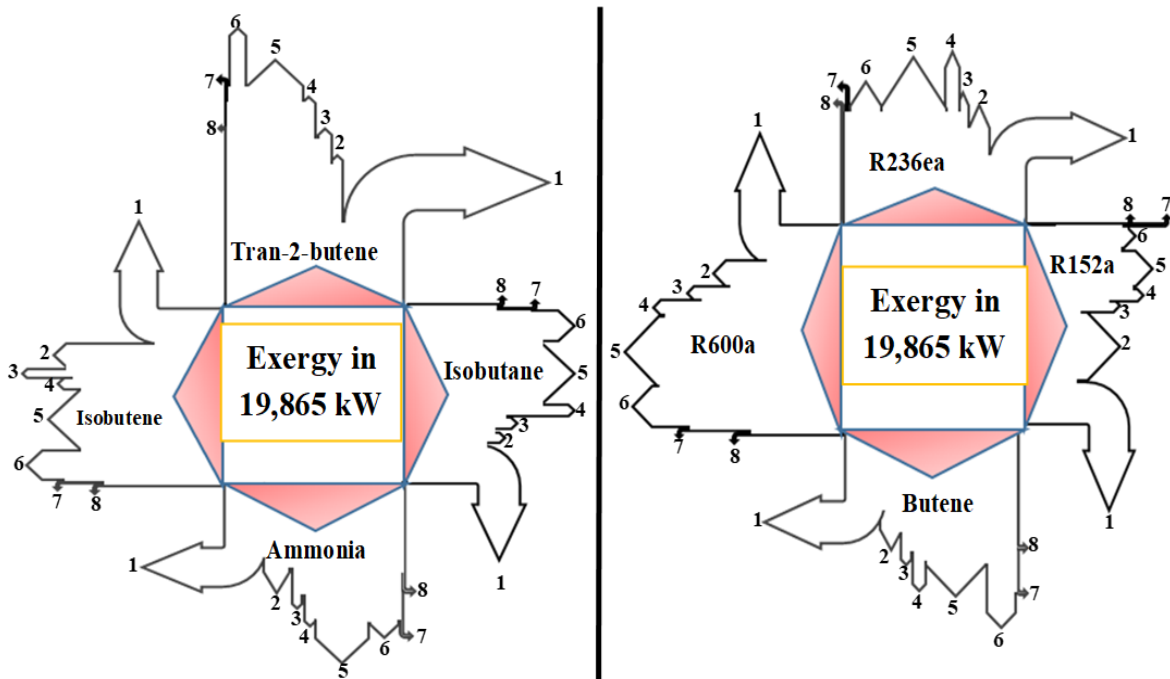
Figure 4.36: Exergy in and exergy destruction flow diagram for each component. The ratio of each component in relation to the exergy into the system is shown in Table 4.22.

Figure 4.36 shows net work as the main portion of exergy flow in the systems for most of the working fluids above 30% except for trans-2-butene and R152a, which have the main exergy destruction in reinjection and evaporator, respectively. Higher exergy of 34.9 % (6,870 kW) for tran-2-butene is because of higher reinjection temperature, T_c at 99°C. Table 4.22 and Figure 4.36 least exergy destruction is in the working fluid pump (number 7 in Figure 4.36) and the unaccounted/irreversibility (number 8 in Figure 4.36), both less than 1%. Grassman exergy flow diagram shows reinjected exergy and net work generated are the main proportions of the total exergy into the system. The exergy reinjected is between 18% and 34% for R236ea and trans-2-butene, respectively. Net work proportion to the input exergy is 12.69% for R152a working fluid and 34,5% for the case of isobutane and R600a.

On the objective of the most efficient and better reinjection temperature working fluid, trans-2-butene has η_{th} of 11.67 %, η_u of 29.41% η_{u2} of 45.18, and T_C at 99.14^{o}C. Retrofitting of ORC unit to maximize the available exergy in Olkaria II can generate at least 3,394 kWe using R236ea or higher 6,792 kWe using isobutane in addition to the SF 105 MWe. The least exergy

destruction is in the trans-2-butene because of the high reinjection temperature (99.14°C), where brine has more exergy wasted than other working fluids.

4.12 Conclusion

Energy, exergy, and economics analysis used to optimise power plants in Olkaria geothermal field. Exergy and exergoeconomic analysis of power plants if a multi-objective approach. The following conclusions are made from optimising power plants by exergy, energy, exergoeconomic, pinch point and sustainability index in EES code for Olkaria geothermal power plants.

4.12.1 Proposed Olkaria I binary power plant

Recent and related research on exergoeconomic analysis of power plants has provided a complete understanding of the thermal flow processes. One of the main components in industrial and power plant designs is the cooling tower, but most studies did not include a wet-cooling tower. Current findings suggest a whole investigation of the power plants to the cooling tower. In this research study, wet and dry-cooled binary geothermal power plants from the viewpoint of thermal and exergoeconomic analyses were conducted for optimum utilisation of geothermal brine at 156°C and a flow rate of 67.14 kg/s at Olkaria I, Kenya. Using EES code, modelling and optimisation were performed based on the variable-metric method by varying turbine inlet and outlet pressures and reinjection temperatures. The thermal and economic parameters were compared for eight different working fluids parametrically.

The sum of exergy destruction for the plants indicates that the optimum operating turbine inlet pressures are between 2,000 and 3,000 kPa. Exergy irreversibility is lower (between 8.98 kW and 20.84 kW) in water-cooled power plants than in dry cooling (between 98.61 kW and 396.8 kW). Air-cooled has higher costs than wet cooling for the two types of power plants. The main reason for higher cost rates in wet cooling is the capital cost of the cooling tower. The proposed exergoeconomic equation (4.40) for the cooling tower is more than 99% in agreement with the equation available from the literature (equation (4.28)).

The following are the main conclusions of the combined cooling analysis of the ORC power plant studied:

- The main parameter affecting optimum operations of binary power plants is turbine inlet pressure.
- Optimum reinjection temperatures for proposed Olkaria I binary units is 100°C based on energy and mass balance equations.

- SI, a function of exergy, was applied in the exergoeconomic analysis of geothermal power plant designs.

- R600 and isobutane have the lowest cost of products at 18.3 $/GJ for wet-system while isobutane is the least for dry-cooling at 20.87 $/GJ.

- Exergoeconomic factor, f compares the power plants' investment cost rate and the exergy destruction cost associated costs. Lower f translates to a high-cost rate of exergy destruction in a system and will be costly to operate or improve the efficiency. Wet cooling has lower values of f between 39.28% and 47.47% compared to dry cooling at 89.21% and 92.11%.

- The sustainability index (SI) cost rate is lower than the investment cost but higher than the exergy destruction rate. SI cost rates for the two systems range from 49.12 to 102.3 $/hr are lower than the corresponding capital investment rates of between 90.9 and 135.5 $/hr.

Based on the energy and exergy concept, the most suitable plant is a water-cooled type for isobutane and R600a that can generate 2,590 kWe and 2,594 kWe net work, respectively, while R600a is the suitable fluid for air-cooled binary plant generating 2,469 kWe net work with 59.37% utilisation efficiency and 1.612 SI. Cooling tower exergoeconomic estimated from the cooling systems' mass flow rate of cooling water.

The results of these two models and the proposed energy, exergy, and exergoeconomic analysis will be beneficial. The proposed method will be applicable in the complete exergy and economic analysis of geothermal power plants. SI can classify geothermal resources worldwide as the variation is minimal, unlike inefficiencies or generated net power. The variable metric optimisation method is robust for locating the global minimum by positive definiteness.

The cooling system is influenced by the ambient temperatures on the heat rejection capacity. The heat capacities are estimated to be 20,806-20,610 kW for isobutene, 24,153-23,928 kW for isobutane, 13,727-13,595 kW for cis-2-butene and, 16,772-16611 kW for n-butane for ambient temperatures between 0ºC and 40ºC. Application of air-cooled units would be advisable where water is scarce and in colder regions because of the huge heat capacity requirements and the area of heat exchangers. Dry cooling can eliminate heat without damaging the outside environment (no direct contact with ambient) since makeup water is not required. Environmental contaminants related to wet-cooling are eliminated by using air-cooled condensers. Dry-cooling can also be an option in regions where the plume is not allowed in

restricted and protected areas. Thermo-economic concept concluded that the complete exergoeconomic of power plants presents a better investment decision.

4.12.2 Optimisation of proposed binary at Olkaria II geothermal power plant

4.12.2.1 Combined pinch point analysis and exergy

Optimum utilisation of geothermal brine from Olkari II SF power plant for an ORC unit depends on many parameters. The main parameters are; turbine inlet pressure, efficiencies, maximum power generated, reinjection temperature of geothermal fluid, sustainability index, pinch point, and total exergy destroyed. Most studies have been on optimisation based on other parameters by applying a fixed pinch point for different working fluids, cases not supported by graphical representation by heat transfer diagrams, and energy and mass balance equations. Combining pinch point analysis and exergy optimisation of binary power plants is worthwhile. The results show that the optimum and practical pinch point is 8°C for reinjection temperatures above 80°C.

Exergy efficiency and net power generated plots identify the optimum pressure. Turbine inlet pressure affects the efficiencies, net power generated, and reinjection temperatures. Working fluid selection is a multi-criteria process depending on the objective function and the cycle configurations. For the six working fluids investigated, based on reinjection temperatures and exergy efficiency, a suitable fluid would be trans-2-butene.

The ORC cycle has higher net output power compared to regenerative. The first and second laws efficiencies correspond to the simple ORC with a preheater. Selection of the suitable fluid is a multi-objective criterion; it can be based on pinch point difference, exergy efficiency, and reinjection temperature.

According to the optimum design conditions at fixed condenser temperature, a simple ORC cycle had the highest net power output. The optimum pressures for the simple ORC are less than 2,000 kPa, whereas, for the regenerative cycle, they are about 3,000 kPa. The analysis showed that for unlimited reinjection temperatures, basic ORC is suitable. The regenerative cycle would be best applied where brine's geochemistry constraints reinjection temperature. Pinch points in heat exchangers affect efficiencies/effectiveness, net power output, reinjection, heat transfer rates, and working fluid flow rates.

4.12.2.2 Energy and exergy analysis in relation to sustainability index

The ORC power plant proposed in Olkaria II geothermal power plant in Kenya was analysed by energy, exergy, and sustainability index for eight different working fluids. The

working fluid selection for ORC is multi-objective and multivariable. Heat exchangers contribute to the highest exergy destruction of approximately 60% due to lower heat transfer rates at low temperatures. Exergy destruction is always higher than the net power generated; for example, isobutane generates 6,791 kWe net work, and 7,562 kW exergy is destroyed. It indicates that in every system that generates work, there is positive exergy destruction. Higher turbine inlet pressure decreases entropy, thus reducing the energy in the system. Isentropic efficiency can also be defined as exergy efficiency as in the case of the turbine, 86%, and pumps, 76% on average. Correlating with the case of heat exchangers, the manufacturers can specify isentropic/exergy effectiveness values of between 72-79% in design for preheater and evaporator. A system with higher efficiency, sustainability index, and reinjection temperatures is the best model for implementation. SI variations are not much compared to efficiencies; thus, SI can classify power plants.

Trans-2-butene generates 5,792 kW with thermal, exergy, and second utilisation efficiencies of 11.67%, 29.41%, and 45.18%, respectively, with higher reinjection temperature at higher 99.14°C. The selection of the suitable model will depend on the objective function of the power plant designers. The most suitable working fluid for Olkaria II is trans-2-butene to convince *geochemists* of acceptable reinjection temperatures of 99.14°C and the least exergy destruction. For both the isobutane and R600a systems, operating conditions for maximum net output power are similar. High ratios of 19,685 kW exergy are reinjected exergy and net work as summarised in the Grassman exergy flow diagram.

4.12.3 Optimisation of Olkaria IV single flash by energy, exergy and exergoeconomic concepts

Olkaria IV single flash and a back pressure topping unit were analysed exergoeconomically. Using EES code to model and simulate the power plant equations using the Olkaria IV operating data shows that the topping unit has additional benefits. The units were optimised by varying the turbine inlet pressures with fixed condenser pressure of 8.5 kPa. The additional power using a backpressure turbine is 29,294 kWe. The economic analysis for power plants' 30 years' life cycle for a fuel cost of 1.3 $/GJ. The capital cost increases from 1.850E8 to 2.199E8 $ by adding a topping unit. The main reason for the increase is the additional cost of the backpressure turbine with the benefits of reducing the cost of products by 27 $/GJ. Exergy destruction was reduced with improved thermal and exergy efficiencies from 15 to 18% and 57 to 70%, respectively. Exergoeconomic analysis of power plants is essential for linking economic, energy, and exergy analysis. Even though there is an additional

investment cost for topping unit, the main advantage is the reduced cost of products and improved thermal efficiency by 3%.

Nomenclature

A	heat transfer area (m^2)
c	cost per exergy unit ($/kJ or $/GJ)
$\dot{C}$	cost rate ($/hr)
CRF	capital recovery factor (-)
$\dot{C}_D$	exergy destruction cost rate ($/hr)
c_f	unit cost of exergy ($/GJ)
c_{brine}	specific heat capacity of brine (kJ/K/kg)
e	specific exergy (kJ/kg)
f	exergoeconomic factor (-)
$\dot{E}_{available}$	available exergy entering the plant (kW)
$\dot{E}x$	exergy rate (kW)
$\dot{E}x_{in}$	exergy rate into the plant (kW)
$\dot{E}x_{out}$	exergy out of the system/component (kW)
G	mass flow rate of air in cooling tower (kg/s)
h	specific enthalpy (kJ/kg)
i	interest rate (%)
L	mass flow rate of cooling water (kg/s)
$\dot{m}$	mass flow rate (kg/s)
ORC	organic Rankine cycle
P	pressure (kPa)
P_{cr}	critical pressure (kPa)
$\dot{Q}$	heat transfer rate (kW)
R	universal gas constant (kJ/kmol K)
r_n	nominal escalation rate (%)
s	specific entropy (kJ/kg K)
SI	sustainability index (-)
$Sum_{Exd/EX|D}$	total exergy destruction (kW)
T	temperature ($^{\circ}$C or K)
T_{cr}	critical temperature ($^{\circ}$C)
T_{pp}	pinch point temperature ($^{\circ}$C)
U	heat transfer coefficient (Wm^{-2} K^{-1})
$\dot{W}_{gross}$	gross turbine power output (kW)
$\dot{W}_{net}$	net power output (kW)
Z	capital cost of component ($)
$\dot{Z}$	cost rate ($/hr)

Greek letters

Δ	change (-)
η_t	isentropic efficiency of the turbine (-)
η_{th}	thermal efficiency (-)
η_u	utilisation/exergy efficiency (-)

142

η_{u2}	second utilisation efficiency (-)
τ	annual plant operation (hours)
γ	maintenance factor (-)
ε	component exergy efficiency/effectiveness (-)

Subscripts

0	reference environment
CD	condenser
cr	critical
CT	cooling tower
DC	destruction condenser
EV	evaporator
f	fuel
gal	gallons
irr	irreversibility
O&M	operations and maintenance
P	pump
PH	pre-heater
T	turbine
W	work
Q	heat
w	water
wf	working fluid

CHAPTER FIVE

5.0 NUMERICAL METHODS: WELLBORE SIMULATION AND WELLBORE

RESERVOIR COUPLING OF OLKARIA DOMES GEOTHERMAL

RESERVOIR

5.1 Introduction

This chapter will link surface and sub-surface in Olkaria Domes using field data, wellbore simulation, and exergy analysis. Numerical methods are constructing and running models that resemble actual reservoir performance. Mathematical expressions and sub-surface features, like porosity and permeability, and other thermophysical parameters, are analysed to deliver reservoir fluids to the surface for optimisation via wellbore. The main equations applied are partial differential equations to solve, calibrate, and check reservoir performance with field data. The main representative parameters in geothermal energy are temperature and pressure. The wellbore simulator gives the two parameters for further interrogation in line with the research objectives. One of the objectives is to consider the coupling of the reservoir in Olkaria Domes with a wellbore simulator. The Olkaria Domes reservoir has been modelled and updated as part of the entire Olkaria prospect. Linking the surface and sub-surface by exergy concept is performed for Olkaria Domes. For sustainable development of geothermal resources in Kenya, it is vital to model a reservoir that would predict the actual field data. Wellbore simulator gives pressure and temperature results close to the actual field flowing data for some wells in Olkaria Domes. Chapter two of the thesis discussed some of the conceptual models for the Olkaria geothermal reservoir.

5.2 Reservoir simulation and well production

Reservoir engineering attempts to describe the geothermal environment in a porous and fractured rock formation likely to change over time due to geologically dynamic systems [7]. Reservoir modelling and simulation helps in refining the geometry, boundary conditions and rock properties [131], [216]. In exploring new geothermal fields and siting next appraisal or production wells, the reservoir should be understood to site new wells for drilling. Computer modelling has been remodelled as standard practice for geothermal field planning, development, and management [138]. Geothermal reservoir management is a work in progress and requires extensive monitoring during the entire development from exploration and exploitation to production; it is an essential part of geothermal development that contributes to the sustainable development of the fields.

5.3 Fluid flow equations

The most critical measurements are the temperature, pressure, and mass flow rates, made either in the wellbore or at the surface [82]. In geothermal fields, fluid withdrawal from reservoirs leads to pressure drop near production wells [216].

Computer modelling synthesizes conflicting opinions, interpretation, and extrapolation of data to set up a coherent and sensible conceptual model [138]. As shown in equation (5.1), Darcy's law yields fluid velocity for a medium with homogeneous permeability, k, absolute viscosity, μ, under pressure gradient dp/dx. Typical permeability for the geothermal reservoir is between 10-70 mD [7].

$$v = -\frac{K}{\mu}\frac{dP}{dx} \qquad (5.1)$$

Well deliverability plots show a linear relationship between bottom hole pressures and fluid production rates. Applying Darcy's law and continuity, the pressure distribution, P_r (MPa) in the reservoir can be applied n equation (5.2) to estimate its volume.

$$P_r = \frac{\mu\dot{V}_w}{2\pi KL_R}\ln r_{dw} \qquad (5.2)$$

$\dot{V}_w$ in equation (5.2) is the volumetric flow rate into the well at the well-reservoir interface, L_R is the reservoir thickness. Drawdown, the pressure difference between the far-field reservoir pressure and the well pressure is expressed in equation (5.3) as:

$$\Delta P = \frac{\mu\dot{V}_w}{2\pi KL_R}\ln\frac{r_R}{r_{wl}} \qquad (5.3)$$

Volumetric flow rate into the well is calculated using equation (5.4) [217];

$$\dot{V}_w = \frac{2\pi KL_R}{\mu\ln\dfrac{r_R}{r_{wl}}}\Delta P \qquad (5.4)$$

Geothermal reservoir performance deliverability enmeshes three phases viz. wellbore, inflow, and reservoir performances [218]. The wellbore transports fluid from reservoir to wellhead due to the pressure drop between the reservoir and feed zone [218]. The reservoir case is dynamic and will show/predict its performance with time [218]. These three characteristics will interact and affect production in the geothermal fields, thus influencing the power plant rated output.

The flow between reservoir and feed zone in geothermal fields is assigned laminar flows [218]. The well inflow production is directly proportional to drawback, known as productivity index (P.I) in equation (5.5).

$$P.I = \frac{\dot{m}}{P_R - P_{wf}}$$
(5.5)

Constant of probability, P.I. is the inverse of the slope of mass, flow rate, $\dot{m}$, graph versus the corresponding flowing pressure drop results [218]. Well productivity in TOUGH2 (well deliverability feature) assumes steady radial flow in wells, allowing fluid to flow against the downhole pressure. P.I. in TOUGH2 is calculated using equation (5.6).

$$P.I = \frac{2\pi K \Delta Z}{\ln\left(\frac{r_e}{r_{wl}}\right) + s + 0.5}$$
(5.6)

K-permeability (m^2), ΔZ -layer thickness (m), s-skin factor, r_e, element radius (m), r_{wl}, well radius (m).

Partial differential equations solved by finite-element simulate multiphase energy and mass transport in porous media and wellbore phenomena [129], [219].

Mass, energy, and momentum equations for steam, s, and water, w, are shown in equations (5.7) and (5.8), respectively [127], [130]:

$$-\frac{\partial(\overline{w}_s \rho_s)}{\partial x_i} + q_s + d_v = \frac{\partial(\emptyset S_s \rho_s)}{\partial t}$$
(5.7)

and

$$-\frac{\partial(\overline{w}_w \rho_w)}{\partial x_i} + q_w - d_w = \frac{\partial(\emptyset S_w \rho_w)}{\partial t}$$
(5.8)

where $\overline{w}$, is phase average velocity, ρ is average density, q is the source term, d_v is the rate of evaporation, $\emptyset$ is the porosity and S is saturation for $S_w + S_s = 1$. Conceptual reservoir modelling determines reservoir existence and its response to exploitation [220]. Geothermal reservoir modelling can be divided into free convection models under natural conditions before exploitation and models which examine exploitation. The models can further be subdivided into lumped or distributed parameter models where the governing equations are solved numerically [131]. Modelling the reservoir leads to predicting reservoir behaviour regarding exergetic development.

The mathematic model of the Olkaria field developed a descriptive model [131]. With the availability of data from the areas (well tests and flowing data sets), models should incorporate

fluid source, transport mechanisms (conductive and convective), heating process in the deep sections, fluid dispersion into chargeable aquifers, reservoir cooling effects due to reinjection and impermeable boundaries.

5.4   Geothermal wellbore simulation.

Wellbore profile is mainly a hydrostatic pressure integral from the well bottom to the wellhead. Models have been developed for temperature-pressure profile for a given mass flow rate (both steam and brine), well diameter(s) and depths(s), pipe roughness, and wellhead pressure [221]. The wellbore model is a good indication of the flowing profile of geothermal well/fields, which is difficult to measure in most cases. The model would best be coupled to the reservoir using TOUGH2. It is improved to include the frictional pressure drop and velocity pressure gradient. Analysis of well discharge can be done using the Lip pressure method or separator method [222], [223]. Mubarok et al., (2015) showed 95% accuracy of the Lip pressure method compared to the separator method. The Lip pressure method application for the Olkaria Domes field has been recorded and well documented for most wells at different pipe diameters. In the Olkaria field, KENGEN uses the Lip pressure method during well tests to measure the steam and brine flow rates. The flow rates are the main input parameters in the wellbore simulator. Two main equations applied in calculating brine discharge during geothermal well discharge are Russel James and Hiriart Equations and have been compared by statistical method in previous studies [224]–[227].

Injectivity Index has been compared with well output obtained during flow testing to be applied for future drilling [228]. Reservoir conditions that include enthalpy are considered to predict the steam flow rates based on the Injectivity Index [228]. The Injectivity Index method for predicting future wells has a probable potential to link the sub-surface to the surface in addition to exergy, temperature, and pressure profiles. Geothermal wells are mainly of two types: vertical or directional wells, as shown in Figure 5.1. Directional wells are more productive than vertical wells because of the increased potential to encounter permeable zones.

Integrating Darcy's law estimated average reservoir and wellbore viscosities using Gwell and SwelFlo [229]. In simulating geothermal production well, McGuinness, （2014）showed that change in viscosity in the wellbore indicates the feed point. The difference is large in the case of two-phase flow [229]. The trapezoidal rule calculates average viscosities. McGuinness (2014) developed the model SwelFlo, which allowed steady-state simulation for two-phase flow and non-condensable gases for a productivity index of 10^{-12} m^3 using a generic well of

2,000 m depth, cased at 900 m and the reservoir pressure of 14,000 kPa and enthalpy of 1,200 kJ/kg. In geothermal energy flow in a wellbore, heat transfer should be considered within the wellbore, for there exists temperature and pressure gradient.
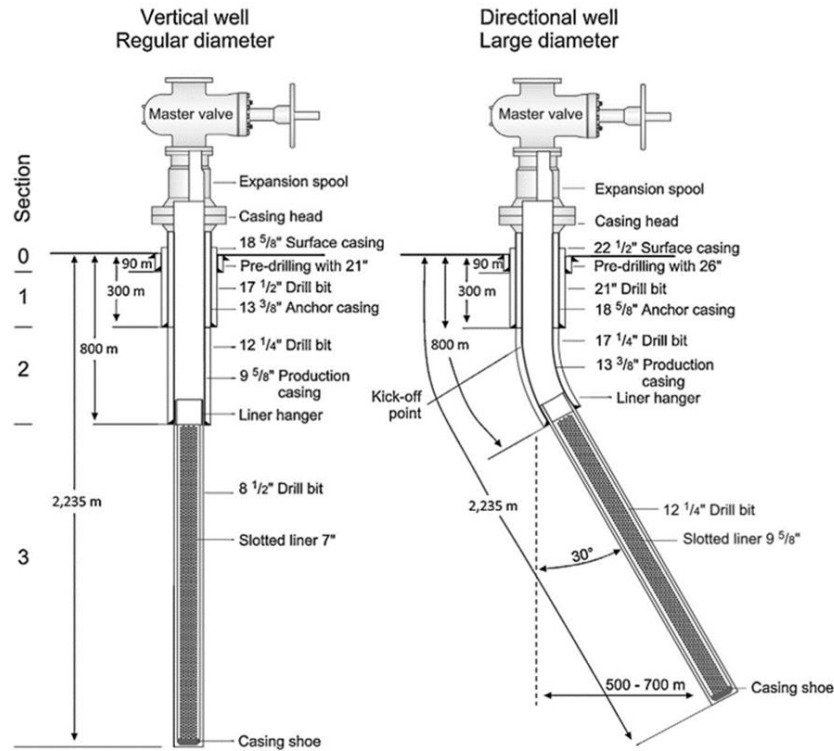
Figure 5.1: Figures of the two types of geothermal wells. Usually directional well has a larger diameter [228].

Wellbore flows and modelling affect isotherm plots constructed using temperature log data in geothermal field simulation to obtain reliable results [138], [230]. Simulation of the flow in geothermal fields is the first step in coupling a reservoir with well-flowing data. In wellbore temperature calculations, the assumption ignores heat losses between the wellhead and downhole conditions [231].

Flashing in the wellbore is the driving force that uplifts the geothermal fluid due to expansion and reduction in hydrostatic pressure [231]. Wellbore simulation is applied in matching the available down-log data sets. The downhole measurements are analysed before matching the analysis of the measured parameters and simulated estimates (temperature and pressure). The wellbore is a unifying feature for geothermal reservoir analysis [10]. The vital parameter governing wellbore flow in geothermal wells is the reservoir temperature [232].
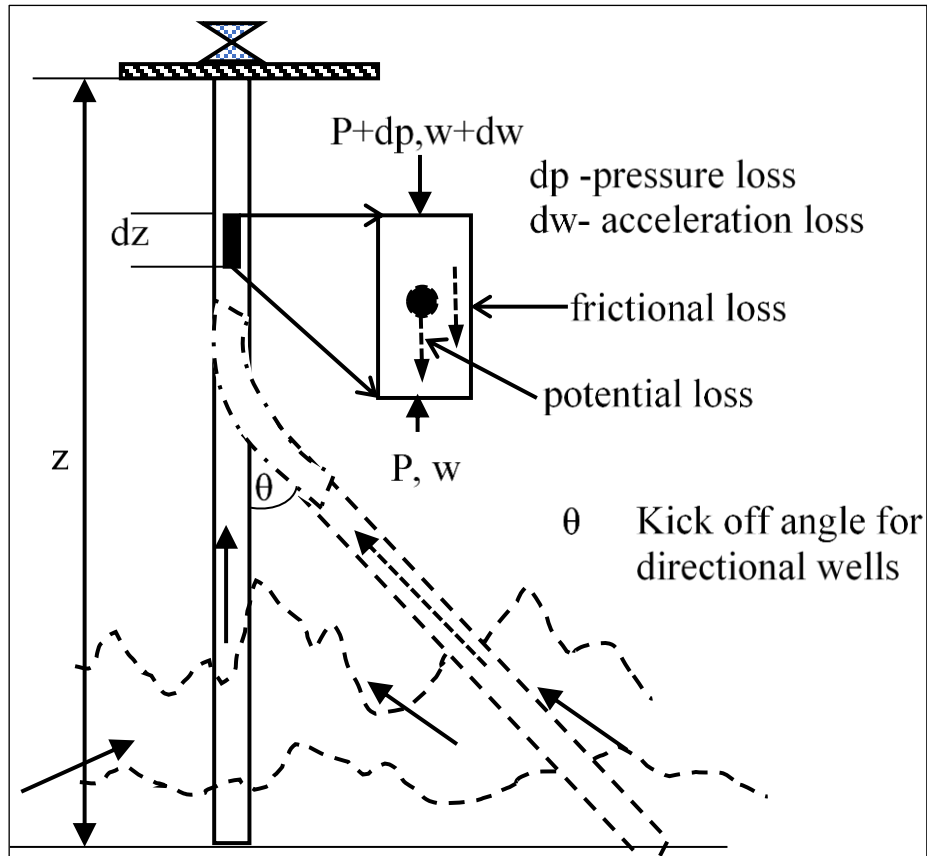
Figure 5.2: Basic wellbore model showing fluid flow from the reservoir up to wellhead [87].

Figure 5.2 shows a simplified mathematical model of a typical geothermal well.
The mass, momentum and energy equations (5.9), (5.10), and (5.11), respectively, are the main foundational equations applied in wellbore analysis [87].

$$w = \frac{\dot{m}v}{A} \tag{5.9}$$

$$dp + \frac{dw^2}{2v} + \frac{\lambda w^2}{2Dv}dz + gdz = 0 \tag{5.10}$$

$$di + \frac{dw^2}{2} + gdz = dq \tag{5.11}$$

where A is the well cross-sectional area (m^2), $\dot{m}$ is the geothermal fluid flow rate (kg/s), D is the wellbore diameter (m), z is the well true vertical depth (m), p is the pressure in (Pa), w is the velocity (m/s), v is the specific volume ($\frac{m^3}{kg}$), λ is the frictional factor (-), i is the specific enthalpy (J/kg) and q is the heat energy (J/kg).

For momentum balance, the average velocities, $\bar{w}$ (m/s), for multiphase is given by equations (5.12) and (5.13) for steam and water, respectively [127], [129], [219]:

149

$$\overline{w}_s = \frac{K_T k_s}{\mu_s \left(\frac{\partial p_s}{\partial x_j} - \rho_s g \right)} \tag{5.12}$$

and

$$\overline{w}_w = \frac{K_T k_w}{\mu_w \left(\frac{\partial p_w}{\partial x_j} - \rho_w g \right)} \tag{5.13}$$

where K_T (m^2) is the permeability tensor.

Combining equations (5.7) with (5.12) and (5.8) with (5.13) gives

$$-\frac{\partial}{\partial x_i} \left\{ \frac{K_T k_s \rho_s}{\mu_s} \left(\frac{\partial p_s}{\partial x_j} - \rho_s g \right) \right\} + q_s + d_v = \frac{\partial (\emptyset S_s \rho_s)}{\partial t} \tag{5.14}$$

and

$$-\frac{\partial}{\partial x_i} \left\{ \frac{K_T k_w \rho_w}{\mu_w} \left(\frac{\partial p_w}{\partial x_j} - \rho_w g \right) \right\} + q_w - d_v = \frac{\partial (\emptyset S_w \rho_w)}{\partial t} \tag{5.15}$$

For the flow in a porous medium and two-phases the, the phase pressure difference give rise to capillary pressure, P_c, expressed as:

$$P_c = P_s - P_w \tag{5.16}$$

The effect of P_c (equation (5.16)) in the geothermal reservoir is to lower the vapour-pressure curve [233]. In Mercer et al., (1974), the mathematical model did not consider capillary pressure. The details and importance of capillary pressure in geothermal reservoirs need to be investigated further. For a mixture and average density, ρ, is given in equation (5.17), and neglecting the effect of capillary pressure, equations (5.14) and (5.15) yields equation (5.18):

$$\rho = \rho_s S_s + \rho_w S_w \tag{5.17}$$

$$\frac{\partial}{\partial x_i} \left\{ \frac{K_T k_w \rho_w}{\mu_w} \left(\frac{\partial p}{\partial x_j} - \rho_w g \right) \right\} + \frac{\partial}{\partial x_i} \left\{ \frac{K_T k_s \rho_s}{\mu_s} \left(\frac{\partial p}{\partial x_j} - \rho_s g \right) \right\} + q_w + q_s = \frac{\partial (\emptyset \rho)}{\partial t} \tag{5.18}$$

Thermal equilibrium is assumed to be instantaneous. The specific volume, ν in equation (5.19) is a function of the void fraction, α, equation (5.20), as per Smith's formula [234]. The void fraction in geothermal fluid flow varies. A comparison of 52 void fraction correlations showed 18 void correlations performed satisfactorily [235].

$$\nu = \frac{1}{\alpha \, \rho_s + (1 - \alpha) \rho_s} \tag{5.19}$$

The simulation of directional wells approximates the cosine value of the angle between the wellbore axis and the vertical direction from the kick-off point [230].

$$\alpha = \left\{ 1 + \rho_s/\rho_l \, (1-x)/x \left[0.4 + 0.6 \left(\frac{\frac{\rho_l}{\rho_s} + 0.4\left(\frac{1}{x}-1\right)}{1 + 0.4\left(\frac{1}{x}-1\right)} \right)^{0.5} \right] \right\}^{-1} \tag{5.20}$$

For steady-state analysis, simulation and measurements boiling point for depth curve and conductive heat flux as a function of thermal conductivity is considered as shown in equation (5.21) [10].

$$\dot{q}_{(z)} = \lambda(P_s, T_s)\left(\frac{dT}{dz}\right) \tag{5.21}$$

5.5 Olkaria Domes geothermal field

Geothermal resources in Kenya are estimated to be water-dominated with high enthalpy. Sub-surface geology has classified the litho-stratigraphic units of the Olkaria Geothermal area into six distinct groups [67]. Pyroclastic and commendites are predominant within this minor interbed of trachyte and basalt [67]. Olkaria volcanic formation underlain by Olkaria basalt. Basaltic lavas are predominant with alternating thin tuffs, minor trachyte, and sporadic rhyolites. The formation intersected by wells at a depth between 1,900 and 2,500 m forming the caprock [67]. Volcanic centres and volcanic plugs are dominant features of volcanism associated with the geothermal systems. Prime geothermal systems are associated with volcanism, the main feature in Olkaria [236].

Olkaria geothermal systems are fracture-dominated with the flow paths controlled by N-S, NW-SE and NE-SW trending faults [237]. Structures in the Greater Olkaria geothermal complex include; the ring structure, the Ol'njorowa gorge, the ENE-WSW Olkaria fault [238]. The rhyolitic domes forming a ring structure are associated with major fractures and magmatic activity [82].

Extrusion of the lava domes, which were of comendite composition, in the Olkaria Volcanic Complex was preceded by the extrusion of pyroclastic. The Olkaria Volcanic Complex constitutes a portion of the central Kenya peralkaline province, which agrees with the Kenya Dome. A significant portion of the pumice fall and pyroclastic deposits have originated from Longonot and Suswa volcanoes [67]. The faults are more prominent in the East, Northeast and

West Olkaria fields but are scarce in the Olkaria Domes area, possibly due to the thick pyroclastic cover. The NW-SE and WNW-ESE faults are the oldest and are associated with the rift development. The most prominent of these faults is the Gorge Farm fault, which bounds the geothermal fields in the North-Eastern part and extends to the Domes area [238]. In Domes field, inner and outer ring structures connect to the Gorge Farm fault, located North and East of the main production area, possibly extending north to Lake Naivasha. Recharge flows into the Olkaria system through the N-S fault system along the Ololbutot fault, associated with geothermal surface manifestations [237].
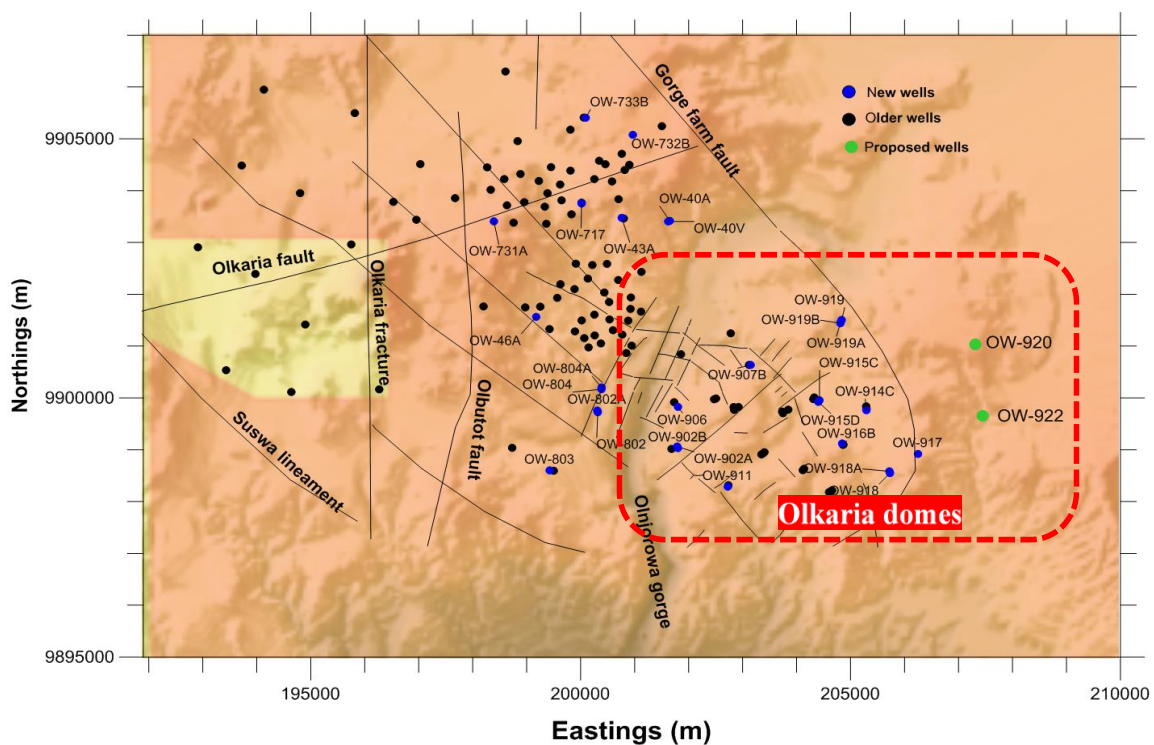
Figure 5.3: Drilled geothermal wells in Olkaria modified from [135].

Figure 5.3 shows the old, new, and proposed wells as of 2017. Most of the new wells are targeting the Domes. The region is one of the best reservoirs enclosed by the ring structure and Olnjorowa gorge [238], [239].

There were 180 (148 production and 32 injection) geothermal wells in Olkaria in 2020 [240]. Nyandigisi (2020) reported an 88% success rate of production wells, and wells on well pads 904 and 921 have the most productive wells, with OW 904 recording 363ºC. OW 921A is the most producing well, with an output of 24.7 MWe [240].

Table 5.1: Olkaria Domes well completion details. For wells 902A-921 the casing shoe assumptions is 956 m for directional wells and 950 m for vertical wells. Field data from KENGEN. The data for the wells in red colour was not available.

WELL NO	COMPLETION DATE	ELEVATION (M)	EASTINGS	NORTHINGS	DRILLED DEPTH (m)	CASING SHOE (m) 9 5/8"
OW-901	20/11/99	1,890.308	201,865.236	9,900,848.539	2,199.15	758.47
OW-902	13/2/99	2,201.00	201,668.860	9,898,995.020	2,201.00	648.28
OW-903	19/5/99	2,043.060	202,840.870	9,899,769.030	2,202.00	697.14
OW-904A	19-Aug-07	2,002.796	202,506.899	9,899,988.952	2,799.00	1,250.00
OW-903A	10-Nov-07	2,043.116	202,834.171	9,899,824.272	2,810.00	1,197.00
OW-905A	14-Jan-08	1,946.929	202,777.748	9,901,245.491	2,800.00	1,269.00
OW-905	--	-	-	-	3,000	940.5
OW-907A	27-May-08	1,972.087	203,113.003	9,900,635.792	2,581.00	1,250.00
OW-908	13-Aug-08	2,012.276	203,378.169	9,898,929.201	2,988.00	1,201.00
OW-909	21-Jan-09	2,086.995	204,138.056	9,898,631.681	3,000.00	1,205.00
OW-908A	26-Jan-09	2,011.982	203,348.999	9,898,911.173	3,000.00	950.00
OW-910A	28-Mar-09	1,985.718	203,847.998	9,899,774.438	2,882.00	956.00
OW-911A	26-May-09	1,978.307	202,736.133	9,898,315.193	3,007.00	951.00
OW-912	06-Aug-09	2,072.272	204,602.369	9,898,181.674	3,010.00	856.00
OW-913A	18-Oct-09	1,979.638	202,341.870	9,899,117.509	3,010.00	1,200.00
OW-909A	10-Dec-09	2,086.861	204,115.880	9,898,603.874	3,008.00	903.00
OW-904	20-Dec-09	1,987.663	202,481.750	9,900,131.597	3,000.00	1,204.00
OW-914	13-Feb-10	2,008.005	205,290.775	9,899,836.945	3,000.00	952.00
OW-910	07-Feb-10	1,993.757	203,733.158	9,899,737.594	3,000.00	950.00
OW-915A	10-Apr-10	1,979.342	204,327.366	9,900,010.083	2,960.00	1,020.00
OW-916	16-Apr-10	2,034.422	204,858.848	9,899,094.309	2,993.00	956.00
OW-912A	06-Jun-10	2,072.298	204,634.343	9,898,198.266	2,989.70	856.00
OW-914A	11-Aug-10	2,009.271	205,292.590	9,899,792.620	3,000.00	858.53
OW-916A	12-Oct-10	2,034.438	204,879.244	9,899,063.804	3,000.00	956.72
OW-915	31-Oct-10	1979.385	204,308.619	9,899,978.964	3,010.00	808.00
OW-902A	-	1,953.873	201,788.014	9,899,062.377	3,000.00	956.00
OW-906	-	1,974.820	201,802.580	9,899,827.439	2,000.00	956.00
OW-911	-	1,979.519	202,725.670	9,898,287.453	3,000.00	956.00
OW-917	-	2,108.498	206,249.243	9,898,918.512	3,000.00	956.00
OW-918	-	2,078.257	205,730.345	9,898,550.277	3,000.00	956.00
OW-918A	-	2,078.558	205,718.911	9,898,584.633	3,000.00	956.00
OW-919	-	1,983.915	204,834.468	9,901,506.620	3,000.00	956.00
OW 919C	-	1,984.134	204,778.127	9,901,372.940	3,000.00	956.00
OW 921	-	1,944.606	202,691.708	9,900,772.225	3,000.00	956.00
OW 921A	-	1,944.406	202,656.004	9,900,766.260	3,000.00	956.00

Table 5.1 shows drilled wells in Olkaria Domes considered in wellbore reservoir coupling. The specific wells supplying steam to the Olkaria IV power plant are shown in the appendix.
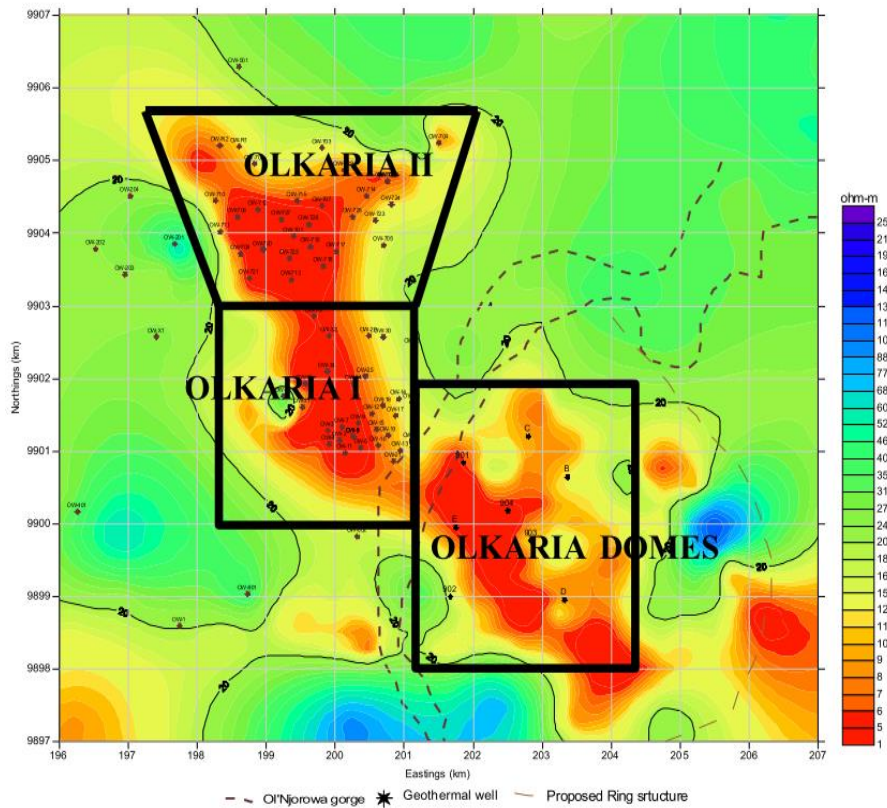
Figure 5.4: Geophysical anomaly of potential resource areas for Olkaria East, North East and Domes [241].

Figure 5.4 shows the geophysical anomaly of the Olkaria geothermal complex, including the Domes area. Two potential reservoirs are seen in the central location and the Southeast part. Down-hole temperature profiles indicate a high-temperature field shown in $200 - 360$ºC shown in Figure 5.5.
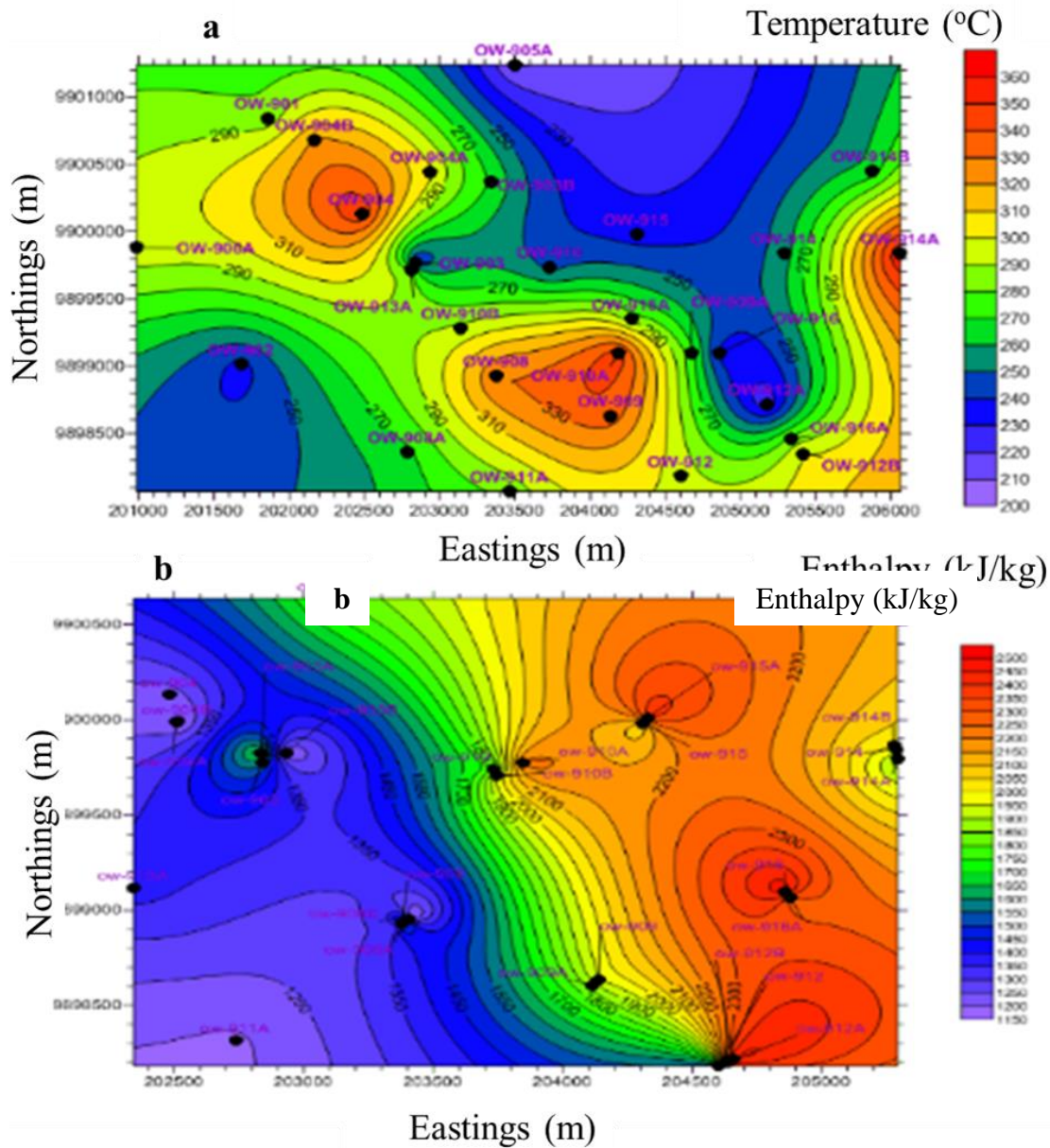
Figure 5.5: Olkaria Domes field (a) temperature contour maps in Olkaria Domes field and (b) enthalpy contour maps in Olkaria Domes wells at -500 m.a.s.l with the wells and the power plants locations [135].

Rop et al., (2018) updated the numerical model of the Olkaria geothermal system using Petrasim (pre-processor and post-processor for TOUGH 2) (Figure 5.6). The latest models of Olkaria use temperature and pressure profiles to guide decision-making.

Model area	30 X 23 km
Model depth	4 km
Number of blocks	112288
Number of connections	328548
Minimum block area	200 m X 200 m
Minimum layer thickness	200 m
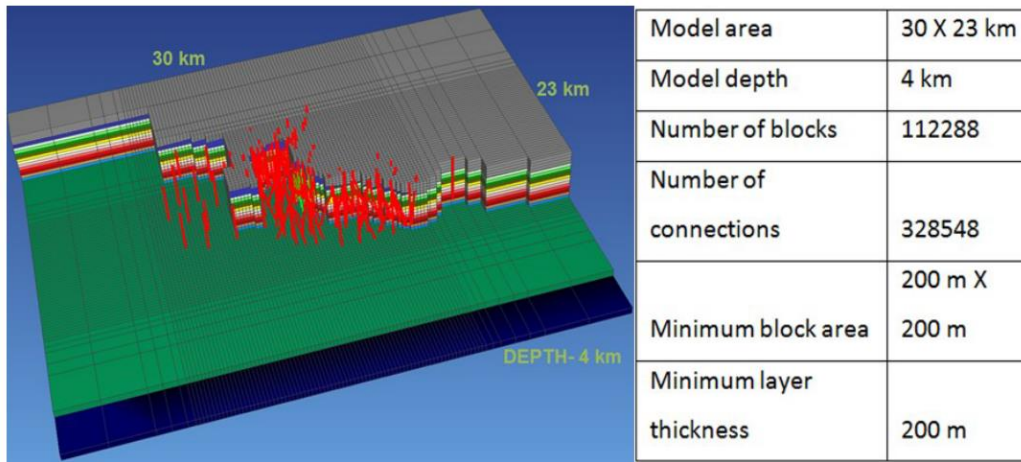
Figure 5.6: Numerical model for Olkaria geothermal field measuring 30×23×4 km [83].

Rop et al., (2018) described the past numerical and conceptual models (e.g. Mannvit/Isor/Vatnaskil/Verkis (2011) and Saitet et al., (2016) for the entire Olkaria system between 1987 and 2004 [237], [238], [242]. Figure 5.7 shows the results of the numerical model in Figure 5.6. Mapped plan view at -500 m.a.s.l shows each field associated upflow zones. The Domes field has a major upflow zone and feed zones at depths of approximately 1,700-2,000 m below the surface (about 500-0 m.a.s.l) from the temperature profiles of OW-918A well [83]. The reservoir temperatures are high at 368°C.

Previous studies have not investigated the wellbore exergy profiles as a tool to connect reservoir and surface from simulated or calculated data log measurements in geothermal fields. Under sustainable development, the Olkaria Domes geothermal field needs optimisation by exergy and wellbore simulation. Table 5.1 shows wells' details for the Olkaria Domes field.

In this chapter, the wellhead to reservoir exergy profile was investigated. The objective is to carry out an exergy analysis of the geothermal field in Kenya. A wellbore simulator connects the surface and sub-surface by the exergy concept. Wellbore simulation is used to couple reservoir and wellhead by exergy profiling of water-dominated geothermal wells. The research links the geothermal sub-surface to the surface via exergy analysis. The exergy concept is used to plot the profiles of geothermal wells in a liquid-dominated and high enthalpy geothermal fluid. The obtained results were discussed and compared with literary sources for interpretation.
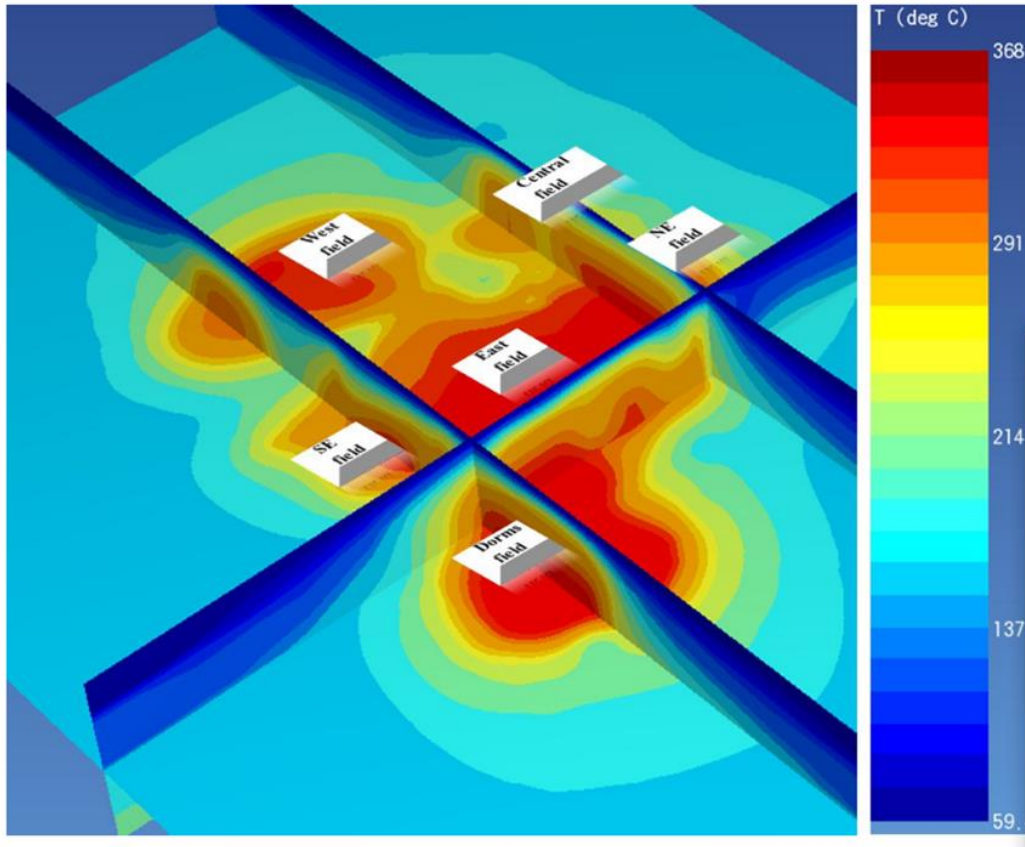
Figure 5.7: Results of the latest numerical model of Olkaria field system [83].

5.6 Results and discussion

The presented study projected the link between wellhead and reservoir by exergy profile. Feed zones, strata, and heat transfer type were predicted using a wellbore simulator for the well in Olkaria Domes. The research investigated liquid-dominated Olkaria Domes wells, OW-901, OW-902, OW-903, OW-904, OW-908, OW-909, OW-910, OW-914, OW-921, and OW-924. The wells considered are all vertical. The directional wells data are analysed to locate the trajectory profile of the actual drilling path.

Wellbore simulation profiles represent well-flowing data under steady-state conditions and can be used to couple reservoir and wellhead. Exergy profiles of geothermal wells predict some sub-surface behaviour of geothermal reservoirs. The estimated caprock depth of the sub-surface is in the hypothesis of the study. The well downhole recorded data identified feed zones and lateral flows. The depths of exergy losses and gain correspond to the inferred feed zones. In geothermal reservoirs, convective heat transfer is in the reservoir, while conductive heat transfer is from a hot rock.

Reservoir characteristics obtained after well simulation are shown in Table 5.2. For wellhead temperatures of between $148.6 - 207.9°C$, the reservoir temperatures from the wellbore

157

simulator are high at 296.8ºC in OW 916. The formation pressures simulated are between 1,077 to 12,487.9 kPa for wellhead pressure of 459 to 1,720 kPa. The temperature gradient was plotted for the well bottom and wellhead exergy profiles.

Table 5.2: Results of simulated temperature and pressure of wells in Olkaria Domes.

Well	Wellhead			Steam	Water	Simulated	
	P (kPa)	T (ºC)	Enthalpy (kJ/kg)	flow rate (t/hr)		Bottom T (ºC)	Formation P (kPa)
OW-901	735	166.93	1630.52	16.40	20.10	218.1	2,237.2
OW-902	618	160	1050.9	9.20	41.8	244	1,077.8
OW-903	459	148.6	1001.5	14.6	67.8	233.8	1,163.9
OW-903A	1,120	184		52	39	250	3,978
OW-904	1,300	191.6	1,284.4	28.60	91.40	290.3	12,487.9
OW-904B	1,040	182		32.7	43.9	250	3,946
OW-905	1,070	182.8	1,728.5	14.42	15.89	268.44	5,372.7
OW-908	1,200	188		25.9	130	239	3,307
OW-909	1,290	191.3	1,923.1	78.8	61.2	279.9	6,405.9
OW-910	1,830	207.9	1,909.2	34.8	30.2	259.1	4, 625.5
OW-911	550	155.5	1,309.5	15.5	34.2	265.4	5,119
OW-912	1,260	190.2	1,867.09	23.2	20.1	241.2	3,417
OW-914	1,720	205		39	80	292	7,710
OW-915	16.3	202.3	1,894.3	40.1	34.9	261.0	4,772
OW-916	1,030	181.2	1,886.0	100.2	79.9	296.8	8,211.3
OW-921	1,184	187.36	1,698.20	48.7	58.5	267.52	5,295.1
OW-924	1,174	187		12.6	31.4	285	6,900

For OW-901, OW-902, OW-903, OW-921, OW-911 wells, the simulated profile was from the discharge data using a 4-inch Lip pipe and 6-inch Lip pipe for Olkaria well OW-905 discharge parameters. The wellbore simulator could not handle 4-inch Lip pipe discharge data for well OW-905. The wellbore simulator simulated downhole pressure and temperature logs for liquid dominated wells. It could not simulate wells with high steam ratios, such as OW-905.

OW-915 total flow rate of 75 t/hr for input data for simulation. The simulated thermodynamic parameters for OW-916 in Table 5.2 were from discharge data using an 8-inch Lip pipe and obtained results from the simulation deliver the highest bottom hole temperature of 296.8ºC. Field data during production in other wells are the main input parameters. The EES code used P, T from the wellbore simulator to calculate specific exergy and enthalpy. These thermophysical parameters form the base to link exergy and wellbore for Olkaria Domes field conceptual stage in surface-sub-surface connection. Nyandigisi (2020) reported that the best wells in Olkaria are OW-921, OW-904, OW-910, and OW-916. The measures of performance were temperature for OW-904 at 364ºC. Table 5.2 has a good match with earlier results where

158

OW-904 recorded 12,488 kPa formation pressure, and OW-916 recorded a high temperature of 297°C [238], [240], [242].

In the case of boiling curve exergy, the exergy profile is like the temperature profile for the hydrostatic pressure below the surface, as shown in Figure 5.8.
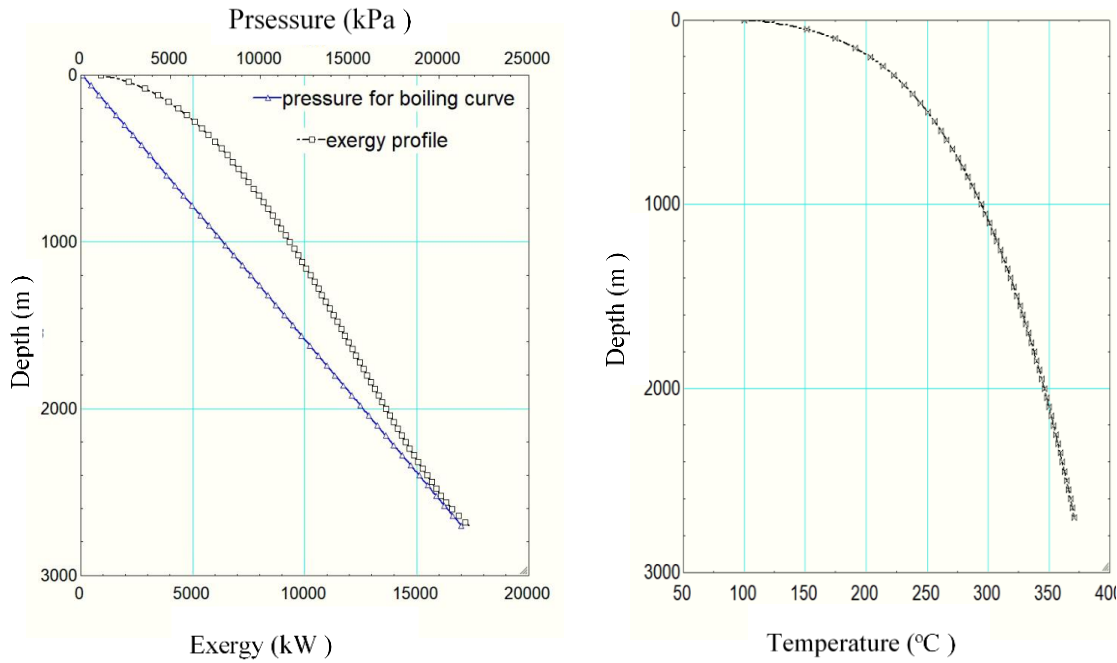
Figure 5.8: Exergy profile vs. depth, depth in m for the boiling curve saturated temperature and pressure simulated using EES code.

The maximum temperature reported in OW-901 is 342.3°C after 59 days of heating. Figure 5.9 shows that the simulated temperature is lower than the formation/reservoir at 218°C. The flowing temperature and pressure data (on 09.02. 2000 and 26.07.1999) for OW-901 shows a good match with the simulated results. The feed zones are predicted to be between 1,550 -1,000 m.a.s.l. The bottom hole temperature increased from 233 to 250°C.

The wellbore simulator is closely related to the flowing field data recorded for OW 901, as shown in Figure 5.9. Pressure and temperature flowing patterns have similar gradients with the wellbore simulator. The good match between flowing and simulated data approves the reliability of the wellbore simulator to couple reservoir and wellbore.

As in the case of T profiles, the flowing well data shows a good match to the wellbore simulated, with the good match being 1999 flowing data.
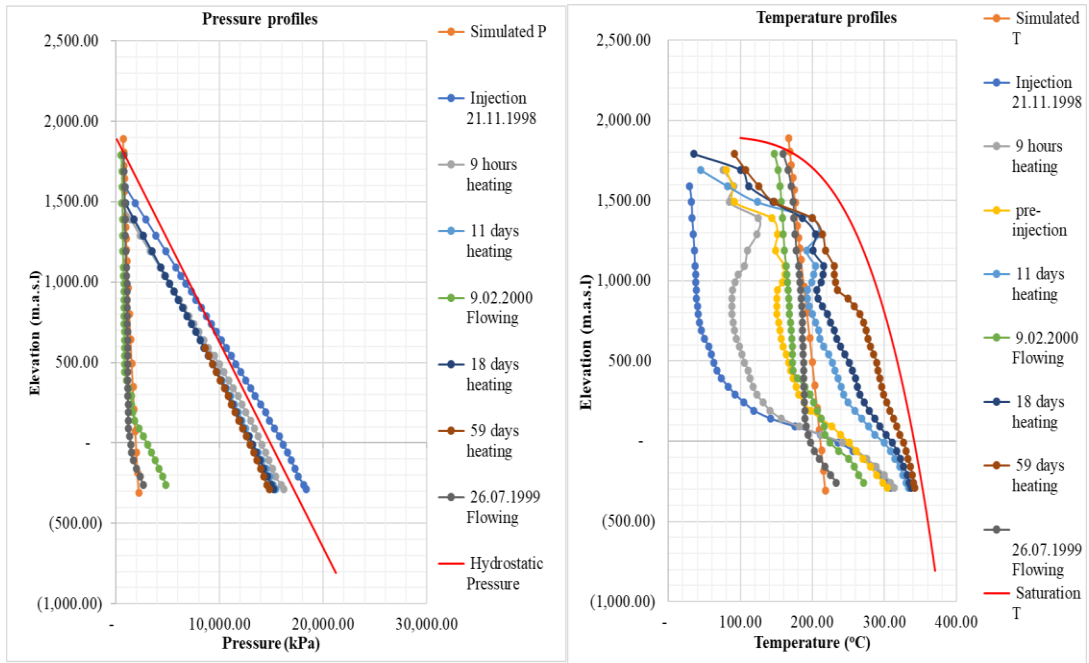
Figure 5.9: OW-901 pressure and temperature profiles vs.m.a.s.l.
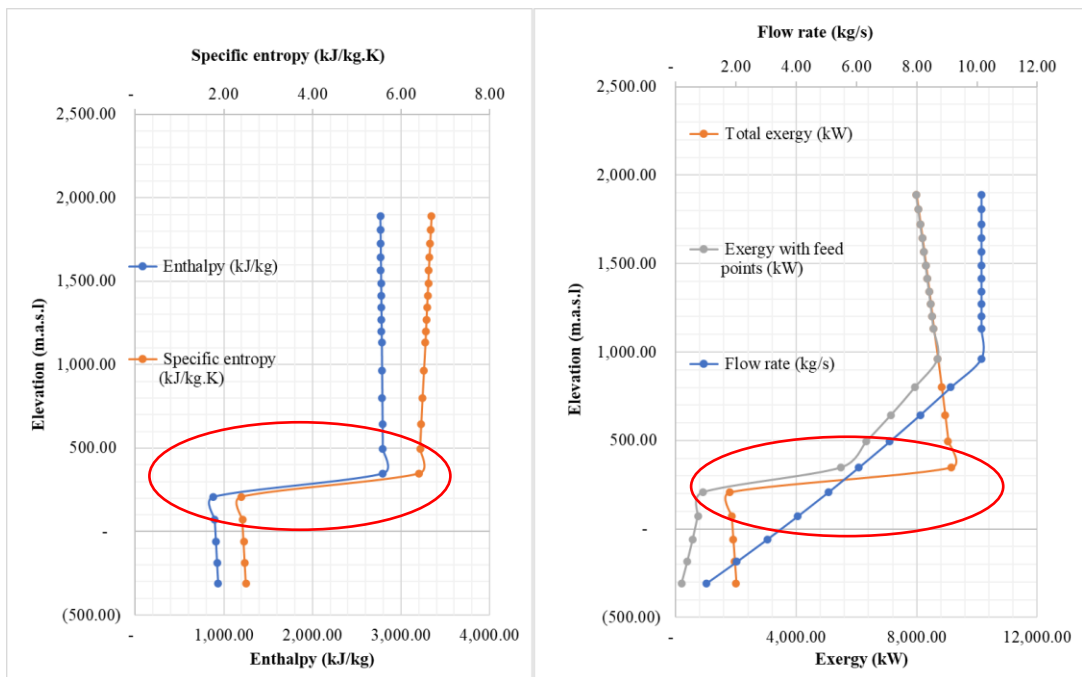
Figure 5.10: OW-901 exergy, enthalpy, and flow rate diagrams.

Figure 5.10 shows the exergy, enthalpy, and entropy profiles for OW-901. The exergy values at inferred reservoir location are at a minimum, and depths of around 250 m.a.s.l exergy increase then follow a steep gradient to the wellhead. Figure 5.10 was plotted for the exergy profiles with depth for optimum utilisation of the available exergy. The feed zone points

inferred below the casing shoe and exact locations are unclear. For the exergy profiles, the gradient is linear to depths beneath caprock. The caprock is predicted to levels where abrupt changes in exergy. The exergy changes correspond to the same depths for the enthalpy and entropy changes shown in Figure 5.10 for OW-901.
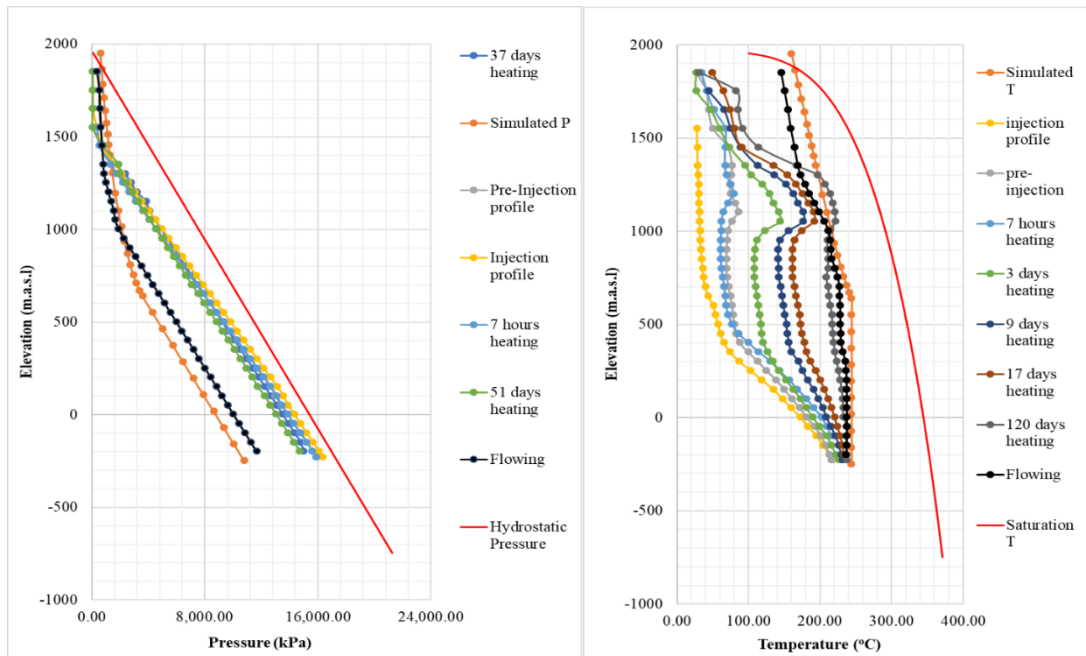
Figure 5.11: Pressure and temperature profiles during well tests, flowing and simulated using wellbore simulator for OW-902.

Figure 5.11 shows the OW-902 profiles with depth. The exciting part is that the flowing and simulated data have similar trends: the maximum formation pressure and temperature are almost identical. The simulated bottom hole pressure and temperature are 1,078 kPa and 244ºC, respectively.

Figure 5.12 shows OW-902 exergy and enthalpy profile and the flow rate relation to m.a.s.l. At depths of approximately 1400 m.a.s.l, the well shows exergy losses and gains.

For wells OW-901 and OW-902, the actual exergy assumes that the flow rate is uniform from well bottom to wellhead, which is not the case in all the wells. The exergy and flow rates diagrams (as a possible scenario) consider a multi-feed zone between the well bottom and production casing depth. In the plots for flow rates, the flow rate and exergy increase with depth, and actual and total exergy are the same at the production casing depth. Exergy insights are to couple the wellbore and reservoir because the data simulated are approximately close to actual flowing data, as seen in the cases of OW-902 and OW-901.

From the exergy profiles, with gain and losses with depth, wells OW-903A, OW-904B, OW-908 and OW-924 are used to conceptualise the sub-surface structure to interpret the likely scenario in the reservoir using specific exergy.
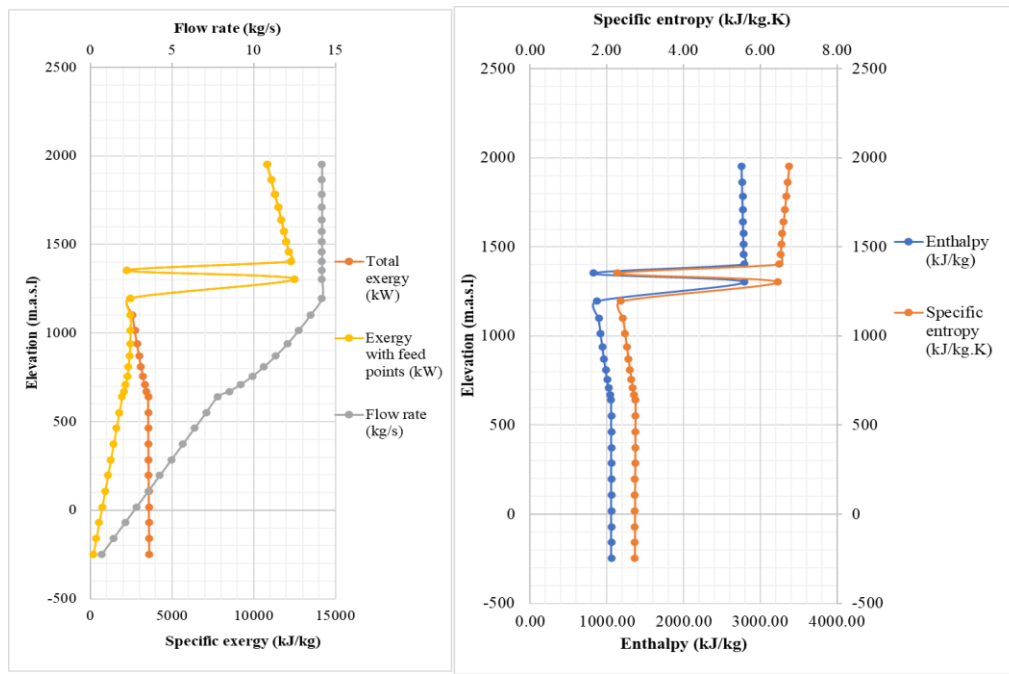
Figure 5.12: OW-902 exergy, enthalpy, and flow rate diagrams.

Figure 5.13 shows the well test completion tests for well OW-903A. The exergy profile of the well shows two distinct parts, the lower section of convective heat transfer and upper convective heat transfer above the caprock. At a depth of 1,000 m.a.s.l, the temperature reduces, and there is exergy gain. For the reservoir beneath OW-903A, the section with sharp exergy change is inferred to be the caprock layer.

Figure 5.14 shows the profile of well OW-904B. Exergy values vary between the wellhead and well bottom in the wellbore. The wellbore shows many feed zones and discontinuities of convective heat transfer. Three reservoir sections are predicted in sections below the caprock, at 0 m.a.s.l and -500 m.a.s.l. The many sections indicate that directional wells are more productive and have higher power output potential.
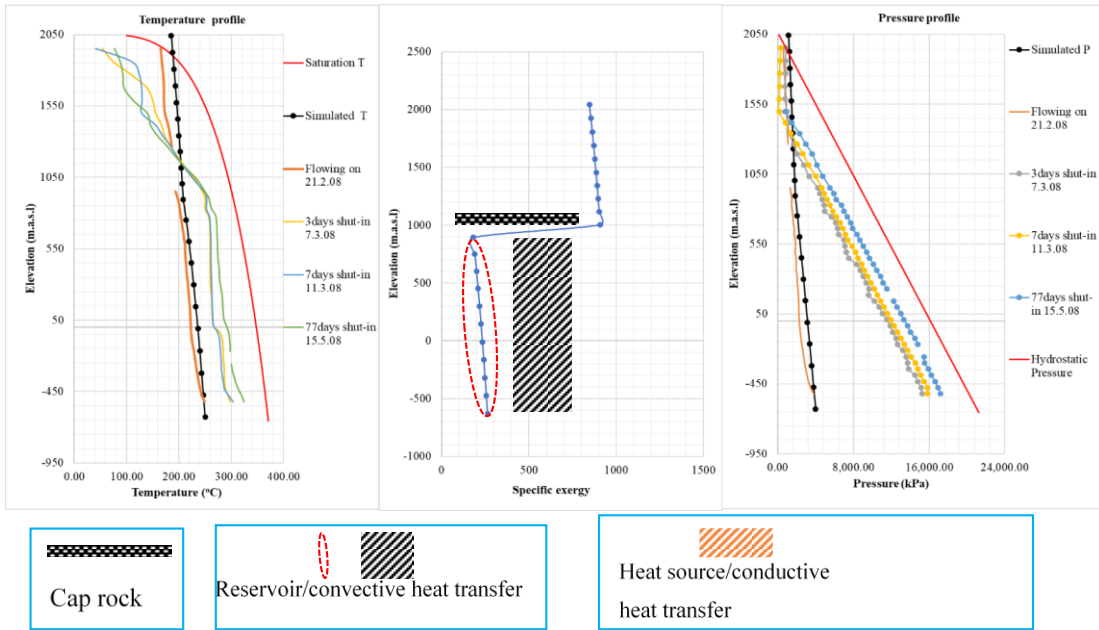
Figure 5.13: Well, OW-903A downhole pressure-temperature log profiles during well testing and simulated temperature, exergy, and pressure profiles.
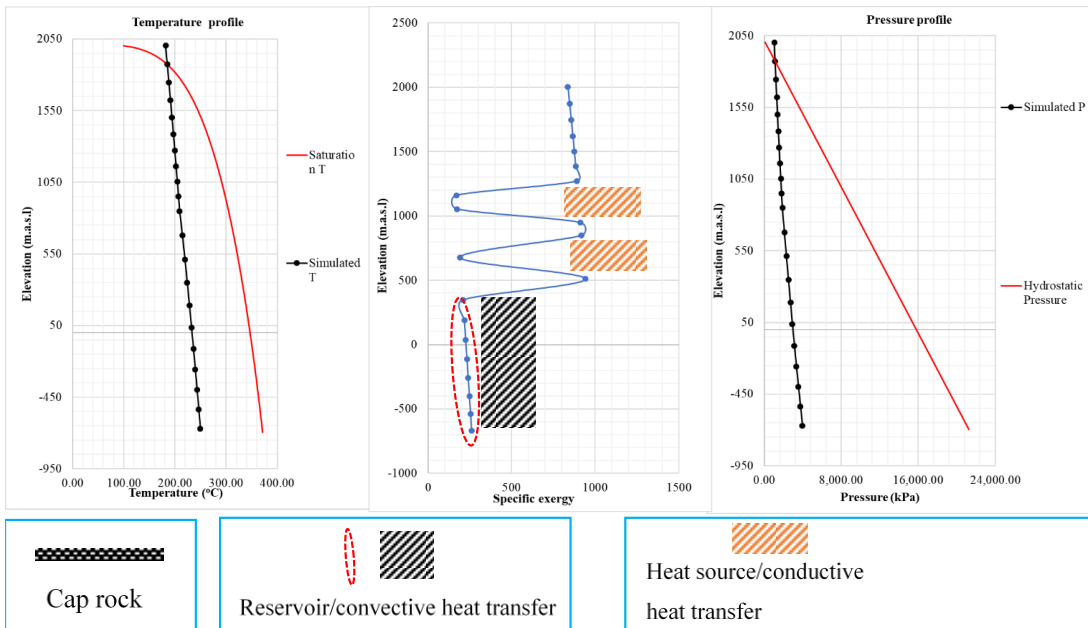
Figure 5.14: Well OW-904B simulated temperature, pressure and specific exergy profiles.

163
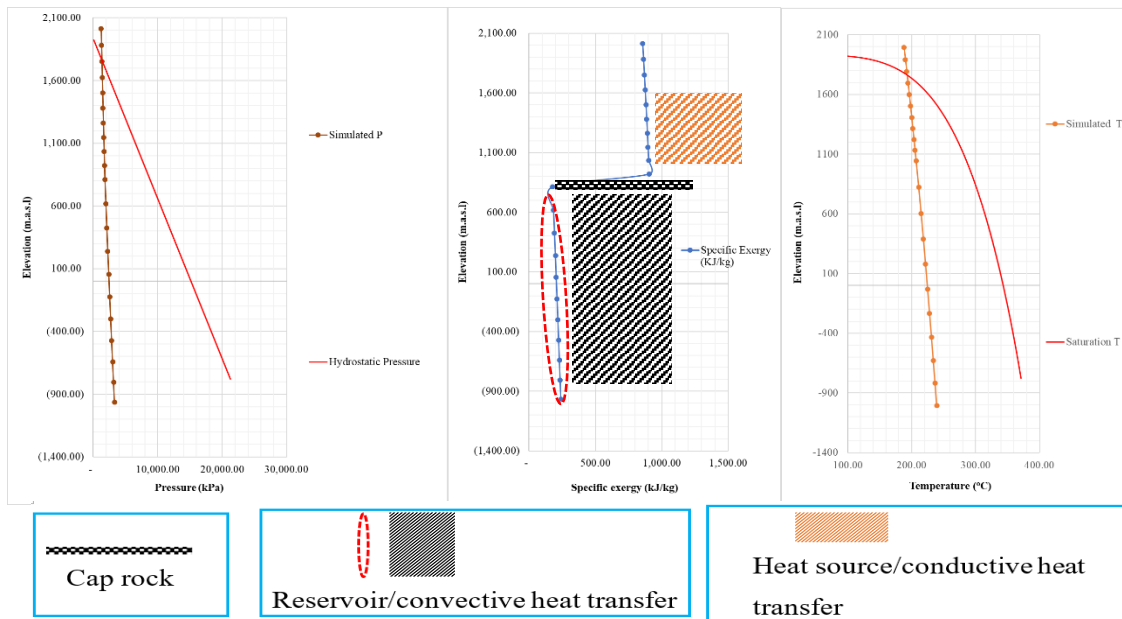
Figure 5.15: Pressure, exergy and temperature profiles of well OW-908.

Figure 5.15 shows that the location of caprock is at approximately 100 m.a.s.l in between two convective heat transfer sections. The formation pressure and temperature below OW-908 are 3,946 kPa and 250°C, respectively.
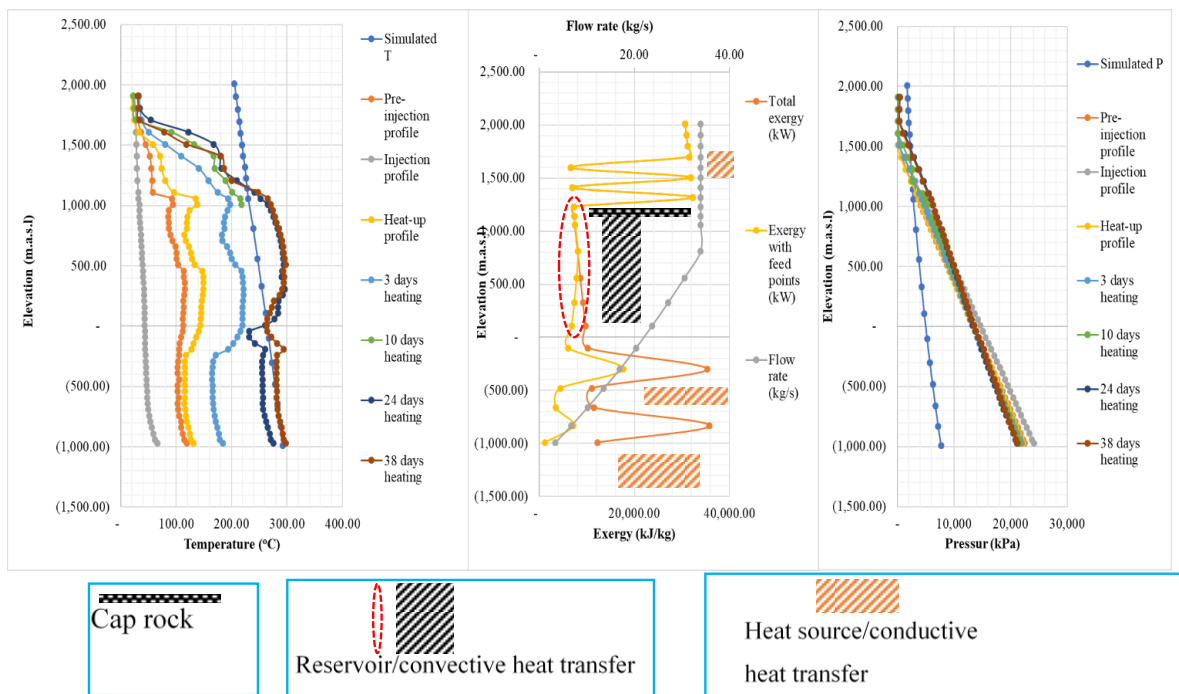
Figure 5.16: Well OW-914 well testing logs and simulated temperature, exergy, and pressure profiles.

Caprock

Reservoir/convective heat transfer

Heat source/conductive heat transfer
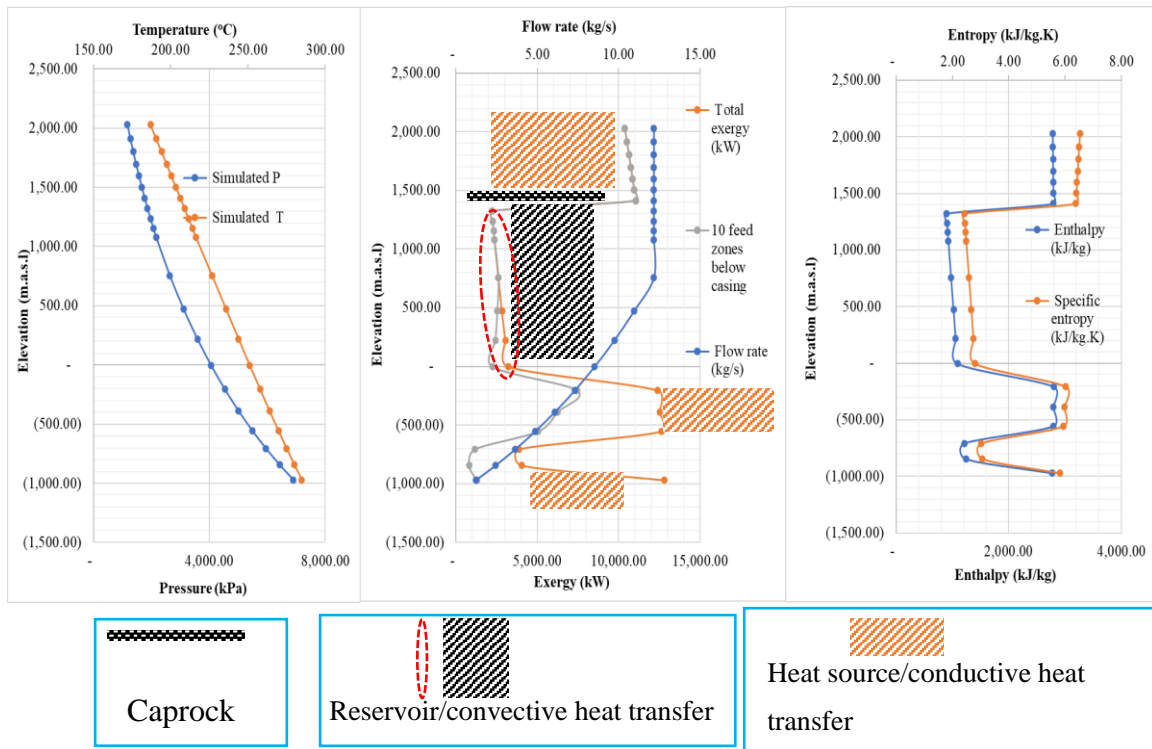
Figure 5.17:Well OW-924 wellbore simulated profiles for temperature, exergy, and pressure.

Figures 5.4 and 5.5 show well OW-914 surrounding is in a high temperature, low enthalpy, and low resistivity region. The exergy profile shown in Figure 5.16 has several exergy losses and gains locations. Well, OW-914 resource targets are at depth of 1,000-0 m.a.s.l. At the reservoir, the heat transfer is a convective type.

For well OW-924, no downhole data was available to locate the feed zones or heat transfer zones. Using exergy profile and lithology map for validation of hypothesis, they agree. The simulated exergy profiles show that the feeds zones are at different depths regions. The elevations 1,500-0 m.a.s.l is predicted to be the reservoir and convective heat transfer section from Figure 5.17.
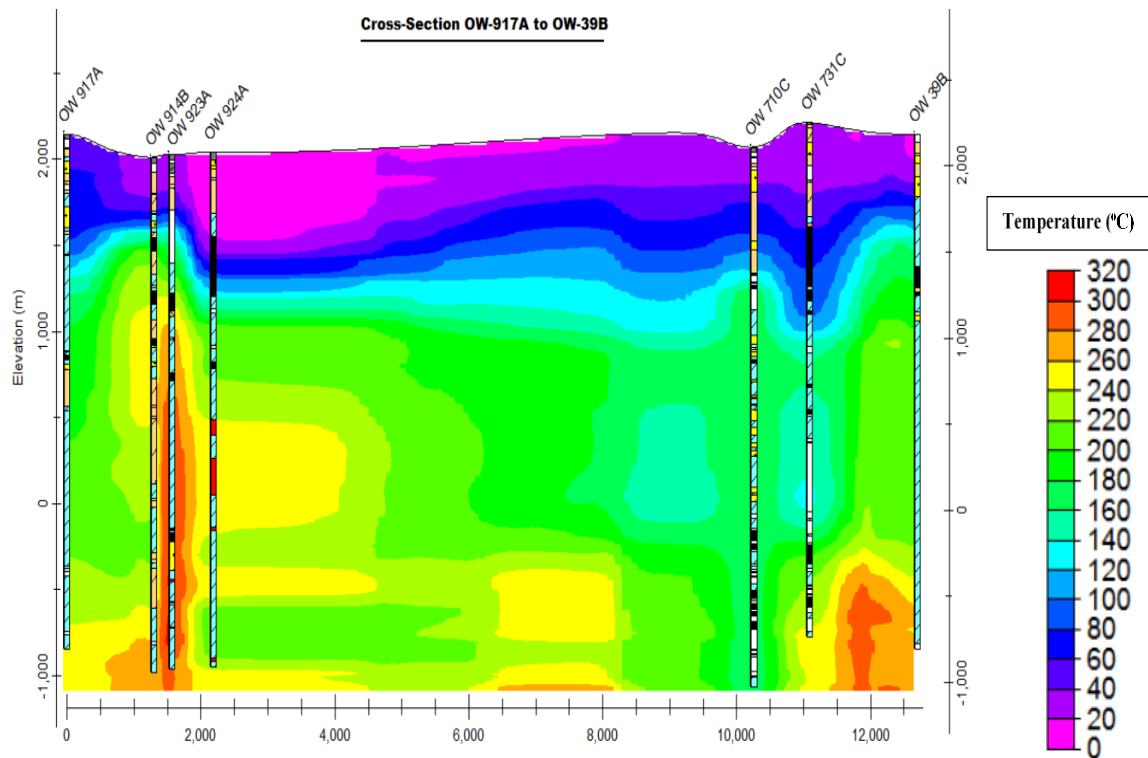
Figure 5.18: A cross section map of Olkaria field showing temperature amd lithology that have OW-914B and and OW 924A modified from [243]. The well pads for OW 914B and OW-924A are the same for OW-914 and OW-924, respectively.

OW-924 exergy profile shows some correlation to the lithology profile shown in Figure 5.19. At approximately 1,500 m.a.s.l is the caprock strata seen in the lithology map Figure 5.19. Convective heat transfer is in the reservoir section below caprock and above 0 m.a.s.l.The region below 500 m.a.s.l has high temperatures and is interpreted as a reservoir [243]. The lower part elucidated a conductive heat transfer section or hot rock from the exergy profile plot. Well, 904B exergy values vary between the wellhead and well bottom in the wellbore with three reservoir sections, indicating that directional wells are more productive and have higher power output potential.

For wells OW-901, OW-903B, OW-904, OW-908 and OW-924, the exergy profiles in the proposed reservoir section have negative gradients. The region loses the exergy as the fluid moves up the wellbore, indicating the heat or fluid is cooling with depth. The exergy profile with depth tool links the reservoir and wellbore as a function of enthalpy and entropy with reference to ambient conditions at the wellhead. OW-902 and depths below the caprock have

a positive exergy gradient. The study proposes that the positive exergy gradient results from heat gain
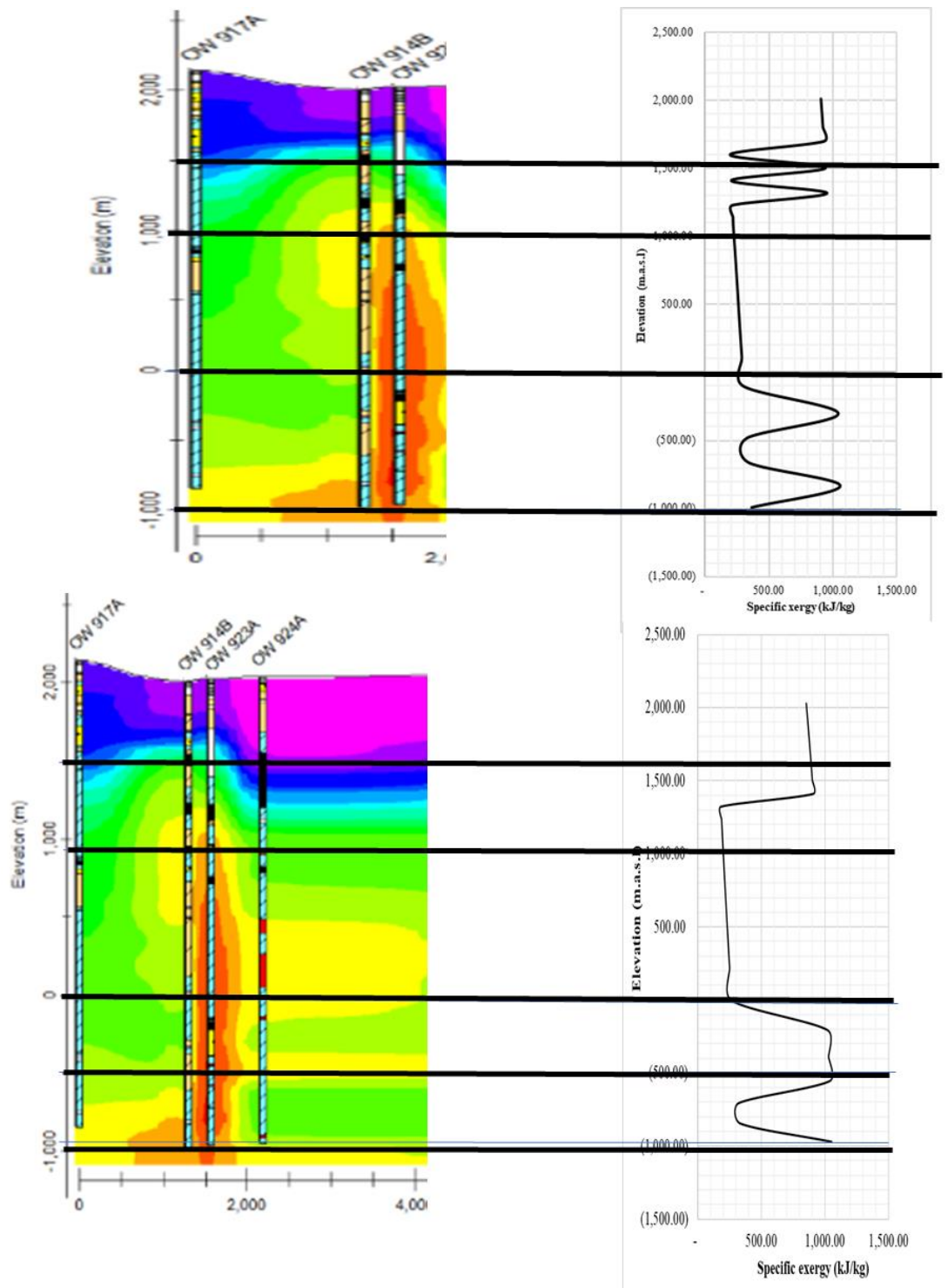
Figure 5.19: Cross- section lithology map of Olkaria field section and simulated exergy profile connected to show their relationship for OW-914 and OW-924, the upflow zone beneath OW-914 is predicted by the exergy profile to have exergy loss and gains. Exergy profile gives some sub-surface phenomenon related to layers locations [243].

OW-902 in the field is a hot reinjection well. The field information and other research-related reservoir interpretations support the hypothesis. Rop (2018), and Nyangisi (2020) reported upflowing zones beneath OW-914 in the dome area [84]. OW-902 gaining exergy acceptable because of reinjection. The brine reinjected gains heat from the hot reservoir fluid or formation.

With the 1-D, reservoir P, T, h, s and exergy profiles, the wellbore results are used to plot 2-D contour maps using the 3-D ordinary kriging method. Python 3.10 software executed the 3 D Kriging method to couple reservoir and wellbore.

The loop to reach between surface and reservoir conditions is the next hot topic worth investigating in geothermal management and optimisation. The hinted concept is wellbore reservoir coupling in addition to this study's exergy profiles.

5.7 Wellbore reservoir coupling

The wellbore simulated profiles are considered for coupling using python and 3 D Kriging equation. Exergy (total and specific), temperature, pressure, entropy, and enthalpy are mapped as a proposal to couple surface and sub-surface conditions. Coupling reservoirs with wellbore results tend to provide a longer life span of a reservoir because lower well bottom pressures are seen to be less than the test pressures during reinjection and heating. Simulated pressure profiles plotted for the wells investigated are lower than the formation pressures. This phenomenon will increase the productivity of geothermal reservoirs hence a longer lifespan under sustainable exploitation. The comparative studies of exergy profiles in other geothermal fields give information about feed zones, heat transfer, and strata.

5.7.1 3D kriging method

Python console was used to execute the 3D kriging method for coupling the reservoir with the wellbore. The tabulated P, T, h, exergy, and flow rates with 2-D contour maps couple the wellbore and the reservoir for Olkaria Domes field. Thermophysical parameters at any depth were plotted for reservoir interpretation and compared with the previous methods (using commercial software, e. g TOUGH2 or iTOUGH2). Wellbore simulator simulated temperature and pressure profiles for vertical wells of OW-901, OW-903, OW-902, OW-904, OW-905, OW-908, OW-909, OW-910, OW-911, OW-912, OW-914, OW-915, OW-916 and OW-921 from field data. The obtained temperature and enthalpy were applied for the conceptual wellbore reservoir coupling.

5.7.2   2D-conceptual contour maps

The wellbore simulated P, T data were used to plot contour maps. Specific exergy and enthalpy were calculated from the simulated parameters in the EES code to couple the wellbore and the reservoir.
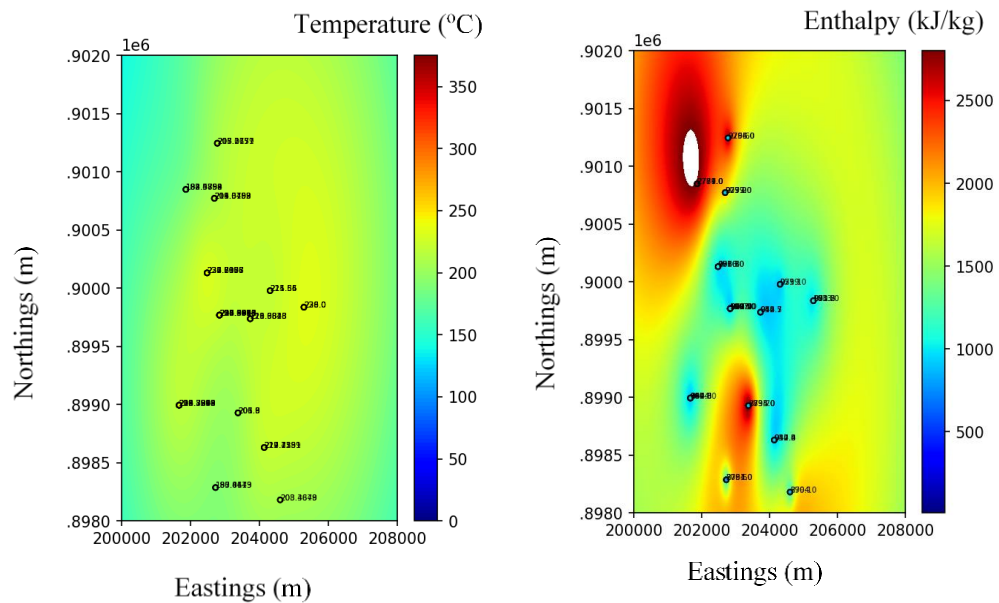
Figure 5.20: 2D – Contour maps for Olkaria Domes at 1000 m.a.s.l

The figures in this section present the temperature and enthalpy contours for the Domes area for vertical wells. The temperature increases with depth from 1,000 m.a.s.l to -1000 m.a.sl. The contours show thet the temperature is centralized in the dome. The enthalpy contours from simulated wellbore flow for vertical wells show the high enthalpy regions at different locations. Figures 5.20, 5.21, 5.22, 5.23 and 5.24 show the temperature and enthalpy contours of wellbore reservoir coupling at 100, 500, 0, -500, and -1000 m.a.s.l, respectively.
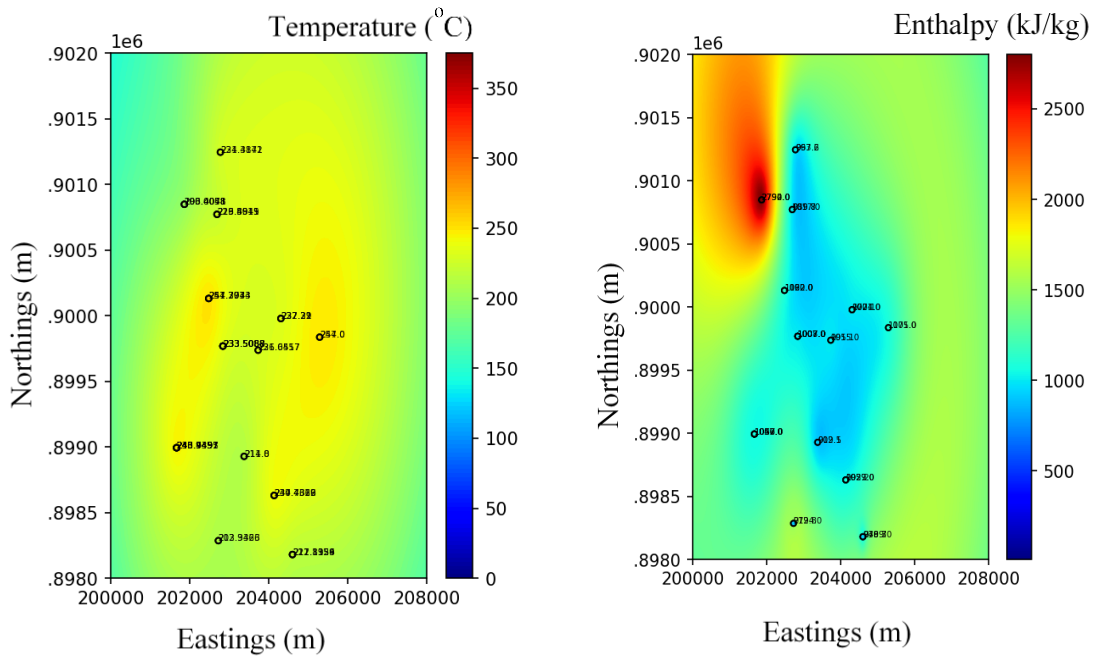
Figure 5.21: 2D – Contour maps fo Olkaria Domes at 500 m.a.s.l
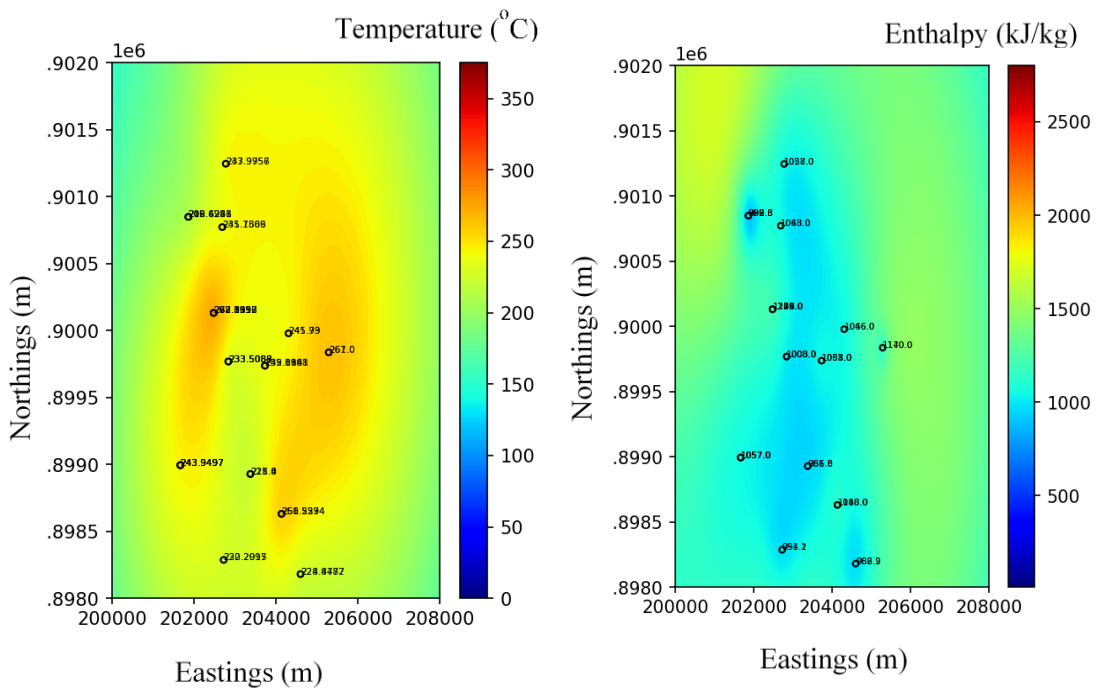
Figure 5.22: 2D – Contour maps for Olkaria Domes at 0 m.a.s.l.

170
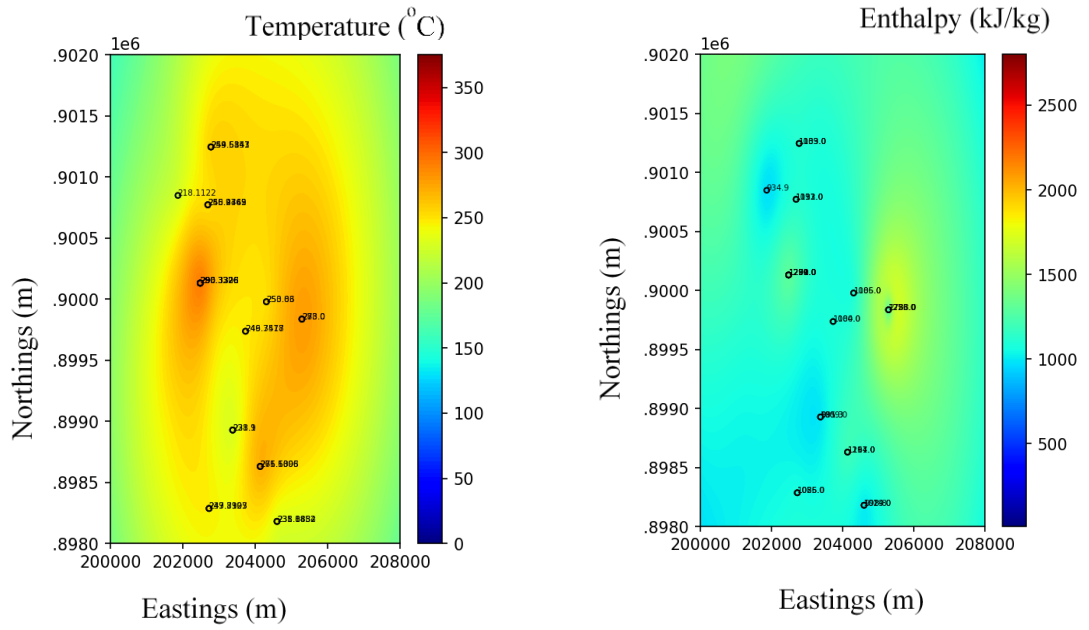
Figure 5.23: 2D – Contour maps for Olkaria Domes at -500m.a.s.l.
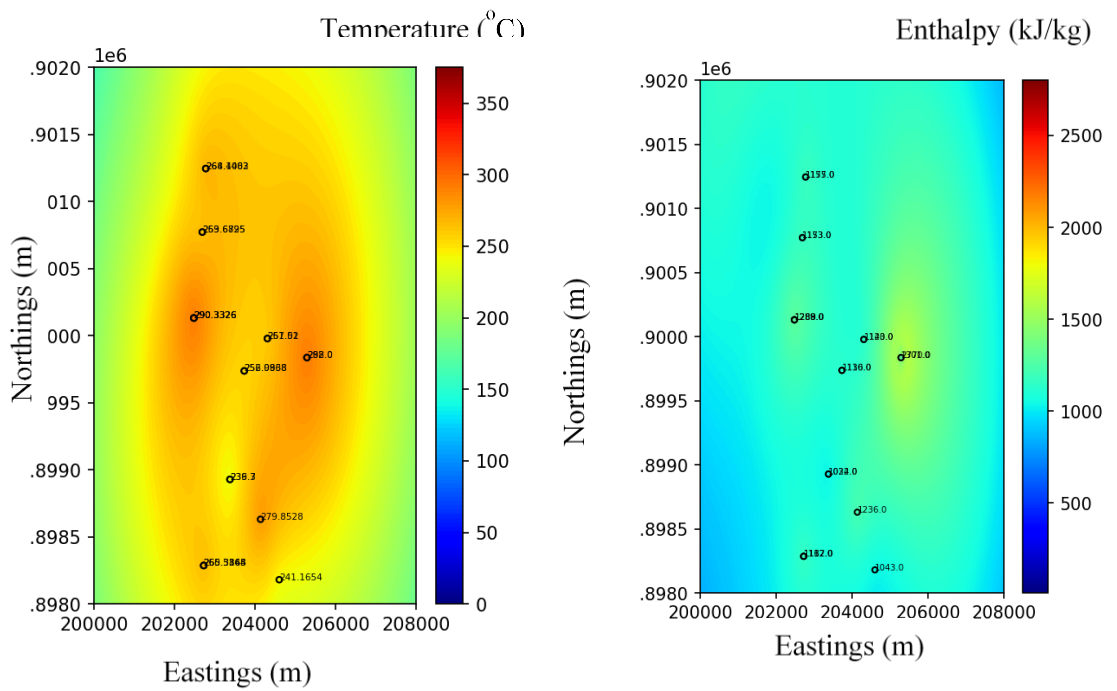
Figure 5.24: 2D – Contour maps fo Olkaria Domes at -1000 m.a.s.l.

171

5.8   Conclusion

5.8.1   Wellbore simulation of Olkaria Domes production wells

Exergy is a powerful tool for optimal utilisation of geothermal resources at the surface and power plants. A wellbore simulator was used to obtain temperature and pressure profiles of water-dominated geothermal wells in Olkaria Domes geothermal field. The exergy concept is applied to plot corresponding exergy profiles.

Exergy profiles show a close correlation to the lithology profile. At 1,500 m.a.s.l is the caprock strata seen in the lithology map. Convective heat transfer is in the reservoir section below caprock and above 0 m.a.s.l. The region below 500 m.a.s.l has high temperatures and is interpreted as the upflow zone, especially at the well bottom for OW-914 and OW-924.

The following conclusions were arrived at;

•   There is a need to link reservoir analysis with the wellhead conditions to check exergy losses and gains.

•   The exergy profile shows the convective and conductive heat transfer regions and upflow zone. From the exergy profile, the location of the reservoir, caprock, and heat source are hypothesised. Thus, the need to couple wellbore and reservoir.

•   Directional wells (OW-904B and OW-903A) are more productive and have higher power output potential.

5.8.2   Coupling reservoir and wellbore simulator

Exergy profile and exergy optimisation of geothermal wells are the next frontiers in optimising the geothermal resource. The studies on exergy profiles can predict feed zones, heat transfer, and strata. Reservoir wellbore coupling concepts need more developments to visualise the 2-D data and proceed to outcomes of exergy conceptual models..

Nomenclature

A	area (m^2)
c_p	specific heat capacity (kJ/K/kg)
i	enthalpy (J/kg)
g	Acceleration of gravity (9.81 m/s^2)
K	permeability (m^2
L_R	reservoir thickness (m)
$\dot{m}$	mass flow rate (kg/s)
P	pressure (MPa or kPa)
q	heat energy (J/kg)
$\dot{q}$	heat flux (W/m^2)
r	radius (m)
r_{dw}	radial distance from centre of the well (m)
w	velocity(m/s)
$\overline{w}$	average velocity (m/s)
v	specific volume (m^3/kg)
$\dot{V}_w$	volumetric flow rate (m^3/s)
x	flow quality(-)

Greek letters

α	void fraction (-)
μ	viscosity (kg/m.s)
ρ	density (kg/m^3)
∅	porosity (-)
λ	thermal conductivity (W/m·K)

.

Subscripts

R	reservoir
g	gas
l	liquid
s	steam
w	water
wl	well
c	capillary
wf	wellbore fluid

That which has been is what will be, That which is done is what will be done, And there is nothing new under the sun. Ecclesiastes 1:9".

CHAPTER SIX

6.0 CONCLUSION AND RECOMMENDATIONS ON OPTIMISATION OF GEOTHERMAL RESOURCES IN KENYA

6.1 General conclusions

This dissertation optimises geothermal resources in Kenya by geochemical analysis, energy, exergy, and reservoir-wellbore coupling. The main objectives were to update the geothermal manifestations map of Kenya, optimise the brine at Olkaria geothermal field and propose a surface and sub-surface linking. For the exploration stages, to update the geothermal prospects map of Kenya, geochemistry and QGIS tools were applied. On the developed power plants in Olkaria geothermal field, existing and proposed power plants were analysed and optimised using EES code. Exergy analysis and optimisation have been applied to SF and proposed binary units, but no binary unit so far operated by KENGEN. Exergy is a powerful tool to optimise geothermal energy, especially at surface facilities. The surface and sub-surface were linked using the exergy concept, the wellbore simulator, and the 3 D Kriging method. This research applies exergy in the Olkaria Domes geothermal field reservoir to develop conceptual contours of thermophysical properties results from the wellbore simulator.

The research can be classified into three main sections;

- The geothermal exploration involved geochemical analysis of new low enthalpy hot springs in Kenya and mapping them using QGIS.
- The optimisation of the geothermal powers plant by exergoeconomic analysis. Binary cycle configurations were proposed, modelled, and analysed using EES code.
- Coupling reservoir and wellbore for Olkaria Domes geothermal field was performed using 3 D Kriging method and Python code.

General conclusion and recommendation for future work are summarised in this chapter.

The geothermal waters have different chemical compositions and vary from one field to another. Geothermal manifestations in Kenya have been mapped mainly with the EARS high potentials. In chapter 3, resources studied are low enthalpy hot springs and new hot springs Kipsegon and Olchorro were added to the geothermal manifestations map of Kenya. The hot springs are

mainly neutral waters with pH 6-8. The temperatures recorded at the surface are low, between 30 and 75°C. Cation geothermometers inferred a very high and wide range of reservoir temperatures. Silica and quartz geothermometers were the most suitable for estimating reservoir temperatures. Na-K-Ca geothermometer without Mg correlation figured similar results to quartz geothermometers. Based on cation and Giggenbach ternary plots, most of the waters are immature and peripheral types except for the samples from Homa hills that are fully equilibrated and of peripheral type. The dominant cations are Na+K in almost all sites. The hot spring waters from six sites have mainly Cl in terms of anions. The water mainly belongs to the Na+K facies. The isotopic analysis showed that most geothermal systems in Kenya are meteoric water. The most suitable applications of low enthalpy resources are direct use. Of the six fields studied, Eburru hot springs show good promise to develop power plants and direct use because of high estimated reservoir temperatures above 340°C.

Recent and related research on the exergoeconomic analysis of power plants has provided a complete understanding of the thermal flow processes. Both surface and sub-surface parameters of geothermal resources in Kenya were optimised using exergy. The parameters unique in this research and exergy concept are sustainability index (SI), objective function f(obj) and pinch point for optimising geothermal power plants. SI as a function of exergy efficiency shows that the higher the exergy efficiency, the higher the SI values proposed.

This research conducted thermal and exergoeconomic analyses for wet and dry-cooled binary geothermal power plants for optimum utilisation of geothermal brine at 156°C and a flow rate of 67.14 kg/s at Olkaria I. Using EES code, modelling and optimisation were performed based on the variable-metric method by varying turbine inlet and outlet pressures and reinjection temperatures. For the proposed power plants, SI values are between 1.3 and 1.8. The objective function, the ratio of net power generated to the total area of heat exchangers, decreases with the increase in area. The total heat exchanger area is higher for optimising the air-cooled power plant than the water-cooled power plant proposed. For the working fluid studied, cis-2-butene has the least area of heat exchangers at 968.9 m2 and 1,724 m2 for water-cooled and air-cooled, respectively. An increase in the area will affect the overall cost of the power plant; thus, it is essential to define the objective function in optimising binary power plants. The objective function will affect the cost of products and the availability of land.

Optimum utilisation of geothermal brine from Olkaria II SF power plant for an ORC unit depends on many parameters. The main parameters are turbine inlet pressure, efficiencies,

maximum power generated, reinjection temperature of geothermal fluid, sustainability index, pinch point, and total exergy destroyed. Most studies have been on optimisation based on other parameters by applying a fixed pinch point for different working fluids, cases not supported by graphical representation by heat transfer diagrams, and energy and mass balance equations. Combining pinch point analysis and exergy optimisation of binary power plants is worthwhile.

Energy, exergy, and sustainability index were used to analyse the ORC power plant proposed in Olkaria II geothermal power plant using eight different working fluids. Exergy destruction is always higher than the net power generated; for example, isobutane generates 6,791 kWe net work, and 7,562 kW exergy destroyed. The binary power plants proposed in Olkaria I and II show that isobutane is the most suitable working fluid. The exergy efficiencies for ORC using isobutane are between 43 and 44%. Optimising the ORC power plant by exergy and pinch point shows isobutane is the most suitable and generates net power output of between 6,534-7,403 kWe. Pinch point application for the isobutane resulted in more power output for lower pinch point values. At the pinch point of 5°C, the net power output is 7,403 kWe, while at a pinch point of 10°C, the net work generated is 5,534 kWe. The results show that the optimum and practical pinch point is 8°C for reinjection temperatures above 80°C. The optimisation of brine at Olkaria IV considered two working fluids. ORC power plant optimised based on total exergy destruction, and net work generated noted an "apex" at optimum turbine inlet pressure. As the net power output increased, total exergy destruction decreased, and the values were the same at the "apex". It is another point considered for optimising geothermal energy to ensure the slightest difference between practical work generated and the total irreversibilities in the power plant.

A wellbore simulator was used to obtain temperature and pressure profiles of water-dominated geothermal wells in Olkaria Domes geothermal field. The exergy at any depth within the well was calculated in EES code using wellbore simulator results. Exergy profile with depth identified exergy losses and gains interpreted or predicted as either convective or conductive heat transfer zones. Python code was used to couple wellbore and reservoir in the Domes field to implement the 3 D Kriging method. The exergy concept is applied to plot corresponding conceptual contours of enthalpy and temperature.

6.2   Recommendation and future work

As a result of the optimisation of geothermal energy in Kenya by exergy and energy concepts, this study concludes that geothermal resources in Kenya are widespread and thus need a comprehensive best application scenario. The low-temperature resources are suitable

for direct use from the geochemical and update of the manifestations map. Quartz geothermometers are the most reasonable for estimating the reservoir temperatures of the low enthalpy resources. Only geochemistry and stable isotope analysis data are available; other exploration techniques like geophysics would be suitable for understanding the sub-surface of the new low enthalpy prospects.

To operate and maintain power plants for sustainable development, all the available exergy in the Olkaria field should be put into good use and optimised exergoeconomically for a green energy revolution and as a marketing tool to convince other nations and decision-makers to develop and optimise geothermal resources. For optimum utilisation of brine in Olkaria, the most suitable reinjection temperatures can be decided based on amorphous silica concentration at reinjection temperatures. This research constrained the reinjection temperatures to be between 70 and 100°C. Silica concentration at the proposed reinjection temperatures will help know the silica scaling potential.

The Olkaria Domes field has high wellhead pressures and temperatures. Exergy analysis noted that exergy destruction is between the wellhead and turbine inlet. As a recommendation, the brine can be flashed at higher pressures to reduce exergy losses considering the possibility of double flash power plants.

To link, the surface and sub-surface more investigations on geothermal wellbore simulators need to be considered, and two-phase or geothermal steam resources can be analysed. The wellbore-reservoir coupling using the exergy concept is at the early stages of development. The thermophysical parameters of the wellbore simulator can be used in a calibrated 3 D reservoir model to check the 3 D Kriging method.

Acknowledgement

References

[1] S. K. Munyiri, Structural Mapping of Olkaria Domes Geothermal Field Using Geochemical Soil Gas Surveys , Remote Sensing and GIS, 2016.

[2] J. Maithya and Y. Fujimitsu, Analysis and interpretation of magnetotelluric data in characterization of geothermal resource in Eburru geothermal field, Kenya, *Geothermics*, vol. **81**, no. September 2018, pp. 12–31, 2019.

[3] D. L. Mendive, P. E. Green, L. Green, and P.E., Wellhead Geothermal Power Plant at Eburru, Kenya, *GRC Trans.*, vol. **Vol. 36**, no. unbekannt, pp. 13–16, 2012.

[4] C. E. Campos Rodríguez *et al.*, Exergetic and economic comparison of ORC and Kalina cycle for low temperature enhanced geothermal system in Brazil, *Appl. Therm. Eng.*, vol. **52**, no. 1, pp. 109–119, 2013.

[5] K. Li, C. Liu, S. Jiang, and Y. Chen, Review on hybrid geothermal and solar power systems, *J. Clean. Prod.*, vol. **250**, p. 119481, 2020.

[6] L. Thorvaldsson, H. Pálsson, H. Stefánsson, and Á. Valfells, Tools to evaluate strategies for utilization of low temperature geothermal resources, 2010.

[7] R. DiPippo, *Geothermal Power Plants*, 4th ed. Elsevier, 2016.

[8] G. Magnus and L. Victor, Geothermal Handbook: Planning and Financing Power Generation. Energy Sector Management Assistance Program (ESMAP), 2012.

[9] R. Shortall, B. Davidsdottir, and G. Axelsson, Geothermal energy for sustainable development: A review of sustainability impacts and assessment frameworks, *Renewable and Sustainable Energy Reviews*, vol. **44**. Elsevier Ltd, pp. 391–406, 2015.

[10] A. Watson, *Geothermal Engineering*, 1st ed. New York, NY: Springer New York, 2013.

[11] G. W. Huttrer, Geothermal Power Generation in the World 2015-2020 Update Report, in *World Geothermal Congress*, 2020, p. 17.

[12] R. Basosi, R. Bonciani, D. Frosali, G. Manfrida, M. L. Parisi, and F. Sansone, Life cycle analysis of a geothermal power plant: Comparison of the environmental performance with other renewable energy systems, *Sustain.*, vol. **12**, no. 7, pp. 1–29, 2020.

[13] I. Blanc *et al.*, *LCA Guidelines for Geothermal Installations*, no. February. GEOENVI, 2020.

[14] F. Pierie, J. Bekkering, R. M. J. Benders, W. J. T. van Gemert, and H. C. Moll, A new approach for measuring the environmental sustainability of renewable energy production systems: Focused on the modelling of green gas production pathways, *Appl. Energy*, vol. **162**, pp. 131–138, 2016.

[15] S. Jalilinasrabady and R. Itoi, Classification of Geothermal Energy Resources in Japan Applying Exergy Concept, *Int. J. Energy Res.*, vol. **37**, no. 14, pp. 1842–1850, 2013.

[16] L. Lijó *et al.*, Life cycle assessment of electricity production in italy from anaerobic co-digestion of pig slurry and energy crops, *Renew. Energy*, vol. **68**, no. 2014, pp. 625–635, 2014.

[17] L. Ball, *Handbook of Geothermal Energy*. Gulf Publishing Company, 1982.

[18] *Sustainable Energy Handbook-Geothermal Energy*, no. February. European Union, 2016.

[19] M. Brito, M. H. Dickson, and M. Fanelli, *Geothermal energy Utilization and technology*. UNESCO, 2003.

[20] S. Jalilinasrabady, Optimum Utilization of Geothermal Energy Employing Exergy Analysis and Reservoir Simulation, Kyushu University, 2011.

[21] W. E. Glassley, Geothermal Energygeothermalenergy, Geologygeothermalenergygeologyand Hydrologygeothermalenergyhydrologyof, in *Encyclopedia of Sustainability Science and Technology*, R. A. Meyers, Ed. New York, NY: Springer New York, 2012, pp. 4179–4190.

[22] H. Puppala and S. K. Jha, Identification of prospective significance levels for potential geothermal fields of India, *Renew. Energy*, vol. **127**, pp. 960–973, 2018.

[23] E. Kaya, S. J. Zarrouk, and M. J. O'Sullivan, Reinjection in geothermal fields: A review of worldwide experience, *Renew. Sustain. Energy Rev.*, vol. **15**, no. 1, pp. 47–68, 2011.

[24] Z. Kamila, E. Kaya, and S. J. Zarrouk, Reinjection in geothermal fields: An updated worldwide review 2020, *Geothermics*, vol. **89**, no. June 2020, p. 101970, 2021.

[25] K. C. Lee, Classification of geothermal resources by exergy, *Geothermics*, vol. **30**, no. 4, pp. 431–442, 2001.

[26] S. M. Bina, S. Jalilinasrabady, H. Fujii, and N. A. Pambudi, Classification of geothermal resources in Indonesia by applying exergy concept, *Renew. Sustain. Energy Rev.*, vol. **93**, no. April, pp. 499–506, 2018.

[27] B. Fričovský, L. Vizi, M. Gregor, M. Zlocha, M. Surový, and R. Černák, Thermodynamic Analysis and Quality Mapping of a Geothermal Resource at the Ďurkov Hydrogeothermal Structure , Košice Depression , Eastern Slovakia, in *Workshop on geothermal reservoir engineering*, 2018, no. 43, pp. 1–9.

[28] E. Hancıoğlu Kuzgunkaya, Karaelmas Science and Engineering Journal, *Karaelmas Fen ve Müh. Derg*, vol. **8**, no. 1, pp. 63–72, 2018. [Online]. Available: http://fbd.beun.edu.tr

[29] M. Rajaobelison, J. Raymond, M. Malo, and C. Dezayes, Classification of geothermal systems in Madagascar, *Geotherm. Energy*, vol. **8**, no. 1, p. 22, 2020.

[30] I. Renewable Energy Agency, *RENEWABLE CAPACITY STATISTICS 2020 STATISTIQUES DE CAPACITÉ RENOUVELABLE 2020 ESTADÍSTICAS DE CAPACIDAD RENOVABLE 2020*. International Renewable Energy Agency, 2020. [Online]. Available: www.irena.org

[31] H. Baek, J. Kim, and S. Yu, Technical Supports and Education Programs for Geothermal Industries in Korea, *Renew. Energy*, no. April, pp. 2006–2008, 2010.

[32] M. E. J. Feliks, T. P. Elliott, G. D. Day, G. D. Percy, and P. L. Younger, Direct Use of Low Enthalpy Deep Geothermal Resources in the East African Rift Valley, in *Proceedings World Geothermal Congress*, 2015, p. 6.

[33] M. 2012 Mburu, Cascaded use of geothermal energy: Eburru case study, *Geo-Heat Center Quarterly Bulletin*, vol. **30**, no. 4, pp. 21–26, 2012.

[34] J. Lagat, Direct Utilization of Geothermal Resources in Kenya, in *Proceedings World Geothermal Congress*, 2010, p. 7. [Online]. Available: https://www.geothermal-energy.org/pdf/IGAstandard/WGC/2010/2810.pdf

[35] M. Pham, C. Klein, C. Ponte, R. Cabeças, R. Martins, and G. Rangel, Production / Injection Optimization Using Numerical Modeling at Ribeira Grande , São Miguel , Azores , Portugal, in *World Geothermal Congress*, 2010, p. 6.

[36] L. Lu, P. Zhonghe, X. Ejun, F. Zengcai, and W. Yingchun, A Comparative Study on the Energy Potential of Geothermal Fields along the Qinghai-Tibet Railway in China, in *World Geothermal Congress*, 2015, p. 6.

[37] S. Jalilinasrabady, R. Itoi, P. Valdimarsson, G. Saevarsdottir, and H. Fujii, Flash cycle optimization of Sabalan geothermal power plant employing exergy concept, *Geothermics*, vol. **43**, pp. 75–82, 2012.

[38] D. Fiaschi, G. Manfrida, E. Rogai, and L. Talluri, Exergoeconomic analysis and comparison between ORC and Kalina cycles to exploit low and medium-high temperature heat from two different geothermal sites, *Energy Convers. Manag.*, vol. **154**, no. November, pp. 503–516, 2017.

[39] Y. Nakao, Y. Mugikura, K. Ogata, and N. Katsuki, Development of hybrid Geothermal Power Plants in Japan, *Trans. - Geotherm. Resour. Counc.*, vol. **41**, pp. 794–805, 2017.

[40] S. Jalilinasrabady, H. Palsson, G. Saevarsdottir, R. Itoi, and P. Valdimarsson, Experimental and CFD simulation of heat efficiency improvement ingeothermal spas, *Energy*, vol. **56**, pp. 124–134, 2013.

[41] S. Kinyanjui, Direct use of geothermal energy in Menengai, Kenya: proposed geothermal spa and crop drying, no. 9, 2014. [Online]. Available: http://rafhladan.is/handle/10802/7392

[42] J. Ngethe and S. Jalilinasrabady, Considering Future Feasible Agricultural Projects for Direct Use of Geothermal Energy at Eburru Geothermal Field, in *GRC Transactions*, 2020, vol. **44**, pp. 268–283.

[43] F. Tinti *et al.*, Ground temperature monitoring for a coaxial geothermal heat exchangers field: practical aspects and main issues from the first year of measurements, *The Mining-Geology-Petroleum Engineering Bulletin*, vol. **33**, no. 5, pp. 47–57, Dec. 20, 2018.

[44] P. Bombarda, M. Gaia, C. Invernizzi, and C. Pietra, Comparison of Enhanced Organic Rankine Cycles for Geothermal Power Units, in *World Geothermal Congress*, 2015, p. 10.

[45] P. Collings, Z. Yu, and E. Wang, A dynamic organic Rankine cycle using a zeotropic mixture as the working fluid with composition tuning to match changing ambient conditions, *Appl. Energy*, vol. **171**, pp. 581–591, 2016.

[46] O. Özkaraca and A. Keçebaş, Performance analysis and optimization for maximum exergy

efficiency of a geothermal power plant using gravitational search algorithm, *Energy Convers. Manag.*, vol. **185**, no. January, pp. 155–168, 2019.

[47]   J. Han, X. Wang, J. Xu, N. Yi, and A. S. S. Talesh, Thermodynamic analysis and optimization of an innovative geothermal-based organic Rankine cycle using zeotropic mixtures for power and hydrogen production, *Int. J. Hydrogen Energy*, vol. **45**, no. 15, pp. 8282–8299, 2020.

[48]   J. W. Lund, Geothermal energy, *Encyclopedia Britannica*, 2018. https://www.britannica.com/science/geothermal-energy (accessed Oct. 16, 2021).

[49]   J. W. Lund and A. N. Toth, Direct utilization of geothermal energy 2020 worldwide review, *Geothermics*, no. July, p. 101915, 2020.

[50]   P. Omenda, P. Mangi, C. Ofwona, and M. Mwangi, Country Update Report for Kenya 2015-2019, 2020.

[51]   B. Ruggero, Geothermal power generation in the world 2005–2010 update report, in *Worl Geothermal Congress*, 2010, p. 29.

[52]   G. W. Huttrer, The status of world geothermal power generation 1995-2000, *Geothermics*, vol. **30**, no. 1, pp. 1–27, 2001.

[53]   J. W. Lund, D. H. Freeston, T. L. Boyd, and C. Rica, Direct utilization of geothermal energy 2010 worldwide review, *Geothermics*, vol. **40**, no. 3, pp. 159–180, 2011.

[54]   J. K. Kiplagat, R. Z. Wang, and T. X. Li, Renewable energy in Kenya: Resource potential and status of exploitation, *Renew. Sustain. Energy Rev.*, vol. **15**, no. 6, pp. 2960–2973, 2011.

[55]   M. Takase, R. Kipkoech, and P. K. Essandoh, A comprehensive review of energy scenario and sustainable energy in Kenya, *Fuel Commun.*, vol. **7**, p. 100015, 2021.

[56]   *Development ot Kenya's power sector 2015-2020*. Power Africa, 2020.

[57]   Ministry of Energy. www.energy.go.ke (accessed Jun. 12, 2020).

[58]   M. W. Murage and C. L. Anderson, Contribution of pumped hydro storage to integration of wind power in Kenya: An optimal control approach, *Renew. Energy*, vol. **63**, no. 2014, pp. 698–707, 2014.

[59]   P. A. Omenda, Status of geothermal exploration in Kenya and future plans for its development, in *World Geothermal Congress*, 2010, no. April.

[60]   IEA, Kenya primary energy demand and GDP in the Africa Case, 2010-2040, IEA, Paris. https://www.iea.org/data-and-statistics/charts/kenya-primary-energy-demand-and-gdp-in-the-africa-case-2010-2040 (accessed Mar. 20, 2021).

[61]   A. H. Kazimierczuk, Wind energy in Kenya: A status and policy framework review, *Renew. Sustain. Energy Rev.*, vol. **107**, no. December 2018, pp. 434–445, 2019.

[62]   J. M. G. Glen, G. Connard, J. Casteel, and P. Walsh, Assessing Structural Controls on Geothermal Fluids from a Three-dimensional Geophysical Model of Warner Valley, Oregon USA, in *World Geothermal Congress*, 2015, no. April, p. 13.

[63]   C. B. Kwambai, Exergy Analysis for Olkaria I Geothermal Power Plant, Kenya, 2010.

[64]   J. Mulwa, J. Barongo, D. Fairhead, N. Mariita, and J. Patel, Integrated Geophysical Study of Lake Bogoria Basin , Kenya : Implications for Geothermal, *Proc. World Geotherm. Congr. 2010*, vol. **4**, no. April, pp. 1–4, 2010.

[65]   I. Kanda, Y. Fujimitsu, and J. Nishijima, Geological structures controlling the placement and geometry of heat sources within the Menengai geothermal field, Kenya as evidenced by gravity study, *Geothermics*, vol. **79**, no. December 2018, pp. 67–81, 2019.

[66]   M. K. Kibet, P. K. S. Magut, and J. Varet, Geological Conceptual Model of Olkaria Geothermal System, *J. Appl. Geol. Geophys.*, vol. **7**, no. 3, pp. 25–28, 2019.

[67]   M. K. Kibet *et al.*, Rock Types and Alteration Mineralogy Occurring In Rock Types And Alteration Mineralogy Occurring In Olkaria Geothermal Field , *J. Appl. Geol. Geophys.*, vol. **7**, no. 1, pp. 47–57, 2019.

[68]   A. K. Bett, S. Jalilinasrabady, and L. K. Langat, Energy and Exergy Analysis of Olkaria Domes Field : Well Head and Single Flash Power Plants Comparison, in *GRC Transactions*, 2020, vol. **44**, pp. 980–989.

[69]   R. K. Langat, Topping Unit at Olkaria IV geothermal power plant, Naivasha Kenya, The United Nations University (UNU), Reykjavik, 2015.

[70]   C. B. Kwambai, Exergy Analysis of Olkaria I Power Plant , Kenya, The United Nations University (UNU), Reykjavik, 2005.

[71]   A. K. Bett and S. Jalilinasrabady, Optimization of ORC Power Plants for Geothermal Application in Kenya by Combining Exergy and Pinch Point Analysis, *Energies*, vol. **14**, no. 20, p. 6579, 2021.

[72]   Thráinn Fridriksson and Halldór Ármannsson, Application of geochemistry in geothermal resource assesments, Reykjavik, 2007.

[73]   J. Sun, Q. Liu, and Y. Duan, Effects of reinjection temperature on thermodynamic performance of dual-pressure and single-pressure geothermal ORCs, *Sci. Energy Procedia*, vol. **158**, pp. 6016–6023, 2019.

[74]   M. Astolfi, M. C. Romano, P. Bombarda, and E. Macchi, Binary ORC (Organic Rankine Cycles) power plants for the exploitation of medium–low temperature geothermal sources – Part B: Techno-economic optimization, *Energy*, vol. **66**, pp. 435–446, 2014.

[75]   P. Wan, L. Gong, and Z. Bai, Thermodynamic analysis of a geothermal-solar flash-binary hybrid power generation system, *Energy Procedia*, vol. **158**, pp. 3–8, 2019.

[76]   S. Jalilinasrabady, R. Itoi, H. Gotoh, and R. Yamashiro, Exergetic Optimization of Proposed, Takigami Binary Geothermal Power Plant, Oita, Japan, in *GRC Transactions*, 2011, pp. 1305–1312.

[77]   A. M. Syed, S. R. Qureshi, and W. A. Khan, Exergetic and Energetic Analysis of Power Generation from Geothermal Resources in, in *World Geotermal Congress*, 2015, no. April.

[78]   M. Zeyghami and J. Nouraliee, Effect of different binary working fluids on performance of combined flash binary cycle, in *World Geothermal Congress*, 2015, no. April, pp. 1–12.

[79]   N. Fukuda, K. Norito, A. Fujii, K. Ogata, and S. Saito, Development and Case Study of a Geothermal Power Generation System, 2015. [Online]. Available: https://pdfs.semanticscholar.org/68ac/ce3b0940f3dd4f8f70d2b5f9d143a8d8de8c.pdf

[80]   A. Franco and M. Villani, *Optimal design of binary cycle power plants for water-dominated, medium-temperature geothermal fields*, vol. **38**, no. 4. 2009.

[81]   R. S. El-Emam and I. Dincer, Exergy and exergoeconomic analyses and optimization of geothermal organic Rankine cycle, *Appl. Therm. Eng.*, vol. **59**, no. 1–2, pp. 435–444, 2013.

[82]   E. Rop, Interpretation of Recent Temperature and Pressure Data and Updated Conceptual Model of the Greater Olkaria Geothermal System , Kenya, 2013.

[83]   E. Rop, H. Fujii, and S. Jalilinasrabady, An updated numerical model of the Greater Olkaria geothermal system, Kenya, in *43rd Workshop on Geothermal Reservoir Engineering*, 2018, p. 13.

[84]   R. Kandie, P. Mbuthia, and J. Stimac, Use of leapfrog geothermal software in data integration and 3D visualization of Olkaria Domes geothermal system, in *Proceedings, 6th African Rift Geothermal Conference*, 2016, p. 12. [Online]. Available: http://theargeo.org/presentations/geology/Use of leapfrog GEOTHERMAL DATA INTEGRATION.pdf

[85]   L. Daheron, S. Jacques-Beyssen, P. Pommez, and F. Reutenauer, Updated conceptual model and capacity estimates for greater Olkaria geothermal system, Kenya, 2013.

[86]   J. Okoo, A. Omiti, K. Kamunya, and D. Saitet, Updated Conceptual Model of Olkaria Geothermal Field, in *Geothermal Resources Council Transactions*, 2017, vol. **41**, p. 19.

[87]   R. Itoi, Y. Kakihara, M. Fukuda, and A. Koga, Numerical simulation of well characteristics coupled with steady radial flow in a geothermal reservoir, in *International Symposium on Geothermal Energy, 1988: Exploration and Development of Geothermal Resources*, 1988, no. 3, pp. 201–204. [Online]. Available: https://www.geothermal-library.org/index.php?mode=pubs&action=view&record=1009186

[88]   Y. Tateishi, R. Itoi, T. Tanaka, N. Hiraga, and J. Takayama, Numerical simulation of devolution and evolution of steam-water two-phase zone in a fractured geothermal reservoir at Ogiri, Japan, in *Transactions - Geothermal Resources Council*, 2013, vol. **37**, no. PART 2, pp. 915–920.

[89]   M. Rosen and C. A. Bulucea, Using Exergy to Understand and Improve the Efficiency of Electrical Power Technologies, *Entropy*, vol. **11**, no. 4, pp. 820–835, 2009.

[90]   A. Minissale, G. Magro, O. Vaselli, C. Verrucchi, and I. Perticone, Geochemistry of water and gas discharges from the Mt. Amiata silicic complex and surrounding areas (central Italy), *J. Volcanol. Geotherm. Res.*, vol. **79**, no. 3–4, pp. 223–251, 1997.

[91]   M. P. Tole, The potential of geothermal systems in Kenya for balneological use, *Environ.*

Geochem. Health, vol. **24**, no. 2, pp. 103–110, 2002.

[92]   R. Sonney and F. Vuataz, Use of Cl / Br ratio to decipher the origin of dissolved mineral components in deep fluids from the Alps Range and neighbouring areas, in *World Geotermal Congress*, 2010, p. 13.

[93]   F. Ben Brahim, E. Boughariou, J. Makni, and S. Bouri, Evaluation of groundwater hydrogeochemical characteristics and delineation of geothermal potentialities using multi criteria decision analysis: Case of Tozeur region, Tunisia, *Appl. Geochemistry*, vol. **113**, no. August 2019, p. 104504, 2020.

[94]   M. P. Tole, Geochemical studies of the geothermal systems in Kenya: II. The Majimoto geothermal field, *J. African Earth Sci.*, vol. **14**, no. 3, pp. 387–391, 1992.

[95]   W. C. Kamondo, Possible uses of geothermal fluids in Kenya, *Geothermics*, vol. **17**, no. 2–3, pp. 489–501, 1988.

[96]   W. Pulfrey, J. Walsh, and W. B. Se, THE GEOLOGY THE GEOLOGY AND AND MINERAL MINERAL RESOURCES OF RESOURCES OF KENYA, 1969.

[97]   M. W. Mutonga, A. Sveinbjornsdottir, G. Gislason, and H. Amannsson, The Isotopic and Chemical Characteristics of Geothermal Fluids in Hengill Area, SW-Iceland (Hellisheidi, Hveragerdi and Nesjavellir Fields), in *Proceedings World Geothermal Congress*, 2010, no. April, pp. 25–29.

[98]   S. M. Mwangi, Application of Geochemical Methods in Geothermal Exploration in Kenya, *Procedia Earth Planet. Sci.*, vol. **7**, no. 12, pp. 602–606, 2013.

[99]   N. Javanshir, S. M. S. Mahmoudi, and M. A. Rosen, Thermodynamic and Exergoeconomic Analyses of a Novel Combined Cycle Comprised of Vapor-Compression Refrigeration and Organic Rankine Cycles, 2019.

[100] C. Coskun, Z. Oktay, and I. Dincer, Performance evaluations of a geothermal power plant, *Appl. Therm. Eng.*, vol. **31**, no. 17–18, pp. 4074–4082, 2011.

[101] M. G. M. Zhahata, A. Fronda, A. K. Bett, and S. Jalilinasrabady, Energy and Exergy Analysis of BN-06 Wellhead Geothermal Power Plant in Province of Biliran , in *GRC Transactions*, 2020, vol. **44**, pp. 1003–1017.

[102] A. K. Bett, M. Dyson, S. Jalilinasrabady, and H. Shimada, Optimization of geothermal Binary Unit by Energy, Exergy and Sustainability Index: Comparative study of Olkaria Geothermal Field in Kenya and Chiweta Geothermal field in Malawi, in *International Symposium on Earth Science and Technology*, 2019, pp. 19–24.

[103] M. Yari, Exergetic analysis of various types of geothermal power plants, *Renew. Energy*, vol. **35**, no. 1, pp. 112–121, 2010.

[104] A. Golberg, Environmental exergonomics for sustainable design and analysis of energy systems, *Energy*, vol. **88**, pp. 314–321, 2015.

[105] A. K. Bett and S. Jalilinasrabady, Exergoeconomic Analysis for Optimized Combined Wet and Dry Cooling BinaryPower Plant at Olkaria I, Kenya, *Geothermics*, vol. **95**, no. May, p. 102160, 2021.

[106] H. Kianfard, S. Khalilarya, and S. Jafarmadar, Exergy and exergoeconomic evaluation of hydrogen and distilled water production via combination of PEM electrolyzer, RO desalination unit and geothermal driven dual fluid ORC, *Energy Convers. Manag.*, vol. **177**, no. August, pp. 339–349, 2018.

[107] S. Mohammadzadeh Bina, S. Jalilinasrabady, and H. Fujii, Thermo-economic evaluation of various bottoming ORCs for geothermal power plant, determination of optimum cycle for Sabalan power plant exhaust, *Geothermics*, vol. **70**, no. June, pp. 181–191, 2017.

[108] S. Mohammadzadeh Bina, S. Jalilinasrabady, and H. Fujii, Energy, economic and environmental (3E) aspects of internal heat exchanger for ORC geothermal power plants, *Energy*, 2017.

[109] Y. Feng, T. Hung, K. Greg, Y. Zhang, B. Li, and J. Yang, Thermoeconomic comparison between pure and mixture working fluids of organic Rankine cycles (ORCs) for low temperature waste heat recovery, *Energy Convers. Manag.*, vol. **106**, pp. 859–872, 2015.

[110] L. Ozgener and D. Yildirim, Thermodynamics and exergoeconomic analysis of geothermal power plants, *Renew. Sustain. Energy Rev.*, vol. **16**, pp. 6438–6454, 2012.

[111] C. Coskun, Z. Oktay, and I. Dincer, Modified exergoeconomic modeling of geothermal power plants, *Energy*, vol. **36**, no. 11, pp. 6358–6366, 2011.

[112] A. Yıldız and M. A. Ersöz, Energy and exergy analyses of the diffusion absorption refrigeration system, *Energy*, vol. **60**, pp. 407–415, 2013.

[113] K. A. Bacus, E. Kaya, and S. J. Zarrouk, Exergy analysis of Southern Negros Geothermal field , Philippines, in *41st New Zealand Geothermal Workshop*, 2019, no. 41, pp. 1–8.

[114] L. Pan and W. Shi, Investigation on the pinch point position in heat exchangers, *J. Therm. Sci.*, vol. **25**, no. 3, pp. 258–265, 2016.

[115] J. G. Andreasen, M. R. Kærn, and F. Haglind, Assessment of methods for performance comparison of pure and zeotropic working fluids for organic Rankine cycle power systems, *Energies*, vol. **12**, no. 9, pp. 1–25, 2019.

[116] S.-Y. Wu, S.-M. Zhou, L. Xiao, Y.-R. Li, C. Liu, and J.-L. Xu, Determining the optimal pinch point temperature difference of evaporator for waste heat recovery, *J. Energy Inst.*, vol. **87**, no. 2, pp. 140–151, 2014.

[117] F. Heberle and D. Brüggemann, Thermo-economic analysis of zeotropic mixtures and pure working fluids in Organic Rankine Cycles for waste heat recovery, *Energies*, vol. **9**, no. 4, 2016.

[118] A. Saito, Y. Sasaki, K. Kimbara, and M. Sudou, Evaluation of the power generation efficiency of a hot spring heat binary power generation system, *J. Geotherm. Res. Soc. Japan*, vol. **42**, no. 2, pp. 76–82, 2016.

[119] C. He, Y. Jiao, C. Tian, Z. Wang, and Z. Zhang, The exergy loss distribution and the heat transfer capability in subcritical Organic Rankine Cycle, *Entropy*, vol. **19**, no. 6, 2017.

[120] D. Walraven, B. Laenen, and W. D'haeseleer, Minimizing the levelized cost of electricity production from low-temperature geothermal heat sources with ORCs: Water or air cooled?, *Appl. Energy*, vol. **142**, pp. 144–153, 2015.

[121] D. Budisulistyo and S. Krumdieck, Thermodynamic and economic analysis for the pre-feasibility study of a binary geothermal power plant, *Energy Convers. Manag.*, vol. **103**, pp. 639–649, 2015.

[122] J. Moore, R. Grimes, A. O. Donovan, E. Walsh, A. O'Donovan, and E. Walsh, Design and testing of a novel air-cooled condenser for concentrated solar power plants, *Energy Procedia*, vol. **49**, pp. 1439–1449, 2014.

[123] M. A. Ehyaei *et al.*, Investigation of an integrated system combining an Organic Rankine Cycle and absorption chiller driven by geothermal energy: Energy, exergy, and economic analyses and optimization, *J. Clean. Prod.*, vol. **258**, no. 8, p. 120780, 2020.

[124] J. Liao, X. Xie, H. Nemer, D. E. Claridge, and C. H. Culp, A simplified methodology to optimize the cooling tower approach temperature control schedule in a cooling system, *Energy Convers. Manag.*, vol. **199**, no. June, p. 111950, 2019.

[125] F. A. Kareem, M. J. Al-Dulaimi, and N. S. Lafta, Investigation the exergy performance of a forced draft wet cooling tower, *Int. J. Eng. Technol.*, vol. **7**, no. 4, pp. 2575–2580, 2018.

[126] W. Asvapoositkul and M. Kuansathan, Comparative evaluation of hybrid (dry/wet) cooling tower performance, *Appl. Therm. Eng.*, vol. **71**, no. 1, pp. 83–93, 2014.

[127] C. R. Faust and J. W. Mercer, Geothermal Reservoir Simulatio 1. Mathematical Models for Liquid- and Vapor-Dominated Hydrothermal Systems, *Water Resour. Res.*, vol. **15**, no. 1, pp. 23–30, 1979.

[128] A. Ashat, H. B. Pratama, and R. Itoi, Updating conceptual model of Ciwidey-Patuha geothermal using dynamic numerical model, in *IOP Conference Series: Earth and Environmental Science*, 2019, vol. **254**, no. 1.

[129] C. R. R. Faust *et al.*, Numerical Solution Techniques for Liquid- and Vapor-Dominated Hydrothermal Systems, *Water Resour. Res.*, vol. **15**, no. 1, pp. 31–46, 1979.

[130] J. W. Mercer and C. R. Faust, Geothermal reservoir simulation: 3. Application of liquid- and vapor-dominated hydrothermal modeling techniques to Wairakei, New Zealand, *Water Resour. Res.*, vol. **15**, no. 3, pp. 653–671, 1979.

[131] A. W Manyonge, Mathematical modelling of the Olkaria geothermal reservoir, University of Nairobi, 1996.

[132] Gudni Axelsson et al, Updated Conceptual Model and Capacity Estimates for the Greater, in *Thirty-Eighth Workshop on Geothermal Reservoir Engineering Stanford University*, 2013, no. February 11-13, 2013. [Online]. Available: https://pangea.stanford.edu/ERE/pdf/IGAstandard/SGW/2013/Axelsson.pdf

[133] G. Blöcher *et al.*, Conceptual Model for Coupling Geothermal Power Plants with Deep Reservoirs, in *World Geothermal Congress*, 2010, no. April, pp. 25–29.

[134] T. Hadgu, R. W. Zimmerman, and G. A. Bodvarsson, Coupling of a reservoir simulator and a well bore simulator for geothermal applications, in *Transactions - Geothermal Resources Council*, 1993, vol. **17**, pp. 499–505.

[135] E. Rop, Results of well production test for Olkaria Domes f ield , Olkaria Kenya, in *Proceedings of the 4th African Rift Geothermal Conference*, 2012, p. 6. [Online]. Available: www.eapicforum.com

[136] S. Hirakawa and H. Mitsuishi, Numerical model on simultaneous flow of steam and hot water in geothermal Well, *J. Geotherm. Res. Soc. Japan*, vol. **3**, no. 2, pp. 115–130, 1981.

[137] C. I. M. Gunn, D. H. Freeston, and T. Hadgu, Principles for wellbore simulator validation and calibration using matching analysis - I analytical techniques., *Geothermivs*, vol. **21**, no. 3, pp. 341–361, 1992.

[138] M. J. J. O'Sullivan *et al.*, Geothermal reservoir simulation: the state-of-practice and emerging trends, *World Geotherm. Congr.*, no. May, pp. 4065–4070, 2000.

[139] H. Tokita, E. T. Lobato, and R. Itoi, Development of technique for the coupled simulator of reservoir, wellbore and fluid-gathering pipeline networks to provide optimum operation management of geothermal power plant, *J. Geotherm. Res. Soc. Japan*, vol. **28**, no. 1, pp. 77–93, 2006.

[140] A. H. A. Hussain, Pressure transient analysis in injection wells, Universiti Teknologi PETRONAS, 2012.

[141] H. Gudmundsdottir, M. T. Jonsson, and H. Palsson, The wellbore simulator FloWell, in *38th Workshop on Geothermal Reservoir Engineering*, 2013, p. 9.

[142] H. Gudmundsdottir, A coupled wellbore-reservoir simulator utilizing measured wellhead conditions, University of Iceland, Reykjavik, 2012.

[143] Khasani, R. Itoi, T. Tanaka, and M. Fukuda, A numerical study on the effects of initial water saturation of a geothermal reservoir on well characteristics, *Memoirs of the Faculty of Engineering, Kyushu University*, vol. **64**, no. 1. p. 15, 2004.

[144] G. Bjornsson and G. S. Bodvarsson, A multi-feedzone wellbore simulator, in *Geothermal Resources Council*, 1987, no. July, p. 9.

[145] H. Tokita and R. Itoi, Development of the Mulfews Multi-Feed Wellbore Simulator, in *PROCEEDINGS, Twenty-Ninth Workshop on Geothermal Reservoir Engineering, Stanford University, Stanford, California*, 2004, p. 9.

[146] A. J. Ellis and W. A. Mahon, J, *Chemistry and Geothermal Systems*. Academic Press, 1977.

[147] R. O. Fournier, Chemical geothermometers and mixing models for geothermal systems, *Geothermics*, vol. **5**, pp. 41–50, 1977.

[148] S. Arnorsson, Ed., *Isotopic and Chemical Techniques in Geothermal Exploration, Development and Use*. Vienna: International Atomic Energy Agency, 2000.

[149] T. Powell and W. Cumming, Spreadsheets for geothermal water and gas geochemistry, in *Thirty-Fifth Workshop on Geothermal Reservoir Engineering*, 2010, vol. **SGP-TR-188**.

[150] S. Arnórsson, The use of mixing models and chemical geothermometers for estimating underground temperatures in geothermal systems, *J. Volcanol. Geotherm. Res.*, vol. **23**, no. 3–4, pp. 299–335, 1985.

[151] S. Arnorsson, The use of mixing models and chemical geothermometers for estimating underground temperatures in geothermal systems, *J. Volcanol. Geotherm. Res.*, vol. **23**, pp. 299–335, 1985.

[152] R. . Fournier, D. E. White, and A. H. Truesdell, Geochemical indicators of subsurface temperature Part 1, Basic assumptions, *J. Res. U.S Geol. Surv.*, vol. **2**, no. 3, pp. 259–262, 1974.

[153] H. Saiba, Numerical Modeling Based on Gravity and Hydro-Geochemical Data- A Case Study of Obama Geothermal Field, Southestern Japan, Kyushu University, 2007.

[154] S. J. Zarrouk and M. H. Purnanto, Geothermal steam-water separators: Design overview, *Geothermics*, vol. **53**, pp. 236–254, 2015.

[155] X. Wang, G. L. Wang, H. N. Gan, Z. Liu, and D. W. Nan, Hydrochemical Characteristics and Evolution of Geothermal Fluids in the Chabu High-Temperature Geothermal System, Southern Tibet, *Geofluids*, vol. **2018**, pp. 1–15, 2018.

[156] J. Nouraliee, S. Porkhial, D. Ebrahimi, and M. R. Rahmani, Chemical studies on warm springs of West Azarbaijan province in the north west of Iran, *J. Sci. Res. Stud.*, vol. **1**, no. 4, pp. 65–72, 2014. [Online]. Available: http://www.modernrespub.org/jsrs/index.htm

[157] I. K. Kanda, Geological, geophysical and geochemical studies on the hydrothermal system of Menengai geothermal field, Kenya, Kyushu, 2019.

[158] K. M. Kamunya, *δD and δ 18 O systematics in geothermal fluids, Olkaria Geothermal system, Kenya*, no. November. 2018.

[159] A. Fahrurrozie Pradana S. M., Nugraha T., The Application of Na-K-Mg, Na-K/Mg-Ca and K-Mg/Quartz Diagrams to Evaluate Water\rGeochemistry in West Java Geothermal Prospects, Indonesia, *Proc. World Geotherm. Congr.*, no. April, p. 8, 2015.

[160] T. T. Mnjokava, Interpretation of Exploration Geochemical Data for Geothermal Fluids from the Geothermal Field of the Rungwe Volcanic Area, SW Tanzania, *UNU-GTP Reykjavík, Iceland, Reports*, no. 14, pp. 303–332, 2007. [Online]. Available: /citations?view_op=view_citation&continue=/scholar?hl=en&start=10&as_sdt=0,5&scilib=1&citilm=1&citation_for_view=sLrkqmIAAAAJ:mVmsd5A6BfQC&hl=en&oi=p%5Cnhttp://scholar.google.com.ph/citations?view_op=view_citation&continue=/scholar?hl=en%25

[161] A. Jilali, A. Chamrar, and A. El Haddar, Hydrochemistry and geothermometry of thermal water in northeastern Morocco, *Geotherm. Energy*, vol. **6**, no. 1, p. 9, 2018.

[162] I. Can, A new improved Na/K geothermometer by artificial neural networks, *Geothermics*, vol. **31**, no. 6, pp. 751–760, 2002.

[163] W. F. Giggenbach, Geothermal solute equilibria. Derivation of Na-K-Mg-Ca geoindicators, 1988.

[164] H. Chenaker, B. Houha, and V. Vincent, Hydrogeochemistry and geothermometry of thermal water from north-eastern Algeria, *Geothermics*, vol. **75**, no. April, pp. 137–145, 2018.

[165] V. Cruz, V. Vargas, and K. Matsuda, Geochemical characterization of thermal waters in the Borateras geothermal zone, Peru, in *Water-Rock Interaction*, CRC Press, 2010, pp. 157–160.

[166] M. Shah, A. Sircar, V. Shah, and Y. Dholakia, Geochemical and Geothermometry study on hot-water springs for understanding prospectivity of low enthalpy reservoirs of Dholera Geothermal field, Gujarat, India, *Solid Earth Sci.*, vol. **6**, no. 3, pp. 297–312, 2021.

[167] H. Mutlu and A. Kılıç, Geochemical and Isotopic Characteristics of the Balıkesir Thermal Waters , Turkey, *Water*, no. April, pp. 25–29, 2010.

[168] A. Chiodi *et al.*, New geochemical and isotopic insights to evaluate the geothermal resource of the hydrothermal system of Rosario de la Frontera (Salta, northern Argentina), *J. Volcanol. Geotherm. Res.*, vol. **295**, 2015.

[169] M. W. Mutonga, Stable isotopic composition of geothermal fields in Kenya ; The relationship between geothermal fields and Kenya Rift lakes waters, in *World Geothermal Congress*, 2015, p. 9.

[170] Partners For Resilience, Building resilient communities: Case studies from PFR Kenya, 2015.

[171] M. P. Tole, Low enthalpy geothermal systems in Kenya, *Geothermics*, vol. **17**, no. 5–6, pp. 777–783, 1988.

[172] I. Dincer and M. A. Rosen, *Exergy: Energy, Environment and Sustainable Development*, 2nd ed. Elsevier, 2013.

[173] H. Caliskan, I. Dincer, and A. Hepbasli, Exergoeconomic, enviroeconomic and sustainability analyses of a novel air cooler, *Energy Build.*, vol. **55**, pp. 747–756, 2012.

[174] V. Zare, A comparative exergoeconomic analysis of different ORC configurations for binary geothermal power plants, *Energy Convers. Manag.*, vol. **105**, pp. 127–138, 2015.

[175] N. Shokati, F. Ranjbar, and M. Yari, Exergoeconomic analysis and optimization of basic, dual-pressure and dual-fluid ORCs and Kalina geothermal power plants: A comparative study, *Renew. Energy*, vol. **83**, pp. 527–542, 2015.

[176] E. Rubio-Castro, M. Serna-Gonzalez, J. M., and A. Jimenez-Gutierrez, Optimal Design of Cooling Towers, in *Heat and Mass Transfer - Modeling and Simulation*, no. September, 2012, pp. 117–142.

[177] Z. Zou, Z. Guan, H. Gurgenci, and Y. Lu, Solar enhanced natural draft dry cooling tower for geothermal power applications, *Sol. Energy*, vol. **86**, no. 9, pp. 2686–2694, 2012.

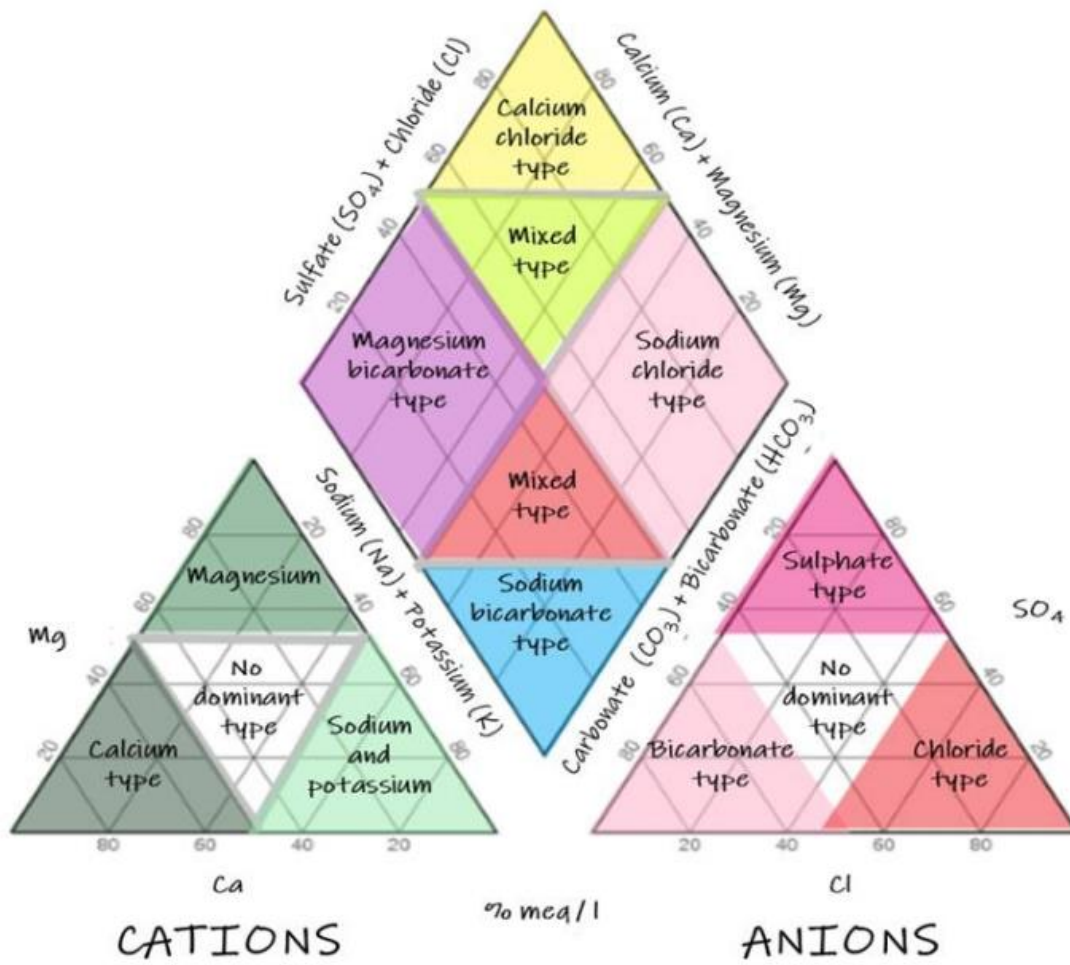[178] K. Hooman, Advanced Air-Cooled Heat Exchangers for Geothermal Power Plants, *World*

Geotherm. Congr. 2015, no. April, p. 8, 2015.

[179] T. Ishido, Theoretical Study on Sustainability of Geothermal Power Generation, *J.Geotherm*, vol. **26**, no. 2, pp. 171–180, 2004.

[180] N. H. Mokarram and A. H. Mosaffa, A comparative study and optimization of enhanced integrated geothermal flash and Kalina cycles: A thermoeconomic assessment, *Energy*, vol. **162**, pp. 111–125, 2018.

[181] D. Luo and D. Huang, Thermodynamic and exergoeconomic investigation of various SCO2 Brayton cycles for next generation nuclear reactors, *Energy Convers. Manag.*, vol. **209**, no. February, p. 112649, 2020.

[182] S. Mohammadzadeh Bina, S. Jalilinasrabady, and H. Fujii, Exergoeconomic analysis and optimization of single and double flash cycles for Sabalan geothermal power plant, *Geothermics*, vol. **72**, no. October 2017, pp. 74–82, 2018.

[183] Y. Zhao and J. Wang, Exergoeconomic analysis and optimization of a flash-binary geothermal power system, *Appl. Energy*, vol. **179**, pp. 159–170, 2016.

[184] Z. Nourani, A. Naserbegi, S. Tayyebi, and M. Aghaie, Thermodynamic evaluation of hybrid cooling towers based on ambient temperature, *Therm. Sci. Eng. Prog.*, vol. **14**, no. September, p. 100406, 2019.

[185] H. Kazemi and M. A. A. Ehyaei, Energy, exergy, and economic analysis of a geothermal power plant, *Adv. Geo-Energy Res.*, vol. **2**, no. 2, pp. 190–209, 2018.

[186] S. M. Bina, S. Jalilinasrabady, and H. Fujii, Thermo-Economic Evaluation and Optimization of a Regenerative ORC Cycle Utilizing Geothermal Energy, in *Transactions - Geothermal Resources Council*, 2017, vol. **41**, pp. 2527–2539. [Online]. Available: https://www.geothermal-library.org/index.php?mode=pubs&action=view&record=1033887

[187] O. S. Onyeguo, Energy, Exergy and Exergeconomic Analysis of Forced Draft Cooling Tower, *Energy, Enviroment Carbon Credit.*, vol. **3**, no. 2, pp. 1–10, 2013.

[188] F. Pratama *et al.*, Thermoeconomic assessment and optimization of wells to flash–binary cycle using pure R601 and zeotropic mixtures in the Sibayak geothermal field, *Geothermics*, vol. **85**, no. July 2019, p. 101778, 2020.

[189] N. Nyambane, Hybridization of Cooling System of Olkaria II Geothermal Power Plant: Utilization of Energy and Exergy Analysis Concepts, University of Nairobi, 2015.

[190] J. Sun, Q. Liu, and Y. Duan, Effects of evaporator pinch point temperature difference on thermo-economic performance of geothermal organic Rankine cycle systems, *Geothermics*, vol. **75**, no. February, pp. 249–258, 2018.

[191] S. Van Erdeweghe, J. Van Bael, B. Laenen, and W. D'haeseleer, Optimal combined heat-and-power plant for a low-temperature geothermal source, *Energy*, vol. **150**, no. 1, pp. 396–409, 2018.

[192] W. C. Davidon, Variable metric method for minimization, *SIAM J. Optim.*, vol. **1**, no. 1, pp. 1–17, 1991.

[193] L. Lukšan and E. Spedicato, Variable metric methods for unconstrained optimization and nonlinear least squares, *J. Comput. Appl. Math.*, vol. **124**, no. 1–2, pp. 61–95, 2000.

[194] M. A. Rosen, I. Dincer, and M. Kanoglu, Role of exergy in increasing efficiency and sustainability and reducing environmental impact, *Energy Policy*, vol. **36**, no. 1, pp. 128–137, 2008.

[195] W. Beckman and S. Klein, Engineering   Equation Solver User's Manual, 2008. [Online]. Available: http://www.fchart.com/ees/ees.shtml

[196] N. Chagnon-Lessard, F. Mathieu-Potvin, and L. Gosselin, Optimal design of geothermal power plants: A comparison of single-pressure and dual-pressure organic Rankine cycles, *Geothermics*, vol. **86**, no. 10787, p. 101787, 2020.

[197] G. V Tomarov, A. A. Shipkov, and E. V Sorokina, Investigation of a binary power plant using different single-component working fluids, *Int. J. Hydrogen Energy*, vol. **41**, pp. 23183–23187, 2016.

[198] X. Wang *et al.*, Working fluid selection for organic Rankine cycle power generation using hot produced supercritical CO 2 from a geothermal reservoir, *Appl. Therm. Eng.*, vol. **149**, no. December 2018, pp. 1287–1304, 2019.

[199] T. Kowalczyk, P. Ziółkowski, and J. Badur, Exergy losses in the Szewalski binary vapor cycle,

Entropy, vol. **17**, no. 12, pp. 7242–7265, 2015.

[200] S. Quoilin, S. Declaye, B. F. Tchanche, and V. Lemort, Thermo-economic optimization of waste heat recovery Organic Rankine Cycles, *Appl. Therm. Eng.*, 2011.

[201] A. Rettig *et al.*, Application of Organic Rankine Cycles (ORC), 2011.

[202] G. Chen *et al.*, The active design of mixtures based on transition temperature of heat source for organic Rankine cycle, *Energy Procedia*, vol. **158**, pp. 1730–1736, 2019.

[203] J. Gamit and A. K. Patel, Overview on Organic Rankine Cycle (ORC), *Int. J. Adv. Eng. Res. Dev.*, vol. **3**, no. 12, pp. 300–303, 2016.

[204] J. Bao, L. Zhang, C. Song, N. Zhang, X. Zhang, and G. He, Comparative study of combined organic Rankine cycle and vapor compression cycle for refrigeration : Single fluid or dual fluid ?, *Sustain. Energy Technol. Assessments*, vol. **37**, no. July 2019, p. 100595, 2020.

[205] F. Valić and D. Beritić-Stahuljak, Chlorofluorocarbons--a new environmental health problem, *Lijec. Vjesn.*, vol. **112**, no. 1–2, pp. 1–6, 1990.

[206] B. H. Edrisi and E. E. Michaelides, Effect of the working fluid on the optimum work of binary-flashing geothermal power plants, *Energy*, vol. **50**, no. 1, pp. 389–394, 2013.

[207] M. Tunc, S. Sisbot, and U. Camdali, Exergy analysis of electricity generation for the geothermal resources using organic rankine cycle: Kizildere-denizli case, *Environ. Prog. Sustain. Energy*, 2013.

[208] Y. Liang and Z. Yu, Working fluid selection for a combined system based on coupling of organic Rankine cycle and air source heat pump cycle, *Energy Procedia*, vol. **158**, no. 2018, pp. 1485–1490, 2019.

[209] R. DiPippo, Geothermal Power Generating Systems, in *Geothermal Power Plants*, 2008.

[210] S. Jalilinasrabady, R. Itoi, P. Valdimarsson, H. Fujii, and T. Toshiaki, Energy and Exergy Analysis of Sabalan Binary Geothermal Power Plant, *J. Geotherm. Res. Soc. Japan*, vol. **33**, no. 3, pp. 113–121, 2011.

[211] E. Akrami, A. Chitsaz, H. Nami, and S. M. S. Mahmoudi, Energetic and exergoeconomic assessment of a multi-generation energy system based on indirect use of geothermal energy, *Energy*, vol. **124**, pp. 625–639, 2017.

[212] M. Yari, A. S. Mehr, V. Zare, S. M. S. Mahmoudi, and M. A. Rosen, Exergoeconomic comparison of TLC (trilateral Rankine cycle), ORC (organic Rankine cycle) and Kalina cycle using a low grade heat source, *Energy*, vol. **83**, pp. 712–722, 2015.

[213] H. R. Jacobs, R. F. Boehm, and A. C. Hansen, Application of direct contact heat exchangers to geothermal power production cycles, 1978.

[214] A. S. Naumova, S. V. Lepeshkin, and A. R. Oganov, Hydrocarbons under Pressure: Phase Diagrams and Surprising New Compounds in the C-H System, *J. Phys. Chem. C*, vol. **123**, no. 33, pp. 20497–20501, 2019.

[215] M. A. Ehyaei, A. Ahmadi, M. A. Rosen, and A. Davarpanah, Thermodynamic Optimization of a Geothermal Power Plant with a Genetic Algorithm in Two Stages, *Processes*, vol. **8**, no. 10, p. 1277, 2020.

[216] K. Pruess, Mathmatical Modeling of Fluid Flow and Heat Transfer, 2002.

[217] R. DiPippo, Geothermal power plants, in *Comprehensive Renewable Energy*, 2012.

[218] A. W Manyonge, Prediction of the future performance of geothermal reservoirs using the concept of deliverability, in *NZ Geothermal Workshop*, 1998, pp. 369–373.

[219] C. R. Faust, J. W. Mercer, C. D. Andrus, and V. E. McKelvey, Finite-difference model of two-dimensional, single-, and two-phase heat transport in a porous medium-version I, 1977.

[220] M. A. Grant and P. F. Bixley, *Geothermal Reservoir Engineering (Second Edition)*, Second Edi. Boston: Academic Press, 2011.

[221] R. Itoi and S. J. Zarrouk, The utilization of transient output measurement to characterize geothermal reservoir properties using AWTAS for well 2H-21 at Hatchobaru geothermal field, Japan, in *World Geothermal Congress*, 2015, p. 7.

[222] M. H. Mubarok, Y. D. Cahyono, S. Patangke, and E. E. Siahaan, A statistical analysis for comparison between lip pressure and separator in production well testing at Lahendong and Ulubelu Field, in *World Geothermal Congress*, 2015, no. 19-25 April 2015, p. 7.

[223] M. F. Biru, Analysis of Well Testing , Temperature and Pressure in, Reykjavik, 2016.

[224] M. Nizami, A Comparison analysis between Russel James Equation and Hiriart Equation in

horizontal discharge lip pressure for production test at geothermal well Using statistical method A Comparison Analysis between Russel James Equation and Hiriart Equation in Horiz, 2016.

[225]   R. James and T. Gould, Bleeding Characteristics of geothermal wells, in *Twelfth workshop on Geothermal reservoir engineerng*, 1987, pp. 297–300.

[226]   A. T. Wibowo, M. Thasril, and P. Sirait, Production Test Analysis of XYZ-Well at Dieng Geothermal Field Using Horizontal Discharge Lip Pressure Method with Russel James Equation and Hiriart Equation, *World Geotherm. Congr. 2015*, no. April, p. 9, 2015.

[227]   Y. Sueyoshi *et al.*, Exploratory well drilling and discharge test of wells MT-1 and MT-2 in the Mataloko geothermal field, Flores, Indonesia, *Bull. Geol. Survery Japa*, vol. **53**, no. 2/3, pp. 307–321, 2002.

[228]   B. M. Sveinbjornsson and S. Thorhallsson, Geothermics Drilling performance , injectivity and productivity of geothermal wells, *Geothermics*, vol. **50**, pp. 76–84, 2014.

[229]   M. J. McGuinness, Feedpoint viscosity in geothermal wellbore simulation, *Geothermics*, vol. **50**, pp. 24–29, 2014.

[230]   M. Marcolini, A. Battistelli, and I. Consultant, Modeling of wellbore flow within geothermal reservoir simulations at field scale, no. September 2012, 2014.

[231]   M. A. Grant, I. G. Donaldson, and P. F. Bixley, *Geothermal reservoir engineering*. Antalya: Kluwer Academic Publishers, 1988.

[232]   J. Ortiz-Ramirez, Two-phase flow in geothermal wells: Development and use of computer code, Stanford, 1983.

[233]   J. W. Mercer, Jr, C. R. Faust, and G. F. Pinder, Geothermal reservoir simulation, New Jersey, 1974.

[234]   P. V. Godbole, C. C. Tang, and A. J. Ghajar, Comparison of void fraction correlations for different flow patterns in upward vertical two-phase flow, *Heat Transf. Eng.*, vol. **32**, no. 10, pp. 843–860, 2011.

[235]   Z. Tugcu, Bilicki, R. DiPippo, E. E. Michaelides, J. Kestin, and P. F. Maeder, Geothermal two-phase flow: A selective, annotated guide to the literature, 1980.

[236]   I. S. Moeck, Catalog of geothermal play types based on geologic controls, *Renew. Sustain. Energy Rev.*, vol. **37**, pp. 867–882, 2014.

[237]   Gudni Axelsson et al, Updated Conceptual Model and Capacity Estimates for the Greater Olkaria Geothermal Systems, Kenya, in *Proceedings, Thirty-Eighth Workshop on Geothermal Reservoir Engineering Stanford University, Stanford, California, February 11-13, 2013 SGP-TR-198*, 2013, no. February 11-13, 2013. [Online]. Available: https://pangea.stanford.edu/ERE/pdf/IGAstandard/SGW/2013/Axelsson.pdf

[238]   U. K. Mbithi, Interpretation of feed zones to map sub-surface permeability structures and natural state simulation : A case study of Olkaria Domes geothermal system in Kenya, University of Iceland, 2016.

[239]   C. O. Ofwona, An update of the natural state numerical model of Olkaria geothermal system , Kenya, in *International Geothermal Conference*, 2003, p. 5.

[240]   J. A. Nyandigisi, Geothermal wells productivity controls case study of wells drilled in the greater Olkaria geothermal area, Kenya, in *8th African Rift Geothermal Conference*, 2020, p. 18.

[241]   P. A. Ouma, *Geothermal exploration and development of the Olkaria geothermal field*. United Nations University, 2007. [Online]. Available: http://www.os.is/gogn/flytja/JHS-Skjol/Kenya 2007/Papers/43_Ouma.pdf

[242]   V. K. Koech, Numerical geothermal reservoir modelling and infield reinjection design, constrained by tracer test data: Case study for the Olkaria geothermal field in Kenya, University of Iceland, 2014. [Online]. Available: https://orkustofnun.is/gogn/unu-gtp-report/UNU-GTP-2014-05.pdf

[243]   M. K. Kibet and P. K. S. Magut, Developing a geo-thermometry and measured down-hole temperature to identify feed-zones., *J. Appl. Geol. Geophys.*, vol. **8**, no. 4, pp. 1–15, 2020.

[244]   A. Baba, J. Bundschuh, and D. Chandrasekharam, Eds., *Geothermal systems and energy Resources: Turkey and Greece*, 7th ed. Taylor & Francis. [Online]. Available: https://books.google.co.jp/books?id=iFvLBQAAQBAJ&lpg=PA101&ots=CisneJcaF3&dq=ex plaining giggenbach ternary geo&pg=PR5#v=onepage&q&f=true

Piper diagram for classifying the types of geochemical waters

(https://hatarilabs.com/ih-en/what-is-a-piper-diagram-and-how-to-create-one)

Cation geothermometry equations [148], [209], [244].

Geothermometer	Equations (concentration of Na, K mg/L)	
Na–K (100–275°C)	$T = 856 / (\log Na/K + 0.857) - 273.15$	Truesdell (1976)
Na–K	$T = 883 / (\log Na/K + 0.780) - 273.15$	Tonani (1980)
Na–K (25–250°C)	$T = 933 / (\log Na/K + 0.993) - 273.15$	Arnorsson et al. (1983)
Na–K (250–350°C)	$T = 1319 / (\log Na/K + 1.699) - 273.15$	Arnorsson et al. (1983)
Na–K	$T = 1217 / (\log Na/K + 1.483) - 273.15$	Fournier (1979)
Na–K	$T = 1178 / (\log Na/K + 1.470) - 273.15$	Nieva and Nieva (1987)
Na–K	$T = 1390 / (\log Na/K + 1.750) - 273.15$	Giggenbach (1988)
K–Mg	$T = 2330 / (\log K^2/Mg + 7.35) - 273.15$	Fournier (1991)
K–Mg	$T = 1077 / (\log K^2/Mg + 4.033) - 273.15$	Fournier (1991)
K–Mg	$T = 4410 / (\log K/Mg + 14.0) - 273.15$	Giggenbach (1988)
K–Li	$T = 2200 / (\log Li/Mg + 5.470) - 273.15$	Kharaka and Mariner (1989)
Na–Li	$T = 1590 / (\log Na/Li + 0.779) - 273.15$	Kharaka et al. (1982)
Na–Li (Cl > 0.3 M)	$T = 1195 / (\log Na/Li + 0.130) - 273.15$	Fouillac and Michard (1981)
Na–Li (Cl < 0.3 M)	$T = 1000 / (\log Na/Li + 0.389) - 273.15$	Fouillac and Michard (1981)
Na–Li	$T = 1267 / (\log Na/Li + 0.07) - 273.15$	Verma and Santoya (1997)
Li–Mg	$T = 2200 / (\log Li/(Mg)^{1/2} + 5.47) - 273.15$	Kharaka and Mariner (1989)
Na–Ca	$T = 1096.7 / (\log Na/\sqrt{Ca} + 2.37) - 273.15$	Tonani (1980)
K–Ca	$T = 1930 / (\log K/\sqrt{Ca} + 2.920) - 273.15$	Tonani (1980)
Na–K–Ca	$T = 1647 / (\log(Na/K) + \beta[\log(\sqrt{Ca}/Na) + 2.06 + 2.47) - 273.15$ $\beta = 4/3$ for $T < 100°C$; $= 1/3$ for $> 100°C$	Fournier and Truesdell (1973)

Production wells connected to Olkaria IV power plant

No	Well No	Location	Plant	Year production started	Separator Station	Current Status
1	OW-901A	Domes	Olkaria IV	2019	OW-921	Producing
2	OW-901B	Domes	Olkaria IV	2019	OW-921	Producing
3	OW-903A	Domes	Olkaria IV	2014	SD1	Producing
4	OW-903B	Domes	Olkaria IV	2014	SD1	Producing
5	OW-904	Domes	Olkaria IV	2014	SD1	Producing
6	OW-904A	Domes	Olkaria IV	2014	SD1	Producing
7	OW-904B	Domes	Olkaria IV	2014	SD1	Producing
8	OW-907A	Domes	Olkaria IV	2014	SD4	Producing
9	OW-908	Domes	Olkaria IV	2014	SD2	Producing
10	OW-908A	Domes	Olkaria IV	2014	SD2	Producing
11	OW-908B	Domes	Olkaria IV	2015	SD2	Producing
12	OW-909	Domes	Olkaria IV	2015	SD2	Producing
13	OW-909A	Domes	Olkaria IV	2015	SD2	Producing
14	OW-910	Domes	Olkaria IV	2015	SD2	Producing
15	OW-910A	Domes	Olkaria IV	2015	SD2	Producing
16	OW-910B	Domes	Olkaria IV	2015	SD2	Producing
17	OW-914	Domes	KWG 06 & 07	2014	OW-914	Producing
18	OW-914A	Domes	KWG 04	2014	OW-914A	Producing
19	OW-914B	Domes	KWG 05	2014	OW-914B	Producing
21	OW-921	Domes	Olkaria IV	2019	OW-921	Producing
22	OW-921A	Domes	Olkaria IV	2019	OW-921	Producing
23	OW-926A	Domes	Olkaria IV	2019	OW-926	Producing
24	OW-926B	Domes	Olkaria IV	2019	OW-926	Producing

Reinjection wells for Olkaria IV.

No	Well	Location	Year Inj. Started	Remarks
1	OW-906A	Domes	2015	Brine Reinjection
2	OW-911	Domes	2015	Brine Reinjection
3	OW-911A	Domes	2015	Brine Reinjection
4	OW-913A	Domes	2015	Brine Reinjection
5	OW-902A	Domes	2015	Condensate Reinjection
6	OW-921B	Domes	2019	Hot Reinjection
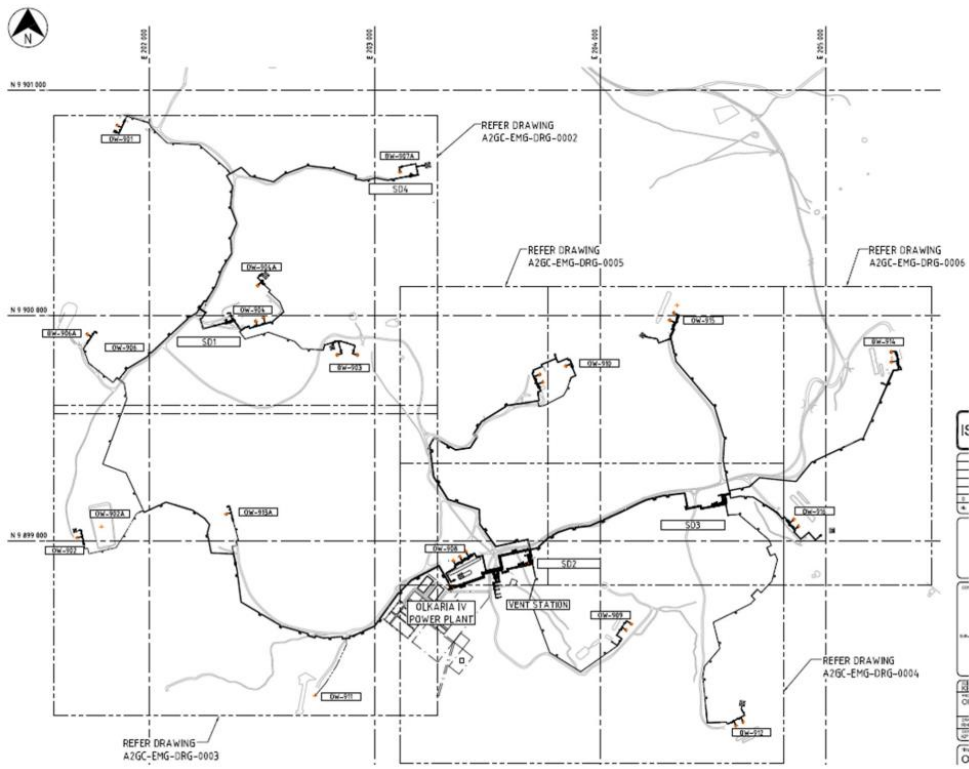
Pipe line connection and well locations supplying steam to Olkaria IV power plant [69].

EES code for optimisation of Olkaria IV power plant

```
{Current  Olkaria IV with out modifications, optimisation}
T_o=23
P_o=86
h_o=enthalpy(Steam_IAPWS,x=0,T=T_o)
s_o=entropy(Steam_IAPWS,x=0,T=T_o)
T_ambient = T_o + 273.15
 m_dot[0]=m_dot[1]
P[0]=13600                                       {Formatiom pressure from Wellbore simulator}
x[0]=0
h[0]=enthalpy(Steam_IAPWS,x=x[0],P=P[0])
s[0]=entropy(Steam_IAPWS,P=P[0],x=x[0])
T[0]=temperature(Steam_IAPWS,P=P[0],x=x[0])
Ex[0]=m_dot[0]*((h[0]-h_o) - T_ambient*(s[0]- s_o)) {Two phase Wellhead flow 142 t/hr}
{Wellhead. The WHP from data collected from KenGen}
m_dot[1]= 430[kg/s]                              {Two phase Wellhead flow 142 t/hr}
P[1]=1180
T[1]=187
h[1]=enthalpy(Steam_IAPWS,P=P[1],x=x[1])
s[1]=Entropy(Steam_IAPWS,x=x[1],t=t[1])
x[1]=x[2]
Ex[1]=m_dot[1]*((h[1]-h_o) - T_ambient*(s[1]- s_o))
Q_dot_in=m_dot[1]*h[1]
Eta_th=W_net/Q_dot_in
{Before separator}
P[2]=1180
h[2]=enthalpy(Steam_IAPWS,P=P[2],x=x[2])
s[2]=Entropy(Steam_IAPWS,T=T[2],x=x[2])
T[2]=Temperature(Steam_IAPWS,P=P[2],x=x[2])
x[2]=0.65                                        {Itoi Senseis model}
Ex[2]=m_dot[1]*((h[2]-h_o) - T_ambient*(s[2]- s_o))
Ex|d[1]=Ex[2]-Ex[3]-Ex[4]                        {Separator exergy destroyed}
Ex_available=Ex[1]-Ex[3]
eta_utz=W_net/Ex_available
eta_2=W_net/Ex[1]
{Reinjection point}
T[3]=T[4]
x[3]=0
m_dot[1]-m_dot[3]=m_dot[5]
h[3]=Enthalpy(Steam_IAPWS,x=x[3],T=T[3])
s[3]=Entropy(Steam_IAPWS,x=x[3],h=h[3])
Ex[3]=m_dot[3]*((h[3]-h_o) - T_ambient*(s[3]- s_o)) {Wasted exergy for hot reinjection}
{After separtion and before turbine inlet}
P_5top=640
x_5top=1
T_5top=Temperature(Steam_IAPWS,P=P_5top,h=h_5top)
h_5top=Enthalpy(Steam_IAPWS,x=x_5top,P=p_5top)
s_5top=Entropy(Steam_IAPWS,h=h_5top,P=P_5top)
s[4]=s_s5top
h_s5top=Enthalpy(Steam_IAPWS,s=s_s5top,P=P[5])
Ex_5top=m_dot[5]*((h_5top-h_o) - T_ambient*(s_5top- s_o))
Eta_turbinet=(h_5top-h_s5)/(h_5top-h_s5top)
W_grosstop=(h_5top-h_s5)*(m_dot[5])*Eta_ele*Eta_mech*Eta_gen
Eta_turbinet=0.9
Ex|d[6]=Ex[4]-Ex[5]-W_grosstop                   {turbine exergy destroyed}
P[4]=1100 [kPa] {!Optimisation}
x[4]=1
T[4]=Temperature(Steam_IAPWS,P=P[4],h=h[4])
h[4]=Enthalpy(Steam_IAPWS,x=x[4],P=P[4])
```

s[4]=Entropy(Steam_IAPWS,x=x[4],P=P[4])
Ex[4]=m_dot[5]*((h[4]-h_o) - T_ambient*(s[4]- s_o))
Eta_turbine=0.86
Eta_gen=0.98
Eta_mech=0.97
Eta_ele=0.98
Spcefic_powerout=W_net/m_dot[5]
eta_t=0.85
Eta_turbine=(h[5]-h[8])/(h[5]-h[7])
W_gross=(h[5]-h[8])*(m_dot[5]-m_dot[13])
W_gtotal=W_gross+W_grosstop
W_gross-W_parasitic=W_net
W_gej[2]+W_gej[2]+Work_fan+W_p2[9]=W_parasitic
eta_parasitic=W_parasitic/W_gross
Work_fan= 2500   {!!Approximated from the cooling curve characteristics
Fekuda for 12024.8 t/hr}
W_turbineb=(h[5]-h_7b)*m_dot[5]
A=0.425*(h[5]-h[7])
h_7b=(h[5]-A*(1-h_4/(h_g-h_4))/(1+A/(h_g-h_4)))
x[5]=1
m_dot[5]=x[2]*m_dot[1]
T[5]=Temperature(Steam_IAPWS,P=P[5],h=h[5])
h[5]=Enthalpy(Steam_IAPWS,x=x[5],P=P[5])
s[5]=Entropy(Steam_IAPWS,h=h[5],P=P[5])
Ex[5]=m_dot[5]*((h[5]-h_o) - T_ambient*(s[5]- s_o))
Ex|d[2]=Ex[5]-Ex[8]-W_gross   {turbine exergy destroyed}
{Steam Ejectors twostages, analysed as hybrid}
P[6]=P[5]
x[6]=1
P[5]=500[kPa]   {!Turbine inlet pressure varied}
P[8]=8.5[kPa]   {!OPtimise}
T[13]= 39
P[13]= 22   {!Optimise. Intercondenser pressure, these pressure is also
optimised to have minimum NCG work}
Ncg=0.25/100   {Olkaria NCG at 0.25 mass of steam from ! Kwambai}
T[17]= T[16]+273
P_sat[13]=p_sat(Steam_IAPWS,T=T[13])   {first stage ejector}
Total_Wncg=W_ncg+Outputd
R=8.314
k=1.3
x[13]=1
T[18]=T[13]+273
 P_sat[4]=p_sat(Steam_IAPWS,T=T[7])
NcgPP[1]=P[7]-P_sat[13]   {Ncg Partial pessure P condenser less P sat at
intercondenser}
m_dot_CO2=(Ncg*m_dot[5])/44   {kmol/s}
m_dot_stCO2=m_dot_CO2*(P_sat[13]/NcgPP[1])
m_dot_steam[1]=m_dot_stCO2*18   {kmol/s of accccompanying steam}
TotalMols[1]=m_dot_CO2 +m_dot_stCO2   {kmol/s of accccompanying steam + CO2/NCG}
h[13]=enthalpy(Steam_IAPWS,T=T[13],x=x[13])
sg[13]=entropy(Steam_IAPWS,x=x[13],P=p[13])
sf[13]=entropy(Steam_IAPWS,x=0,P=p[13])
hg[13]=enthalpy(Steam_IAPWS,x=x[13],P=p[13])
hf[13]=enthalpy(Steam_IAPWS,x=0,P=p[13])
ratio_13=(s[5]-sf[13])/(sg[13]-sf[13])
ha[13]=hf[13]+ratio_13*(hg[13]-hf[13])
DELTAh[13]=h[5]-ha[13]   {Enthalpy drop in the motive steam from main pipeline to
intercondenser at Pressure 13}

{!Exergy destroyed in the gas removal system}

```
Q_dot_intercoolers=(h[13]-h[19])*m_dot[13]
T[19]=T[8]
x[19]=0
h[19]=enthalpy(Steam_IAPWS,T=T[19],x=x[19])
s[19]=Entropy(Steam_IAPWS,h=h[19],x=x[19])
Ex[19]=m_dot[19]*((h[19]-h_o) - T_ambient*(s[19]- s_o))
m_dot[19]=m_dot[21]+m_dot[13]-ncg*m_dot[13]
Q_dot_intercoolers=(h[19]-h[12])*m_dot[21]
m_dot[20]=ncg*m_dot[5]                              {NCG from the condenser}
m_dot[22]=ncg*m_dot[13]+m_dot[20]                   {NCG discharged to the atmosphere}
hncg[20]=Enthalpy(CarbonDioxide,T=T[8],P=P[8])
sncg[20]=entropy(CarbonDioxide,T=T[8],P=P[8])
sncg[20]=sncg[22]
hncg[22]=Enthalpy(CarbonDioxide,T=T_o,s=sncg[22])
hncg_o=Enthalpy(CarbonDioxide,T=T_o,P=P_o)
sncg_o=entropy(CarbonDioxide,T=T_o,P=P_o)
Ex[13]=m_dot[13]*((h[13]-h_o) - T_ambient*(s[13]- s_o))
s[13]=entropy(Steam_IAPWS,h=h[13],P=p[13])
Ex[20]=m_dot[20]*((hncg[20]-hncg_o) - T_ambient*(sncg[20]- sncg_o))
Ex[22]=m_dot[22]*((hncg[22]-hncg_o) - T_ambient*(sncg[22]- sncg_o))
Ex|d[5]=Ex[13]-Ex[19]+Ex[21]+Ex[20]-Ex[22]+W_ncg
    {NCG exergy gas extraction system}
T[21]=T[12]
x[21]=0
h[21]=enthalpy(Steam_IAPWS,T=T[21],x=x[21])
s[21]=Entropy(Steam_IAPWS,h=h[21],x=x[21])
Ex[21]=m_dot[21]*((h[21]-h_o) - T_ambient*(s[21]- s_o))
W_gej[1]+W_gej[2]=W_ncg

W_gej[1]=k/(k-1)*R*T[18]*((P[13]/P[7])^((k-1)/k)-1)*TotalMols[1] {Required compression power, }
Eta_ej=0.20
m_dot[13]=W_gej[1]/(DELTAh[13]*Eta_ej)
"!Output decrement from heat balance"
SSC=W_gross/m_dot[5]
Outputd=m_dot[13]*SSC                               {output power reduction}
{2nd stage Stage}                                   {12.4 bar  45.5 C, same as condesers operating
conditions}
T[16]=T[8]
P_sat[16]=p_sat(Steam_IAPWS,T=T[16])
NcgPP[2]=P[13]-P_sat[16] {condenser satutation}
m_dot_steam[2]=m_dot_stCO2*(P_sat[16]/NcgPP[2])
TotalMols[2]=m_dot_steam[2] +m_dot_stCO2
W_gej[2]=R*T[17]*ln(P_o/P[13])*TotalMols[2]/(Eta_m2*Eta_p2)
{Required Power for gas compression in Vacuum pump, isothermal change}
Eta_m2=0.35
Eta_p2=0.90
Eta_pg=0.45
{Condenser point}
s[5]=s[7]
h[7]=Enthalpy(Steam_IAPWS,s=s[7],P=P[7])
                                    {!To vary to ensure positive exergy destruction}
P[7]=P[8]
T[7]=Temperature(Steam_IAPWS,P=P[7],h=h[7])
Ex[7]=m_dot[5]*((h[7]-h_o) - T_ambient*(s[7]- s_o))
h_g=Enthalpy(Steam_IAPWS,P=P[7],x=1)
h_4=Enthalpy(Steam_IAPWS,P=P[7],x=0)
x_7=(h[7]-h_4)/(h_g-h_4)
x_3b=(h[7]-h_4)/(h_g-h_4)
s[8]=Entropy(Steam_IAPWS,h=h[8],P=P[8])
T[8]=Temperature(Steam_IAPWS,P=P[8],s=s[8])
```

Ex[8]=m_dot[5]*((h[8]-h_o) - T_ambient*(s[8]- s_o))
x[8]=quality(Steam_IAPWS,h=h[8],P=P[8])
Ex|d[3]=Ex[8]-Ex[9]-Ex[12]-Ex[20]
    {condenser exergy destroyed}
Q_dot_condeser=Q_dot_cw
m_dot[12]=m_dot[5]*(h[8]-h[9])/(cp*(T[9]-T[12]))
    {COOLING WATER FLOW RATE}
T[9]=Temperature(Steam_IAPWS,P=P[9],x=x[9])
 P[9]=P[8]
T[12]=T_o+3
x[9]=0
h[9]=enthalpy(Steam_IAPWS,T=T[9],x=x[9])
s[9]=Entropy(Steam_IAPWS,h=h[9],x=x[9])
Ex[9]=m_dot[9]*((h[9]-h_o) - T_ambient*(s[9]- s_o))
x[10]=1
h[10]=enthalpy(Steam_IAPWS,P=P[9],x=x[10])
s[10]=Entropy(Steam_IAPWS,h=h[10],x=x[10])
Ex[10]=m_dot[9]*((h[10]-h_o) - T_ambient*(s[9]- s_o))
h[12]=enthalpy(Steam_IAPWS,T=T[12],x=x[12])
s[12]=Entropy(Steam_IAPWS,h=h[12],x=x[12])
Ex[12]=m_dot[12]*((h[12]-h_o) - T_ambient*(s[12]- s_o))
x[12]=0
x[11]=0
T[15]=T[11]
h[11]=enthalpy(Steam_IAPWS,T=T[11],x=x[11])
s[11]=entropy(Steam_IAPWS,T=T[11],x=x[11])
Ex[11]=m_dot[11]*((h[11]-h_o) - T_ambient*(s[11]- s_o))
Q_dot_condeser=m_dot[5]*(h[8]-h[9])
cp=4.182
m_dot[9]=m_dot[12]+m_dot[5]
T[9]=T[14]
T[15]=T_o
T_wb=wetbulb(AirH2O,T=T_o,w=omega[15],P=P_o)
phi[15] = 0.75   "Relative humidity of air"
phi[14] =1   "Relative humidity of air from tower"
omega[14] = humrat(AirH2O, T = T[14], r = phi[14], P=P_o)
omega[15] = humrat(AirH2O, T = T[15], r = phi[15], P=P_o)
h[14]=enthalpy(AirH2O,T=T_o,w=omega[14],P=P_o)
s[14]=entropy(AirH2O,T=T[14],P=P_o,R=phi[14])
h[15]=enthalpy(AirH2O,T=T_o,w=omega[15],P=P_o)
s[15]=entropy(AirH2O,T=T[15],P=P_o,R=phi[15])
W_p2[9]=g*m_dot[9]*H/(Eta_cwp*Eta_mp*1000)
rho=density(Steam_IAPWS,T=T[9],x=x[9])
Eta_cwp=0.85
Eta_mp=0.9
H=30   {Cooling tower height}
g=9.81
V=m_dot[9]/1000
h[9] * m_dot[9] + h[15] * m_dot_a[15]=h[12] * m_dot[12] + h[14] * m_dot_a[14]+h[11] * m_dot[11]
m_dot[9]+m_dot_w[15]=m_dot[12]+m_dot_w[14]+m_dot[11]
m_dot_a[14]= m_dot_a[15]
m_dot_w[15]=omega[15]*m_dot_a[15]
m_dot_w[14]=omega[14]*m_dot_a[14]
epsilon_CT=(T[9]-T[12])/(T[9]-T[15])
Cwratio[1]=m_dot[9]/m_dot[14]
m_dot[14]=m_dot_a[14]
Ex|d[4]=Ex[9]-Ex[12]+Ex[11]+Work_fan
    {cooling tower exergy destroyed}
Sum_EX|DT=Ex|d[1]+Ex|d[2]+Ex|d[3]+Ex|d[4] +Ex|d[5]+Ex|d[6]
{Exergonomics of powe plant}

n= 30 {Number of years}

i=0.10 {Interest rates, i}

tau= 8322 {Annual plant operation hours, }

gamma= 1.06 {Maintenance factor}

r_n= 0.05 {Nominal escalation rate rn}

c_Ex=1.3 {Unit cost of exergy ($/GJ)}

e_pr= 0.1 {Average of electricity price for Kenya, [$/(kW$h)]}

alpha_CO_2= 0.266 {amount of CO2 emission for 1 kWh, $?_{(?CO?_2)}$(kg/kwh)}

alpha_pe=0.849 {amount of petroleum consumed to produce 1 kWh, $?_{pe}$ (L/kwh)}

CRF=(i*(1+i)^n)/((1+i)^n-1)

k_ex=(1+r_n)/(1+i)

f_CEL=(CRF*k_ex*(1+k_ex^n))/(1-k_ex)

v[2]=Volume(Steam_IAPWS,T=T[2],x=x[2])

rho[2]=density(Steam_IAPWS,T=T[2],x=x[2])

rho[1]=density(Steam_IAPWS,T=T[2],x=0)

Q[2]=v[2]*m_dot[5]

v_t=0.069*((rho[1]-rho[2])/rho[1])^0.5

A_ip=Q[2]/v_t

Z_Tur=4405*(W_gross)^0.89 {Turbine}

Z_dot_Tur=(Z_Tur*gamma*CRF)/(tau)

C_dot_F|In=(c_Ex*Ex[1])/1000000

C_dot_1=C_dot_F|In

(c_2*Ex[2])/1000000=(c_3*Ex[3])/1000000+(c_4*Ex[4])/1000000

c_2=c_3

c_Ex=c_2

c_5=c_4

(c_5*Ex[5])/1000000+Z_dot_Tur=(c_8*Ex[8])/1000000+(c_w*W_gross)/1000000

c_5=c_8

(c_8*Ex[8])/1000000+Z_dot_CD+(c_12*Ex[12])/1000000=(c_11*Ex[11])/1000000+(c_9*Ex[9])/1000000

Z_CD|eq=1773*m_dot[5] {Condenser}

Z_dot_CD=(Z_CD|eq*gamma*CRF)/(tau)

c_8=c_9

c_11=c_12

m_dot_cwg=m_dot[9]*0.264172*60 {Mass flow rate of cooling water in gallons}

f=m_dot_cwg

Z_ct=-10^(-10) *f^3-10^(-5)*f^2+70.552*f+61609

Z_ctOM=-8*10^(-6) *f^2+13.291*f+13850

Z_ctTotal=Z_ct+Z_ctOM

Pr_CT=63596*exp(0.0138772*m_dot[9])

Error=abs(Z_ct-Pr_CT)/Z_ct*100

Z_dot_CT=(Z_ctTotal*gamma*CRF)/(tau)

Z_pmwf|eq=1120*(W_p2[9])^0.8 {Working fluid pump}

Z_dot_pwf=(Z_pmwf|eq*gamma*CRF)/(tau)

Z_fan|eq=1120*(Work_fan)^0.8 {Fans}

Z_dot_fan=(Z_fan|eq*gamma*CRF)/(tau)

Z_dot_plant=Z_dot_pwf+Z_dot_CD+Z_dot_Tur+Z_dot_fan+Z_dot_CT

Z_dot_Tplant=Z_dot_plant*(CRF+gamma)

Z_plant=Z_dot_plant*tau/(gamma*CRF)

Cost_Total=C_dot_1+Z_dot_Tplant

Cost_Total=(c_pr*W_net)*36/10000

c_pr*Sum_EX|DT/1000000*3600=C_dot_D

c_plant*Sum_EX|DT*36/10000=Z_dot_Tplant

C_dot_DD=c_Ex*Sum_EX|DT*3600/1000000